The influence of anisotropy on the consolidation behaviour of peat

C. Zwanenburg

October 2005

The influence of anisotropy on the consolidation behaviour of peat

PROEFSCHRIFT

ter verkrijging van de graad van doctor
aan de Technische Universiteit Delft,
op gezag van de Rector Magnificus Prof. dr. ir. J.T. Fokkema,
voorzitter van College voor Promoties,
in het openbaar te verdedigen
op woensdag 7 december 2005 om 10:30 uur
door Cornelis ZWANENBURG
civiel ingenieur
geboren te Rotterdam

Dit proefschrift is goedgekeurd door de promotor:
Prof. dr. ir. F.B.J. Barends

Samenstelling promotiecommissie:

Rector Magnificus,	voorzitter
Prof. dr. ir. F.B.J. Barends,	Technische Universiteit Delft, promotor
Prof. dr. J.P. Magnan,	Laboratoire des Ponts et Chaussées
Prof. dr. ir. F. Molenkamp,	Technische Universiteit Delft
Prof. dr. ir. A. Verruijt,	Technische Universiteit Delft
Prof. ir. A.F. van Tol,	Technische Universiteit Delft
Prof. drs. ir. H. Vrijling,	Technische Universiteit Delft
dr. ir. E.J. den Haan,	GeoDelft

Published and distributed by: DUP Science

DUP Science is an imprint of
Delft University Press
P.O.Box 98
2600 MG Delft
The Netherlands
Telephone: +31 15 27 85 678
Telefax: +31 15 27 85 706
E–mail info@Library.TUDelft.nl

ISBN 90-407-2615-9

Keywords: geotechnics, consolidation, anisotropy, peat

Printed in The Netherlands

Acknowledgement

This study is conducted at Delft University of Technology and financially supported by the DIOC project and GeoDelft. During the four and a half years it took me to complete this study I was supported by a large number of people. With this opportunity I would like thank them.

First of all I would I like to thank my promotor Prof. Frans Barends who gave me the opportunity to enrich my practical experience I was building up as a consultant by a fundamental study at Delft University of Technology. Over the years he taught me how powerful mathematics can be in describing nature in general and soft soil behaviour in particular.

Next I would like to thank the geotechnical engineering group at Delft University of Technology who offered me a quiet place to work, while always willing to help. Especially I would like to mention Han de Visser who helped me to solve all kinds of practical problems in retrieving soil samples and conducting laboratory tests. For example without his help I would not have possessed the perfect membranes needed triaxial testing.

I would like to express gratitude to GeoDelft, especially Gerben Beetstra who enabled my secondment at Delft University of Technology and Jan de Feijter who allowed me to work in the laboratory. I would like thank: Aad Schapers and Aad van Slingerland who taught me the basics of working in a geotechnical laboratory, Lambert Smidt who was always willing to help with the software controlling the test facilities and Willem van Pernis and Ruud van der Berg who helped me in conducting large scale experiments.

I'm especially grateful to Evert den Haan who followed my study critically and, in discussing the results, especially the laboratory measurements, gave me a better understanding in soft soil behaviour and helped me to focus.

Finally but most important I would like to thank Diane who hasn't seen much of me in the last years but was always encouraging me to continue. I hope that I will ever be able to make that up to her.

Abstract

The influence of anisotropy on the consolidation behaviour of peat

Soft soil is often described as an anisotropic heterogeneous material. Standard soil investigation mainly involves vertically retrieved samples. Information on the parameters working in the horizontal direction remains scarce. Principally each soil property like permeability, stiffness or strength might show anisotropic behaviour. This thesis focuses on anisotropy in stiffness and the possibility to use conventional laboratory measurement techniques to determine the level of anisotropy in stiffness.

One type of soft soil that particularly is expected to behave anisotropically is peat. A possible anisotropy in stiffness of peat can be explained by the presence of fibres. Depending on the rate of humification and organic origin the fibres contribute to the stiffness of peat. If the peat fibres are mainly aligned in one plane it is to be expected that the stiffness perpendicular to this plane deviates from the stiffness working in this plane. Anisotropy due to the presence of fibres is known as structural anisotropy. Since peat is a soft and very compressible material asymmetrical loading might also induce anisotropy in stiffness. This type of anisotropy is known as induced anisotropy.

Consolidation behaviour of soil is strongly influenced by the stiffness of the considered material. For special conditions the pore pressure development during consolidation differs from the usually found monotonic decrease. These special conditions are e.g. found when a conventional triaxial sample with a stiff plate on top and bottom is allowed to drain at the outer radius. Then the outer radius of the sample tends to drain at an early stage of the consolidation process while in the inner core of the sample dissipation of pore water takes place at a later stage. Consolidation of the outer radius of the sample leads to volumetric strain in this area. This volumetric strain in combination with the stiff plate on top leads to a redistribution of stresses in which a part of the load carried by the outer radius is transferred to the yet unconsolidated inner core of the sample. The pore pressure development in the inner core will show an initial increase followed by the usual monotonic decrease after reaching some peak value. This effect is known as the Mandel–Cryer effect. Since this peak is strongly influenced by the stiffness parameters of the considered soil the question arises if measurements of this effect can be used for characterization of anisotropy.

The mathematical analysis of the consolidation behaviour of an anisotropic cylindrical soil sample shows the influence of anisotropy in three aspects. First is the Mandel–Cryer effect. The maximum value reached by the peak in pore pressure development depends on the stiffness parameters. The peak is relatively large for samples with a low axial stiffness in combination with a large radial stiffness. A minor peak is found for the opposite conditions. The second aspect is the initial undrained pore pressure reaction. For a fully saturated soil undrained material behaviour means constant volume deformation. Then for isotropic conditions the pore pressure reaction equals the isotropic stress increase. However in anisotropic soil volumetric strain is induced by isotropic stress as well as deviatoric stress, leading to a different undrained pore pressure reaction. The third aspect is the consolidation period, which is not further elaborated.

The mathematical analysis is based on linear elasticity. However, soil behaviour is influenced by plastic deformations. Even at small strain level unrecoverable deformations occur. For over–consolidated samples equivalent elastic moduli can be used which incorporate some plasticity.

When comparing the mathematical analysis to measurements this type of moduli is considered.

Triaxial tests on peat samples are conducted to test the analytical analysis. Pore pressure in the inner core of the sample is measured using a miniature pore pressure transducer connected to a needle, which is pierced through the membrane. Measurements on conventional triaxial samples rarely show the Mandel–Cryer effect. This can be explained by drain resistance in combination to the variable permeability of peat. Since the influence of drain resistance is relatively small for large scale samples, a test on a large scale sample is conducted. Measurements of the drain pressure show that drain resistance is negligible for the large scale test set–up. The test is conducted in two phases. First the pore pressure development is measured for small isotropic pre–loading conditions. Second, the pore pressure development is measured after a large axial pre–consolidation. In the first phase a minor Mandel–Cryer effect is found. The small measured effect cannot be reproduced by the analytical solutions. The second phase, however, shows a large Mandel–Cryer effect, which can be reproduced by the analytical solution. A closer examination of the permeability during the different test phases shows that for the first phase a considerable change in permeability occurs while for the second phase the permeability is nearly constant.

In general, the measurements clearly show the influence of the anisotropy on the initial pore pressure reaction. The influence is illustrated by the angle of the undrained effective stress path (ESP). For over–consolidated isotropic conditions the ESP will be vertical. Anisotropic conditions will lead to a tilted ESP. The level of anisotropy depends strongly on the load history of the tested sample. For isotropically pre–loaded samples the tested peat samples show only a minor degree of anisotropy. Axially pre–loaded samples however show a clear deviation in ESP angle indicating anisotropy. Despite axial pre–loading measurements indicate an increase in radial stiffness. The results can be explained by pre–stressing of the fibres. The samples are retrieved from underneath a flat surface in horizontal and vertical direction. Triaxial tests, oedometer tests and Simple Shear tests on non pre–loaded and isotropic pre–loaded samples show equivalent results for horizontally and vertically retrieved samples, indicating no initial anisotropy. For these conditions the fibres are probably not aligned in some main direction. Due to the pre–loading the fibres are directed and become entangled to one another. This leads to an increase in radial stiffness. The results appear to be independent from the orientation of the sample main axis to the vertical in the field. It is therefore concluded that the presence of fibres in itself do not cause anisotropy. Anisotropy in the tested peat has a strong loading induced component.

It can be concluded that for conventional triaxial testing measurements of the Mandel–Cryer effect can not be used for parameters assessment of peat. Even if adjustments are made to prevent influence of drain resistance the variable permeability will mask the Mandel–Cryer effect. Since a variable permeability can not be avoided, except after severely remoulding the sample, measurements of the Mandel–Cryer effect cannot be used to indicate stiffness parameters of the tested soil. However the angle of the undrained ESP for over–consolidated samples can be used to determine the level of anisotropy of the tested material.

The application of undrained ESP to estimate the level of anisotropy for peat is illustrated by a series of triaxial tests on over–consolidated peat samples retrieved near the dike surrounding the island of Marken. Samples retrieved from underneath the dike are axially considerably more pre–consolidated due to the weight of the dike than samples retrieved at the toe. The samples from underneath the dike show a larger deviation of ESP than found for samples at the toe of the dike. This indicates a larger degree of anisotropy for peat underneath the dike than at the toe.

Another example of radial consolidation is found around vertical drains. Analytical solutions show that for isotropic material behaviour no Mandel–Cryer effect will be found around a vertical drain. For anisotropic soil behaviour the analytical analysis predicts a small Mandel–Cryer effect. Moreover, it shows that anisotropy accelerates or delays the consolidation process. This effect is stronger than can be expected from common variation in consolidation coefficient.

C. Zwanenburg, *The influence of anisotropy on the consolidation behaviour of peat* Ph.D. Thesis, Delft University of Technology. Delft University Press, 2005

Contents

Acknowledgement **v**

Abstract **vii**

List of Symbols **xiii**

1 Scope of research **1**

2 Compressibility of soil constituents **3**
2.1 Parameters of compressibility . . . 3
2.2 Compressibility of the pore fluid, β_{fg} . . . 3
2.3 Compressibility of the solid particles . . . 5
2.3.1 Compression due to isotropic loading, β_{sf} . . . 5
2.3.2 Compression due to inter granular contacts, β_{ss} . . . 6
2.4 Compressibility of the skeleton, β . . . 8
2.5 The effective stress concept . . . 8
2.6 Skempton B–factor . . . 9

3 Cross–anisotropic elasticity **13**
3.1 Hooke's law for cross–anisotropy . . . 13
3.2 Bounding values . . . 17
3.3 Stresses . . . 19

4 Parameter assessment **21**
4.1 Reducing the number of independent parameters . . . 21
4.2 Reported measurements . . . 25
4.3 Undrained tests . . . 28
4.3.1 Initial pore pressure . . . 28
4.3.2 Drained and undrained stiffness parameters . . . 30
4.3.3 The undrained effective stress path . . . 31

5 3D consolidation **35**
5.1 Introduction . . . 35
5.2 Literature overview . . . 35
5.3 Solution for isotropic linear elasticity . . . 38
5.3.1 General assumptions . . . 38
5.3.2 Axial symmetric conditions . . . 39
5.3.3 Plane strain conditions . . . 45
5.4 Solution for cross–anisotropic elasticity . . . 46
5.5 Alternative conditions . . . 52

6 Laboratory measurements **57**
6.1 Tests on peat . . . 57
6.2 Characterisation of tested soil . . . 58
6.2.1 Sample location . . . 58
6.2.2 Descriptive parameters . . . 58
6.2.3 Pre–consolidation and permeability . . . 60
6.3 Shear Modulus . . . 62
6.3.1 Bender element tests . . . 62
6.3.2 Simple Shear measurements . . . 63
6.3.3 Conclusions . . . 67
6.4 Pore pressure measurement at the sample centre . . . 67
6.5 Initial saturation, B–factor measurement . . . 68
6.6 Undrained Young's moduli and Effective Stress Paths . . . 70
6.6.1 Anisotropy after an isotropic pre–consolidation . . . 70
6.6.2 Anisotropy after an anisotropic pre–consolidation . . . 74
6.6.3 Conclusions . . . 76
6.7 The Mandel–Cryer effect . . . 77
6.7.1 Measurements and analysis . . . 77
6.7.2 Influence of drain resistance . . . 80
6.7.3 Conclusions . . . 81

7 Large scale triaxial test **83**
7.1 Large Scale testing . . . 83
7.2 Testing facilities . . . 84
7.3 The tested peat sample . . . 85
7.4 Test results . . . 87
7.4.1 Skempton B–factor . . . 87
7.4.2 Volume strain . . . 89
7.4.3 Pore pressure development . . . 90
7.4.4 Effective Stress Path . . . 92
7.4.5 Radial and Axial deformations . . . 93
7.5 Fitting measurement data . . . 97
7.6 Conclusions . . . 99

8 Practical applications **101**
8.1 Theory, Measurements and Engineering Practice . . . 101
8.2 Parameter determination for anisotropy . . . 101
8.3 Lateral stress reaction . . . 104
8.4 Consolidation around a vertical drain . . . 108

A Compression of a solid sphere **115**

B Lamé constants for cross–anisotropy **119**

C Similarity of three–parameter models **125**

D Drained and Undrained parameters **131**

E Axial–symmetrical isotropic consolidation **135**

F Plane–strain isotropic consolidation **153**

G Axial–symmetrical anisotropic consolidation **169**

H Plane–strain anisotropic consolidation **181**

I 3D Consolidation including compressible solids **189**

Bibliography **195**

Samenvatting **201**

About the Author **205**

List of Symbols

A = stiffness parameter, defined by equation (3.19)
B = Skempton B factor
B = stiffness parameter, defined by equation (3.19)
c = consolidation coefficient
D = stiffness parameter, defined by equation (3.19)
d = drain thickness
E^* = stiffness parameter in Graham & Houlsby model
E = Young's modulus
e = volumetric strain / void ratio
F = loading applied in plane strain problem
F_h = $E_h/(1-\nu_{hh})$
$f(t)$ = function defined by equation (5.3)
G = shear modulus
G' = stiffness parameter defined by equation (4.25)
G^* = stiffness parameter defined by equation (4.11)
G_s = specific gravity of solids, ρ_s/ρ_w
h = sample height
J = stiffness parameter defined by equation (4.12)
J' = stiffness parameter defined by equation (4.27)
K = bulk modulus
K' = stiffness parameter defined by equation (4.26)
K^* = stiffness parameter defined by equation (4.10)
K_0 = coefficient of lateral stress
K_w = bulk modulus of pore fluid
k = permeability
k' = drain resistance
L = compression modulus for virgin loading
l = length dimension in plane strain problem
M_w = water mass
M_s = mass of solid particles
N = Loss on ignition
n = porosity
n_s = number of tests
P = organic content
p = isotropic stress
p' = isotropic effective stress
q = deviator stress
q_0 = maximum contact stress, defined in figure 2.3
R = radius
S_r = initial degree of saturation
s_{ij} = general stiffness parameters

s_j = roots in Laplace inverse transform
T = dimensionless time factor
t = time
U = average degree of consolidation
u = displacement
V = total soil volume
V = Volt, in describing results of bender element tests
V_w = volume occupied by pore fluid
V_p = pore volume
V_s = volume occupied by solids
v = relative volume of bonded air bubbles
W = water content
$\mathrm{d}W$ = increment of work
W_{vp} = water vapour pressure

Greek symbols:
α = Biot coefficient
α = anisotropy factor used in Graham & Houlsby model
β = compressibility of the skeleton
β_f = compressibility the pure pore fluid
β_{fg} = compressibility of the pore fluid including air bubbles
β_{ss} = compressibility of the solids due to inter granular contacts
β_{sf} = compressibility of the solids due to isotropic load increment
χ = decay parameter in permeability
δ, Δ = increment
δ_{ij} = Kronecker delta
ε_{ij} = components of strain tensor
ε^H = natural strain or Henky strain
ε^C = linear strain or Cauchy strain
ε_{ij} = components of strain tensor
ε_q = distortional strain
γ = shear strain
γ_w = volumetric weight of water
η = E_h/E_v
η_{nc} = ratio angle of natural compression line in p'–q space
κ = drain resistance parameter defined by equation (5.11)
λ = Lamé constant
λ_j = $\sqrt{-s_j/c}$
μ = Lamé constant
μ_x = mean of parameter x
ν = Poisson's ratio
ν^* = stiffness parameter in Graham & Houlsby model
ρ = density
ρ_w = density of water
ρ_s = solid density
ρ_d = dry density
σ_x = standard deviation of parameter x
σ_w = pore pressure
σ_{ij} = components of total stress tensor
σ'_{ij} = components of effective stress tensor
$\widehat{\sigma}_{ij}$ = components of inter granular stress tensor
σ_b = applied loading

τ = shear stress
ω = air solubility in water
ψ = angle of effective stress path, $\Delta q/\Delta p'$

subscripts:
h = horizontal
v = vertical
a = axial
r = radial
θ = tangential
i = initial
0 = value at $t = 0$

superscripts:
u = undrained

Chapter 1

Scope of research

When designing a foundation for an embankment its influence on its surroundings is often an important issue. In considering this influence a proper indication of horizontal deformations and horizontal stresses in the subsoil is needed. Many sediment deposits are deposited in horizontal strata, so it is to be expected that their mechanical properties in both horizontal directions might differ from their properties in vertical direction. Standard soil sampling produces mainly vertically retrieved samples. Therefore standard soil investigation gives parameters mainly valid for the vertical direction. In general practice it will take a great effort to retrieve horizontally drilled samples and this is rarely done. So although it is widely recognized that soft soil might show anisotropic behaviour information on parameters in horizontal direction is scarce.

The options to retrieve information on parameters in the horizontal direction would be increased if some information on anisotropy could be found from vertically retrieved samples. If alone the level of anisotropy could be determined from vertically retrieved samples then for particular cases it could be shown when the subsoil behaves anisotropically and the effort of retrieving horizontal soil samples is worthwhile.

Anisotropy might be found in all types of soil properties, like permeability, stiffness, strength etc. This thesis focuses on anisotropy in stiffness. Soil stiffness is an important parameter in describing the consolidation process of soft soil. In special cases the pore pressure development deviates from the usual transient decay, [57], [22], [41]. This can be explained by a redistribution of stresses. Since the deviation of pore pressure development from the usual transient decay is largely determined by the stiffness parameters it is to be expected that anisotropy influences this behaviour. The question arises if this phenomenon can be activated in standard laboratory testing and when measured if pore pressure development can be used for parameter determination.

One type of soft soil that especially is to be expected to behave anisotropically is peat. Peat consists of mainly organic material. Depending on the degree of humification and the organic origin, fibres at different scales are present in peat. It is to be expected that if there is a dominant direction along which the fibres are aligned the peat will show anisotropic behaviour. The reaction of peat when loaded perpendicular to the main fibre direction will be different than when loaded in the main fibre direction.

In discussing anisotropy of peat a distinction can be made between induced anisotropy and structural anisotropy. Structural anisotropy depends solely on the structure of the material e.g. anisotropy caused by the presence of the fibres. If stiffness is stress or strain dependent an asymmetrical stress or strain distribution might lead to anisotropy in stiffness. This type of anisotropy is known as induced anisotropy. For induced anisotropy anisotropic behaviour is a consequence of the loading applied in the past. Since peat is a soft, compressible material it might show induced anisotropy besides structural anisotropy.

So two questions emerge:

- is it possible to establish the influence of anisotropy in the consolidation behaviour in standard laboratory testing?
- if pore pressure measurements reveal information on anisotropy can they be used to unravel the nature of anisotropy of peat?

Before answering these questions two important restrictions are made. The first involves the type of anisotropy. It is assumed that in describing the anisotropy in stiffness of peat there is one axis of symmetry. This means that when e.g. this axis corresponds to the vertical the stiffness parameters in the horizontal plane are independent from the stiffness in the vertical direction. This type of anisotropy is known as cross–anisotropy. So for peat it is assumed that the fibres are mainly aligned in one plane. Within this plane there is no dominant fibre direction. For a better understanding it will often be assumed that this plane is the horizontal plane. However this assumption is not necessary.

The second restriction involves material behaviour. It is widely recognized that a proper description of soft soil behaviour includes plasticity. This holds especially for large deformations. For small deformations and over–consolidated material conditions in engineering practice soil behaviour is often described by elastic material behaviour using equivalent elastic parameters that include some plasticity. In the following chapters it is assumed that a linear elastic material model can be used to describe behaviour of peat during consolidation. As a consequence deformations are assumed to be small during consolidation and the tested soil is over–consolidated. The main reason for assuming elastic material behaviour is that analytical solutions for the relevant phenomenon can be derived. These analytical solutions give an understanding in the basic nature of the studied phenomena. Once understanding the basic features the analysis can be extended to plastic soil behaviour.

To answer the two questions stated above chapter 2 starts with a discussion on the stiffness of the individual soil constituents, solids and pore fluid in relation to the bulk stiffness parameters. Chapter 3 gives a mathematical description of linear elastic cross–anisotropic material behaviour. Chapter 4 gives a literature review on the topic of parameter assessment for a cross–anisotropic soil model. This chapter shows some measurement results presented in literature and discusses the physical boundaries for individual parameters or group of parameters. Chapter 5 discusses influence of stress redistribution on the consolidation behaviour of soft soil, starting with a literature overview. The second part of chapter 5 presents several analytical solutions in which the influence of cross–anisotropic soil stiffness to the pore pressure development during consolidation plays a role. The analytical solutions clearly show that anisotropy in stiffness influences the pore pressure development for a conventional cylindrical soil sample. Chapter 6 shows measurements on peat conducted on conventional samples. Chapter 7 illustrates some size effects by discussing measurements on a large scale triaxial test. Finally chapter 8 gives three illustrations showing the practical implications for some aspects of the derived theory. The mathematical derivations of the solution for the different consolidation problems derived in the main text are presented in appendices.

Chapter 2

Compressibility of soil constituents

2.1 Parameters of compressibility

A soil volume contains solids and pores. Since pores might be filled by fluid and/or gas, a soil volume might contain three constituents, solids, pore fluid and pore gas. When describing the mechanical behaviour of soil the compressibility of the individual constituents play an essential role at micro level, while at macro level a bulk modulus is used. In soil mechanics solids (or grains) are often assumed to be incompressible. This assumption seems to hold for materials like sand and clay. Peat and organic clay however contain organic material. It might be possible that the organic fibres contain air pockets that are not connected to the pores. Such fibres can be seen as a compressible solid. A possible compressibility of the solids influences the mechanical behaviour of soil in several ways, three of which are explicitly considered:

- The stress dependency of the compressibility
- The concept of effective stress
- The Skempton B–factor in an undrained triaxial test

The first two items are used to illustrate the importance of the assumption of incompressible solids. The third item is used to validate measurement data that are presented in detail in section 6.5.

In chapters 2, 3, 4, 6, 7 and 8 the general sign convention is adopted in which all stress and strain are chosen positive for tension and negative for compression. When discussing analytical solutions to the consolidation problem chapter 5 uses, in contrast to the general sign convention, a positive sign for pore pressure. As explained in section 5.3 this sign convention makes direct comparison to solutions presented in literature possible.

2.2 Compressibility of the pore fluid, β_{fg}

The degree of saturation is defined as ratio of pore volume occupied by pore fluid and total pore volume:

$$S_r = \frac{V_w}{V_p} \tag{2.1}$$

S_r = degree of saturation
V_w = volume occupied by the pore fluid
V_p = pore volume

For $S_r = 1$ the soil is completely saturated. Then all pores are filled with water and no gas phase is present. For $S_r = 0$ the soil is dry and no pore fluid is present. For unsaturated soils, $0 < S_r < 1$ a further subdivision is possible. For a small amount of gas, the gas phase consists of individual bubbles present in the pore fluid. According to Fredlund & Rahardjo [31] this phase is reached for $S_r = 0.90$. For $S_r < 0.80$ a continuous gas-phase is present. In the transition zone both occur. For a continuous gas-phase the motion of the pore fluid is considerably hindered by the presence of the gas. In the following these conditions are excluded and it is assumed that $S_r > 0.85$. The pore fluid–gas bubble mixture is then described as a fluid in which the properties of gas bubbles and original fluid are incorporated. Under the assumption of constant temperature figure 2.1 defines the pore fluid compressibility β_{fg} due to a pore pressure increment $\mathrm{d}\sigma_w$.

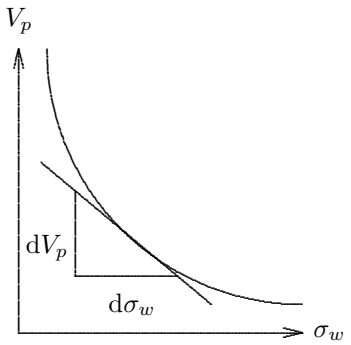

Figure 2.1: Definition of compressibility

$$\beta_{fg} = -\frac{1}{V_p}\frac{\mathrm{d}V_p}{\mathrm{d}\sigma_w} \tag{2.2}$$

The presence of the gas bubbles mainly involves the compressibility of the fluid. As indicated by several authors a small number of bubbles in the pore fluid reduces the stiffness of the pore fluid considerably, [6], [65] and [31]. Barends [6] gives an extended description of the stiffness of a pore fluid–gas bubble mixture:

$$\beta_{fg} = \beta_f + \frac{\dfrac{\left[1-(1-\omega)\,S_r\right]^2}{S_r}}{(1-\omega)\left[1-(1-\omega)\,S_{ri}\right]\left[\sigma_{wi} - W_{vp} + \dfrac{2\sigma}{r_i}\right] - \dfrac{2\sigma}{3r_i}\left[1-(1-\omega)\,S_r\right]^2\sqrt[3]{\dfrac{(1-S_{ri}-v)}{(1-S_r-v)^4}}} \tag{2.3}$$

In which:

β_f	= compressibility of the pure pore fluid
ω	= air solubility in water
S_{ri}	= initial degree of saturation
σ_{wi}	= initial pore pressure
W_{vp}	= water vapour pressure
σ	= fictitious water-air surface tension of the gas-fluid mixture
r_i	= initial free air bubble radius
v	= relative volume of bonded air bubbles

As the gas-bubbles have a relative large compressibility the volume occupied by air bubbles decreases when the fluid pressure σ_w increases, leading to an increase in S_r. Following Barends [6], the relation between σ_w and S_r is given by:

$$\sigma_w = W_{vp} - \frac{2\sigma}{r_i}\sqrt[3]{\frac{(1-S_{ri}-v)}{(1-S_r-v)}} + \frac{\left[1-(1-\omega)\,S_{ri}\right]\left[\sigma_{wi} - W_{vp} + 2\dfrac{\sigma}{r_i}\right]}{\left[1-(1-\omega)\,S_r\right]} \tag{2.4}$$

Figure 2.2 illustrates equations (2.3) and (2.4). The equations are elaborated for two values of the initial degree of saturation, $S_{ri} = 0.85$ and 0.92. The coefficients in equation (2.3) are taken from [6], with p_0 the atmospheric pressure;

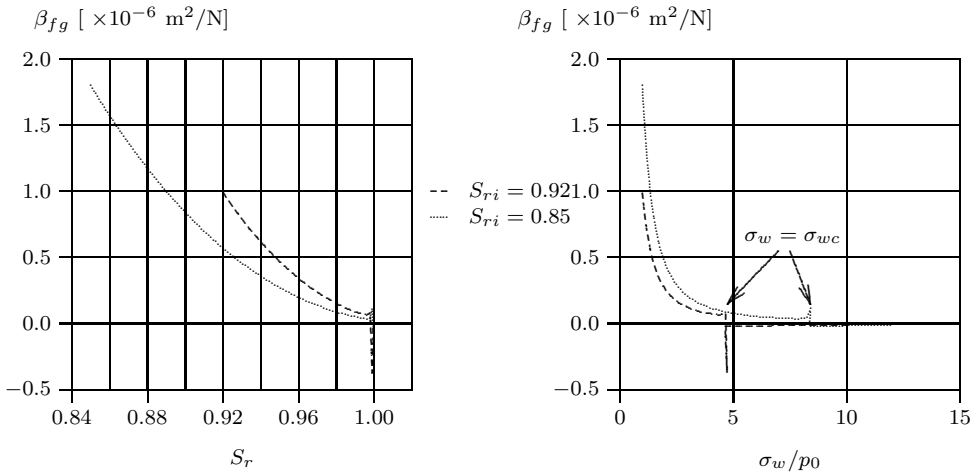

Figure 2.2: β_{fg} vs S_r and β_{fg} vs σ_w/p_0, after Barends [6]

$\omega \quad = 0.02$
$p_0 \quad = 10^5$ N/m^2
$W_{vp} \quad = 1000$ N/m^2
$\sigma/r_i \quad = 10\ 000$ N/m^2
$v \quad = 10^{-7}$
$\beta_f \quad = 10^{-9}$ m^2/N

As explained by Barends [6] an increase in σ_w leads to an increase in S_r according to equation (2.4). At some critical pressure σ_{wc} the air bubbles are no longer stable and collapse. Then the gas phase is completely dissolved in the pore fluid and air bubbles are no longer present. When reaching σ_{wc} equation (2.3) predicts a sudden jump in β_{fg}. This leads to a singular point in equation (2.3) depicted by a vertical line in figure 2.2. The negative values for β_{fg} presented in figure 2.2 have no physical meaning but are a consequence of the singular point at $\sigma_w = \sigma_{wc}$. Figure 2.2b shows that for $\sigma_w = \sigma_{wc}$ the stiffness of the pore fluid jumps from β_{fg} for $\sigma_w < \sigma_{wc}$ to β_f for $\sigma_w > \sigma_{wc}$. Figure 2.2b shows also that the value for σ_{wc} depends on S_{ri}. Note, that for a large S_{ri} complete saturation is found at a smaller pore pressure increase while for a lower S_{ri} a larger stress increment is required. So, for $S_{ri} = 0.85$ complete saturation is found when $\sigma_{wc}/p_0 \approx 8.4$ while for $S_{ri} = 0.92$ is found $\sigma_{wc}/p_0 \approx 4.6$. The sudden jump in the stiffness of the pore fluid at the critical pressure is also found in figure 2.2a when S_r reaches 1.0. Only for $S_r = 1.0$ the compressibility of the fluid-gas mixture is equal to the compressibility of the pure fluid. Figure 2.2 illustrates the reasoning of using a back–pressure to improve S_r in standard triaxial testing.

2.3 Compressibility of the solid particles

2.3.1 Compression due to isotropic loading, β_{sf}

An individual solid particle will face an isotropic stress caused by the surrounding pore fluid. As explained by Verruijt [77], despite the presence of contact points, where the individual grains touch each other, the pressure from the pore fluid is considered to act around the entire surface. The compressibility of the solid particles under an isotropic stress increment is indicated by β_{sf}:

$$\beta_{sf} = -\frac{1}{V_s}\frac{\mathrm{d}V_s}{\mathrm{d}\sigma_w} \tag{2.5}$$

With V_s the volume of the solid material and M_s the mass of the solid material, ρ_s is defined by $\rho_s = M_s/V_s$. Since M_s is independent of $\mathrm{d}\sigma_w$ the following is found:

$$\frac{\mathrm{d}M_s}{\mathrm{d}\sigma_w} = 0 \quad \rightarrow \quad \frac{\mathrm{d}\left(\rho_s V_s\right)}{\mathrm{d}\sigma_w} = 0 \quad \rightarrow \quad \frac{\mathrm{d}\rho_s}{\rho_s \mathrm{d}\sigma_w} = -\frac{\mathrm{d}V_s}{V_s \mathrm{d}\sigma_w}$$

and with equation (2.5) it follows that:

$$\beta_{sf} = \frac{\mathrm{d}\rho_s}{\rho_s \mathrm{d}\sigma_w} \tag{2.6}$$

2.3.2 Compression due to inter granular contacts, β_{ss}

In contrast to other researchers like Cheng [20] and Fjær at el. [30], Verruijt [77] makes a distinction between the compressibility due to isotropic stress and inter granular stress. To visualise the difference between both effects a soil skeleton of ideal spheres is considered. Due to inter granular stress the spheres are in contact and are indented around their contact points. An analytical solution for the size of the indented area is presented in appendix A. Appendix A shows that the volume loss of a sphere as a function of the load at a contact point is given by :

$$V_{sp} = 2\pi \left[\frac{1}{3}R^3 - \frac{1}{3}R^2\sqrt{R^2 - a^2} + \frac{1}{3}\left(R^2 - a^2\right)\sqrt{R^2 - a^2}\ln\left(\frac{\sqrt{R^2 - a^2}}{R}\right)\right] \tag{2.7}$$

with:

V_{sp} = indented volume
R = radius of the spheres
a = radius of indented area

Figure 2.3 shows an analytical solution, for the Young's modulus $E = 10\ 000$ kPa, Poisson ratio $\nu = 0.3$ and the sphere radius $R = 10$ μm. The corresponding isotropic compression, given by equation (2.5), becomes in this case:

$$\beta_{sf} = \frac{3\left(1 - 2\nu\right)}{E} = 0.00012 \quad \mathrm{m}^2/\mathrm{kN}$$

If β_{sf} is constant, equation (2.5) represents a linear relation between σ_w and $\ln V_s$. For this reason a straight line is found for isotropic conditions in figure 2.3. Equation (2.7) gives the loss in volume of a sphere when compressed in one contact point. In figure 2.3 the dotted line, indicated as 1 contact point, represents equation (2.7). Since the isotropic stress acts on the entire surface, while the contact stress acts on a relatively small contact area a unit increase in isotropic stress leads to a larger volume change than a unit increase in contact stress. This explains why in figure 2.3 the line representing isotropic loading is located left of the line representing one contact point.

Equivalent to the definition of β_{sf}, equation (2.5), a compression index due to inter granular compression, β_{ss} can be defined. According to Barends [7] the total stress σ_{ij} can be decomposed in a part due to fluid pressure $\sigma_w\delta_{ij}$ and inter granular stress $\widehat{\sigma}_{ij}$:

$$\sigma_{ij} = \widehat{\sigma}_{ij} + \sigma_w\delta_{ij} \tag{2.8}$$

With $\widehat{\sigma}$ the isotropic component of the isotropic inter granular stress increment β_{ss} is defined by:

$$\beta_{ss} = -\frac{1}{V_s}\frac{\mathrm{d}V_s}{\mathrm{d}\widehat{\sigma}} \tag{2.9}$$

For a constant β_{sf} a linear relation between $\ln V_s$ and σ_w is found. However a constant β_{ss}–value leads to a non–linear relation as shown by figure 2.3. Appendix A assumes the pressure distribution

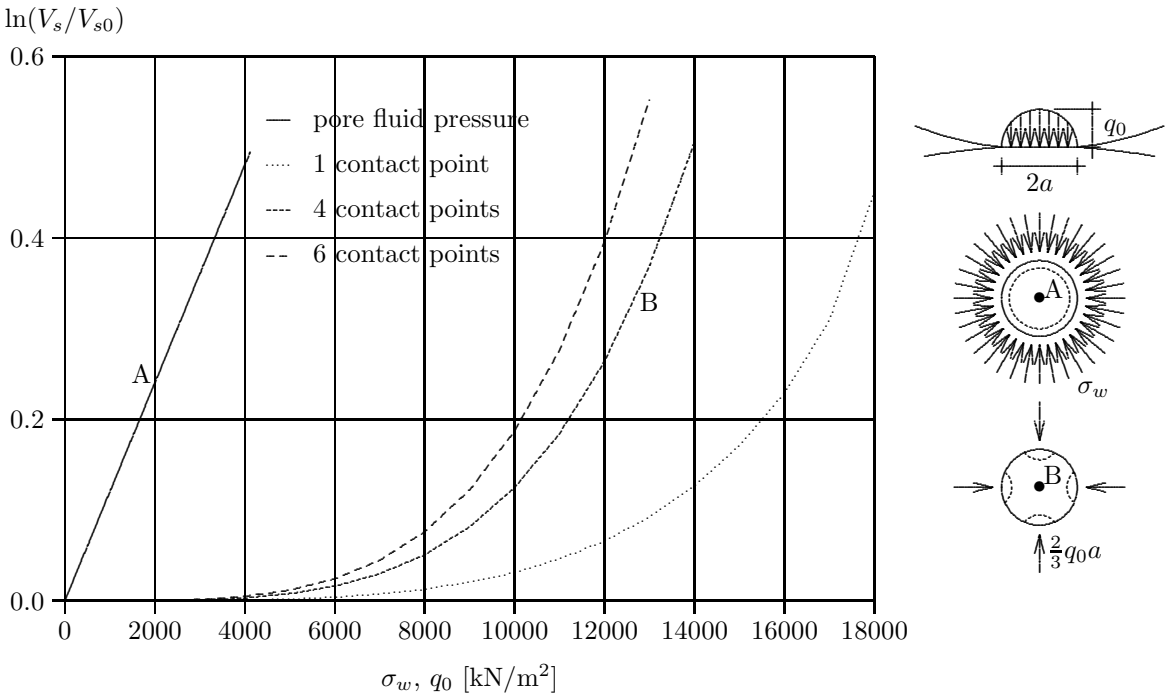

Figure 2.3: Stress–strain curve for an isotropic stress σ_w, condition A and inter granular stress q_0, condition B

in the contact area, with radius a, to be semi–spherical with q_0, the maximum pressure at the centre of the area. Appendix equation (A.5) gives a linear relation between q_0 and a. When a increases, the part of the sphere that is lost due to denting of the sphere increases disproportionally, leading to a non–linear relation between a and V_{sp}.

The grains in a skeleton will usually have more than one contact point. Considering only small volume changes it can be assumed that the individual contact points do not interact. So for a grain having 4 contact points the total volume loss can be estimated by 4 times the volume loss at one contact point. In figure 2.3 the loss in volume is given for 4 and 6 contact points.

The tangent of the isotropic compression line gives β_{sf}. The tangent of the inter granular compression lines gives a value for β_{ss}. From figure 2.3 the difference between β_{ss} and β_{sf} is evident. For low values of q_0 the volume loss of the solid particles due to contact stress can be neglected. When q_0 increases β_{ss} increases and may finally exceed β_{sf}.

Equivalent to the equations (2.5) and (2.6) a definition of β_{ss} and a relation between $\beta_{ss}$and ρ_s can be found.

$$\frac{\mathrm{d}M_s}{\mathrm{d}\widehat{\sigma}} = 0 \quad \rightarrow \quad \frac{\mathrm{d}\left(\rho_s V_s\right)}{\mathrm{d}\widehat{\sigma}} = 0 \quad \rightarrow \quad \frac{\mathrm{d}\rho_s}{\rho_s \mathrm{d}\widehat{\sigma}} = -\frac{\mathrm{d}V_s}{V_s \mathrm{d}\widehat{\sigma}}$$

with equation (2.9):

$$\beta_{ss} = \frac{\mathrm{d}\rho_s}{\rho_s \mathrm{d}\widehat{\sigma}} \tag{2.10}$$

Under the assumption that interaction between compression due to an isotropic fluid pressure and inter granular stress is negligible the density as a function of σ_w and $\widehat{\sigma}$ is found by a summation of both the individual density changes:

$$\frac{\mathrm{d}\rho_s}{\rho_s} = \beta_{sf}\mathrm{d}\sigma_w + \beta_{ss}\mathrm{d}\widehat{\sigma} \tag{2.11}$$

Or expressed in terms of change in V_s:

$$\frac{\mathrm{d}V_s}{V_s} = -\beta_{sf}\mathrm{d}\sigma_w - \beta_{ss}\mathrm{d}\widehat{\sigma} \tag{2.12}$$

And expressed in terms of the bulk volume, with n representing porosity:

$$\frac{\mathrm{d}V_s}{V} = -\left(1-n\right)\left(\beta_{sf}\mathrm{d}\sigma_w + \beta_{ss}\mathrm{d}\widehat{\sigma}\right) \tag{2.13}$$

2.4 Compressibility of the skeleton, β

The total volume change of a soil mass involves a rearrangement of the solid particles. This is caused by sliding, rolling or crushing of the grains. The compressibility which accounts for these effects as well as for the inter granular compression is denoted by β. Since the stress exerted by the pore fluid on the grains is an isotropic stress, sliding, rolling and crushing of the grains is influenced by the inter granular stress only.

Terzaghi, [71] defines the effective stress, indicated by σ', as that part of the total stress tensor leading to deformation of the skeleton. Equivalent to equation (2.5) compressibility of the skeleton β is defined, with $\mathrm{d}\sigma'$ the isotropic effective stress increment, by:

$$\beta = -\frac{1}{V}\frac{\mathrm{d}V}{\mathrm{d}\sigma'} \tag{2.14}$$

The fact that β includes compression of the individual grains as well as a reduction in pore volume can be visualised by considering a compression test on a dry sample. For these conditions the grains only face increments of inter granular stress, so $\Delta\sigma = \Delta\widehat{\sigma} = \Delta\sigma'$. From a reduction in volume of the solids it can then be found, using equation (2.9):

$$\Delta V_s = \Delta\left(1-n\right)V = \left(1-n\right)\Delta V - V\Delta n$$

$$\left(1-n\right)\Delta V = \Delta V_s + V\Delta n$$

$$\Delta V = -\beta_{ss}\Delta\sigma' V + V\frac{\Delta n}{1-n}$$

With equation (2.14) it can be found:

$$\beta = \beta_{ss} - \frac{\Delta n}{\left(1-n\right)\Delta\sigma'}$$

Since $\Delta n/\Delta\sigma' < 0$ it is found $\beta > \beta_{ss}$. For most soils β_{ss} is at least one order magnitude smaller than $\Delta n/\Delta\sigma'$ and hence, $\beta \approx -\Delta n/\Delta\sigma'$.

2.5 The effective stress concept

By definition the effective stress, indicated by σ', is that part of the total stress tensor which controls the deformation of the skeleton. Terzaghi [71] introduced the concept of effective stress in 1925. Biot extended the definition for compressible solids [12], [13] and [14] and shows that the effective stress tensor is defined by:

$$\sigma'_{ij} = \sigma_{ij} - \alpha\sigma_w\delta_{ij}, \qquad \alpha = 1 - \frac{\beta_{sf}}{\beta} \tag{2.15}$$

In equation (2.15) the coefficient α represents the Biot factor. In soil mechanics the solid particles are usually assumed to be incompressible. For these conditions β_{sf} reduces to 0, leading

to $\alpha = 1$. For incompressible solids, $\alpha = 1$, the Terzaghi formulation of effective stress is found. For compressible solids α is smaller than 1.

Since the effective stress is defined as that part of the total stress that causes skeleton deformation, the pore pressure of a soil type with compressible solids partly contributes to the skeleton deformation. According to equation (2.15) the part of the pore pressure that contributes to the effective stress is given by $\beta_{sf}\sigma_w/\beta$.

2.6 Skempton B–factor

Skempton, [65], introduces the B–factor as a function of pore water stiffness K_w and skeleton stiffness K. With $K = 1/\beta$ and $K_w = 1/\beta_{fg}$, the Skempton B–factor is represented by:

$$B = \frac{1}{\dfrac{nK}{K_w} + 1} = \frac{1}{\dfrac{n\beta_{fg}}{\beta} + 1} \tag{2.16}$$

The Skempton B–factor is an important parameter to validate the degree of saturation in laboratory tests. As shown by Verruijt [77] a reformulation of the Skempton B–factor can be found using $\beta_{ss}, \beta_{sf}, \beta_{fg}$ and β. For initial, undrained, conditions no dissipation of pore water takes place. So when loading the total volume change equals the summation of pore volume reduction and solid volume reduction:

$$\Delta V = \Delta V_p + \Delta V_s$$

Using equations (2.2), (2.13) and (2.14) and definitions (2.8) and (2.15) a more general expression for the B–factor is found:

$$B = \frac{\mathrm{d}\sigma_w}{\mathrm{d}\sigma} = \frac{\beta - (1-n)\,\beta_{ss}}{\beta - (1-n)\,\beta_{ss} - n\beta_{sf} + n\beta_{fg}} = \frac{1}{1 + \dfrac{n\,(\beta_{fg} - \beta_{sf})}{\beta - (1-n)\,\beta_{ss}}} \tag{2.17}$$

In equation (2.17) the compressibility of the solids is incorporated by the parameters β_{ss} and β_{sf}. It can easily be verified that neglecting the compressibility of the solid particles, $\beta_{sf} = \beta_{ss} = 0$, reduces equation (2.17) to (2.16).

Equation (2.3) gives the stiffness of the pore fluid as a function of the degree of saturation, S_r. So equations (2.17) and (2.3) can be used to draw graphs of the B–factor versus S_r. Figure 2.4 shows these graphs for different values for β_{ss}/β_{sf}, β_{sf}/β and S_{ri}. By definition β includes β_{ss}, so $\beta \geq \beta_{ss}$. Since negative values for α are not expected for soil, β is also limited by β_{sf}.

Figure 2.4 shows a considerable reduction in the B–factor for a small amount of air bubbles. For $S_r = S_{ri} = 0.85$ the B–factor = 0.5 while for $S_r = 1.0$ the B–factor equals to 1.0. The large fluctuation in B–factor corresponds to the values presented in literature. Skempton presented measurements of the B–factor versus S_r [65], where even lower values for the B–factor are presented, approximately 0.25 for $S_r = 0.85$. In [65] the initial degree of saturation and the total pressure at which the tests are conducted are not presented. Therefore, equation (2.3) can not be used to reproduce the measurements to explain the difference between test results of [65] and figure 2.4.

Figure 2.4 shows in the lower graphs that the line representing $\beta_{sf} = \beta$ deviates strongly from the other curves. This is explained by equation (2.17). The curve represents $\beta_{ss} = \beta_{sf} = \beta$ and equation (2.17) is then reduced to $B = n\beta/\beta_{fg}$. Since β_{fg} is strongly influenced by S_r and even reduces to 0 when S_r reaches 1.0. B grows to infinity for S_r reaching 1.

Figure 2.4 indicates that if β_{sf} is small in comparison to β the influence of β_{sf} on the B–factor is negligible. When β_{sf} is of the order in magnitude of β the B–factor tends to increase for increasing β_{sf}. It is remarkable that for compressible solids the B–factor becomes larger than 1.0. This means that when a soil skeleton, which consists of compressible solids, is loaded by a load equal to σ_b, the

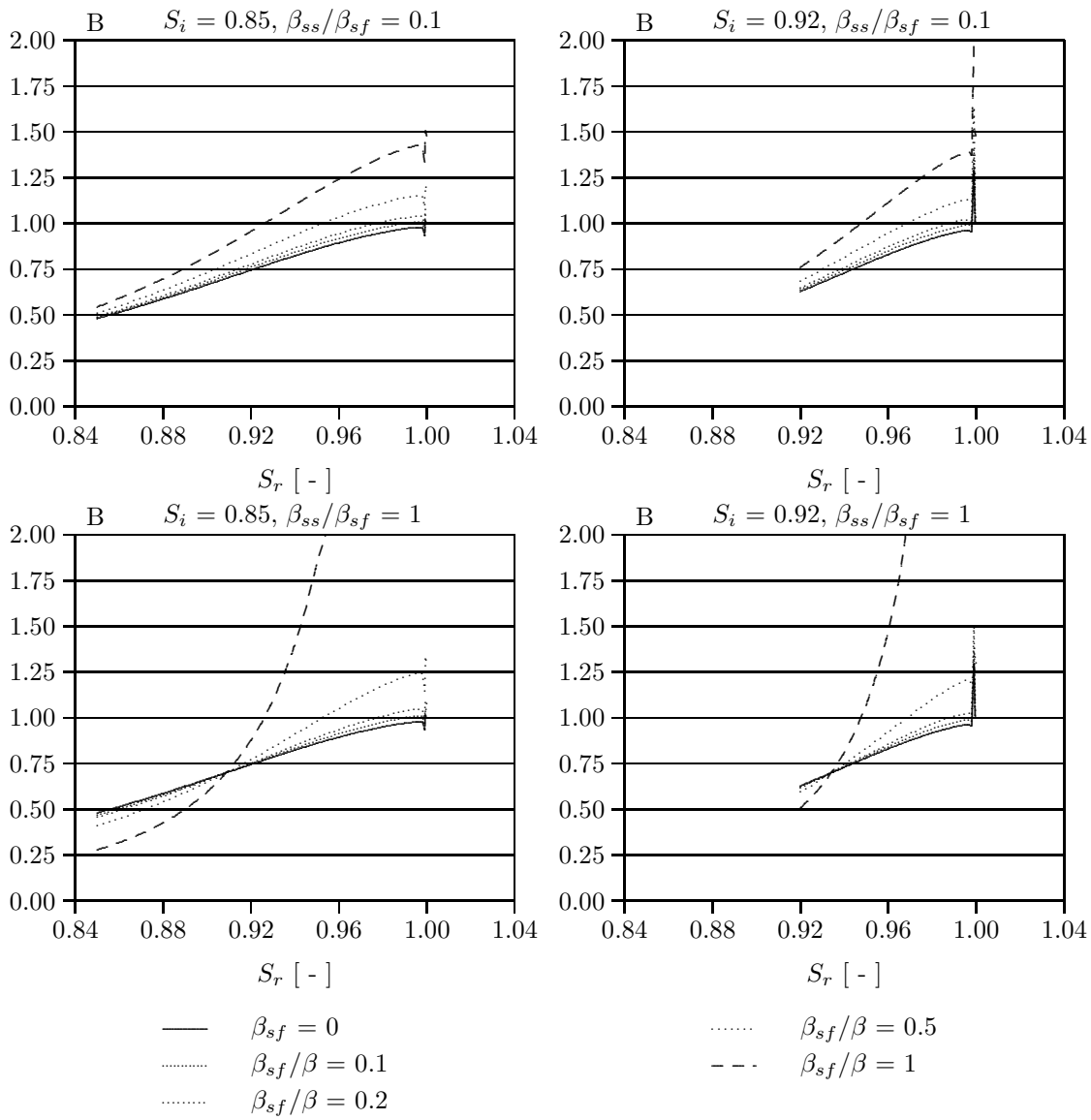

Figure 2.4: B vs S_r

pore pressure increases by more than σ_b if the compressibility of the pore fluid is small. Verruijt [77] explained this by the fact that a fluid pressure increment will lead to a compression of the solids. He states that if the pore fluid is incompressible and if there is no drainage, the decrease in pore space is balanced by an increase in pore space due to compression of the solids. An increase in pore space due to compression of the solids leads to a reduction in inter granular stress. Since an increment in total stress should be balanced by the sum of the increment of pore pressure and inter granular stress a decrease in inter granular stress leads to further increase in pore pressure. Therefore the increment in pore pressure will exceed the increment in total stress, leading to $B > 1$.

The maximum B value at $S_r = 1$ for different ratio's of β_{ss}/β_{sf} is presented in table 2.1. Table 2.1 shows that if the compressibility of the solids reaches up to 10 % of the bulk compressibility,

Table 2.1: Skempton B–factor for compressible solids at $S_r = 1$

β_{sf}/β	0	0.02	0.1	0.2	0.5	1.0
$\beta_{ss}/\beta_{sf} = 0.1$	1.00	1.01	1.03	1.06	1.18	1.47
$\beta_{ss}/\beta_{sf} = 1.0$	1.00	1.01	1.03	1.07	1.30	500 (∞)
$\beta_{ss}/\beta_{sf} = 10$	1.00	1.01	1.11			

the influence of the solid stiffness remains small. The deviation of the B–factor is then 3%.

Chapter 3

Cross–anisotropic elasticity

3.1 Hooke's law for cross–anisotropy

Figure 3.1 visualises a cross–anisotropic material. The discs located in the x–y plane represent the plane of isotropy. The stress and strain in the plane of the discs follow from the disc properties. The stress and strain in the z–direction follow from the properties of the bar. The stress and strain in the x–z and y–z plane follow from the interaction of the bar and discs. For normal stress and strain the most general description of the normal stress–strain relationship is given by equation (3.1), with a s_{ij} a general stiffness matrix.

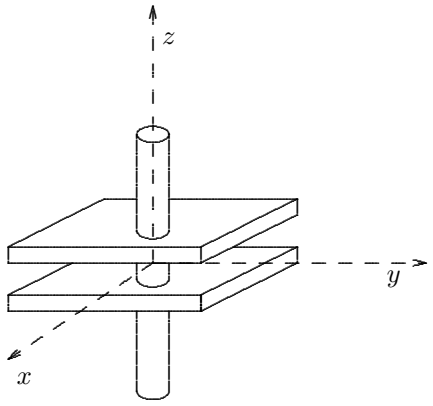

Figure 3.1: Cross–anisotropic material

$$\begin{aligned} \varepsilon_{xx} &= s_{xx}\sigma_{xx} + s_{xy}\sigma_{yy} + s_{xz}\sigma_{zz} \\ \varepsilon_{yy} &= s_{yx}\sigma_{xx} + s_{yy}\sigma_{yy} + s_{yz}\sigma_{zz} \\ \varepsilon_{zz} &= s_{zx}\sigma_{xx} + s_{yz}\sigma_{yy} + s_{zz}\sigma_{zz} \end{aligned} \tag{3.1}$$

Note that in equation (3.1) increments of normal stress and normal strain are presented. For sake of simplicity the δ sign is omitted.

According to equation (3.1), if σ_{xx} is the only stress active it will provoke strain in each of the three principal directions. For ε_{xx} is found $\varepsilon_{xx} = s_{xx}\ \sigma_{xx}$. If a linear elastic stress–strain relationship is considered, it follows that $s_{xx} = 1/E_x$, where E_x represents the Young's modulus. In the same way s_{yy} and s_{zz} can be defined.

With σ_{yy} the only active stress gives $\varepsilon_{yy} = s_{yy}\ \sigma_{yy}$, with $s_{yy} = 1/E_y$. In [35] the Poisson's ratio is defined as the ratio of principal strain in two independent directions under uniaxial loading[1] :

$$\frac{\varepsilon_{(jj)}}{\varepsilon_{(ii)}} = -\nu_{ij}, \quad \text{if} \quad \sigma_{(ii)} = \sigma, \quad \sigma_{(jj)} = 0$$

Again with σ_{yy} the only stress acting gives $\varepsilon_{xx} = s_{xy}\sigma_{yy}$ leading to s_{xy} = - ν_{yx}/E_y. Equivalent expressions for the coefficients s_{yx} to s_{zz} can be found. Hooke's law for normal stress and strain becomes:

$$\begin{pmatrix} \varepsilon_{xx} \\ \\ \varepsilon_{yy} \\ \\ \varepsilon_{zz} \end{pmatrix} = \begin{pmatrix} \frac{1}{E_x} & \frac{-\nu_{yx}}{E_y} & \frac{-\nu_{zx}}{E_z} \\ \frac{-\nu_{xy}}{E_x} & \frac{1}{E_y} & \frac{-\nu_{zy}}{E_z} \\ \frac{-\nu_{xz}}{E_x} & \frac{-\nu_{yz}}{E_y} & \frac{1}{E_z} \end{pmatrix} \begin{pmatrix} \sigma_{xx} \\ \\ \sigma_{yy} \\ \\ \sigma_{zz} \end{pmatrix} \tag{3.2}$$

The stiffness matrix presented in equation (3.2) is symmetrical. In [35] this is proved in the following way. If the normal stress in e.g. x direction is increased from σ_{xx} to $\sigma_{xx} + d\sigma_{xx}$, the increment of work dW done becomes:

$$dW = \varepsilon_{xx} d\sigma_{xx} = (s_{xx}\sigma_{xx} + s_{xy}\sigma_{yy} + s_{xz}\sigma_{zz})\, d\sigma_{xx}$$

Thus:

$$\frac{dW}{d\sigma_{xx}} = s_{xx}\sigma_{xx} + s_{xy}\sigma_{yy} + s_{xz}\sigma_{zz}$$

$$\frac{\partial^2 W}{\partial^2 \sigma_{xx}} = s_{xx}; \quad \frac{\partial^2 W}{\partial \sigma_{xx}\partial \sigma_{yy}} = s_{xy}; \quad \frac{\partial^2 W}{\partial \sigma_{xx}\partial \sigma_{zz}} = s_{xz}$$

The same holds for a stress increment in the y and z direction, leading to:

$$\frac{\partial^2 W}{\partial \sigma_{yy}\partial \sigma_{xx}} = s_{yx}; \qquad \text{etc.}$$

Since the order of differentiation is immaterial it is found that:

$$\frac{\partial^2 W}{\partial \sigma_{xx}\partial \sigma_{yy}} = \frac{\partial^2 W}{\partial \sigma_{yy}\partial \sigma_{xx}}; \qquad \text{etc.}$$

And therefore:

$$s_{xy} = s_{yx}; \quad \text{etc.} \tag{3.3}$$

Combination of equation (3.3) and (3.2) gives in a more general notation:

$$\frac{-\nu_{ij}}{E_i} = \frac{-\nu_{ji}}{E_j} \tag{3.4}$$

Note that for anisotropic conditions, $E_i \neq E_j$, leads to $\nu_{ij} \neq \nu_{ji}$ and vice versa. Love in [56] gives a more thorough proof of the symmetry of the elasticity matrix.

Figure 3.2 shows the shear stress and shear deformations active in the x–z plane. Rotational equilibrium of plate *abcd* in figure 3.2 gives $\tau_{ij} = \tau_{ji}$.

[1]The subscript (ii) in $\varepsilon_{(ii)}$ indicates a cyclic permutation of x, y and z, while ε_{ii} indicates the summation $\varepsilon_{xx} + \varepsilon_{yy} + \varepsilon_{zz}$

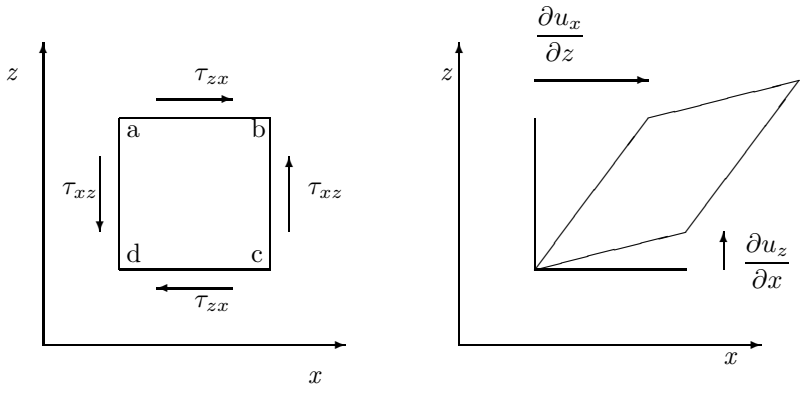

Figure 3.2: Shear deformations in x-z plane

In correspondence to figure 3.1 in figure 3.2 the x–y plane is the plane of isotropy. So the x–z plane depicted in figure 3.2 is perpendicular to the plane of isotropy, including both E_h and E_v. The shear strain γ is defined by:

$$\gamma_{ij} = (u_{i,j} + u_{j,i}) \tag{3.5}$$

From equation (3.5) it can easily be seen that $\gamma_{zx} = \gamma_{xz}$. For linear elastic behaviour the shear modulus, G, connects shear deformation to shear stress.

$$\gamma_{zx} = \frac{\tau_{zx}}{G_{zx}} \tag{3.6}$$

Since $\gamma_{zx} = \gamma_{xz}$ and $\tau_{zx} = \tau_{xz}$ it follows that $G_{xz} = G_{zx}$. The same holds for the y–z and x–y plane. So the shear stress–strain relationship is given by

$$\begin{pmatrix} \gamma_{xy} \\ \\ \gamma_{yz} \\ \\ \gamma_{zx} \end{pmatrix} = \begin{pmatrix} \frac{1}{G_{xy}} & 0 & 0 \\ 0 & \frac{1}{G_{yz}} & 0 \\ 0 & 0 & \frac{1}{G_{zx}} \end{pmatrix} \begin{pmatrix} \tau_{xy} \\ \\ \tau_{yz} \\ \\ \tau_{zx} \end{pmatrix} \tag{3.7}$$

Since the x–y plane is the plane of isotropy, the shear characteristics of the z–x plane equals the z–y plane, $G_{zx} = G_{yz}$, (see [16]).

In low–land sedimented soils the layering is mostly horizontal. So the subscripts x and y can be replaced by h, indicating horizontal and z can be replaced for v indicating vertical. Section 2.5 introduces the effective stress as the particular part of the stress tensor causing deformation of the soil skeleton, for $\alpha = 1$;

$$\sigma_{ij} = \sigma'_{ij} + \sigma_w \delta_{ij} \tag{3.8}$$

Combination of equation (3.2), (3.7) and (3.8) gives the complete description of Hooke's law for cross–anisotropic linear elastic soil behaviour:

$$\begin{pmatrix} \varepsilon_{xx} \\ \varepsilon_{yy} \\ \varepsilon_{zz} \\ \gamma_{xy} \\ \gamma_{yz} \\ \gamma_{zx} \end{pmatrix} = \begin{pmatrix} \frac{1}{E_h} & \frac{-\nu_{hh}}{E_h} & \frac{-\nu_{vh}}{E_v} & 0 & 0 & 0 \\ \frac{-\nu_{hh}}{E_h} & \frac{1}{E_h} & \frac{-\nu_{vh}}{E_v} & 0 & 0 & 0 \\ \frac{-\nu_{vh}}{E_v} & \frac{-\nu_{vh}}{E_v} & \frac{1}{E_v} & 0 & 0 & 0 \\ 0 & 0 & 0 & \frac{1}{G_{hh}} & 0 & 0 \\ 0 & 0 & 0 & 0 & \frac{1}{G_{vh}} & 0 \\ 0 & 0 & 0 & 0 & 0 & \frac{1}{G_{vh}} \end{pmatrix} \begin{pmatrix} \sigma'_{xx} \\ \sigma'_{yy} \\ \sigma'_{zz} \\ \tau_{xy} \\ \tau_{yz} \\ \tau_{zx} \end{pmatrix} \tag{3.9}$$

Timoshenko & Goodier [72] show that within the plane of isotropy, here the x–y plane, the shear modulus G_{hh} can be expressed in E_h and ν_{hh}. The left side of figure 3.3 shows a rectangular

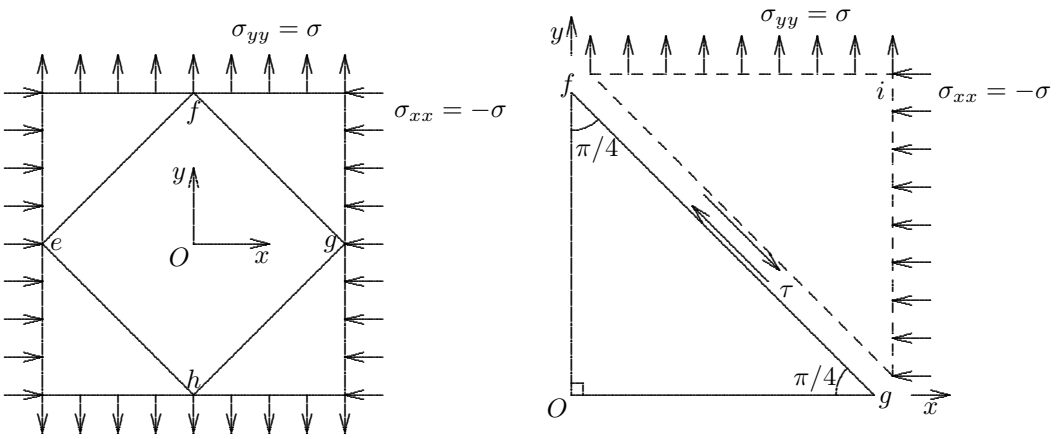

Figure 3.3: Shear deformation in isotropic plane

shape loaded by $\sigma_{xx} = -\sigma$, $\sigma_{yy} = \sigma$ and $\sigma_{zz} = 0$. Within this rectangular shape an element $efgh$ with planes parallel to the z axis and 45° to the x and y axis is found. Equilibrium of forces e.g. of element fgi, depicted at the right–hand side of figure 3.3, shows that only a shear stress τ is active on the sides; $\tau = (\sigma_{yy}$ - $\sigma_{xx})/2 = \sigma$. The loading condition depicted by figure 3.3 produces elongation of Of and Oh and shortening of Og and Oe. Furthermore the angles efg and ghe will decrease while the angles fgh and hef will increase. The length of the sides fg, gh, he and ef is considered constant by assuming small deformations and neglecting second order effects. If the angle efg changes by γ is found after deformation:

$$\frac{Og}{Of} = \tan\left(\frac{\pi}{4} - \frac{\gamma}{2}\right) = \frac{1 + \varepsilon_{xx}}{1 + \varepsilon_{yy}} \tag{3.10}$$

from equation (3.9) is found:

$$\varepsilon_{xx} = \frac{1}{E_h}\left(\sigma_{xx} - \nu_{hh}\sigma_{yy}\right) - \frac{\nu_{vh}}{E_v}\sigma_{zz} = -\frac{1 + \nu_{hh}}{E_h}\sigma$$
$$\varepsilon_{yy} = \frac{1}{E_h}\left(\sigma_{yy} - \nu_{hh}\sigma_{xx}\right) - \frac{\nu_{vh}}{E_v}\sigma_{zz} = \frac{1 + \nu_{hh}}{E_h}\sigma$$

Equation 3.10 and small value for γ gives:

$$\tan\left(\frac{\pi}{4}-\frac{\gamma}{2}\right)=\frac{\tan\left(\frac{\pi}{4}\right)-\tan\left(\frac{\gamma}{2}\right)}{1+\tan\left(\frac{\pi}{4}\right)\tan\left(\frac{\gamma}{2}\right)}=\frac{1-\frac{\gamma}{2}}{1+\frac{\gamma}{2}}$$

substitution gives:

$$\gamma=\frac{2\left(1+\nu_{hh}\right)}{E_h}\tau \tag{3.11}$$

Equation (3.11) defines the shear modulus in horizontal plane, here the plane of isotropy, by:

$$G_{hh}=\frac{E_h}{2\left(1+\nu_{hh}\right)} \tag{3.12}$$

As shown by [16] five parameters suffice to describe cross-anisotropy. The number of independent parameters used in the matrix of equation (3.9) equals five:

E_h = Young's modulus in horizontal direction
E_v = Young's modulus in vertical direction
ν_{vh} = Poisson's ratio for horizontal strain due to vertical strain
ν_{hh} = Poisson's ratio for horizontal strain due to horizontal strain
G_{hv} = Shear modulus in vertical plane, equals G_{vh}

3.2 Bounding values

Although the five parameters presented in the previous section are independent they need to fulfil some requirements. De Josselin de Jong, [40] and Pickering [61] give a clear analysis of the bounding values for the five parameters. Since these analyses provide a valuable insight in the behaviour of cross-anisotropic materials the main points of these analyses are reported in this section. From equation (3.9) an expression for the volumetric strain e can be derived:

$$e=\varepsilon_{ii}=\left(\frac{1}{E_h}-\frac{\nu_{hh}}{E_h}-\frac{\nu_{vh}}{E_v}\right)\left(\sigma'_{xx}+\sigma'_{yy}+\sigma'_{zz}\right)+\left(\frac{1}{E_v}-\frac{\nu_{vh}}{E_v}-\frac{1}{E_h}+\frac{\nu_{hh}}{E_h}\right)\sigma'_{zz} \tag{3.13}$$

De Josselin de Jong states that compressive stress should lead to compression and requires both terms of the right-hand side of equation (3.13) to be positive. Pickering does not use this requirement and finds for exceptional conditions material behaviour, which expands under axial compression. Pickering claims this as an option to model dilatancy by linear elastic material behaviour. Since the Pickering analysis is more general, it is followed in this section.

With equation (3.9) $\varepsilon_{ij}=C_{ijkl}\sigma'_{kl}$ the strain energy per unit volume is expressed by $dW=1/2\sigma'_{ij}\ C_{ijkl}\ \sigma'_{kl}$. From thermodynamic requirements it follows that $dW\geq 0$. Pickering states that this requirement is fulfilled when all principal minors of matrix C_{ijkl} are positive. The principal

minors of C_{ijkl} are:

$$\begin{aligned}
C_1 &= \frac{1}{E_h} \\
C_2 &= \frac{1}{E_h^2}\left(1+\nu_{hh}^2\right) \\
C_3 &= \frac{1}{E_v^2}\left(\frac{E_v}{E_h}-\nu_{vh}^2\right) \\
C_4 &= \frac{1}{E_v^2 E_h}\left[\frac{E_v}{E_h}\left(1-\nu_{hh}\right)-2\nu_{vh}^2\right]\left(1+\nu_{hh}\right) \\
C_5 &= \frac{C_3}{G_{hh}} = \frac{2C_3\left(1+\nu_{hh}\right)}{E_h} \\
C_6 &= \frac{C_5}{G_{vh}}
\end{aligned}$$

C_1 to C_6 are all positive if:

$$\begin{aligned}
&E_h, E_v, G_{vh} \geq 0 \\
&\nu_{hh} \geq -1 \\
&\frac{E_v}{E_h}\left(1-\nu_{hh}\right)-2\nu_{vh}^2 \geq 0
\end{aligned} \tag{3.14}$$

The third condition of (3.14) also gives the upper bound for ν_{hh}. Rewriting gives:

$$\frac{E_v}{E_h}\left(1-\nu_{hh}\right) \geq 2\nu_{vh}^2$$

Since $\nu_{vh}^2 \geq 0$ and according to the first condition of (3.14) $E_h, E_v \geq 0$ follows, $(1-\nu_{hh}) \geq 0$, $\nu_{hh} \leq 1$. Note that in conditions (3.14) ν_{hv} is not an independent parameter, since equation (3.4) relates ν_{hv} to E_v/E_h and ν_{hv}. Pickering, [61], uses ν_{hv} instead of ν_{vh} and finds for minor C_4 the expression:

$$C_4 = \frac{1}{E_h^3}\left[\frac{E_h}{E_v}\left(1-\nu_{hh}\right)-2\nu_{hv}^2\right]\left(1+\nu_{hh}\right)$$

which with $C_4 \geq 0$ gives the condition:

$$\frac{E_h}{E_v}\left(1-\nu_{hh}\right)-2\nu_{hv}^2 \geq 0 \tag{3.15}$$

Figure 3.4 shows condition (3.15) in combination to the first and second condition given by (3.14). They are fulfilled if the state is within or on the envelope shown.

Isotropic materials do not show distortion under an isotropic load. Figure 3.4 shows that there is a combination of stiffness parameters for which a cross–anisotropic material also does not distort under an isotropic load. This type of behaviour is found when $\varepsilon_{(ii)} = \varepsilon_{(jj)}$ under an isotropic stress, $\sigma'_{(jj)} = \sigma'$ and $\tau_{ij} = 0$. From equation (3.9) with equation (3.4) follows:

$$\begin{aligned}
&\varepsilon_{xx} = \varepsilon_{yy} = \varepsilon_{zz} = \left(\frac{1}{E_h}-\frac{\nu_{hh}}{E_h}-\frac{\nu_{vh}}{E_v}\right)\sigma' = \left(-2\frac{\nu_{vh}}{E_v}+\frac{1}{E_v}\right)\sigma' \\
&\frac{E_h}{E_v}-1 = \nu_{hv}-\nu_{hh}
\end{aligned} \tag{3.16}$$

A material that fulfils equation (3.16) does not show distortion under an isotropic load and vice versa no volume change when loaded such that the isotropic load remains 0. The triangle ABC in figure 3.4 represents this type of material, for which volumetric strain and distortional strain are uncoupled. Isotropic materials are a part of this group of materials, which are represented by the

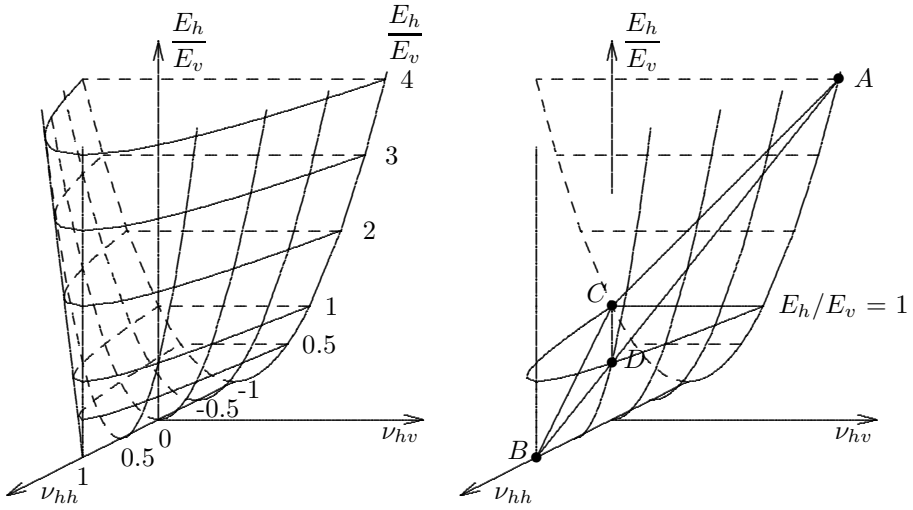

Figure 3.4: Bounding values for anisotropic linear elastic parameters after [61]

line CD, $E_h/E_v = 1$, $\nu_{hh} = \nu_{hv}$. Since G_{hv} is an independent parameter an anisotropic material can still be represented by the line CD.

From equation (3.9) it is found that the strain energy for isotropic loading, $\sigma'_{(ii)} = \sigma', \tau_{ij} = 0$, is given by:

$$dW = \frac{1}{2E_h}\left[(1 - 4\nu_{vh})\frac{E_h}{E_v} + 2(1 - \nu_{hh})\right]\sigma^2$$

Constant volume deformation requires $dW = 0$ with $\nu_{vh} = \nu_{hv}E_v/E_h$ leading to:

$$\frac{E_h}{E_v} + 2 - 4\nu_{hv} - 2\nu_{hh} = 0 \tag{3.17}$$

The intersection with the third condition given by equation (3.14) and (3.15) yields:

$$\nu_{hv} = \frac{1}{2}\frac{E_h}{E_v}, \qquad \nu_{hh} = 1 - \frac{1}{2}\frac{E_h}{E_v}$$

The intersection produces a straight line although the shape presented by figure 3.4 is strongly curved. In figure 3.4 the line AB represents the intersection. In soil mechanics constant volume deformations are found when soil behaves undrained which is further discussed in section 4.3.2.

3.3 Stresses

Any deformation of a soil volume can be expressed in terms of volumetric strain and distortional strain. A familiar way to express stress in terms of strain uses the Lamé constants. For an isotropic linear elastic material is found:

$$\sigma'_{ij} = \lambda e\delta_{ij} + 2\mu\varepsilon_{ij} \tag{3.18}$$

In which λ and μ are known as Lamé constants:

$$\lambda = K + \frac{2}{3}G = \frac{\nu E}{(1+\nu)(1-2\nu)}, \quad \mu = G = \frac{E}{2(1+\nu)}$$

For a cross–anisotropic material stress can be expressed into strain in an equivalent manner. In literature references up to now are not known to the author. The complete derivation is presented in appendix B.

$$\begin{aligned}
\sigma'_{xx} &= Ae + 2G_{hh}\varepsilon_{xx} + B\varepsilon_{zz} \\
\sigma'_{yy} &= Ae + 2G_{hh}\varepsilon_{yy} + B\varepsilon_{zz} \\
\sigma'_{zz} &= (A+B)\,e + D\varepsilon_{zz} \\
\tau_{xy} &= G_{hh}\gamma_{xy} \\
\tau_{yz} &= G_{vh}\gamma_{yz} \\
\tau_{zx} &= G_{vh}\gamma_{zx}
\end{aligned} \tag{3.19}$$

with:

$$\begin{aligned}
A &= \frac{\nu_{hh}E_hE_v + \nu_{vh}^2E_h^2}{(1+\nu_{hh})\,(E_v\,(1-\nu_{hh}) - 2E_h\nu_{vh}^2)} \\
B &= \frac{E_hE_v\,(\nu_{vh}\,(1+\nu_{hh}) - \nu_{hh}) - \nu_{vh}^2E_h^2}{(1+\nu_{hh})\,(E_v\,(1-\nu_{hh}) - 2E_h\nu_{vh}^2)} \\
D &= \frac{E_v^2\,(1-\nu_{hh}) - E_hE_v\nu_{vh}}{E_v\,(1-\nu_{hh}) - 2E_h\nu_{vh}^2} \\
G_{hh} &= \frac{E_h}{2\,(1+\nu_{hh})}
\end{aligned}$$

Note that for isotropic conditions, $E_h = E_v = E$, $G_{hh} = G_{vh} = G$ and $\nu_{hh} = \nu_{vh} = \nu$ is found: $A = \nu E/[(1+\nu)(1-2\nu)] = \lambda$, $B = 0$ and $D = 2G = 2\mu$ and equation (3.19) reduces to (3.18). Equation (3.19) gives a 5–parameter model which is in agreement with the requirements for a cross-anisotropic model according to section 3.1.

Chapter 4

Parameter assessment

4.1 Reducing the number of independent parameters

Not all the independent parameters in equation (3.9) can be determined by standard triaxial tests. Since no shear stress is applied nor shear strain measured, the part of the compliance matrix which can be determined is the top left corner of the matrix in equation (3.9). When the axis of symmetry for a cross–anisotropic material corresponds to the axial direction equation (4.1) gives the stiffness matrix involved in standard triaxial testing:

$$\begin{bmatrix} \varepsilon_a \\ \varepsilon_r \end{bmatrix} = \frac{1}{E_v} \begin{bmatrix} 1 & -2\nu_{vh} \\ -\nu_{vh} & (1-\nu_{hh})/\eta \end{bmatrix} \begin{bmatrix} \sigma'_a \\ \sigma'_r \end{bmatrix}, \qquad \eta = \frac{E_h}{E_v} \tag{4.1}$$

with

ε_a = axial strain
ε_r = radial strain
σ'_a = axial stress
σ'_r = radial stress

Equation (4.1) involves four independent parameters, E_h, E_v, ν_{hh} and ν_{vh}. No information about the shear modulus G_{vh} can be derived. Graham & Houlsby, [34] show that only three independent parameters can be deduced from standard triaxial testing since ν_{hh} and E_h cannot be found independently. This section discusses four three–parameter models, presented in literature. These models are suggested to make parameter determination for anisotropy with standard triaxial testing possible.

In soil mechanics the deformation of soil is often investigated in terms of volumetric strain e due to an isotropic effective stress p', and distortion ε_q due to a deviator stress q. For general conditions p' and q are given by (see a.o. [80]):

$$\begin{aligned} p' &= \frac{\sigma'_{xx} + \sigma'_{yy} + \sigma'_{zz}}{3} \\ q &= \sqrt{\frac{(\sigma_{yy} - \sigma_{zz})^2 + (\sigma_{zz} - \sigma_{xx})^2 + (\sigma_{xx} - \sigma_{yy})^2}{2} + 3\left(\tau_{yz}^2 + \tau_{zx}^2 + \tau_{xy}^2\right)} \end{aligned} \tag{4.2}$$

Furthermore e and ε_q are given by:

$$\begin{aligned} e &= \varepsilon_{xx} + \varepsilon_{yy} + \varepsilon_{zz} \\ q &= \frac{1}{3}\sqrt{2\left[(\varepsilon_{yy} - \varepsilon_{zz})^2 + (\varepsilon_{zz} - \varepsilon_{xx})^2 + (\varepsilon_{xx} - \varepsilon_{yy})^2\right] + 3\left(\gamma_{yz}^2 + \gamma_{zx}^2 + \gamma_{xy}^2\right)} \end{aligned} \tag{4.3}$$

Using axial symmetry, triaxial test conditions, equations (4.2) and (4.3) can be simplified to:

$$p' = \frac{(\sigma'_a + 2\sigma'_r)}{3} \tag{4.4}$$

$$q = \sigma'_a - \sigma'_r \tag{4.5}$$

$$e = \varepsilon_a + 2\varepsilon_r \tag{4.6}$$

$$\varepsilon_q = \frac{2\,(\varepsilon_a - \varepsilon_r)}{3} \tag{4.7}$$

Inserting equations (4.4) to (4.7) into equation (3.9) for isotropic conditions gives the relation between p' and q on one hand and e and ε_q on the other hand by:

$$\begin{bmatrix} p' \\ q \end{bmatrix} = \begin{bmatrix} K & 0 \\ 0 & 3G \end{bmatrix} \begin{bmatrix} e \\ \varepsilon_q \end{bmatrix} \tag{4.8}$$

For cross–anisotropic conditions an increase in p' also induces an ε_q increment and an increase in q also induces an increment in e. So the stiffness matrix of equation(4.8) for cross–anisotropic conditions is no longer a diagonal matrix. If parameter J represents the cross dependency, relation (4.8) for anisotropic material becomes:

$$\begin{bmatrix} p' \\ q \end{bmatrix} = \begin{bmatrix} K^* & J \\ J & 3G^* \end{bmatrix} \begin{bmatrix} e \\ \varepsilon_q \end{bmatrix} \tag{4.9}$$

In equation (4.9) the parameters are marked with a * to distinguish them from their isotropic equivalents. The parameters K^*, G^* and J can be expressed in E_v, E_h, ν_{hh} and ν_{vh}, see appendix C. When the axis of symmetry is in axial direction the following set is found:

$$K^* = \frac{E_v}{9}\left[\frac{(1-\nu_{hh})\,E_v + 2\,(1+2\nu_{vh})\,E_h}{(1-\nu_{hh})\,E_v - 2\nu_{vh}^2 E_h}\right] \tag{4.10}$$

$$G^* = \frac{E_v}{6}\left[\frac{2\,(1-\nu_{hh})\,E_v + (1-4\nu_{vh})\,E_h}{(1-\nu_{hh})\,E_v - 2\nu_{vh}^2 E_h}\right] \tag{4.11}$$

$$J = \frac{E_v}{3}\left[\frac{(1-\nu_{hh})\,E_v - (1-\nu_{vh})\,E_h}{(1-\nu_{hh})\,E_v - 2\nu_{vh}^2 E_h}\right] \tag{4.12}$$

Equation (4.9) can be rewritten to a compliance matrix, with $D = 3K^*G^* - J^2$:

$$\begin{bmatrix} e \\ \varepsilon_q \end{bmatrix} = \frac{1}{D}\begin{bmatrix} 3G^* & -J \\ -J & K^* \end{bmatrix} \begin{bmatrix} p' \\ q \end{bmatrix} \tag{4.13}$$

Graham & Houlsby, [34], present a three parameter model. Their model is extensively described in [54] and [80]. The basis of the Graham & Houlsby model is Hooke's law for isotropic conditions and an anisotropy factor α. When Hooke's law is formulated by $\sigma'_{ij} = D_{ijkl}\varepsilon_{kl}$, then is found for isotropic conditions:

$$D_{ijkl} = \frac{E}{(1+\nu)\,(1-2\nu)} \times$$

$$\begin{pmatrix} (1-\nu) & \nu & \nu & 0 & 0 & 0 \\ \nu & (1-\nu) & \nu & 0 & 0 & 0 \\ \nu & \nu & (1-\nu) & 0 & 0 & 0 \\ 0 & 0 & 0 & \frac{1}{2}(1-2\nu) & 0 & 0 \\ 0 & 0 & 0 & 0 & \frac{1}{2}(1-2\nu) & 0 \\ 0 & 0 & 0 & 0 & 0 & \frac{1}{2}(1-2\nu) \end{pmatrix} \tag{4.14}$$

In order to reduce the number of anisotropic parameters it is assumed that anisotropy is characterised by one anisotropy factor α. The corresponding anisotropic stiffness matrix is proposed by multiplying e.g. the stiffness in horizontal directions, the first and second row, by α. To keep the stiffness matrix symmetric the first and second column are multiplied by α leading to α^2 in the top left corner of the stiffness matrix.

$$D^*_{ijkl} = \frac{E^*}{(1+\nu^*)(1-2\nu^*)} \times$$

$$\begin{pmatrix} \alpha^2(1-\nu^*) & \alpha^2\nu^* & \alpha\nu^* & 0 & 0 & 0 \\ \alpha^2\nu^* & \alpha^2(1-\nu^*) & \alpha\nu^* & 0 & 0 & 0 \\ \alpha\nu^* & \alpha\nu^* & (1-\nu^*) & 0 & 0 & 0 \\ 0 & 0 & 0 & \frac{1}{2}(1-2\nu^*)\alpha^2 & 0 & 0 \\ 0 & 0 & 0 & 0 & \frac{1}{2}(1-2\nu^*)\alpha & 0 \\ 0 & 0 & 0 & 0 & 0 & \frac{1}{2}(1-2\nu^*)\alpha \end{pmatrix} \tag{4.15}$$

To express the difference with the isotropic case, the stiffness parameters in equation (4.15) are indicated with the *–sign. When inverting equation (4.15) to $\varepsilon_{ij} = D^{*-1}_{ijkl}\sigma_{kl}$, the following expression is found:

$$D^{*-1}_{ijkl} = \begin{pmatrix} \frac{1}{\alpha^2 E^*} & \frac{-\nu^*}{\alpha^2 E^*} & \frac{-\nu^*}{\alpha E^*} & 0 & 0 & 0 \\ \frac{-\nu^*}{\alpha^2 E^*} & \frac{1}{\alpha^2 E^*} & \frac{-\nu^*}{\alpha E^*} & 0 & 0 & 0 \\ \frac{-\nu^*}{E^*\alpha} & \frac{-\nu^*}{E^*\alpha} & \frac{1}{E^*} & 0 & 0 & 0 \\ 0 & 0 & 0 & \frac{(1+\nu^*)}{2\alpha^2 E^*} & 0 & 0 \\ 0 & 0 & 0 & 0 & \frac{(1+\nu^*)}{2\alpha E^*} & 0 \\ 0 & 0 & 0 & 0 & 0 & \frac{(1+\nu^*)}{2\alpha E^*} \end{pmatrix} \tag{4.16}$$

Comparison of equation(4.16) to equation (3.9) yields:

- $E_v = E^*$
- $E_h = \alpha^2 E^*$
- $\nu_{vh} = \nu^*/\alpha$
- ν_{hh}=ν^*

- $G_{vh} = \alpha E^* / 2\,(1 + \nu^*)$
- $G_{hh} = \alpha^2 E^* / 2\,(1 + \nu^*)$

So a physical meaning of the anisotropy factor α can be seen as $\alpha = \sqrt{E_h/E_v}$. For $\alpha = 1$ equation (4.16) represents isotropic behaviour. The assumption that one anisotropy factor can be used to describe cross–anisotropy has limiting consequences. The ratio's of the different stiffness parameters are no longer independent; $\sqrt{E_h/E_v} = \nu_{hh}/\nu_{vh} = G_{hh}/G_{vh}$. The comparison between the equations (4.16) and (3.9) can be summarised by:

$$\begin{aligned} \alpha &= \sqrt{E_h/E_v} \\ \alpha &= \nu_{hh}/\nu_{vh} \\ \alpha &= G_{hh}/G_{vh} \end{aligned} \tag{4.17}$$

Atkinson, Richardson & Stallebrass [4] use a more general form of equation (4.13):

$$\begin{bmatrix} \delta e \\ \\ \delta\varepsilon_q \end{bmatrix} = \begin{bmatrix} \dfrac{1}{K'} & \dfrac{1}{J_{pq}} \\ \dfrac{1}{J_{qp}} & \dfrac{1}{3G'} \end{bmatrix} \begin{bmatrix} \delta p' \\ \\ \delta q \end{bmatrix} \tag{4.18}$$

The subscripts pq and qp have been used, following Hird & Pierpoint [36]. Due to the distinction between J_{pq} and J_{qp} anisotropy different from cross–anisotropy can also be modelled. For cross–anisotropy, which is assumed here, follows $J_{pq} = J_{qp} = J'$. Atkinson, Richardson & Stallebrass [4] consider the parameters K', J' and G' as tangent moduli. The use of tangent moduli allows equation (4.18) to be used for non–linear elastic behaviour. Then values for K', J' and G' are stress dependent. The δ–sign is used in equation (4.18) indicating that increments of stress and strain are considered. The parameters K', G' and J' are different from K^*, G^* and J. Comparison of (4.18) and (4.13) yields, [54]:

$$G^* = \frac{G' J'^2}{J'^2 - 3K'G'} \tag{4.19}$$

$$K^* = \frac{K' J'^2}{J'^2 - 3K'G'} \tag{4.20}$$

$$J = \frac{-3G'K'J'}{J'^2 - 3K'G'} \tag{4.21}$$

and

$$G' = \frac{3G^*K^* - J^2}{3K^*} \tag{4.22}$$

$$K' = \frac{3G^*K^* - J^2}{3G^*} \tag{4.23}$$

$$J' = \frac{-\left(3G^*K^* - J^2\right)}{J} \tag{4.24}$$

Appendix C shows that K', G' and J' can be expressed in the traditional stiffness parameters, assuming the axis of symmetry in axial direction is found:

$$G' = \frac{3}{4\left[\left(1 + 2\nu_{vh}\right)/E_v + \left(1 - \nu_{hh}\right)/2E_h\right]} \tag{4.25}$$

$$K' = \frac{1}{\left[\left(1 - 4\nu_{vh}\right)/E_v + 2\left(1 - \nu_{hh}\right)/E_h\right]} \tag{4.26}$$

$$J' = \frac{3}{2\left[\left(1 - \nu_{vh}\right)/E_v - \left(1 - \nu_{hh}\right)/E_h\right]} \tag{4.27}$$

In this three parameter description the restriction that one factor, α, controls the ratio of different parameters is not required. The K', J' and G' model therefore represents more general conditions than the α, E^* and ν^* model.

Lings, Pennington & Nash [54] use equation (4.1). It should be noted that the matrix in equation (4.1) is no longer symmetric. Each component can be derived from standard triaxial tests. However since the parameters ν_{hh} and E_h are not expressed independently, the individual values for ν_{hh} and E_h cannot be found. For this reason a parameter F_h is introduced by:

$$F_h = \frac{E_h}{1 - \nu_{hh}} \tag{4.28}$$

Lings, Pennington & Nash, [54], show that the parameters K', J' and G' can be expressed into E_v, F_h and ν_{vh}, according to:

$$G' = \frac{3E_v F_h}{4F_h + 8\nu_{vh}F_h + 2E_v} \tag{4.29}$$

$$K' = \frac{E_v F_h}{F_h - 4\nu_{vh}F_h + 2E_v} \tag{4.30}$$

$$J' = \frac{3E_v F_h}{2F_h - 2\nu_{vh}F_h - 2E_v} \tag{4.31}$$

Rewriting gives:

$$E_v = \frac{9G'K'J'}{6G'K' + G'J' + 3K'J'} \tag{4.32}$$

$$\nu_{vh} = -\frac{1}{2}\frac{3G'K' + 2G'J' - 3K'J'}{6G'K' + G'J' + 3K'J'} \tag{4.33}$$

$$F_h = \frac{-18G'K'J'}{12G'K' - 4G'J' - 3K'J'} \tag{4.34}$$

4.2 Reported measurements

Section 4.1 presents four three-parameter descriptions of cross–anisotropy given in the parameters E^*, ν^*, α or K^*, G^*, J or K', G', J' and E_v, ν_{vh}, F_h. Measurements of these parameters presented in literature are limited. Most of the reported measurements concern stiff clay and sand. Measurements on peat were not found. Using equations (4.19) to (4.21), (4.22) to (4.24), (4.29) to (4.31) and (4.32) to (4.34) the parameters measured for one model can be expressed into the parameters for the other models.

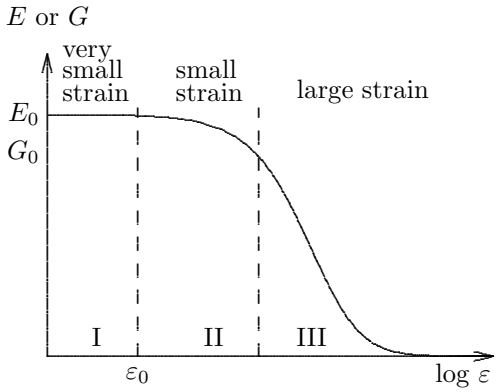

Figure 4.1: Typical stiffness–strain relationship, after [5]

Before discussing reported measurements the strain dependency of stiffness parameters should be noted. Figure 4.1 shows a typical stiffness–strain relationship for soil, according to Atkinson [5]. Three regions can be distinguished. In the first region, for very small strain, the stiffness is relatively large and strain independent. In the second region the stiffness decreases and is clearly non–linear. However in the second region the behaviour can still be described by equivalent elastic tangent moduli. In the third region the plastic deformation is considerable

and stiffness is strongly reduced. Jardine [39] describes the application of this phenomenon to modelling soil behaviour. In a p'–q diagram the corresponding stress condition can be depicted. Even for largely over–consolidated conditions only a small zone around the actual stress condition is found in which soil behaviour is truly linear elastic. This zone is referred to as zone I. Beyond this zone a zone II is defined in which soil behaviour can be described as non–linear elastic. After a loading–unloading cycle within zone II the remaining deformation is negligible. However the stress–strain curve shows a hysteresis. Between zone II and some bounding surface lays zone III in which loading–unloading cycles lead to unrecoverable deformation and an increasing load reduces the stiffness until failure is reached.

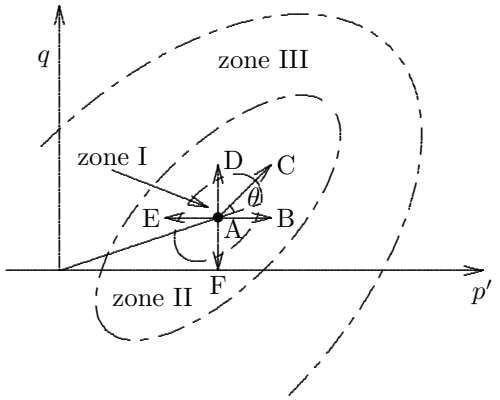

	$\delta p'$	δq
AB	> 0	0
AC	> 0	> 0
AD	0	> 0
AE	< 0	0
AF	0	< 0

Figure 4.2: Different stress path directions for deriving stiffness parameters

The boundary for zone I is reached for very small strain, 10^{-5} ([54], [38]) or even smaller for some clays [39]. This implies that for some soil types true linear–elastic behaviour is beyond measurement accuracy. The non–linearity in zone II is explained by small plastic deformations at micro–level where yielding occurs at the contact points of the solid particles. The boundary for zone II is found for strain of an order of magnitude of 10^{-4} to 4×10^{-4}, [39].

The strain dependency of stiffness parameters has several consequences. Two are discussed in further detail. First, Jardine [39] shows that the boundary of zone I and II is not symmetrical around the considered stress condition. The shape of zone II depends on the stress history and distance to the yield surface. Within zone I and II soil behaviour might be anisotropic, though when elastic parameters are derived by stress paths in different directions around some stress condition an apparent anisotropy might be found due to an irregular shape of zone II. This is also found by Atkinson et al. [4] and Lings et al. [54]. Figure 4.2 shows different stress paths which can be followed to derive stiffness parameters. If a triaxial sample is brought to stress condition A shown by figure 4.2, different stiffness parameters can be derived by applying stress paths like AB, AC, AD, AE or AF. The angle between the stress path before consolidation and applied stress path is indicated by θ in figure 4.2. Atkinson et al. [4] and Lings et al. [54] show that stiffness parameters are θ–dependent.

The second consequence of the strain dependency of stiffness parameters is that comparison of stiffness parameters is only valid when measured at the same strain level. Yimsiri & Soga [82] report an overview of measurements on the full set of five cross–anisotropic parameters. Table 4.2 shows a summary. The reported parameters are derived from triaxial tests in combination to horizontal and vertical shear wave measurements. Shear wave measurements involve very small displacements. The parameters found by shear wave measurements can be considered as initial, zone I, values. Due to the measurement accuracy a reliable measurement for stiffness parameters by conventional axial or radial deformation measurement techniques are usually only found for zone

Table 4.1: Cross–anisotropic elastic parameters for clay

material	ref.	stress condition	G^* G'	K^* K'	J J'	α	E^* E_v	ν^*	ν_{vh}	F_h
Winnipeg Clay	[34]	in situ[c]	$8.5^a \times\sigma'_{vc}$	$14.5^a \times\sigma'_{vc}$	$-5.5^a \times\sigma'_{vc}$	1.33^a	$18.5^e \times\sigma'_{vc}$	0.22^a	0.17^e	$36.7^e \times\sigma'_{vc}$
			$7.8^d \times\sigma'_{vc}$	$13.3^d \times\sigma'_{vc}$	$61.7^d \times\sigma'_{vc}$					
Gault Clay	[54]	in situ	$663^d \times p'_0$	$613^d \times p'_0$	$-715^d \times p'_0$	1.95	$550^f \times p'_0$	0	0^a	$2100^a \times p'_0$
		$K_0 \approx 2$	$385^a \times p'_0$	$356^a \times p'_0$	$990^a \times p'_0$		$550^a \times p'_0$			
London Clay	[4]	isotropic	-	-	-					
		$p'_0 = 200$ kPa	37^a [MPa]	60^a [MPa]						
		OCR = 2								
Oxford Clay	[36]	isotropic	173^d [MPa]	259^d [MPa]	-333^d [MPa]	1.7	43^e [MPa]	-	0.03^e	1030^e [MPa]
	[37]	$p'_0 = 150$	45^a [MPa]	30^a [MPa]	125^{ab} [MPa]					

[a] = measured values [b] $J' = 0.5(J'_{pq} + J'_{qp})$ [c] = K_0 not given in [34], $\phi' = 17.5°$ $K_0 \approx 1 - \sin\phi' = 0.7$
[d] = eq. (4.19) to (4.24) [e] = eq.(4.32) to (4.34) [f] = eq. (4.17)

Table 4.2: Cross–anisotropic elastic parameters according to [82]

Material	ref.	stress condition	E_v [MPa]	E_h [MPa]	G_{vh} [MPa]	G_{hh} [MPa]	ν_{hh}	ν_{vh}	ν_{hv}	α $\sqrt{E_h/E_v}$	α G_{hh}/G_{vh}	α ν_{hv}/ν_{hh}
Dry Mortar sand	[67]	isotropic	242.9	304.0	108.1	132.8	0.145	0.201	0.251	1.12	1.23	1.73
		p'= 85 kPa										
		K_0= 1.7	236.8	320.2	110.6	135.3	0.183	0.066	0.091	1.16	1.22	0.50
		$\sigma'_v = 50$ kPa										
Dry Ticino sand	[11]	$K_0 = 0.5$	386.6	306.2	135.4	127.8	0.198	0.143	0.133	0.89	0.94	0.67
		$\sigma'_v = 300$ kPa										
		$K_0 = 1.5$	245.9	372.5	123.9	156.0	0.194	0.092	0.154	1.23	1.26	0.79
		$\sigma'_v = 150$ kPa										
		$K_0 = 2$	188.5	353.8	104.4	150.9	0.172	0.141	0.264	1.37	1.45	1.53
		$\sigma'_v = 100$ kPa										
		isotropic	287.9	349.4	125.2	149.1	0.172	0.177	0.215	1.10	1.19	1.25
		$p' = 200$ kPa										
Saturated Ham River sand	[50]	$K_0 = 0.45$ $\sigma'_v = 316$ kPa	520	280	154	130	0.07	0.35	0.19	0.73	0.84	2.71
Gault Clay	[54]	in situ stress	550	2186	507	1140	-0.04	0	0	2.0	2.25	0
		$K_0 \approx 2$	$\times p'_0$	$\times p'_0$	$\times p'_0$	$\times p'_0$						

II and III. This difference should be realised when comparing the results of different measurement techniques.

So it is therefore concluded that the actual value for a stiffness parameter depends on load history and strain level at which the parameter is measured. In literature this is not always acknowledged. When gathering measurement data from literature stress history is not always presented or measurements of strain gauges are mixed with shear wave measurements. Keeping these remarks in mind, table 4.1 and 4.2 give the possibility to check some of the assumptions made for the three-parameter models. Table 4.2 shows the values for α found from the measured cross–anisotropic parameters. Except for Ham River sand and Gault Clay, table 4.2 shows that the values for the three α–definitions, as shown by equation (4.17), are of the same order of magnitude. Due to the low value for ν_{hh} respectively ν_{hv} the definition of $\alpha = \nu_{hv}/\nu_{hh}$ for Ham River sand and Gault Clay does not correspond to the values for the other definitions. The assumption $\alpha = \sqrt{E_h/E_v} = \nu_{hh}/\nu_{vh} = G_{hh}/G_{vh}$ seems not to hold for small values for ν_{hv} and ν_{hh}.

Another important assumption is the symmetry of matrix in equation (4.18), $J'_{pq} = J'_{qp} = J'$. For Gault Clay and Oxford Clay separate measurements of J'_{pq} and J'_{qp} are presented in [54] and [37] respectively. For Oxford Clay a distinction has been made between loading and unloading conditions, ($\delta q > 0, \delta q < 0$). For unloading conditions it is found that $J_{pq} \approx J_{qp} \approx J' \approx 70$ kPa. For loading conditions however J_{pq} reaches 180 kPa for small strain, J_{qp} corresponds to the values found for unloading. Larger strain gives $J_{pq} \approx J_{qp} \approx J'$. The value for J' presented in table 4.1 follows from $J' = 0.5\ (J_{pq} + J_{qp})$. The presented value for α is calculated using this average value. It should be noted that $J' \to \infty$ indicates isotropic conditions. Small J'–values indicate strong anisotropy, $J' = 70$ kPa corresponds to $\alpha = 4.89$.

For Gault Clay [54] values for J_{pq} and J_{qp} are derived in tests with constant p' and constant q. For small strain energy it is found that $J_{pq} \approx J_{qp} \approx J' = 800$–$1000$ kPa at small strain level. The differences in the measured J'-value are explained by the difficulty in measuring J' at small strain levels.

4.3 Undrained tests

4.3.1 Initial pore pressure

An important feature in undrained loading is the development of excess pore pressure under constant volume deformation. In engineering practice undrained behaviour plays an important role when dealing with soft, low permeable soil types like clay and peat. Initially after loading these soil types behave undrained. Pore pressure will then decrease and deformations emerge when consolidation proceeds. Loading can be considered as instantaneous, since the time needed for load application is considerably smaller than the hydrodynamic period. The amount of pore pressure directly after loading is referred to as initial pore pressure. In the laboratory undrained triaxial testing can be used to reproduce these initial conditions. In the following expressions are derived for initial pore pressure reaction for axial symmetric isotropic and cross–anisotropic material behaviour. The expressions show that the initial pore pressure is strongly influenced by anisotropy.

The isotropic case
De Josselin de Jong [41] presents a mathematical formulation for calculating the initial pore pressure when loading a soil sample for the isotropic case. Starting point is the initial volume change e_0 which equals the initial change in pore water volume. So, with K for soil bulk modulus and K_w for pore water stiffness the following is found:

$$e_0 = \frac{p'}{K} = \sigma_{w0}\frac{n}{K_w} \tag{4.35}$$

followed by:

$$p' = Ke_0 \qquad \sigma_{w0} = \frac{K_w}{n} e_0$$

$$p = p' + \sigma_{w0} = Ke_0 + \frac{K_w}{n} e_0 = \left(\frac{nK + K_w}{n} \right) e_0$$

$$e_0 = p \left(\frac{n}{nK + K_w} \right) = \sigma_{w_0} \frac{n}{K_w}$$

$$\sigma_{w_0} = Bp; \qquad B = \left(\frac{1}{\frac{nK}{K_w} + 1} \right) \tag{4.36}$$

The parameter B in equation (4.36) represents the Skempton B–factor [65]. For fully saturated soil $K_w \gg K$ and $B = 1$. Equation (4.36) shows that the initial pore pressure equals the isotropic stress increase for an isotropic, fully saturated, soil type. In standard triaxial testing with $\sigma_r = 0$ and $p = \sigma_a/3$ is found:

$$\sigma_{w0} = \frac{\sigma_a}{3} \tag{4.37}$$

The cross–anisotropic case
The relation between the anisotropic stiffness parameters and the initial pore pressures is given by equation (4.18)

$$e_0 = \frac{p'}{K'} + \frac{q}{J'} = \sigma_{w_0} \frac{n}{K_w} \tag{4.38}$$

reformulation gives:

$$K'J'e_0 = J' \left(p - \sigma_{w0} \right) + K'q, \qquad \sigma_{w0} = \frac{K_w}{n} e_0$$

$$e_0 = \left(\frac{n}{nK' + K_w} \right) \left(p + \frac{K'}{J'} q \right) = \frac{n}{K_w} \sigma_{w0} \tag{4.39}$$

$$\sigma_{w0} = B \left(p + \frac{K'}{J'} q \right), \qquad B = \left(\frac{1}{\frac{nK'}{K_w} + 1} \right) \tag{4.40}$$

The influence of anisotropy on the Skempton B–factor is given by the replacement of K by K'. For isotropic conditions $K' \to K$ and $K'/J' \to 0$ is found that equation (4.40) reduces to (4.36). Equation (4.40) shows the influence of anisotropy on σ_{w0}. For fully saturated soil in standard triaxial testing, $\sigma_r = 0$, $p = 1/3\sigma_a$ and $q = \sigma_a$ is found:

$$\sigma_{w0} = \left(\frac{1}{3} + \frac{K'}{J'} \right) \sigma_a \tag{4.41}$$

It should be noted that expression (4.41) presents the initial excess pore pressure for initial, undrained, conditions in terms of drained stiffness parameters. Another expression for the initial

pore pressure for a fully saturated soil under axial symmetric conditions is presented by Chowdhury [21]:

$$\sigma_{w0} = \frac{(1 - \nu_{hh} - \eta\nu_{vh})\, 2\sigma_r + (\eta - 2\eta\nu_{vh})\, \sigma_a}{\eta - 4\nu_{vh}\eta + 2 - 2\nu_{hh}}, \quad \eta = \frac{E_h}{E_v} \tag{4.42}$$

Application of the equations (4.26) and (4.27) to equation (4.41) shows equations (4.42) and (4.41) to be equivalent.

4.3.2 Drained and undrained stiffness parameters

In engineering practice undrained analyses are often conducted using a total stress analysis in which undrained behaviour is modelled as a constant volume deformation. For isotropic conditions this is achieved by adjusting the stiffness parameters such that the bulk modulus reaches an infinite value while the shear modulus remains unaltered. Drained and undrained stiffness parameters should not be mixed. To distinguish undrained parameters the superscript u is used.

Equation (4.35) shows for partly saturated soil, $B < 1$, that undrained deformations do not correspond to constant volume deformations. Chapter 2 states that partly saturated soil can be modelled by the pore fluid stiffness for $S_r > 0.85$. Elaborating equation (4.35) for this condition in combination to Hooke's law for isotropic conditions gives for the undrained stiffness parameters, [15]:

$$E^u = \frac{3E}{3 - B\,(1 - 2\nu)}; \quad \nu^u = \frac{3\nu + B\,(1 - 2\nu)}{3 - B\,(1 - 2\nu)} \tag{4.43}$$

Section 3.2 discusses the bounding values for the cross anisotropic stiffness parameters. This is visualised by figure 3.4, which is repeated by figure 4.3.

Section 3.2 explains that each valid combination of stiffness parameters falls in or is on the "ship-bow" like shape presented by figure 4.3. Section 3.2 explains that the line AB represents the combination of stiffness parameters which give constant volume deformation. For soil completely saturated by an incompressible fluid these parameters can be regarded as the cross–anisotropic undrained stiffness parameters. It is remarkable that for undrained behaviour the ratio $(E_h/E_v)^u$ is maximised to 4. As shown by figure 4.3 for $E_h/E_v > 4$ no constant volume deformation is possible within the range of valid ν_{hh} values. This illustrates that the level of anisotropy is less distinct for undrained conditions than for drained conditions.

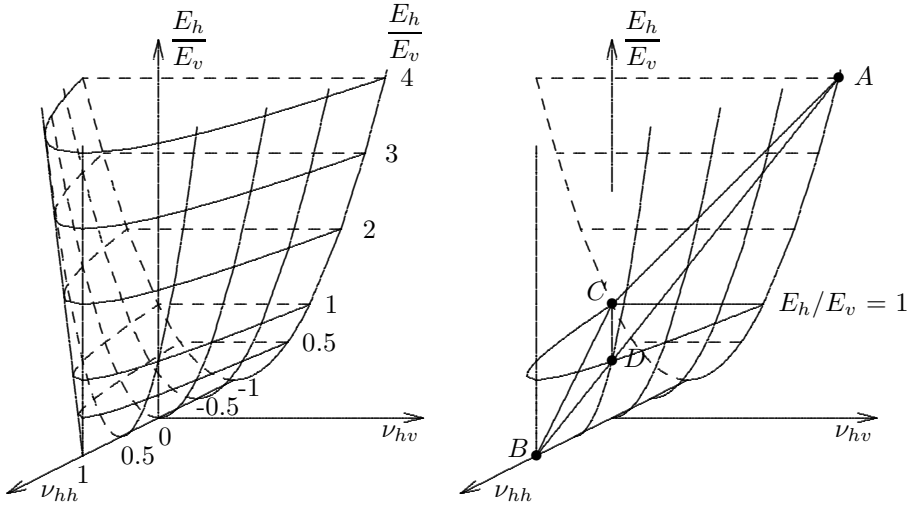

Figure 4.3: Bounding values for anisotropic linear elastic parameters after [61]

For isotropic conditions there is a unique relation between the drained and undrained stiffness parameters as shown by equation (4.43). Cross–anisotropy however does not exhibit such an unique relation. When $B = 1$ the undrained behaviour of a soil type with any combination of drained parameters is represented by some unique point on the line AB in figure 4.3. So any combination of drained parameters can be uniquely mapped to undrained parameters, however some combination of undrained parameters represent a large number of valid combinations of drained parameters.

Elaborating equation (4.38) and (3.9) expresses the undrained stiffness parameters into drained parameters as shown by appendix D. The result is:

$$
\begin{aligned}
E_v^u &= \frac{E_v\left[\left(1-4\nu_{vh}\right)E_h + 2\left(1-\nu_{hh}\right)E_v\right]}{E_h\left[\left(1-4\nu_{vh}\right) - B\left(1-2\nu_{vh}\right)^2\right] + 2\left(1-\nu_{hh}\right)E_v} \\
E_h^u &= \frac{E_v E_h d}{E_v d - B\left[E_v^2\left(1-\nu_{hh}\right)^2 - 2E_v E_h \nu_{vh}\left(1-\nu_{hh}\right) + \nu_{vh}^2 E_h^2\right]} \\
\nu_{vh}^u &= \frac{\nu_{vh}E_h\left[\left(1-4\nu_{vh}\right) - B\left(1-2\nu_{vh}\right)\right] + \left(1-\nu_{hh}\right)E_v\left[2\nu_{vh} + B\left(1-2\nu_{vh}\right)\right]}{E_h\left[\left(1-4\nu_{vh}\right) - B\left(1-2\nu_{vh}\right)^2\right] + 2\left(1-\nu_{hh}\right)E_v} \\
\nu_{hh}^u &= \frac{\nu_{hh}E_v d + B\left[E_v^2\left(1-\nu_{hh}\right)^2 + E_h^2\nu_{vh}^2 - 2E_h E_v \nu_{vh}\left(1-\nu_h\right)\right]}{E_v d + B\left[2E_v E_h \nu_{vh}\left(1-\nu_{hh}\right) - E_v^2\left(1-\nu_{hh}\right)^2 - \nu_{vh}^2 E_h^2\right]}
\end{aligned}
\tag{4.44}
$$

with

$d = \left(1-4\nu_{vh}\right)E_h + 2\left(1-\nu_{hh}\right)E_v$

Note that the shear modulus remains unaffected so, $G_{hh}^u = G_{hh}$ and $G_{vh}^u = G_{vh}$. For E_v^u and E_h^u the expressions for their reciprocal values are also given in appendix D since these expressions nicely show the influence of the B–factor. For completely saturated soil, $B = 1$, is found, a.o. Lings in [55]:

$$\nu_{vh}^u = \frac{1}{2} \quad \nu_{hh}^u = 1 - \frac{1}{2}\frac{E_h^u}{E_v^u}$$

For $B = 1$ the number of independent cross–anisotropic parameters is reduced from 5 to 3, E_v^u, E_h^u and G_{vh}^u. This corresponds to figure 4.3 which depicts undrained deformation by a single line, the line AB.

4.3.3 The undrained effective stress path

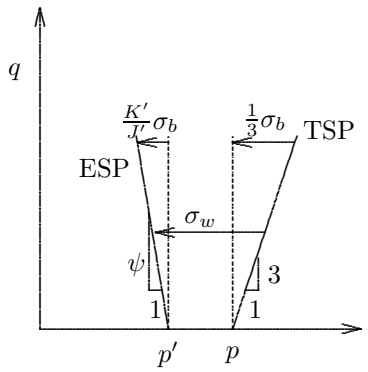

Figure 4.4: Typical stress paths for a linear elastic material

Figure 4.4 shows a typical Total Stress Path (TSP) and an Effective Stress Path (ESP) for undrained elastic conditions. In figure 4.4 σ_b represents the axial load increment applied at the top of the sample. The intercept between both paths corresponds to the pore pressure development inside the sample. For a standard undrained axial compression test, by definition of p and q, the TSP has a slope of 1:3. In an undrained test an increment in vertical load gives a pore pressure reaction as presented in equation (4.40). The slope of the ESP, ψ in fig 4.4, is dictated by the ratio K'/J', $\psi = -J'/K'$. For an isotropic elastic material, $K'/J' = 0$, a vertical ESP is found. For $K'/J' > 0$, the pore pressure development exceeds the increase in p leading to a reduction in p'. A back-

wardly tilting ESP is found. If $K'/J' < 0$, an increase in p' is found producing a forwardly tilting ESP.

The ratio K'/J' can be expressed in E_h, E_v, ν_{hh} and ν_{vh} using the equations given in appendix C. If the axial direction of the sample corresponds to the axis of symmetry, referred to as the vertical direction, is found:

$$\frac{K'}{J'} = \frac{2}{3}\left[\frac{(1-\nu_{vh})\,\eta - (1-\nu_{hh})}{(1-4\nu_{vh})\,\eta + 2\,(1-\nu_{hh})}\right], \qquad \eta = \frac{E_h}{E_v} \tag{4.45}$$

If the axis of symmetry is aligned in one of the radial directions a different expression for J' is found as shown in appendix C. This condition is found when e.g. a sample is retrieved horizontally from a cross–anisotropic soil layer, which has a vertical axis of symmetry. For K'/J' it is then found:

$$\frac{K'}{J'} = \frac{-1}{3}\left[\frac{(1-\nu_{vh})\,\eta - (1-\nu_{hh})}{(1-4\nu_{vh})\,\eta + 2\,(1-\nu_{hh})}\right], \qquad \eta = \frac{E_h}{E_v} \tag{4.46}$$

For isotropic conditions both equations (4.45) and (4.46) give $K'/J' = 0$. However for all other combinations of stiffness parameters equations (4.45) and (4.46) lead to K'/J' values with an opposite sign. If in an undrained triaxial test on a vertically retrieved sample a backward tilting ESP is found then an undrained triaxial test on a horizontally retrieved sample from the same soil layer will show a forward tilting ESP and vice versa. The absolute value of the ESP slopes found from a horizontally retrieved sample is smaller than those from a vertically retrieved sample.

It is remarkable that equations (4.45) and (4.46) show singular points for valid combinations for E_h, E_v, ν_{vh} and ν_{hh}. These values are found when:

$$(1-4\nu_{vh})\,\frac{E_h}{E_v} + 2\,(1-\nu_{hh}) = 0$$

This condition corresponds to $K' = \infty$, according to equation (4.26) or (3.17), it represents constant volume deformation.

For small values for $\nu_{vh} < 0.25$ and $\nu_{hh} < 0.25$ singularity of equations (4.45) and (4.46) does not occur. Then the maximum and minimum values for K'/J' are dominated by the ratio E_h/E_v. According to equation (4.45) for $E_h/E_v = 0$ the lower boundary is found; K'/J' = -1/3. Equation (4.41) shows that, for this lower boundary, no excess pore pressure is created. With K'/J' = -1/3 the slope of ESP is -1:3 and ESP equals TSP. The upper boundary is found if $E_h/E_v \to \infty$ then $K'/J' = 2/3$. The slope of ESP becomes 2:3. Equation (4.41) shows that for $K'/J' = 2/3$ it is found that $\sigma_{w0} = \sigma_a$.

Graham & Houlsby in [34] give the following expression for the ESP in G^*, J and α, ν^*:

$$\frac{q}{p'} = \frac{3G^*}{J} = \frac{3\left(2-2\nu^*-4\alpha\nu^*+\alpha^2\right)}{2\,(1-\nu^*+\alpha\nu^*-\alpha^2)} \tag{4.47}$$

Application of the equations presented in appendix C shows that equation (4.47) corresponds to equation (4.45).

Measurements of the angle of ESP in relation to stiffness parameters are presented by Wesley [81] for Mucking Flat clay and by Graham & Houlsby for Winnipeg Clay [34]. For Winnipeg Clay the slope of ESP ranges from -15.8 to -4.45, with an average value of -6.8. This corresponds to $K'/J' = 0.15$. Table 4.1 presents the values for K' and J', showing $K'/J' = 0.22$.

The influence of anisotropy on the ESP is extensively studied by Wesley [81] for Mucking Flat clay from the bedding of the river Thames. For this type of clay a clear difference in loading and unloading stiffness is found. A triaxial sample loaded undrained in axial direction faces a reduction in radial effective stress due to the pore pressure reaction. So axial loading leads to radial unloading. The K'/J' value then depends not only on the isotropy in stiffness parameters but also on loading conditions. As shown by Parry & Wroth [62] a vertically retrieved sample

of Mucking Flat clay axially loaded shows a vertical ESP corresponding to $K'/J' = 0$ and does not seem to behave anisotropically. A vertical sample loaded into extension gives an angle of ESP equal to 1:-2.18 leading to $K'/J' = 0.46$. For an horizontally retrieved sample the opposite is found. When loaded into extension a vertical ESP is found, while loaded in compression the angle of ESP is 1:-2.4 or $K'/J' = 0.4$.

Lings [55] gives a simplification of figure 3.4 expressed in F_h, E_v and ν_{vh}. With $F_h = E_h/(1 - \nu_{hh})$ applied to equation (3.14) the "ship-bow"-like structure is now reduced to a parabola as shown by figure 4.5. All valid combinations of F_h, E_v and ν_{vh} are located inside or on the parabola. Uncoupled and incompressible behaviour are reduced to lines in this graph. The intersection of those lines gives the point of undrained material behaviour. This means that there is only one combination of F_h^u, E_v^u and ν_{vh}^u. Rewriting equation (4.45) in terms of F_h, E_v and ν_{vh} gives:

$$\frac{K'}{J'} = \frac{2}{3} \frac{(1 - \nu_{vh}) - \dfrac{E_v}{F_h}}{(1 - 4\nu_{vh}) + \dfrac{2E_v}{F_h}} \tag{4.48}$$

Equation (4.48) can be used to depict lines of equal K'/J' values in figure 4.5. Each line runs through the undrained spot. Evidently the line for $K'/J' = 0$ corresponds to the line representing uncoupled materials. Lines above the uncoupled line represent $K'/J' < 0$, a forward tilting ESP, and the lines underneath represent $K'/J' > 0$, a backward tilting ESP. Lings [55] shows that measurements, reported in literature, plot on the right–hand side of the parabola, $\nu_{vh} > 0$.

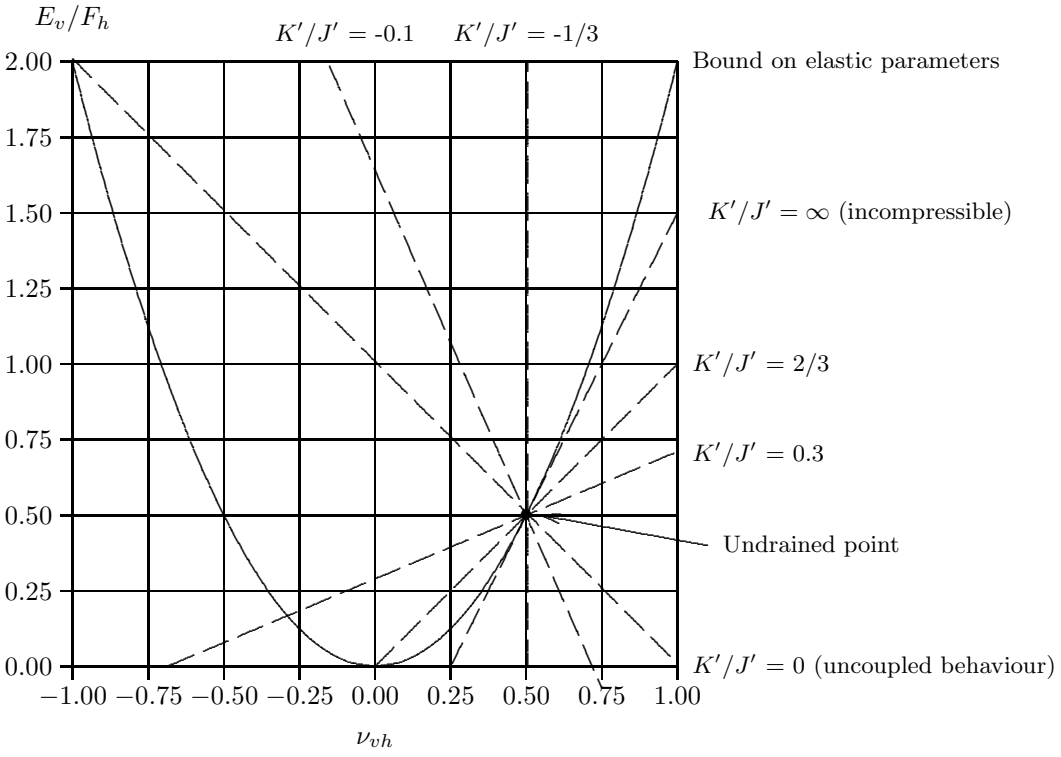

Figure 4.5: Elastic limits, dashed lines present combinations of constant K'/J', from [55]

Chapter 5

3D consolidation

5.1 Introduction

This chapter discusses the influence of anisotropy on the consolidation behaviour of soft soil. Based on Hooke's law for cross–anisotropy derived in chapter 3 the three–dimensional solution for the consolidation problem for axial symmetric and plane strain conditions are given in the appendices E to I.

This chapter first presents a short literature overview, in which the Mandel–Cryer effect is introduced. Based on the mathematical analysis given in appendices E and F section 5.3 highlights some aspects of the 3D consolidation for isotropic linear elastic material behaviour for axial symmetric and plane strain conditions. Section 5.4 discusses the differences in consolidation for isotropic and cross–anisotropic linear elasticity. Once a solution for the consolidation problem is found a large number of alternatives using slightly different boundary conditions are easily derived. Section 5.5 discusses some of these solutions.

5.2 Literature overview

The first who gave a solution for the consolidation problem is Terzaghi in [70], for 1D conditions. Rendulic [64] gives a solution for the consolidation equation based on radial dissipation of pore water. Carillo presented a method to combine both results [17]. By combining vertical and radial dissipation a semi three–dimensional description of the consolidation behaviour is found. In 1947 Barron [10] presents a solution for consolidation around a vertical drain combining axial and radial pore pressure dissipation. Both, the solution of Barron and Carillo, are based on the following assumptions:

- The soil skeleton behaves linear elastic
- The soil is fully saturated by an incompressible fluid
- The soil is homogeneous
- Permeability and stiffness remain constant during consolidation
- Pore water flow is described by Darcy's law
- Deformations remain small

In 1941 Biot published the derivation for a complete three–dimensional description of consolidation behaviour ([12], [13] and [14]). Although the Biot equations are also based on the assumptions given above, a remarkable difference is found between the Biot equations and the

Terzaghi–Rendulic solution. This difference can be illustrated by considering a triaxial sample, which is loaded in axial direction while pore water is allowed to drain in radial direction. When on top of the sample a stiff plate is located, the Biot equations predict an initial pore pressure increase at the middle of the sample due to redistribution of stresses. The stiff plate on top causes the inner core of the sample, at which no pore water has dissipated yet, to carry initially a larger part of the load. This leads to an initial pore pressure increase at the middle of the sample. When time progresses pore water also dissipates from the inner core of the sample leading to a decrease in pore pressure. Figure 5.3 presents a typical pore pressure development predicted by the Biot equations for this situation. The Terzaghi–Rendulic solution does not show such an initial peak and predicts a monotonic pore pressure decay.

Phenomena of this kind were first reported by Mandel [57] in 1953. He gives a mathematical description of the consolidation problem for plane strain conditions. Mandel makes a distinction between direct and transient elastic deformations. The direct deformations are found when the Lamé's constant $\lambda = \infty$, simulating undrained behaviour. For the transient deformations Mandel derives in his paper the 3D–consolidation equation. Although no references are made his derivation corresponds to the Biot theory. Mandel illustrates his solution with a two–dimensional plane–strain situation, which is also presented in appendix F and shown in figure 5.11. The solution shows the initial pore pressure increase.

A decade later in 1963 Cryer compares the Biot solution for three–dimensional consolidation to the Terzaghi–Rendulic solution [22]. Cryer comes to the same conclusions, regarding the initial peak value as Mandel. Where Mandel gives analytical solutions, Cryer proposes laboratory tests to verify the differences found between the two theories. The proposed tests consist of a soil specimen of spherical shape. This sphere is hydrostatically loaded and is able to drain freely at the outer radius. The pore pressure is measured in the heart of the sphere. Results of such tests were presented by Gibson, Knight & Taylor [32] in 1964.

The test results presented by Gibson, Knight & Taylor [32] show a pore pressure development as described by the Biot theory. The maximum value for the peak pore pressure depends on the drained Poisson ratio. The maximum peak value is rather small, 10 - 16 % of the loading applied, which is explained by occurrence of plasticity. With Mandel the first to give a mathematical description of the phenomena and Cryer the first to discuss laboratory tests, the phenomena became known as the Mandel–Cryer effect.

In the period 1963 to 1965 De Josselin de Jong, Verruijt and De Leeuw gave in a series of articles an extended description of the solution for the consolidation problem for spherical and cylindrical conditions ([41], [42], [43], [74], [75] and [52]) and also ([53] and [44]). In these articles the option of using spherical specimen to determine long–term compression parameters is discussed. Verruijt [75] presents laboratory measurements of the Mandel–Cryer effect. In the last article De Leeuw [52] presents the solution for axial symmetric conditions for a linear elastic isotropic material. De Leeuw gives his solution for a massive and a hollow cylinder. The last representing the conditions around a vertical drain. The solution for the massive cylinder corresponds to triaxial test conditions. The mathematical analysis of the consolidation problem discussed in this chapter is based on this approach.

De Josselin De Jong [41] discusses the Biot theory extensively and explains the difference between the Biot theory and Terzaghi–Rendulic theory. The difference between both theories is explained in the way they handle the storage equation and the equilibrium conditions. The storage equation is given by:

$$\frac{k}{\gamma_w}\nabla^2\sigma_w = \frac{n}{K_w}\frac{\partial\sigma_w}{\partial t} + \frac{\partial e}{\partial t} \tag{5.1}$$

and the equilibrium of forces for a linear elastic material, is given by:

$$\left(K + \frac{4}{3}G\right)\nabla^2 e = \nabla^2\sigma_w \tag{5.2}$$

in which:

K = compression modulus of soil
G = shear modulus
e = volumetric strain
σ_w = pore pressure
γ_w = volumetric weight of water
k = permeability
K_w = bulk modulus of pore water
n = porosity
∇^2 = Laplace operator, $\nabla^2 = \partial^2/\partial x^2 + \partial^2/\partial y^2 + \partial^2/\partial z^2$

Following De Josselin de Jong, a relation between e and σ_w can be found by twice integrating equation (5.2).

$$\left(K + \frac{4}{3}G\right) e = \sigma_w + f(x, y, z, t) \tag{5.3}$$

In (5.3) the function $f(x, y, z, t)$ should satisfy the condition $\nabla^2 f = 0$. Eliminating e from equations (5.1) and (5.3) gives the consolidation equation:

$$\frac{k}{\gamma_w}\nabla^2\sigma_w = \frac{n}{K_w}\frac{\partial\sigma_w}{\partial t} + \frac{1}{\left(K + \frac{4}{3}G\right)}\left(\frac{\partial\sigma_w}{\partial t} + \frac{\partial f\,(x, y, z, t)}{\partial t}\right) \tag{5.4}$$

Terzaghi assumes a direct relation between σ_w and e leading to $f = 0$. In absence of $\partial f/\partial t$ equation (5.4) reduces to the well–known heat equation which has been studied extensively and many solutions are available in literature. The presence of the function $f(x, y, z, t)$ in the Biot equations makes the consolidation problem no longer analogous to the heat equation. It constitutes an essential difference between the Biot theory and Terzaghi solution.

De Josselin de Jong shows that in absence of rotations during deformation $f(x, y, z, t)$ reduces to $f(t)$, but not necessarily 0. An important exception is found for a one–dimensional geometry and loading conditions constant in time. Then it follows that the absolute value of f equals the applied load. In equation 5.4 $\partial f/\partial t$ reduces to 0. For these conditions the Terzaghi solution equals the Biot theory.

In his paper on cylindrical consolidation, De Leeuw disregards the compressibility of the pore water in (5.1) and expresses the consolidation equation in terms of volumetric strain. Solving the consolidation equation for e circumvents the need for a definition of $f(x, y, z, t)$ in (5.2). Mandel applied the same strategy in his paper [57] when deriving his solution for plane strain consolidation.

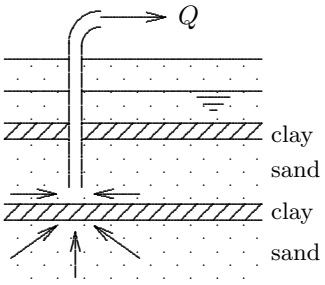

Figure 5.1: Conditions for the Noordbergum effect

De Leeuw [53] presents a three–dimensional solution for the consolidation problem around a vertical drain based on the Biot theory. In this paper De Leeuw shows that the function f becomes a function of the time–derivative of the boundary conditions. The boundary conditions are given in terms of loading on top, pore pressure in the drain and radial deformation of inner and outer radius of the cylinder. For most engineering purposes these boundary conditions are constant. So, in engineering practice, for vertical drains, there is no difference between the Terzaghi and the Biot theory.

In 1969 Verruijt [76] describes the Noordbergum effect. The Noordbergum effect is found in a double layered artesian aquifer, see figure 5.1. When water is extracted from the upper aquifer some water will leak from the lower aquifer through the separating clay layer to the upper aquifer. This leads to consolidation effects in the lower aquifer. Pore pressure measurements in the lower

aquifer show first an increase before a decay to an equilibrium condition. This initial increase is known as the Noordbergum effect. Verruijt shows that this effect can be explained by the Biot theory.

In 1990, Gibson, Gobert & Schiffman [33] apply large strain theory to the consolidation problem of a sphere. Besides large strain a non-constant permeability is applied. It was found that when the outer radius starts to consolidate the decrease in permeability dominates the shortage in drainage length caused by the compression of the sphere. This leads to an increase in hydrodynamic period. In the same time the Mandel–Cryer effect is reduced, a considerable lower maximum peak is found. It is then concluded that the Mandel–Cryer effect is likely to be largest in stiff soils subjected to relatively small strain.

Al–Tabbaa [2] and Al–Tabbaa & Wood [3] discuss results of a numerical analysis and measurements including plastic material behaviour. Equivalent to the linear elastic solutions the numerical analysis predicts the Mandel–Cryer effect for conditions of uniform vertical strain. For the case of free vertical strain the numerical analysis predicts an initial decay in pore pressure preceding a reduced Mandel–Cryer peak in the middle of the sample.

Cui et al. [23] and Abousleiman et al. [1] present a study on the influence of anisotropy to the consolidation behaviour of soft rock. The authors show that anisotropy strongly influences the Mandel–Cryer effect.

5.3 Solution for isotropic linear elasticity

5.3.1 General assumptions

The three-dimensional consolidation problem for a cylinder is solved by De Leeuw ([52] and [53]) for isotropic linear elasticity, addressing the solution for pore pressure development. This solution is presented for general boundary conditions including axial and radial loading and prescribed displacements. This chapter focuses on standard triaxial compression tests. Besides axial symmetric conditions also plane strain conditions are elaborated. The solution for the consolidation problem for the different conditions is presented in the appendices E to I. The graphs E.2 to E.10 and F.2 to F.10 visualise the derived solutions.

In solving the consolidation equation the following assumptions are made:

- soil behaviour is described by Hooke's Law
- the dissipation of pore water is described by Darcy's law
- compressibility of the pore water is disregarded
- for axial symmetric conditions, no changes in tangential direction, all $\partial/\partial\theta = 0$
- for plane strain conditions, no changes in y-direction, all $\partial/\partial y = 0$
- vertical strain is constant in depth, $\partial\varepsilon_z/\partial z = 0$
- stiff plate on top; $\partial\varepsilon_z/\partial r = 0$ or $\partial\varepsilon_z/\partial x = 0$
- incompressible solids, $\alpha = 1$
- small strain deformations

It should be noted that increments of stress and strain are due to a load increment, $\delta\sigma_b$. However, for convenience the δ-sign is omitted. For solving the consolidation problem the sign convention used by De Leeuw ([52] and [53]) is adopted. According to this sign convention tensile stress and pore pressure are positive. This sign convention conflicts with the sign convention used in the previous chapters, where pore pressure is represented by a negative sign. Adopting the sign convention used by De Leeuw makes direct comparison with known solutions possible.

5.3.2 Axial symmetric conditions

The axial symmetric consolidation problem is solved for the following boundary conditions, with σ_b the applied load and q_r expelled pore water flow:

a) at $r = R$, $0 < z < h$, $\sigma_w = 0$

b) at $r = R$, $0 < z < h$, $\sigma_r = 0$

c) at $z = h$, $0 < r < R$, $\sigma_b = \int_0^R \frac{2\pi r \sigma_z}{\pi R^2} \mathrm{d}r$

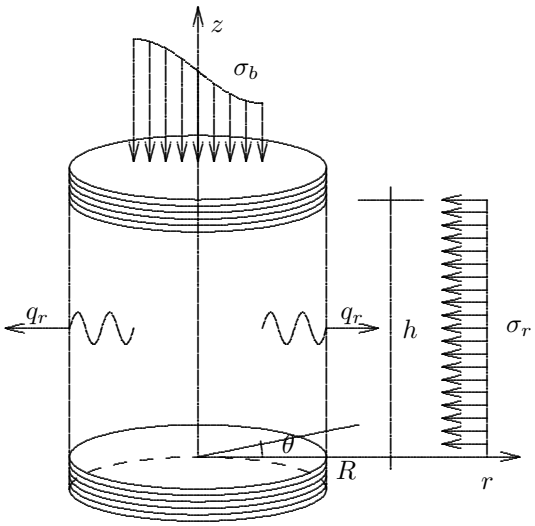

Figure 5.2: Axial symmetric conditions

Figure 5.2 illustrates the boundary conditions. Appendix E gives the full derivation of the solution. Figures 5.3, 5.4, 5.5 and appendix E, graphs E.2 to E.10 illustrate the mathematical solutions for a constant consolidation coefficient, $c = (K + 4G/3)k/\gamma_w = 1 \times 10^{-6}$ m^2/s and $R = 0.5$ m. In which k represents the permeability and γ_w the volumetric weight of water. In general the solution converges slowly for small values for time t and radius r. In the presented graphs a combination of small values for t and r is avoided. Graphs representing the development of the stress and strain in the middle of the cylinder are therefore not presented at $r = 0$, but at a small value for r/R.

Figure 5.3 presents the pore pressure development. Initially σ_w = -1/3 σ_b, as explained in section 4.3.1, note the different sign convention. This holds for all values of r except for $r = R$ due to boundary condition *a*. Figure 5.3 clearly shows the Mandel–Cryer effect. The maximum peak value strongly depends on the Poisson ratio ν. For $\nu = 0$ the maximum is found at σ_w = -0.47 σ_b. For larger values of ν smaller peaks are found. For $\nu = 0.5$ no peak is observed.

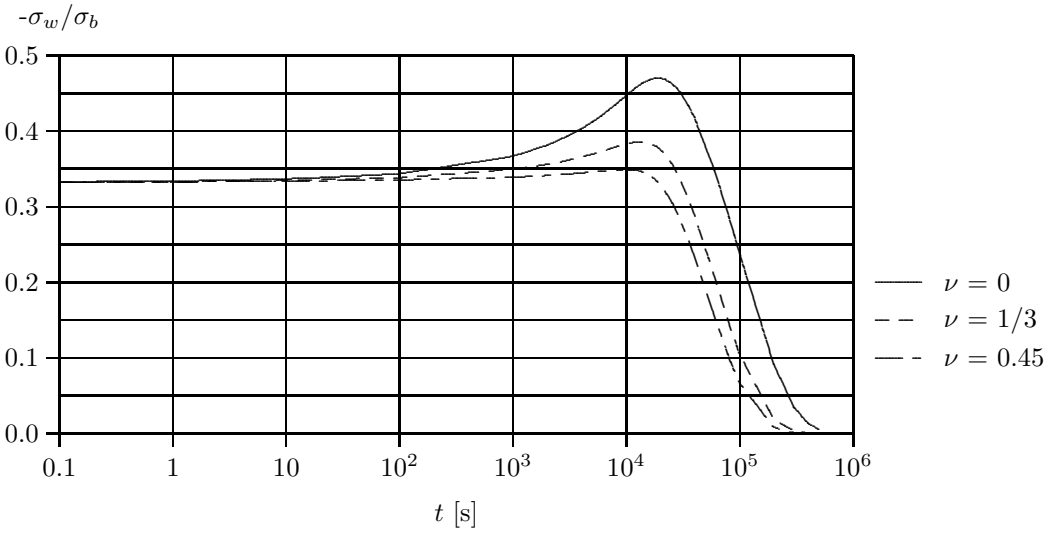

Figure 5.3: Pore pressure development for axial symmetry at $r/R = 0.02$

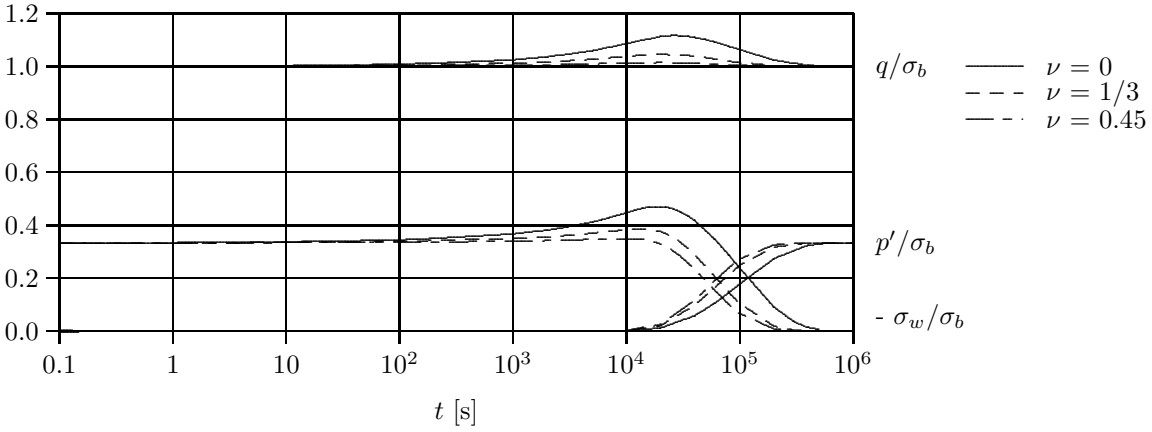

Figure 5.4: Development of p', q and σ_w for axial symmetry at $r/R = 0.1$

Figure 5.4 presents the development of the effective isotropic stress p', deviator stress q as defined by equation 4.2 and σ_w at $r/R = 0.1$. These graphs show that the temporary increase in pore pressure is balanced by an increase in q and does not influence p'. The isotropic effective stress starts to increase when the pore pressure reaches its peak value, at a higher rate for lower ν values. The deviator stress reduces finally to its initial value. Again this effect is strongest for ν = 0. For $\nu = 0.5$ no pore pressure peak and a constant q are found.

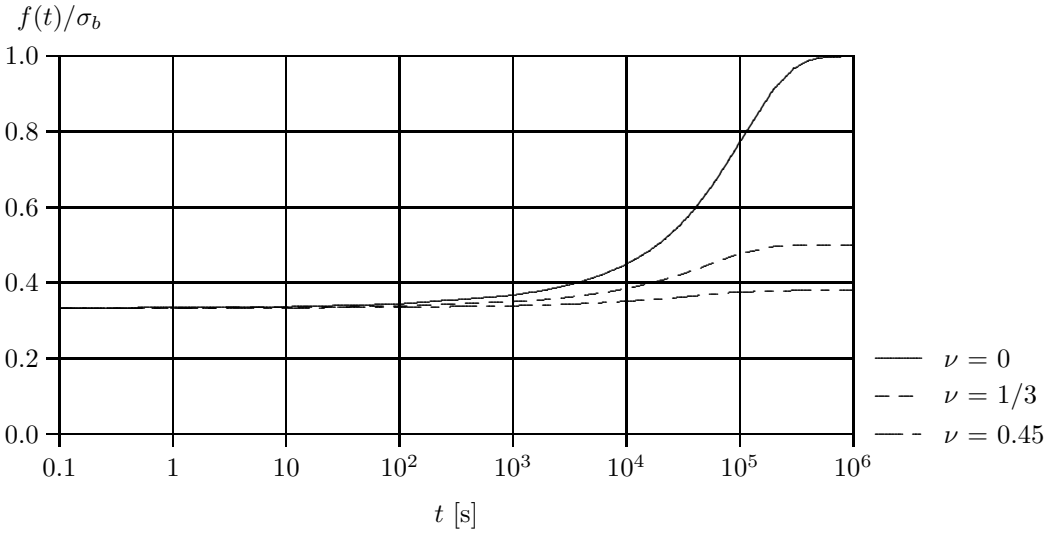

Figure 5.5: Development of function $f(t)$ for axial symmetry

Section 5.2 discusses the differences between the Biot equations and the Terzaghi–Rendulic solutions. The differences are explained in the way integration constants are handled leading to a function $f(t)$ in absence of rotations, which is the case in a triaxial test. For $\partial f(t)/\partial t = 0$ the Biot equations reduce to the Terzaghi–Rendulic solution. Using the expressions for e and σ_w given in appendix E equation (5.3) can be used to find the expression for $f(t)$. Figure 5.5 shows the development of $f(t)$ for three different ν–values. Figure 5.5 clearly illustrates that condition ν = 0 gives the largest change in $f(t)$ which corresponds to the largest peak value and therefore the largest Mandel–Cryer effect in figure 5.3. For $\nu = 0.45$, only a minor change in $f(t)$ is found, which

corresponds to a negligible peak in figure 5.3.

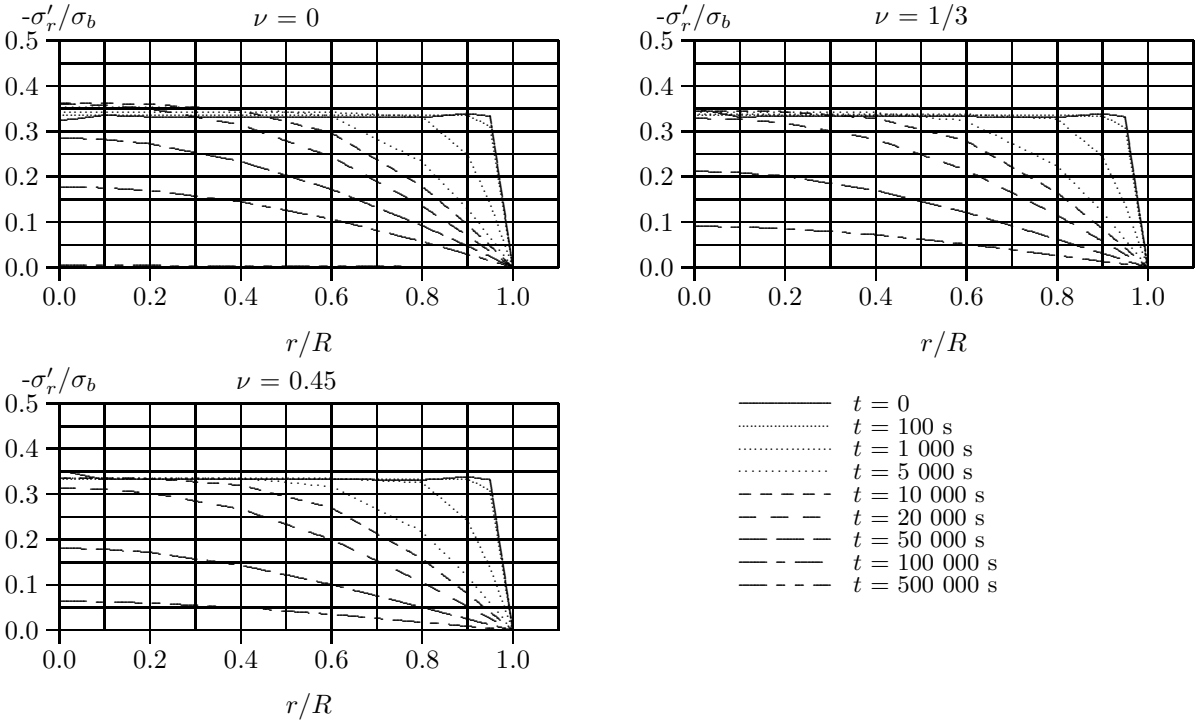

Figure 5.6: Development of radial effective stress for isotropic linear elasticity and axial symmetric conditions

Appendix E, figures E.2 to E.10 present the development of all stresses and strains. The graphs illustrate the following phenomena:

effective stress

Figure 5.6 presents the radial effective stress development. Initially it is found that $\sigma'_r = \sigma'_\theta =$ - 0.33 σ_b. It should be noted that a negative stress symbolises compression. So for a standard triaxial compression test, with a negative value for σ_b, σ'_r and σ'_θ have a positive value, leading to tension or a reduction in effective radial and tangential stress. For $r = R$ the boundary conditions imply $\sigma'_r = 0$ during the entire consolidation period. The Mandel–Cryer effect has only a minor influence, σ'_r and σ'_θ remain virtually unaffected. The largest peak is found for $\nu = 0$, when $\sigma'_{r,max}$ = $\sigma'_{\theta,max}$ = - 0.36 σ_b. For larger values of ν smaller peaks are found. The peak is considerably lower than the peak in pore pressure development.

total stress

Expressions for total stress can either be found by a summation of the expressions for the pore pressure and the effective stress or by deriving an expression directly from the consolidation equation. In order to check the solutions the expressions for total stress are derived in both ways, leading to the same expression, shown in appendix E.

Initially $\sigma_{zz} = \sigma_b$ except on $r = R$, as shown by figure 5.7. As consolidation progresses, the vertical stress increases in the middle of the cylinder while it decreases at the outer radius. This visualises the redistribution of stress that takes place during consolidation. Note that boundary condition *c* still holds and therefore the condition of equilibrium of forces is not violated. When σ_w

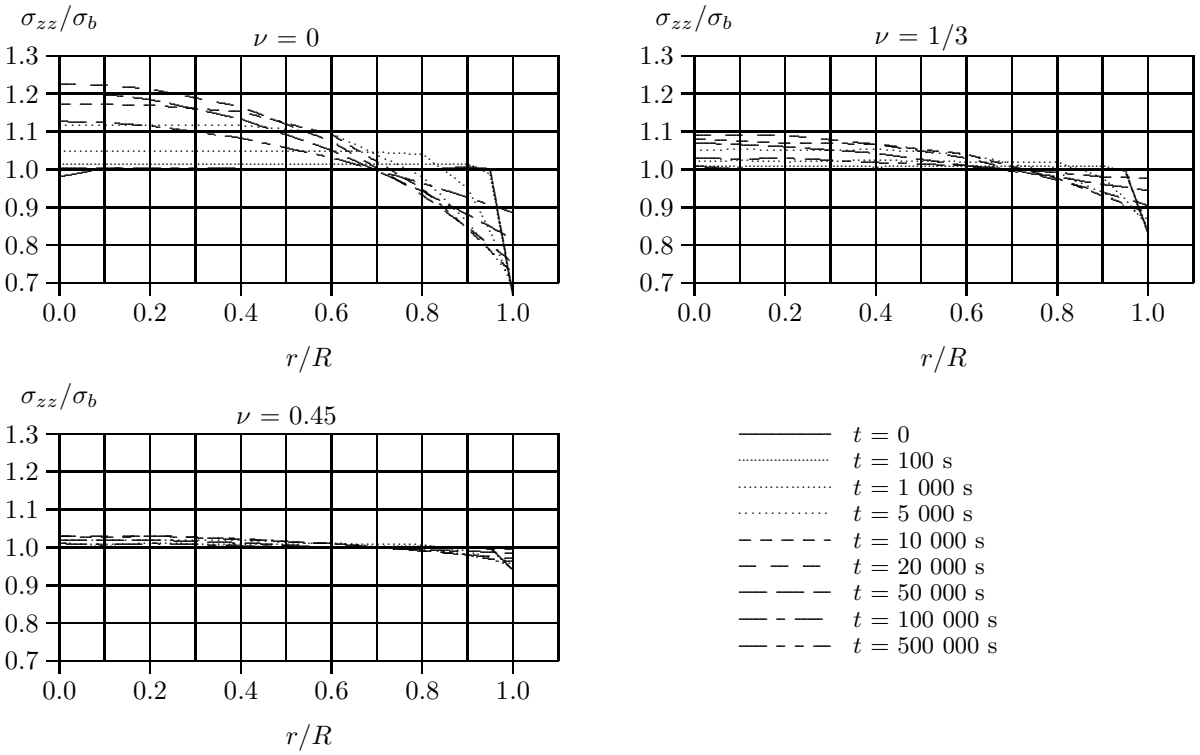

Figure 5.7: Development of vertical total stress for isotropic linear elasticity and axial symmetric conditions

reaches its maximum value the total stress reduces in the middle and increases at the outer radius until $\sigma_{zz} = \sigma_b$ is found along the entire radius. The effect is strongest for $\nu = 0$. For $\nu = 0.5$ no deviation in total vertical stress is found. For σ_r and σ_θ an equivalent development is found, as shown by the figures E.7 and E.8.

strain

Figure 5.8a, b shows the radial deformation. Note that for loading conditions $\sigma_b < 0$ the sign of the ε_r–axis changes. As is to be expected the final value follows directly from Hooke's law. During consolidation the radial deformation develops differently for the different ν-values. In the middle of the cylinder the sample tends to expand. During consolidation this tendency reduces, while at the outer radius the samples bulges initially and keeps on bulging until the radial strain is constant along the radius.

For $\nu = 0$ there is no initial radial strain at $r = R$. When consolidation develops the radial strain becomes temporarily negative at $r = R$, a tendency to reduce the diameter of the sample. When the consolidation is finished radial strain for $\nu = 0$ is again 0. This does not mean that the sample actually shrinks. The radial strain is defined as $\varepsilon_r = \partial u_r / \partial r$. The tangential strain is defined as $\varepsilon_\theta = u_r/r$, leading to $\varepsilon_\theta r = u_r = \int \varepsilon_r \mathrm{d}r$. The actual radial displacement at the outer radius can be found by multiplying ε_θ by R. As can be seen in figure 5.8 for $\nu = 0$ and a negative σ_b (a pressure), initiates a positive value for ε_θ. This shows a positive radial displacement, which is a diameter enlargement. As consolidation progresses ε_θ reduces to 0, leading to zero final radial deformation, which is to be expected for $\nu = 0$. It should be noted that tangential stress and strain occur due to radial displacements. When both sides of an element inside the cylinder move

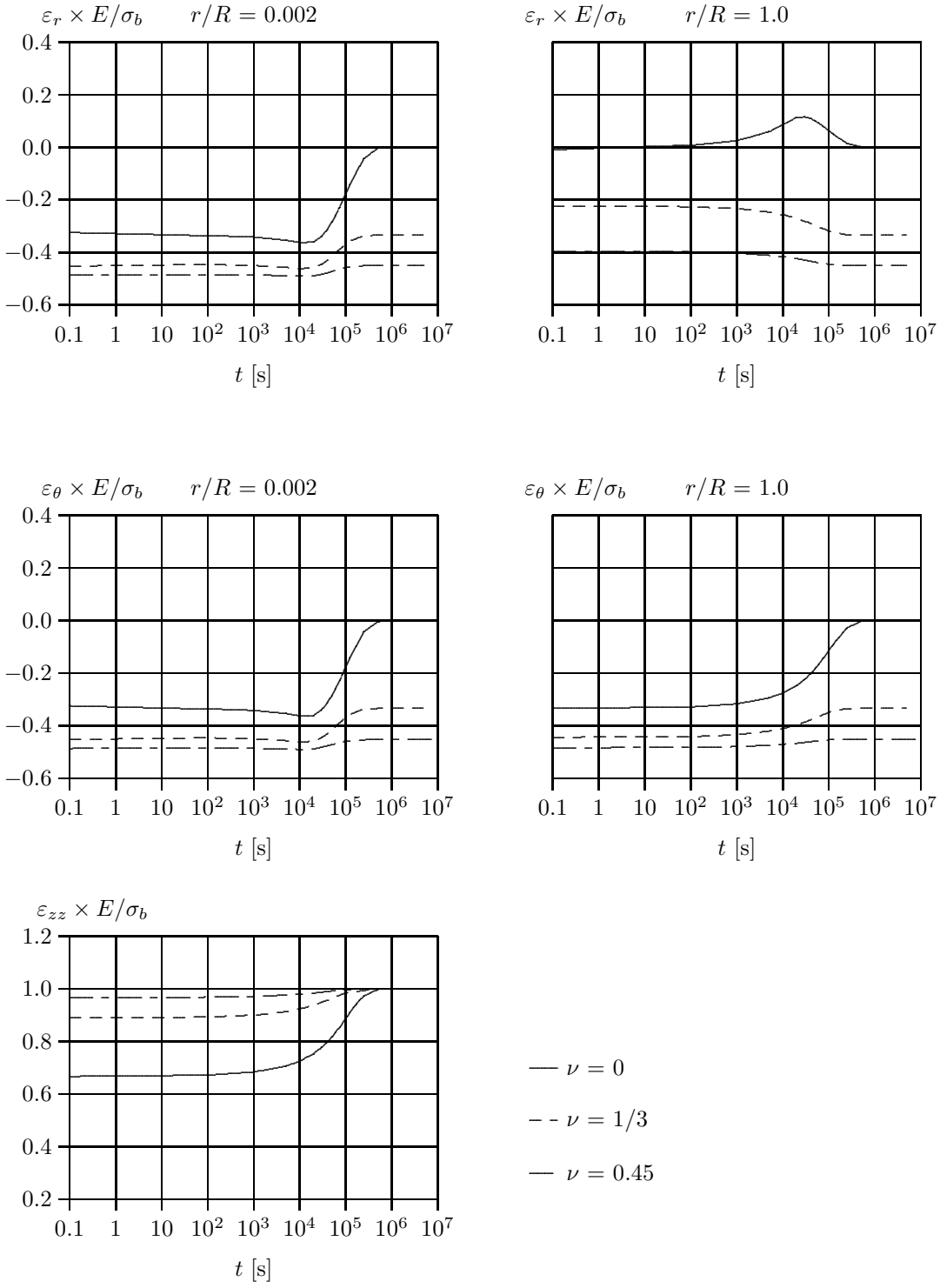

Figure 5.8: Development of vertical, radial and tangential strain for isotropic linear elasticity and axial symmetric conditions

parallel to the radius, they diverge leading to tangential stress and strain. From figure 5.8 it can be concluded that a small element at the outer radius of the cylinder is pushed outwards. Since no rotational displacements occur the sides of this element, parallel to the radius, diverge leading to tangential strain. At the same time the element is compressed in radial direction as $\partial u_r \,/\, \partial r < 0$.

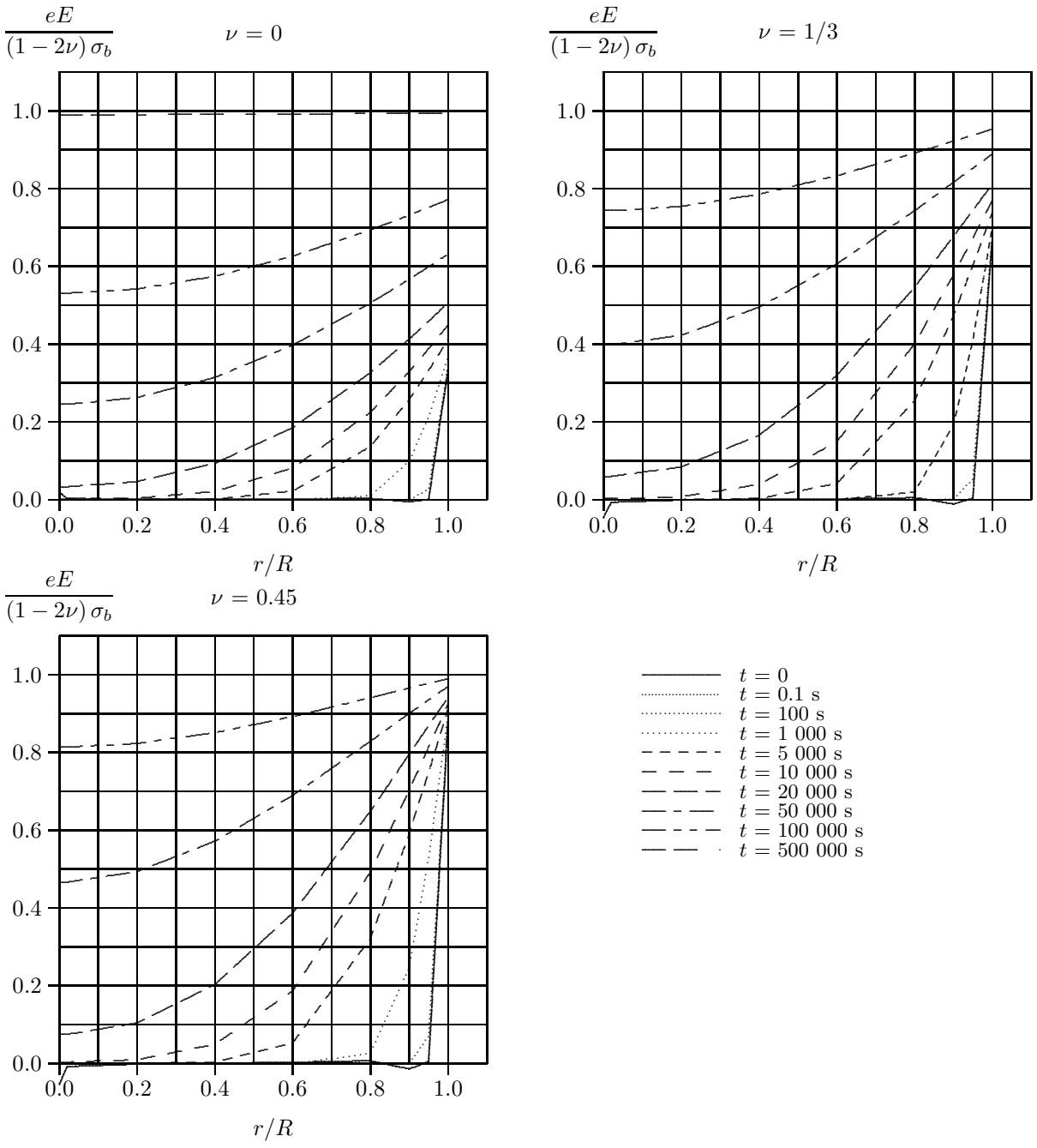

Figure 5.9: Development volumetric strain for isotropic linear elasticity and axial symmetric conditions

Figure 5.9 shows the volumetric strain development. When the consolidation process develops the volumetric strain develops from the outer radius to the inner core of the cylinder. The value of the final volumetric strain depends strongly on the ν–value. For $\nu = 0$ the maximum volumetric strain is found. For ν= 0.45 the volumetric strain becomes negligible, which is to be expected since $\nu = 0.5$ corresponds to constant volume deformation.

5.3.3 Plane strain conditions

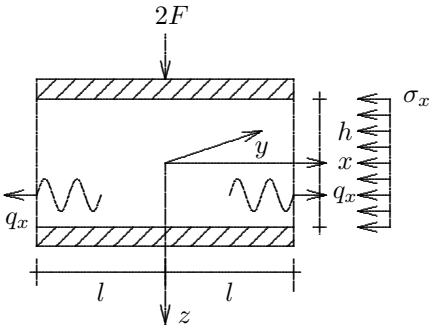

Figure 5.10: Plane strain conditions

The plane strain consolidation problem is solved for the following boundary conditions:

a) at $x = 0$, $\partial\sigma_w/\partial x$ =0

b) at $x = l$, $\sigma_w = 0$

c) at $x = l$, $\sigma_{xx} = 0$

d) at $z = h$, $2F/\ 2l = \int_{-l}^{l} \frac{\sigma_{zz}}{2l} \mathrm{d}x$

Figure 5.10 illustrates the boundary conditions in which q_x represents the expelled pore water flow. Appendix F gives the mathematical derivation. Graphs F.2 to F.10 illustrate the solution for stress and strain for a consolidation coefficient, $c = (K+4G/3)k/\gamma_w$= 1×10^{-6} m^2/s and $l = 1$ m. In general it is found that the solution converges slowly for small values of t.

Figure 5.11 shows the pore pressure development. The presented development is equivalent to the solution given by Mandel [57]. At $x = l$ there is no excess pore pressure, as prescribed by the boundary conditions. At $x = 0$ the pore pressure initially increases. The maximum peak value depends on the ν - value. For $\nu = 0$ the highest peak is found for σ_w = -0.58 F/l, using the sign convention according section 5.3.1. For $\nu = 0.5$ no peak is found. Figure 5.12 presents the

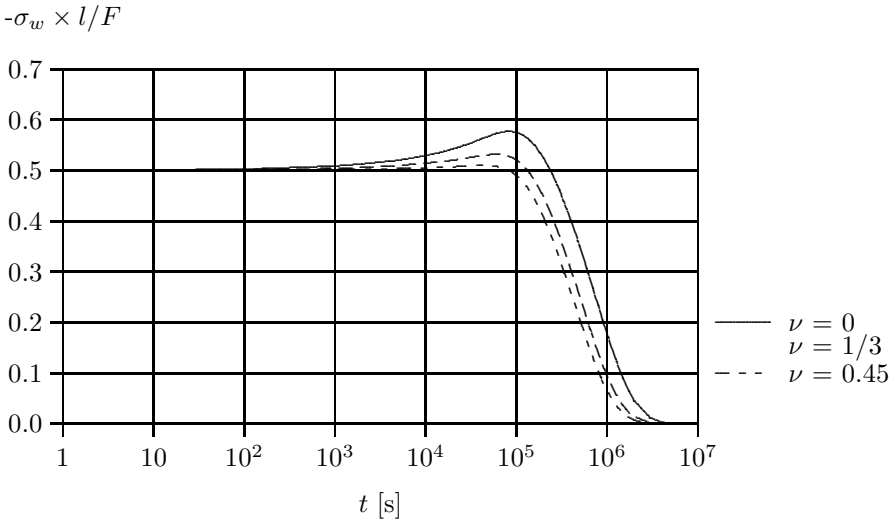

Figure 5.11: Pore pressure development for plane strain conditions at $x = 0$

development p' and q, as defined by equation (4.2) and the pore pressure for $x = 0$. Again it is found that the peak in pore pressure is balanced by the deviator stress. For plane strain conditions the final deviator stress does not equal its initial value due to the stress development in y–direction.

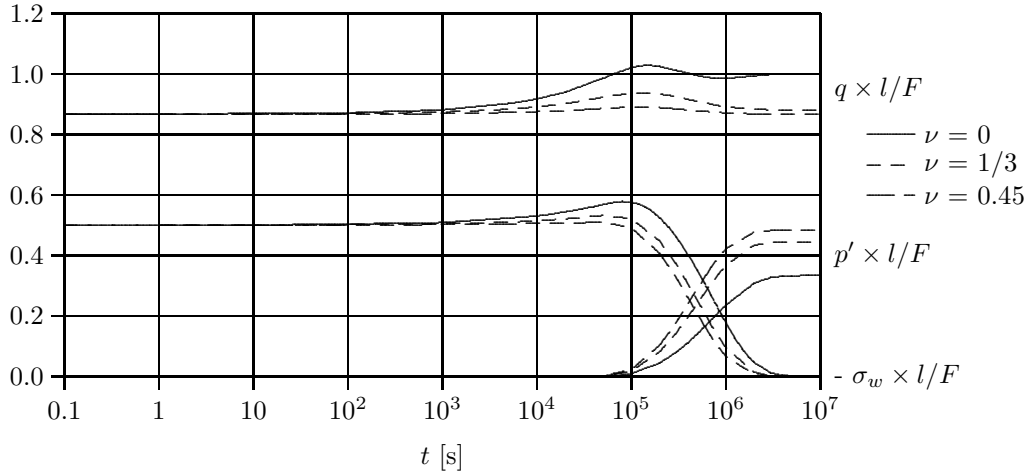

Figure 5.12: Development of p', q and σ_w for plane strain conditions

Graphs F.2 to F.10 present the development of all stresses and strains. Due to boundary condition c it follows that σ_{xx} is zero for all values of x. Figure F.7 shows the total stress in y–direction. Initially σ_{yy} equals the initial pore pressure, since $\sigma'_{yy} = 0$. The final value for σ'_{yy} and therefore σ_{yy} follows directly from Hooke's law and the condition of plane strain deformations. For $\nu = 0$ no final total stress remains in y - direction.

The final strain presented by figures 5.14 and 5.13 is easily checked by Hooke's law for isotropic material behaviour;

$$\begin{pmatrix} \varepsilon_{xx} \\ \varepsilon_{yy} \\ \varepsilon_{zz} \\ \gamma_{xy} \\ \gamma_{yz} \\ \gamma_{zx} \end{pmatrix} = \begin{pmatrix} \frac{1}{E} & \frac{-\nu}{E} & \frac{-\nu}{E} & 0 & 0 & 0 \\ \frac{-\nu}{E} & \frac{1}{E} & \frac{-\nu}{E} & 0 & 0 & 0 \\ \frac{-\nu}{E} & \frac{-\nu}{E} & \frac{1}{E} & 0 & 0 & 0 \\ 0 & 0 & 0 & \frac{1}{G} & 0 & 0 \\ 0 & 0 & 0 & 0 & \frac{1}{G} & 0 \\ 0 & 0 & 0 & 0 & 0 & \frac{1}{G} \end{pmatrix} \begin{pmatrix} \sigma'_{xx} \\ \sigma'_{yy} \\ \sigma'_{zz} \\ \tau_{xy} \\ \tau_{yz} \\ \tau_{zx} \end{pmatrix} \tag{5.5}$$

Boundary conditions b and c, $\sigma_{xx} = \sigma_w = 0$ at $x = l$ yield $\sigma'_{xx} = 0$ at $x = l$. Combination of the boundary conditions b and c and the plane strain condition, $\varepsilon_{yy} = 0$ to equation (5.5) yields:

$$\varepsilon_{zz} = \frac{\left(1 - \nu^2\right)}{E}\sigma_{zz}, \qquad \varepsilon_{xx} = -\frac{\nu\left(1 + \nu\right)}{E}\sigma_{zz}$$

Which corresponds exactly to the final strain presented by figures 5.14 and 5.13

5.4 Solution for cross–anisotropic elasticity

Appendix G and H show the extension of the solution for three dimensional consolidation from isotropic linear elasticity to cross–anisotropic linear elasticity. The solution for isotropic elasticity presented by appendix E and F, uses the Lamé constants to describe the stress–strain relationship.

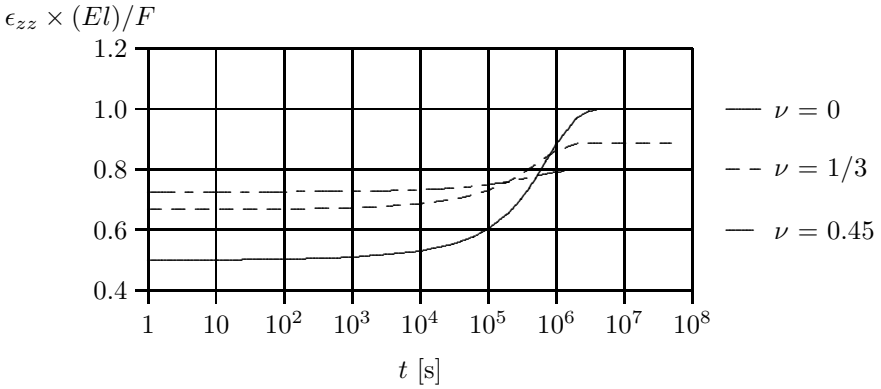

Figure 5.13: Development of vertical strain for plane strain conditions and isotropic linear elasticity

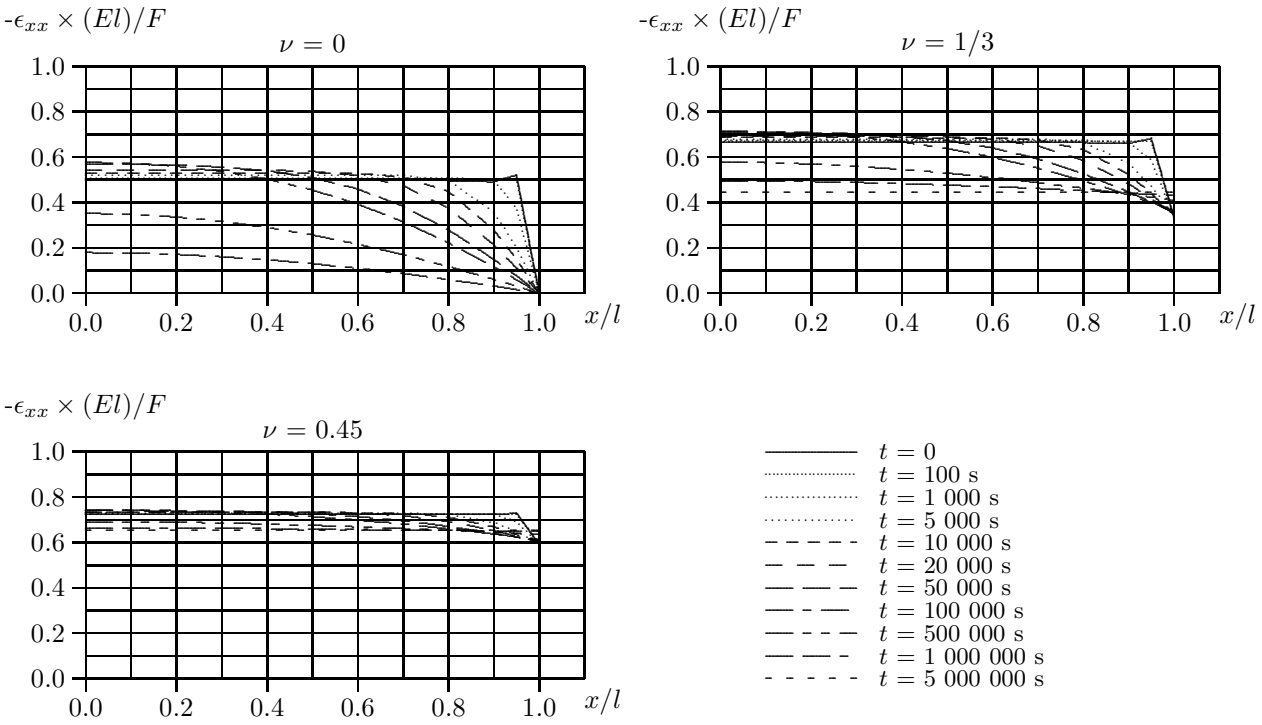

Figure 5.14: Development strain in x-direction for plane strain conditions and isotropic linear elasticity

Application of the cross–anisotropic stress–strain relationship to the consolidation equation needs a reformulation of equation (3.9). This reformulation is discussed in section 3.3 and appendix B.

Appendix G gives the solution of the pore pressure development for axial–symmetric conditions, appendix H for plane–strain conditions. The appendices G and H use the same boundary conditions and assumptions as applied in appendices E and F for the isotropic case. The graphs 5.15 and 5.16 visualise the derived solutions, equations (G.29) and (H.31), for seven cases explained by table 5.1. The permeability applied; $k = 1 \times 10^{-8}$ m/s, $R = 0.5$ m and $l = 1$ m. In section 4.3.1 it

is explained that the parameter K'/J' can be used to describe the level of anisotropy. Table 5.1 includes the value for K'/J' for the seven cases.

Table 5.1: Seven cases for visualisation of the solutions of appendices G and H

case	E_h [kN/m^2]	E_v [kN/m^2]	ν_{hh} [-]	ν_{vh} [-]	K'/J' [-]
a (isotropic)	1000	1000	0	0	0
b	5000	1000	0	0	0.38
c	1000	5000	0	0	-0.24
d	1000	1000	0	0.3	-0.11
e	1000	1000	0.3	0	0.08
f	5000	1000	0.3	0	0.45
g	1000	5000	0	0.3	-0.29

For axial–symmetric conditions the solution converges slowly for small values for r and t. Graph 5.15 shows this especially for case d.

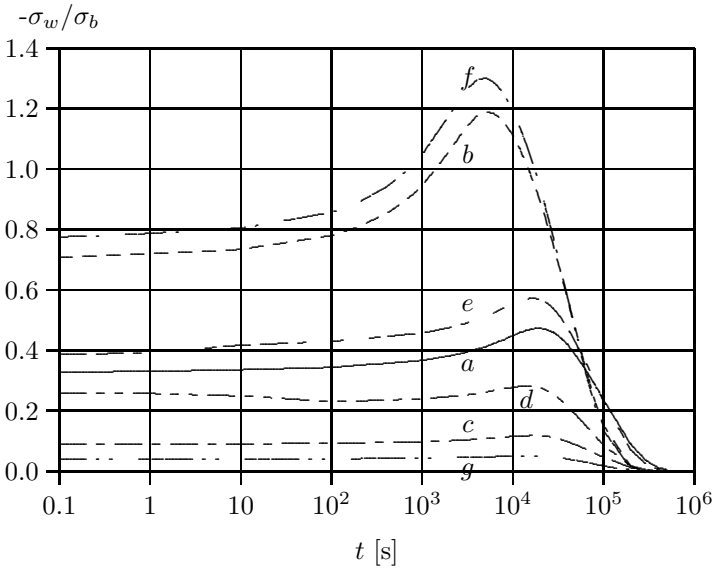

Figure 5.15: Pore pressure development at $r/R = 0.02$ for axial–symmetric cases a to g according to table 5.1

The pore pressure development for cross–anisotropic conditions, shown by figures 5.15 and 5.16, differs clearly from the pore pressure development for isotropic conditions, shown by figures 5.3 and 5.11. Differences are found in the initial pore pressure, the peak value and the consolidation period. Cross–anisotropy clearly influences the Mandel–Cryer effect. Conditions with a positive K'/J' value result in a larger initial excess pore pressure and a larger peak than conditions with a negative K'/J'.

The deviation of the initial σ_w from σ_w = -1/3 σ_b (sign convention according to section 5.3.1) for an axially loaded, cross–anisotropic sample can be explained as follows. Initially after loading the sample behaves undrained which means $e = 0$. However initial axial and radial deformations do occur. To fulfil boundary conditions the summation of the pore pressure increase and instantaneous axial effective stress equals the applied loading. In radial direction the summation of the pore pressure increase and the instantaneous radial effective stress remain 0, since $\sigma_r = 0$ is prescribed

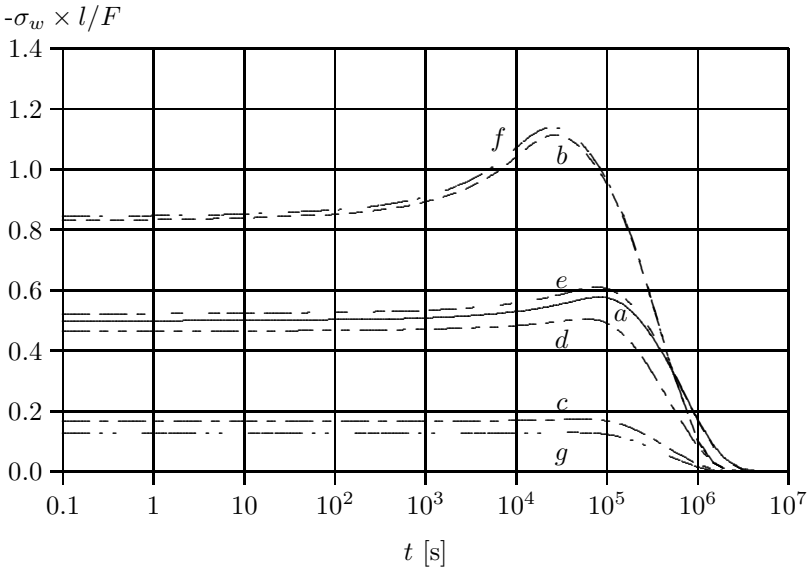

Figure 5.16: Pore pressure development at $x = 0$ for plane–strain conditions, for the cases a to g according to table 5.1

at $r = R$. The instantaneous axial and radial effective stress lead to initial, undrained, axial and radial deformations. Since $e = 0$, is found $\varepsilon_{zz} = -2\varepsilon_r$. For conditions with $E_h > E_v$ a relatively large initial radial effective stress and a relatively small vertical effective stress are needed to fulfil this requirement, leading to a large pore pressure increment. For $E_h < E_v$ the opposite occurs. Now a large initial vertical effective stress and a small initial radial effective stress is needed, leading to a low pore pressure increment.

Section 4.3.1 gives expression (4.40) for the initial pore pressure development for anisotropic conditions. To check the solutions of appendix G equation (4.40) is compared to the values found by equation (G.29) for $t = 0$. To compare the two equations, equation (4.40) is rewritten into an expression for $-\sigma_w/\sigma_b$, using the sign convention according to section 5.3.1. An axially loaded triaxial test is described in terms of σ_a and σ_r by:

$$p = \frac{1}{3}(\sigma_a + 2\sigma_r)$$

$$q = \sigma_a - \sigma_r$$

with:

$$\sigma_r = 0, \quad \sigma_a = \sigma_b$$

follows:

$$-\sigma_{w_0} = \frac{1}{3}\sigma_b + \frac{K'}{J'}\sigma_b$$

$$\frac{-\sigma_w}{\sigma_b} = \frac{1}{3} + \frac{K'}{J'} \tag{5.6}$$

For cases d and e the solution converges badly for small values of t and r. Therefore, table 5.2 shows the pore pressure at $t = 100$ s, still relatively small, between brackets. It can be concluded that (4.40) corresponds well to equation (G.29) for small values of t.

Figure 5.17 shows the development of $f(t)$ for the cases a, f and g and axial symmetry. As is to be expected the largest change in $f(t)$ is found for case f which also gives the largest Mandel–Cryer peak. For case g, $f(t)$ is nearly constant which corresponds to minor Mandel–Cryer peak.

Table 5.2: Initial σ_w, values between brackets for $t = 100$ s

case	a	b	c	d	e	f	g
K'/J'	0	0.38	-0.24	-0.11	0.08	0.45	-0.29
$-\sigma_{w0}/\sigma_b$, eq. (5.6)	$\frac{1}{3}$	0.71	0.09	0.22	0.42	0.78	0.04
$-\sigma_{w0}/\sigma_b$ eq. (G.29)	0.32	0.71	0.09	0.26 (0.22)	0.38 (0.43)	0.77	0.04

eq. = equation
cases a to g correspond to table 5.1

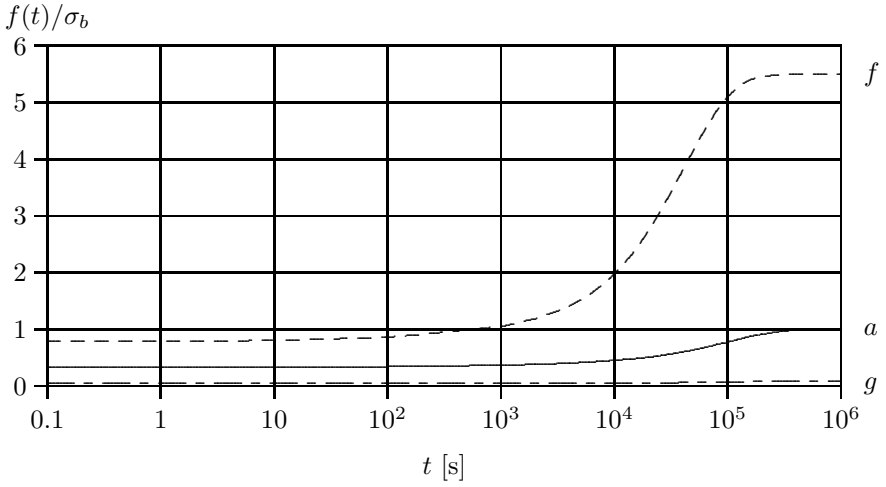

Figure 5.17: Development of function $f(t)$ for axial symmetry, cases a, f and g according to table 5.1

Figures 5.15 and 5.16 show a difference in hydrodynamic period for the cases a to g. Although cases b and f give the largest peak value the longest hydrodynamic period is found for case a. Equation (G.29) shows that for axial–symmetric conditions the pore pressure decays with $\exp(s_j t)$, in which s_j denotes the roots for the Laplace inverse transformation. Using equation (G.27) $\exp(s_j t)$ can be rewritten into:

$$e^{s_j t} = e^{-\frac{\mu_j^2 c}{R^2} t}, \qquad \text{with } \mu_j = \lambda_j R, \quad \lambda_j = \sqrt{\frac{-s_j}{c}} \tag{5.7}$$

Equation (5.7) shows the well–known feature of the dependency of the consolidation period to the consolidation coefficient, c, and the reciprocal value of the drainage path squared. Note that for plane–strain conditions equation (H.31) shows that the pore pressure decays with:

$$e^{-\frac{\lambda_j^2 c}{l^2} t}$$

In which λ_j denotes the roots of the Laplace inverse transformation. The consolidation coefficient for cross–anisotropy is given by equations (G.5) and (H.9):

$$c = \frac{k}{\gamma_w} \left[A + 2G_{hh} \right] \tag{5.8}$$

Since the length of drainage path, R or l, is independent for cases a to g, the difference in consolidation period for the different cases follows from the difference in c–value. With k/γ_w

independent from the compressibility parameters the difference in consolidation coefficient is given by the differences in $A + 2G_{hh}$, which are shown by table 5.3. Here A and G_{hh} are functions of E_h, E_v, ν_{hh} and ν_{vh} given in equation (3.19).

Table 5.3: Values for A and $2G_{hh}$ for the cases a to g

cases	a	b	c	d	e	f	g
A	0	0	0	109.76	329.67	1648.35	18.67
$2G_{hh}$	1000	5000	1000	1000	769.23	3845.15	1000
$A + 2G_{hh}$	1000	5000	1000	1109.76	1098.90	5494.51	1018.67

For cases b and f table 5.3 shows the value for $A+2G_{hh}$ which exceeds strongly the value given for cases a, c, d, e and g. This corresponds to the graphs 5.15 and 5.16 in which despite the large peak in excess pore pressure for cases b and f a shorter consolidation period is found. Case a, explained in table 5.1, acts as a set of base parameters for the cases b to g. For each of the cases b to g E_h, E_v, ν_{hh} or ν_{vh} is increased, leading to material properties which are stiffer than for case a. As is to be expected case a leads to the lowest value for $A + 2G_{hh}$ and therefore to the longest consolidation period.

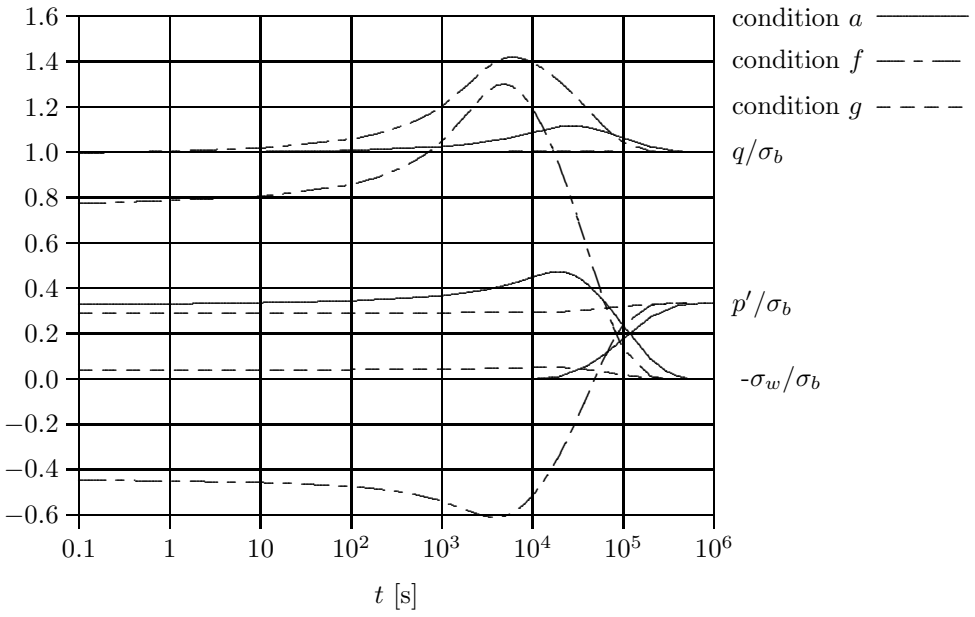

Figure 5.18: Development of σ_w, p' and q at $r/R = 0.02$ for axial symmetry for the cases a, f and g

Figure 5.18 shows for two extreme cases f and g and the isotropic case, case a the development of p', q and σ_w at $r = 0$. The initial value of p' is strongly influenced by the anisotropy of the loaded sample. This can be explained by initial undrained behaviour, which means no initial volumetric strain. As consolidation progresses p' increases to its final value. In section 5.2 equation (4.18) is presented:

$$\begin{bmatrix} e \\ \\ \varepsilon_q \end{bmatrix} = \begin{bmatrix} \frac{1}{K'} & \frac{1}{J'} \\ \frac{1}{J'} & \frac{1}{3G'} \end{bmatrix} \begin{bmatrix} p' \\ \\ q \end{bmatrix} \tag{5.9}$$

For isotropic conditions $1/J' = 0$, so e and p' are directly coupled by the bulk modulus K'. For anisotropic conditions e depends on p' as well as q. Initially after loading e remains unaffected.

Since q has an initial value equation, (5.9) predicts an initial value for p', $p' = -(K'/J')\ q$. Table 5.1 shows for case f a relatively large positive K'/J' - value, resulting in a relatively large, but negative, initial p'. When consolidation progresses p' increases to its final value. For case g table 5.1 shows a negative K'/J'-value. A negative K'/J'-value results in a positive initial p'. For case g the initial p' almost equals its final value which corresponds to the small amount of excess pore pressure which is created by axial loading as shown by figure 5.15. In section 5.3.2 it is concluded that for isotropic conditions the Mandel–Cryer effect is counterbalanced by a peak in the development of q. While p' remains unaffected. Figure 5.18 shows that for anisotropic conditions the Mandel–Cryer effect influences q as well as p'.

5.5 Alternative conditions

With the standard solution available small changes in boundary conditions or basic assumptions easily provide insight in the effects of alternative conditions. This section presents three of the relevant alternative conditions. The first concerns isotropically loaded samples, instead of axially loaded, the second involves the compressibility of the solids and the third clogging of the drain in the triaxial test.

Isotropic loading

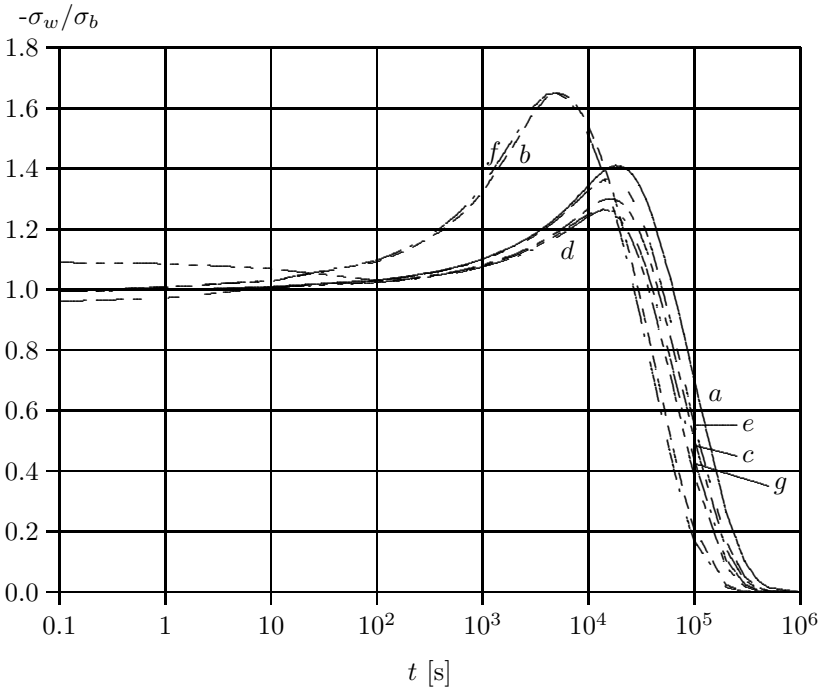

Figure 5.19: Pore pressure development at $r/R = 0.1$ for axial symmetric conditions and isotropic loading, cases a to g according to table 5.1

Appendix H gives the boundary conditions in terms of g_1, g_2 and g_3. In which g_1 represents the pore pressure prescribed at $r = R$, g_2 represents σ_r prescribed at $r = R$ and g_3 represents σ_{zz} prescribed at $z = h$. For $g_2 = g_3 = \sigma_b$ consolidation due to an isotropic load is modelled. Figure 5.19 visualises the results. Again a radial pore pressure dissipation is assumed in combination to a stiff plate on top. The solution is shown for the seven cases presented in table 5.1. Now for each case the initial pore pressure equals the initial loading, $-\sigma_w/\sigma_b = 1$. This corresponds to equation

(4.40) since for isotropic loading $q = 0$ and $p = \sigma_b$. Especially for case d the solution converges badly for small values for t and r. Figure 5.19 shows the short consolidation period for cases b and f and shows the Mandel–Cryer effect clearly for all cases a to g. Even for cases c and g the peak is considerable, $-\sigma_w/\sigma_b$ up to 1.26. Figure 5.19 shows that a large peak value is found for $E_h > E_v$, while for $E_v > E_h$ the peaks are smaller.

Compressible solids

Appendix I gives the derivation for the three–dimensional axial symmetric consolidation including compressible solids. To give a clear view on the individual phenomena that play a role the solution for isotropic material behaviour is extended to compressible solids. Chapter 2 discusses the different compression moduli. Barends [7] gives the storage equation including the solid stiffness. Figure 5.20 shows the results for three cases, each with $\nu = 0$, $E = 1000$ kPa, ($\beta = 0.003$ 1/kPa, $K = 333.33$ kPa), porosity $n = 0.4$ and permeability $k = 1{\times}10^{-8}$ m/s. The condition $\beta_{sf} = \beta_{ss} = 0$ corresponds to case a in figure 5.15 and $\nu = 0$ in figure 5.3. To show the influence of the different compressibility parameters to the pore pressure development for the second case only compression due to inter granular contacts is considered while the solids remain incompressible for a deviation in isotropic stress; $\beta_{ss} = 0.5\beta$, $\beta_{sf} = 0$. The third case presents the opposite condition, $\beta_{sf} = 0.5\beta$, $\beta_{ss} = 0$. Figure 5.20 shows the influence of the parameters β_{ss} and β_{sf}. Compression due to inter

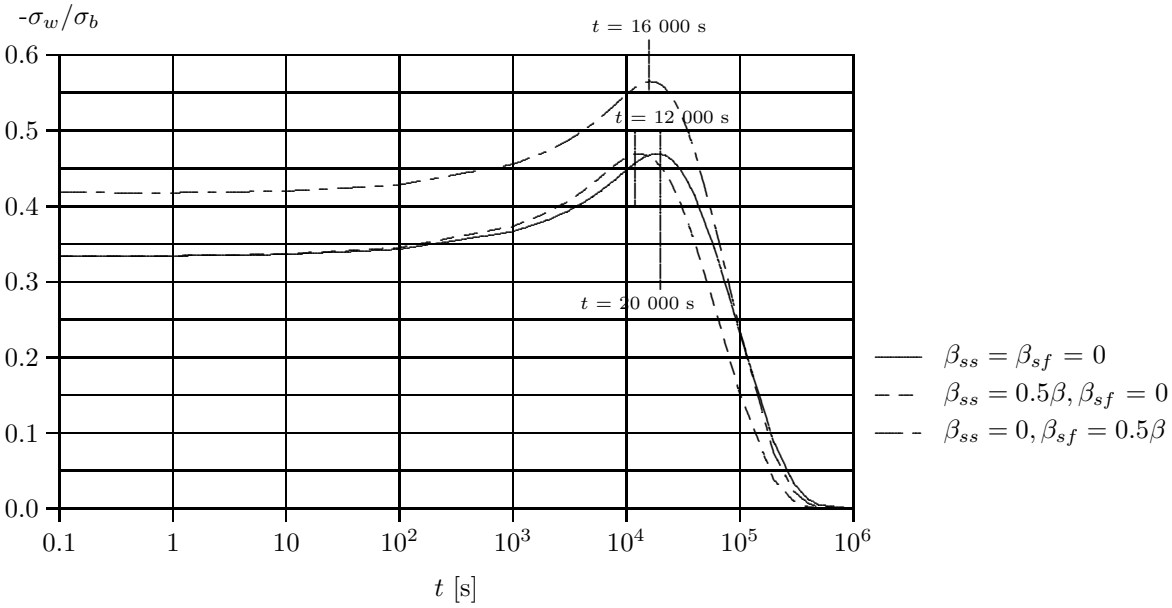

Figure 5.20: Pore pressure development for isotropic material behaviour including compressible solids for axial symmetry at $r/R = 0.1$, $\nu = 0$, $E = 1000$ kPa, $n = 0.4$ and $k = 1{\times}10^{-8}$ m/s

granular contacts, β_{ss} causes a slight acceleration in the consolidation process. Figure 5.20 shows a maximum peak value after 12 000 s, while for the condition with incompressible solids the peak is found at 20 000 s. The shape of the pore pressure development remains unaffected by β_{ss}. The initial value, the maximum peak and the slope of the pore pressure development after the peak are equal to those for the incompressible solids. The compressibility due to isotropic stress, β_{sf} causes a change in shape of the pore pressure development. A larger initial pore pressure, a larger peak value up to $-\sigma_w/\sigma_b = 0.57$, and a steeper slope after the maximum value are found. The maximum value is found at 16 000 s, indicating acceleration of the consolidation process. Note that β_{sf} has the same type of influence on the consolidation process as cross–anisotropy for $K'/J' > 0$. Both lead to a larger initial pore pressure and a larger peak value.

Section 4.3.1 gives an expression for the initial pore pressure, σ_{wi}. With equation (2.17) and the sign convention according to section 5.3.1 is found for an axially loaded sample :

$$\sigma_{w0} = -\frac{1}{3} B \sigma_b, \qquad B = \frac{(1-n)\,\beta_{ss} - \beta}{(1-n)\,\beta_{ss} + n\beta_{sf} - n\beta_{fg} - \beta} \tag{5.10}$$

Figure 5.20 presents the pore pressure development for $\beta_{fg} = 0$ and $n = 0.4$. The solid line in figure 5.20 represents the condition $\beta_{ss} = \beta sf = 0$. Equation (5.10) gives, for these conditions B = 1 and therefore σ_{w0} = -1/3 σ_b. For $\beta_{ss} = 0.5\beta$ while $\beta_{sf} = 0$ also gives $B = 1$ and σ_{wi} = -1/3 σ_b. However for $\beta_{sf} = 0.5\beta$ leads to $B = 5/4$ and $\sigma_{wi} = -5/12\sigma_b \approx -0.42\sigma_b$.

Drainage resistance

The analytical solutions presented sofar all use the boundary condition $\sigma_w = 0$ at $r = R$ during the entire consolidation process. This implies a perfect drainage system. When radial dissipation of pore water is required in standard triaxial testing filter paper can be placed between the membrane and the sample. The drainage system then consists of the filter paper, the porous stones and the tubes for collecting expelled pore water. Each part of the drainage system will induce some resistance to the expelled pore water flow and violate the boundary condition $\sigma_w = 0$ at $r = R$. To estimate the influence of a non–perfect drainage system a different boundary condition is needed. When the drainage valves are still closed the water pressure in the drainage system equals the pore pressure inside the sample. For a stiff drainage system only a negligible pore water flow is needed to equalise the water pressure in the drainage system to the excess pore pressure inside the sample. For such a stiff drainage system the water pressure before opening the valves, σ_{wi} is given by the equations (4.36) or (4.41). A simple alternative boundary condition, which provides a time

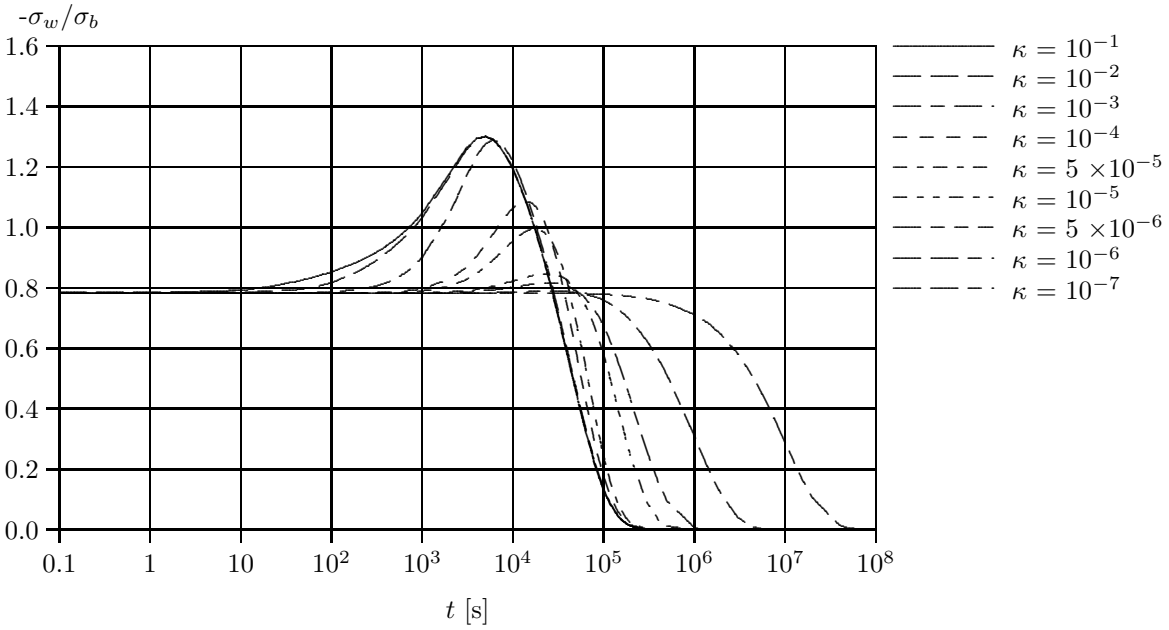

Figure 5.21: Pore pressure development axial symmetry at $r/R = 0.05$, for cross–anisotropy, case f

depending pressure in the draining system, is given by:

$$\sigma_{drain} = \sigma_{w0} e^{-\kappa t} \tag{5.11}$$

In equation (5.11) the parameter κ determines the decay in drain pressure. Note that prescribing equation (5.11) for the boundary condition at $r = R$ gives the drain pressure independent from the amount of pore water expelled from the sample. For a drainage system with a small hydraulic resistance in combination to a soft and permeable sample leading to a large expelled pore water flow the drain pressure might decay relatively slow and vice versa.

In the appendices E and H the analytical solution is extended with the boundary condition (5.11). Figure 5.21 illustrates the influence of a time–depending drain pressure. The maximum Mandel–Cryer effect is found for case f, as given in table 5.1. Figure 5.21 shows the pore pressure development for case f for κ–values ranging from 0.1 to 1 $\times 10^{-7}$. Note that the solution is presented for a sample permeability of $k = 1 \times 10^{-8}$ m/s. Equation (5.8) gives with $\gamma_w = 10$ kN/m^3 and table 5.3 a coefficient of consolidation of the order of $c = 5 \times 10^{-6}$ m^2/s. Figure 5.21 shows clearly that for decreasing κ–value, the Mandel–Cryer peak reduces and even vanishes when the value for κ is in the same order of magnitude as c. So in order to measure the Mandel–Cryer peak in standard triaxial testing the hydraulic resistance should be small enough in relation to the consolidation coefficient of the tested soil.

Chapter 6

Laboratory measurements

6.1 Tests on peat

Chapters 3 to 5 discuss a mathematical description of anisotropy and the influence of anisotropy to consolidation behaviour. As explained in chapter 1 behaviour of peat forms the main objective of this study. This chapter discusses measurements on the consolidation behaviour of peat and compares the results to the analytical solutions presented in chapter 5.

There are three optional causes for peat to behave anisotropically. First, anisotropy can be due to the structure of peat. The stiffness in the main fibre direction differs from the stiffness perpendicular to the fibres. This is known as structural anisotropy. It is assumed that the fibres are mainly oriented in the horizontal plane, which leads to a difference in stiffness in horizontal and vertical direction. The second optional cause is a load-induced anisotropy. Since peat is a soft and compressible material the stiffness depends on the stress level or even on the rate of compression. A deviator load will induce a difference in compressibility in different directions and therefore a difference in stiffness. The third option originates from a difference in loading and unloading conditions. Section 4.2 explains that true elastic behaviour is only found at very small strain level. Exceeding this small strain level already leads to residual deformation. In engineering practice equivalent elastic moduli, which include some plastic deformation, are used. This working method implies a difference in stiffness moduli for loading and unloading conditions. Loading an undrained soil sample in the axial direction gives an effective stress increase in axial direction and a decrease in radial effective stress due to generation of pore pressure. So even for isotropic soil anisotropic behaviour can be found. According to Parry & Wroth [62] this is referred to as stress anisotropy.

This chapter first gives a characterisation of the tested material in section 6.2. Special attention is given to the axial pre–consolidation stress discussed in section 6.2.3. Section 6.3 discusses measurements of the shear modulus, for small strain using bender elements and moderate to large strain using simple shear tests. Chapter 2 deals with the compressibility of the individual phases in relation to the Skempton B–factor. Section 6.5 discusses measurements of the Skempton B–factor in combination with the degree of saturation. Chapter 5 shows that the influence of anisotropy is found in the undrained effective stress path and in the Mandel–Cryer effect. Section 6.6 shows measurements of the effective stress path for small undrained loading steps at different levels of pre–consolidation. Section 6.7 shows measurements on the Mandel–Cryer effect.

6.2 Characterisation of tested soil

6.2.1 Sample location

Figure 6.1: Sample location

The samples are retrieved near Breukelen along the highway A2 near the future junction Breukelen - Vinkeveen. Due to the reconstruction of the highway a field survey is conducted. The soil consists of an approximately 6 m thick peat layer on top of a thick Pleistocene sand layer. The ground water table ranges between 0.6 and 0.3 m below surface. The samples are retrieved horizontally as well as vertically. Photo 6.1 shows that the vertically retrieved samples are taken at a depth of approximately 1 m below surface level, 0.7 to 0.4 m below phreatic level, using a sampling tube with length of 440 mm and diameter of 66 mm. The lower part of the tubes, used for retrieving samples in vertical direction, reached a thin clayey layer. This part of the sample material is disregarded. After retrieving the samples the tubes are sealed and stored in a temperature and humidity controlled room.

Each sampling tube has a unique number. The sample number corresponds to the sampling tube number by which it is retrieved followed by an a, b, c, etc. for the first, second, third, etc. sample taken from this sampling tube. When discussing the measurement results these numbers are mentioned in following sections.

6.2.2 Descriptive parameters

To have a good impression of the tested material several descriptive parameters have been derived from the samples or from parts cut off when trimming.

The water content W is defined as the ratio of pore water mass M_w and mass of dry solid particles M_s:

$$W = \frac{M_w}{M_s} \tag{6.1}$$

The value for M_s is determined after heating the sample to 105° C during 24 hours. Skempton & Petley [66] conclude that the loss on organic matter is insignificant when temperatures up to 105° C are used, while for lower temperatures, 60 to 85° C small amounts of free pore water remain. The difference in mass before and after drying the sample gives the pore water mass. Since peat contains a large amount of pore water and the solids have a relatively low density, compared to sand or clay, the pore water mass easily exceeds the mass of solid material. Typical values of W for peat ranges from 2 to 10.

The loss on ignition N presents the material content that evaporates when heated to a large temperature. Several authors and standard regulations give small differences in the prescription

for the determination of N [66]. The values presented in table 6.1 are found after heating the sample to 500° C during 4 hours. With m_1 the remaining mass of the sample, N is given by:

$$N = \frac{M_s - m_1}{M_s} \tag{6.2}$$

The organic content P, the ratio of mass of organic material to total mass is close to N, (6.2). Skempton & Petley [66] present a correlation between N and P:

$$P = 1 - 1.04\,(1 - N) \tag{6.3}$$

The ash content is the complement of the organic content. Based on equation (6.3) is found:

$$\text{ash content} = 1.04\,(1 - N) \tag{6.4}$$

Equation (6.4) indicates that during heating the anorganic part looses 4% of its mass. For a large organic content, a small ash content, this is a negligible error in comparison to the natural heterogeneity of peat. This results in equating P to N for typical peat conditions [25].

The solid density ρ_s is found by using an automated pycnometer method according to the Dutch regulations NEN5111 [58]. The standard pycnometer method uses the difference in mass of a fluid with a known density, e.g. water and the mass of the same volume of the tested material saturated with this fluid. The solid density presented in tables 6.1 and 6.6 are found using helium.

Skempton & Petley [66] show a strong correlation between the organic content and the specific gravity of solids G_s in which G_s is defined as $G_s = \rho_s/\rho_w$. For soil types in Western Europe without any organic material G_s is of the order of 2.65. Pure organic material has a specific gravity of G_s of the order of 1.4. For intermediate values of the organic content G_s has some intermediate value. With $P = N$ is found:

$$\frac{1}{G_s} = \frac{N}{1.4} + \frac{1 - N}{2.65} \tag{6.5}$$

Den Haan et al [25] show that equation (6.5) applies well for Dutch soils.

Total density ρ is given by the initial sample dimensions and mass. This provides the initial density ρ for each test. The total density is a useful parameter in several correlations ([25], [24]) and for differentiating different types of peat as explained in [69].

Using weight and volume of samples used for the triaxial tests discussed in the following sections, the void ratio e, porosity n and initial degree of saturation S_{ri} can be found by the following equations:

$$\begin{aligned} e &= \frac{V_p}{V_s} = \frac{G_s\rho_w - \rho_d}{\rho_d} \\ \rho_d &= \frac{\rho}{1 + W} \\ n &= 1 - \frac{\rho_d}{G_s\rho_w} \\ S_r &= \frac{W\rho}{n\rho_w\,(1 + W)} = \frac{G_s W}{e} = \frac{\rho - (1 - n)\,\rho_s}{n\rho_w} \end{aligned} \tag{6.6}$$

In which:

V_p = pore volume
V_s = volume solids
ρ_d = dry density, M_s/V
V = total soil volume

Table 6.1: Descriptive parameters for the tested peat

Symbol	Unity	μ_x	σ_x	n_s
W	-	5.2	0.7	20
N	-	0.57 (0.52)	0.1 (0.05)	8 (6)
ρ_s	[kg/m^3]	1690	75	24
ρ	[kg/m^3]	1040	30	20
n	[-]	0.90	0.01	18
e	[-]	9.2	1.0	18
S_r	[-]	0.96	0.03	18

Table 6.1 presents the mean value μ_x, standard deviation σ_x and number of tests n_s for W, N, ρ_s, ρ, n, e and S_r. For each of the parameters the standard deviation exceeds the inaccuracy of measurement by an order in magnitude. So the heterogeneity in the tested material is the main cause for deviation in the values found. For N, only a small number of samples is tested. Two measurements deviate; $N = 0.73$ and 0.70. Table 6.1 shows the values for μ_N, σ_N and n_s between brackets excluding these measurements. Den Haan et al. [25] plot N versus ρ for a large number of samples of Dutch organic soil. The values presented in table 6.1 correspond well to this graph. It is remarkable that the values presented in table 6.1 do not correspond to equation (6.5). $N = 0.57$ gives $G_s = 1.76$, while $G_s = 1.69$ corresponds to $N = 0.64$, assuming $\rho_w = 1000$ [kg/m^3].

6.2.3 Pre–consolidation and permeability

For a proper interpretation of pore pressure measurement information on the permeability and level of natural pre–consolidation is needed. Both are determined from K_0–CRS tests. The K_0–CRS test is a constant rate of strain oedometer test which has the option to measure lateral stress. Den Haan & Kamao [26] and Den Haan & Sellmeijer [27] give an extended description of the apparatus and the analysis of measurement results. In total six tests are conducted, three on vertically retrieved samples and three on horizontally retrieved samples. The initial sample height for each sample is 31 mm. Initially four tests are conducted to measure the different compression indices and the pre–consolidation stress. Later two tests are added when the samples are pre–loaded before conducting simple shear tests, see section 6.3.

The four initial samples are loaded to 60 kPa followed by an unloading (to 30 kPa), then reloading (to 100 kPa) phase, a relaxation phase during 16 hours, a reloading phase to 200 kPa, an unloading phase until 10 kPa and finally a second relaxation phase is applied. All loading and unloading phases occur at a strain rate of 0.0030 mm/min. During relaxation the sample height is kept constant while measuring the vertical force. The two extra tests are loaded to approximately 70 kPa followed by an unloading to 10 kPa and relaxation phase. Figure 6.2a presents the stress–strain curves. It shows the sample number followed by *hor* for the horizontally retrieved samples and *ver* for the vertically retrieved samples. Since horizontally and vertically retrieved samples are plotted in figure 6.2 the horizontal axis denotes the axial effective stress σ'_a. Note that the left axis in figure 6.2a gives the natural strain ε^H.

If peat behaves anisotropically, due to presence of fibres, a clear distinction in stress–strain curve for the horizontally and vertically retrieved samples is to be expected. However figure 6.2a shows almost identical curves for the vertically retrieved sample 4588-1 and the horizontally retrieved sample 24418 as well as for sample 2590 and 22726. The deviations with the other two samples are small. It seems that the heterogeneity of the tested peat has more influence on the measurements than a possible anisotropy. Figure 6.2a clearly shows the bending of the stress–strain curve when the pre–consolidation pressure is reached. Since horizontally and vertically retrieved samples are tested the determined pre–consolidation stress is referred to as axial pre–consolidation stress σ'_{ac}. The individual values for σ'_{ac} are found using the analysis given by Den Haan & Kamao [26]. Table 6.2 shows the results.

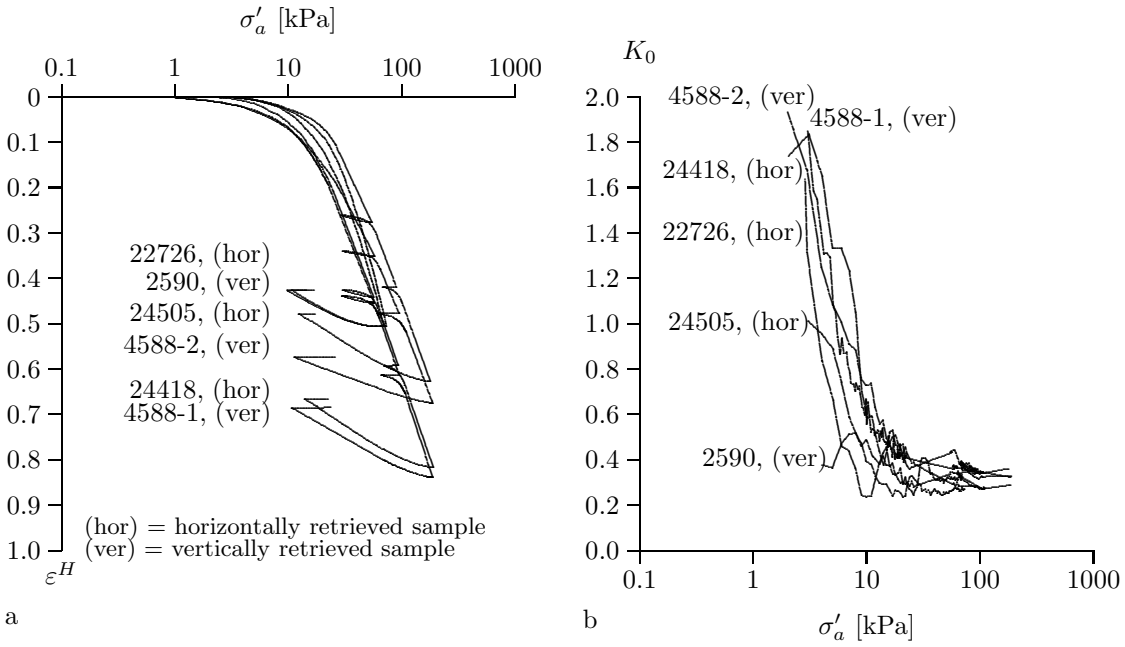

Figure 6.2: Results on 6 K_0–CRS tests, a) stress–strain development b) σ'_a–K_0 development

Table 6.2: Results of the $K_0 - CRS$ tests

Sample nr	σ'_{ac} [kPa]	K_0 [-]	χ [-]	k_0 [m/s]
4588-1 (ver)	11.9	0.36	4.34	1.6×10^{-8}
4588-2 (ver)	16.7	0.29	5.28	2.8×10^{-8}
2590 (ver)	21.8	0.26	5.10	3.2×10^{-8}
24505 (hor)	20.8	0.36	5.26	2.1×10^{-8}
24418 (hor)	11.5	0.36	4.56	2.3×10^{-8}
22726 (hor)	19.1	0.32	5.28	2.8×10^{-8}

with χ and k_0 defined by equation (6.7)

Using the density presented in table 6.1 and the position of the water table the vertical effective stress in the field σ'_{v0} can be estimated. Since the water table is between 0.3 and 0.6 m below surface σ'_{v0} ranges from 4 to 7 [kPa]. Several phenomena might explain the difference in σ'_{ac} and σ'_{v0} like fluctuation of the water table, oxidation of the top layer or aging.

Figure 6.2b shows K_0 versus σ'_a, in which K_0 is defined as the ratio of radial effective stress to axial effective stress, σ'_r/σ'_a. Again it is to be expected that if the fibres are aligned in one plane and if the fibres play an important role in the stiffness characteristics of peat a clear difference between the horizontally and vertically retrieved samples is to be expected. Figure 6.2b shows equivalent behaviour for the six samples. Again heterogeneity of the peat samples seems more important than a possible anisotropy of peat.

During execution of the tests the pore pressure is measured at the bottom of the sample. The measurement data is used to assess the permeability according to the analysis given by Den Haan et al [28]. The results of the loading phases are used to fit the relation:

$$k = k_0 \times \exp(-\chi e) \tag{6.7}$$

Table 6.2 shows the results. Note that the values for k_0 are remarkably low regarding the large porosity found in table 6.1, $n = 0.9$. Possibly this can be explained by a relatively large amount

of bonded pore water which reduces the pore water flow, see Karádi, [47]. Den Haan et al [28] use the relation:

$$k = k_0 \times 10^{-\frac{\varepsilon}{C}}$$

For soft organic clay they report $C \approx 0.2$. Reformulation of the expressions for k shows that $C = 0.2$ corresponds to $\chi = 10$. The tested peat samples show about half this value.

6.3 Shear Modulus

6.3.1 Bender element tests

Shear wave measurements are used to determine the shear modulus at small strain level. These type of measurements are conducted for three reasons. First, chapter 3 shows that not all the five independent parameters of the cross–anisotropic model can be derived from standard triaxial testing. This holds especially for the shear modulus. Second, shear wave measurements are conducted before during and after application of the back–pressure. If the shear wave measurements show different results at different stages of back–pressure application, it might indicate that the back–pressure induces a structural change in peat behaviour. Third, shear wave measurements in combination with Simple Shear measurements give the opportunity to test if the typical stiffness–strain development depicted by figure 6.3 also holds for peat. This stiffness–strain development is discussed in section 4.2. It shows a threshold value ε_0 until which the shear modulus remains constant. In this domain linear elastic behaviour is valid. Thereafter, the shear modulus decays indicating plasticity.

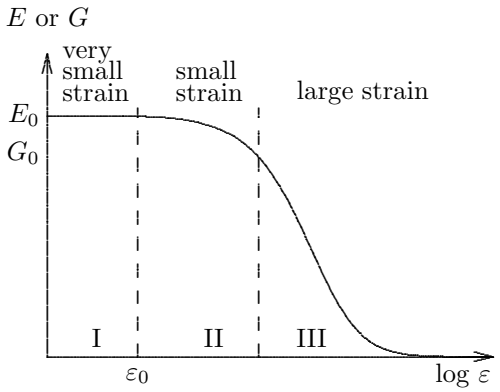

Figure 6.3: A typical stiffness–strain development, after Atkinson [5]

The Bender elements used for the reported tests apply a single block shaped pulse. The pulse is generated twice, once in each direction, referred to as positive and negative wave. The arrival time of the shear wave and the actual height of the sample gives the velocity v at which the shear wave runs through the sample. The actual sample height follows from the axial strain measurement. The sample height is corrected for the length for which the bender elements protrude into the sample. Following Vigianni & Atkinson [78], the relevant travelling path for the shear wave is given by the distance between the tips of the bender elements. Together with the actual density of the sample the Shear modulus is given by:

$$G = \rho v^2 \tag{6.8}$$

The actual density ρ follows from ρ_s, n and the pore fluid density ρ_w. The value for ρ_s is determined for each sample individually after finishing the tests. Assuming the solids to be incompressible and $\rho_w = 998$ kg/m^3 gives with the measured volumetric strain the actual density of the sample. Figure 6.4 shows a typical shear wave measurement for the positive and negative shear wave. The sent shear wave has an amplitude of 10 V. Figure 6.4 shows the positive and negative waves. Figure 6.4 shows initially a gradual increase in measured voltage, instead of a sudden increase, which makes it hard to determine the exact arrival time. Viggianni & Atkinson [78] and Jovičič et al [45] show that near field effects cause a considerable disturbance of the received signal. Using different types of signals and numerical analyses the authors show that not the first deflection but the top of the

first minor peak proceeding the major peak indicates the arrival time of the shear wave. In figure 6.4 this point is indicated by t_0.

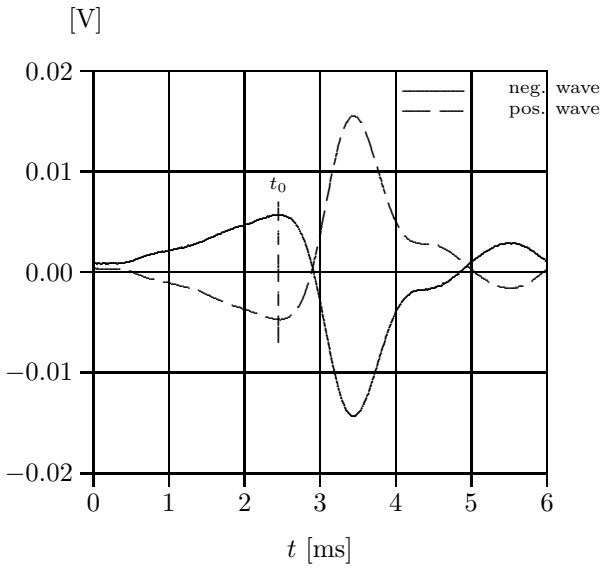

Figure 6.4: Typical result of shear wave measurement, test 2590b initial conditions

Table 6.3 shows the results of shear wave measurements for the sample's initial conditions and during application of the back–pressure. For tests 2590a and 22726a, shear wave measurements are conducted only before and after application of the back–pressure. For the other tests the total back–pressure of 300 kPa is applied in steps of 100 kPa each and shear wave measurements are conducted after each step. Table 6.3 shows clear differences between the different tested samples however the difference in G–value for the different stages in one test remains remarkably small. The shear wave measurements do not indicate any structural change during application of the back–pressure, as shown by figure 6.5.

It should be noted that if the tested soil is cross–anisotropic with the axis of symmetry in vertical direction the shear moduli derived from the vertically retrieved samples correspond to G_{vh}. In this situation the shear wave runs in vertical direction while horizontally polarised. The shear wave measurements run on the horizontally retrieved samples give information on G_{hh} or G_{hv} depending on the orientation of the bender element to the original axis of symmetry. Unfortunately when analysing the measurement data the orientation of the bender elements in relation to the axis of symmetry could not be determined with certainty. Therefore table 6.3 presents the G values without the suffices hh, vh or hv.

Section 6.6.2 discusses the influence of an axial pre–loading on the angle of undrained ESP. During these tests shear wave measurements are conducted to the samples after the reconsolidation at initial conditions. For test 22726a two levels of axial pre–consolidation is used, as shown by the loading of figure 6.12. Table 6.3 shows the results.

6.3.2 Simple Shear measurements

To find information on the shear modulus at moderate to large strain level four simple shear tests are conducted, two on horizontally retrieved samples and two on vertically retrieved samples. The tests are conducted in a Geonor simple shear device, modified to handle samples with a diameter of 66 mm. The initial sample height is 22 mm. The samples are consolidated at a vertical stress of 10 kPa. After consolidation the sample height is reduced to approximately 21 mm. The sample is sheared at constant height, which implies adjustment of the vertical load during the test. The

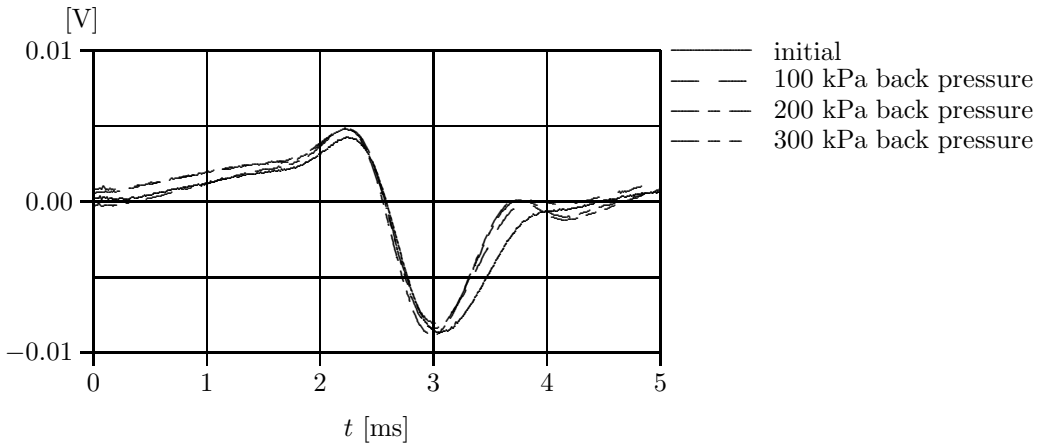

Figure 6.5: Development of the negative shear wave of test 1316a during raising of the back–pressure

Table 6.3: Results of shear wave measurements

	vert. retrieved samples				hor. retrieved samples	
test	2590a	2590b	1316a	3963b	22726a	24482c
	G	G	G	G	G	G
	[kPa]	[kPa]	[kPa]	[kPa]	[kPa]	[kPa]
initial	635	865	960	1715	740	2010
bp 100 kPa		930	970	1770		1208
bp 200 kPa		860	960	1820		1170
bp 300 kPa	665	895	950	1765	735	1170
pre consol at q = 30 kPa					1135	
pre consol. at q = 55 kPa		2335	2145		1450	3215

samples are sheared until the horizontal deformation equals 10 mm. The relevant parameters are given by:

$$\Delta\gamma = \frac{u_{hor}}{h_a}, \qquad \Delta\tau = \frac{\Delta F_h}{A}, \qquad G = \frac{\Delta\tau}{\Delta\gamma} \tag{6.9}$$

with:

u_{hor} = horizontal deformation
h_a = actual sample height
F_h = horizontal force
A = sample surface

The maximum horizontal deformation of 10 mm corresponds to a maximum γ of 47 %. The measured shear stress, τ is corrected for the friction losses in the system and membrane.

To test the influence of an axial pre–consolidation one of the horizontally retrieved samples and one of the vertically retrieved samples is axially pre–consolidated in the K_0–CRS device. The samples are consolidated at an axial strain of 35 %. Figure 6.6 shows the results.

Figure 6.7 shows the development of the measured shear modulus versus the logarithm of the shear strain. The actual value for G is given by the slope of the tangent line of the τ - γ curve,

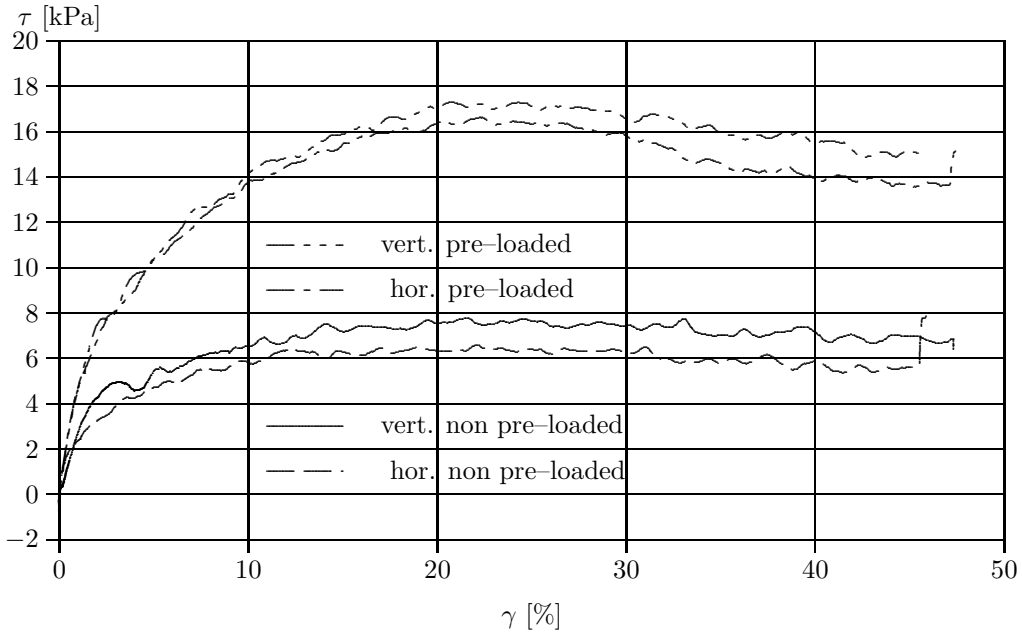

Figure 6.6: Results of simple shear tests

figure 6.6. The G value presented in figure 6.7 is found by application of the least squares method to each set of ten successive measurement data points. The angle of the fitted line represents the shear modulus and is depicted at the average γ for the ten regarded points.

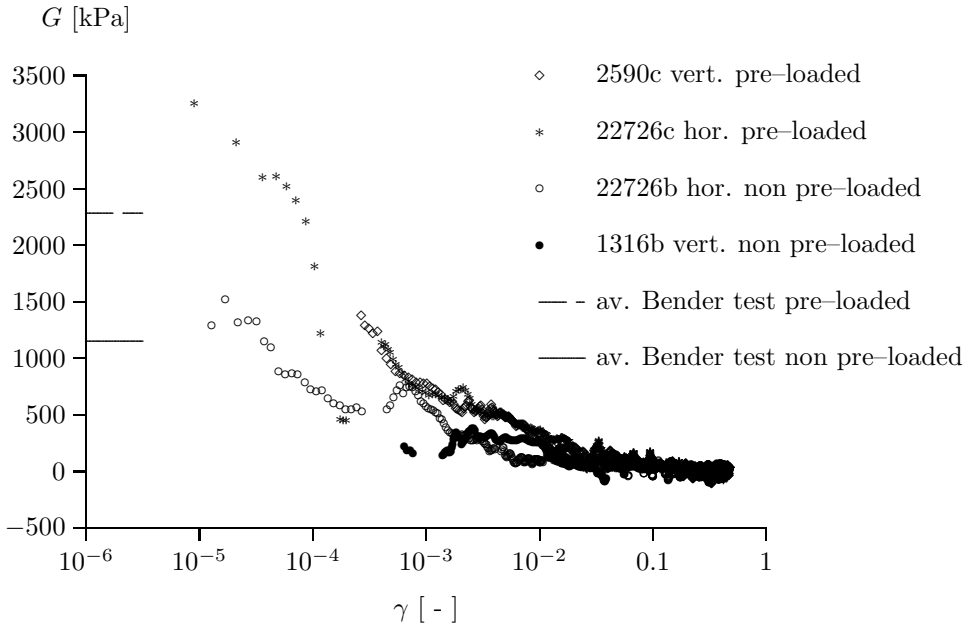

Figure 6.7: Simple Shear tests on pre–loaded and non pre–loaded samples

Figure 6.7 presents the results for fits with a relative least squares sum $R^2 > 0.8$ ($R^2 = 1.0$ represents a perfect fit). Figure 6.6 shows a clearly non–monotone development of the τ–γ curve. The saw tooth shape of the curve can be explained by the presence of the fibres. At small strain

level only a limited number of fits for which $R^2 > 0.8$ can be shown. For $\gamma < 5 \times 10^{-4}$ only for the both horizontally retrieved samples G values are plotted in figure 6.7. The differences between horizontally and vertically retrieved samples are small and can be explained by natural heterogeneity. The differences between the pre–loaded and non pre–loaded samples are clearer. In the range $10^{-3} < \gamma < 10^{-2}$ the G value for the pre–loaded samples is approximately twice the value for the non pre–loaded samples. For large strain the measured G converges. This is to be expected since large strain is dominated by plasticity and the effects of a pre–loading vanishes.

At the left side of figure 6.7 the results of the bender element tests are presented. The Bender element tests present the G–value at a very small strain level, Dyvik & Madshus [29] report a strain level of 10^{-5} for bender element tests. Extrapolation of the simple shear data to small strain level shows that the simple shear data is in agreement with the bender element test results.

Keverling Buisman & Huizinga [46] propose a hyperbolic law to describe the τ–γ relation, which is also elaborated by Kondner & Zelasko [48]. The proposed hyperbolic law is given by:

$$\tau = \frac{\gamma}{a + b\gamma} \tag{6.10}$$

In which a and b are coefficients to be fitted by a curve fitting procedure. Using equation 6.10 an expression for the shear modulus is found:

$$G = \frac{\partial \tau}{\partial \gamma} = \frac{a}{(a + b\gamma)^2}, \qquad G_0 = \frac{1}{a} \tag{6.11}$$

Table 6.4: Determination of G_0 by curve fitting equation (6.10)

test	a	b	R^2	G_0
1316 non pre–loaded	0.0031	0.0848	0.99	320
22726 non pre–loaded	0.0039	0.095	0.99	260
22726 pre–loaded	0.0013	0.051	0.99	790
2590 pre–loaded	0.0018	0.046	0.99	565

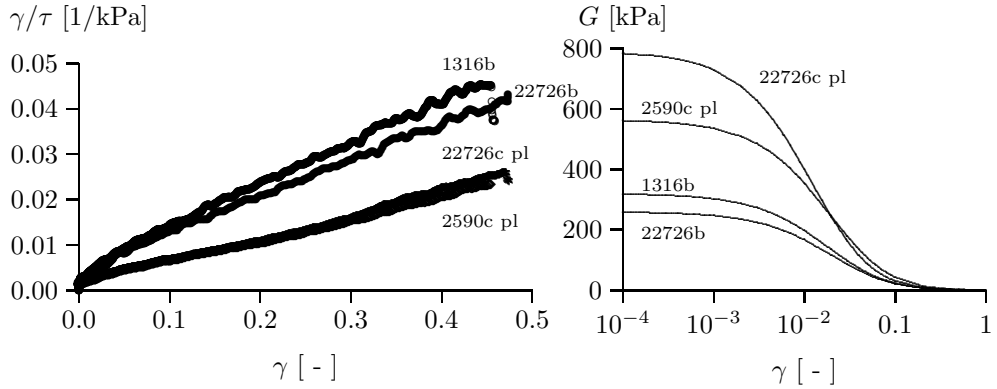

Figure 6.8: Curve fitting for hyperbola law, following Kondner [48], pl = pre–loaded

Table 6.4 shows that the measurement data fit well to a hyperbolic law, with R^2 close to 1.0. The table shows a clear difference in G_0 for the pre–loaded and non pre–loaded samples. The values for G_0 found given by table 6.4 are considerably lower than found by the shear wave measurements. Using equation (6.11) a continuous $G - \gamma$ curve can be found using the coefficients of table 6.4. Figure 6.8 shows the continuous $G - \gamma$ development. Graph 6.7 shows a lower G_0 than found by the shear wave measurements and indicated by figure 6.7. From $\gamma = 5 \times 10^{-3}$ figure 6.7 and 6.8 are in reasonable agreement.

6.3.3 Conclusions

At the beginning of this section three reasons were mentioned for conducting shear wave measurements. The first reason is to derive information on the shear modulus, which can not be found by standard triaxial testing. The results are presented in table 6.3. The bender element tests as well as the Simple Shear tests do not show a clear difference between the horizontally and vertically retrieved samples. The differences found can be explained by natural heterogeneity.

The second reason is to identify possible structural changes during application of the back–pressure. Figure 6.5 shows that the shear wave measurements remain unaffected by the back–pressure. Indications for a change in structure are not found.

The third reason is to check if the typical stress–strain development depicted by figure 6.3 also holds for peat and if a threshold value γ_0 can be found. Figure 6.7 and 6.8 show a stiffness–strain development that corresponds to the theoretical development given by figure 6.3. The shear wave measurement can be regarded as initial stiffness G_0. Figure 6.7 shows that a plateau, a constant value for G could not be distinguished from measurements when looking at the slope of the tangent line for the $\tau - \gamma$ curve. In figure 6.8 such a plateau can be distinguished. However at small strain level the G values presented in figure 6.8 do not correspond to shear wave measurements. Fitting to a hyperbola seems to underestimate G_0 significantly. Flattening of the curve at small strain level as predicted by figure 6.8 does not correspond to the shear wave measurements. It can be concluded that the threshold value for γ_0 can not be distinguished from measurements. If such a threshold value exists it falls beyond measurement accuracy of the Simple Shear device. So even at small strain level a non–linear G should be accounted for.

6.4 Pore pressure measurement at the sample centre

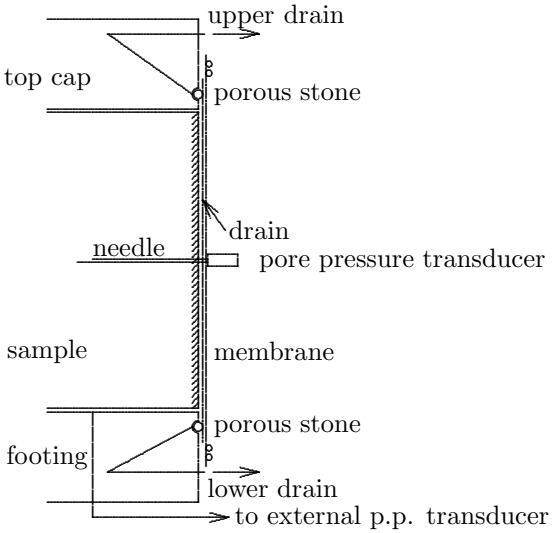

Figure 6.9: Test set-up

To generate the Mandel–Cryer effect in a triaxial test a radial pore water flow is needed. To create a radial pore water flow paper drains are placed between the sample and the membrane. At top and bottom a stiff impermeable plate is placed. This plate prevents direct pore water dissipation from the sample to the porous stone. The paper drains are extended beyond the plate at top and bottom and are connected to the porous stones. At the centre of the footing a connection is made between the sample and a pore pressure transducer. This transducer is referred to as the externally placed transducer. The expelled pore water is collected in the chambers of the hydraulic piston controlling the back–pressure. Neglecting pressure losses in the tubes between triaxial cell and piston, the actual pressure in the hydraulic piston equals the pressure in the drainage system, paper drains and porous stones. Figure 6.9 sketches the test set–up.

The Mandel–Cryer effect is only found at the centre of the sample. So pore pressure measurements inside the sample are needed. Figure 6.10b shows a miniature pore pressure transducer that is connected to a needle. When preparing the sample the needle is pierced through the membrane. The length of the needle is 3 cm. So when placed carefully the tip of the needle reaches the centre of the sample. Some glue is used to connect the needle firmly to the membrane. Application of the

glue also prevents possible leakage of pore water along the needle through the membrane. Figure 6.10a shows the needle placed inside a sample. The casing connecting the end of the needle to the pore pressure transducer contains a porous stone to protect the transducer. Complete saturation of the porous stone is achieved by placing the stone, transducer and needle in a cup of water that is placed in an exicator in which a vacuum is applied for one hour. Saturation of the casing and the needle was easily achieved by flushing both with de–aired water. The saturation of the porous stone, needle and casing was regularly checked by comparing measurements of the needle and external transducer.

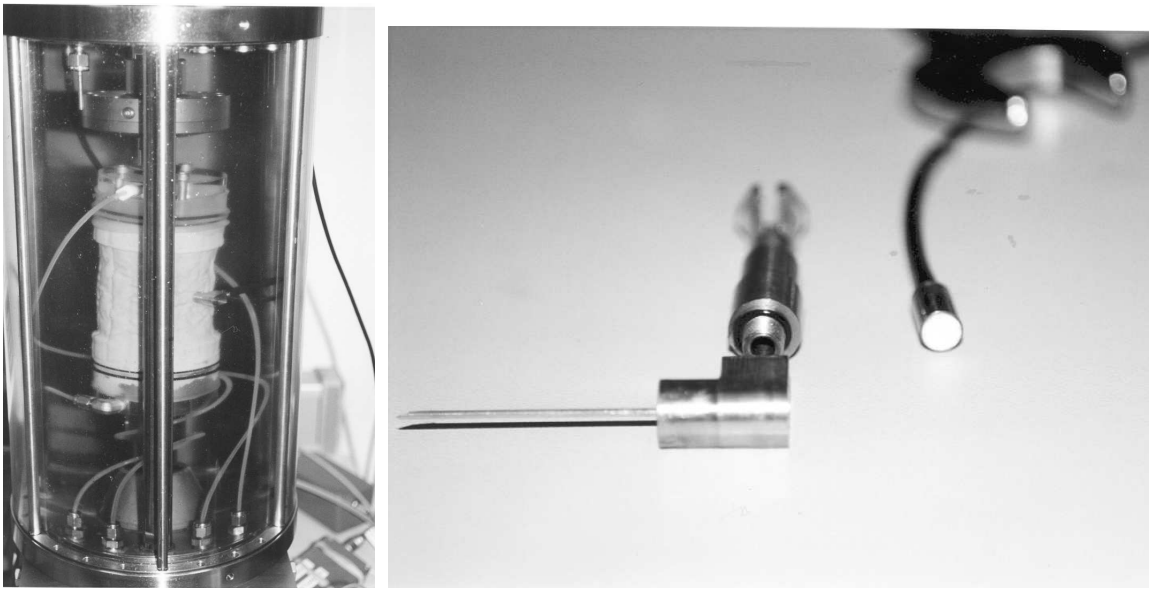

Figure 6.10: a) Test facility, b) Needle, casing and pore pressure transducer

The analytical solutions presented in chapter 5 assume deformations to be uniformly distributed in axial direction. In order to meet this assumption shear stress along the top cap and footing of the sample should be minimised. Therefore a membrane is placed between the sample and top cap respectively footing. Silicone grease is used to reduce further friction.

6.5 Initial saturation, B–factor measurement

Chapter 2 shows the influence of gas bubbles on the compressibility of the pore fluid. Even a small amount of gas raises the pore fluid compressibility considerably. The mathematical description presented in chapter 5 assumes an incompressible pore fluid. In practice this condition is reached when the compressibility of the skeleton exceeds the compressibility of the pore fluid in an order of magnitude. This is illustrated by equation (4.40). Equation (4.40) also illustrates the influence of the Skempton B–factor on the measurement results. When the B–factor is not well controlled a reduced pore pressure is measured. It is therefore important to check the degree of saturation before comparing experimental results to theory.

Chapter 2 introduces the Skempton B–factor which is further discussed in chapter 4. Equation (2.17) shows the Skempton B–factor to be some function of the compressibility of pore fluid, solids and skeleton. For clay and sand the solids can be considered as incompressible. The Skempton B–factor reduces to a function of pore fluid and skeleton compressibility. Therefore, in standard triaxial testing B–factor measurement is usually conducted to check the saturation of the sample.

Since peat has an organic nature, fibres could conceivably contain air pockets. If such an air

pocket is not in contact with the pores a fibre with such an air pocket can be seen as a compressible solid. The Skempton B–factor is then a function of the compressibility of solids, pore fluid and skeleton. If the solids of peat can be considered as compressible B–factor measurement is not enough to check the saturation of the sample. A possible low degree of saturation leading to a low B–factor might be masked by the compressibility of the solids leading to a B–factor increase. To check if compressibility of the solids influences pore pressure development S_{ri} and B–factor are calculated under the assumption of incompressible solids, using equation (2.16). If the measured B–factor corresponds to the calculated value it can be concluded that compressibility of the solids does not influence the measurements.

Table 6.1 presents the average initial values for e, n and S_r for the conducted triaxial tests. Table 6.6 gives the individual values. The initial degree of saturation, S_{ri} is given by the equations (6.6), using the initial values for W, e, n, ρ and ρ_s. For each sample ρ_s is measured after testing. It should be noted that if the solids are compressible ρ_s changes during compression as shown in chapter 2. This means that the initial value for ρ_s is not available. If the solids are compressible the value for ρ_s after the test is an upper bound for the initial value for ρ_s. Since ρ and W follow from direct initial measurement, a smaller value for ρ_s will lead to a larger S_{ri} as shown by equation (6.6). Then, for a larger S_{ri}, σ_{wc} is lower according to figure 2.2. So if, under the assumption that the solids are incompressible, is concluded that complete saturation is achieved according to equation (2.4) then complete saturation will certainly be achieved if the solids are compressible. So the calculated value for S_{ri} under the assumption of incompressible solids is the lower bound value.

Chapter 2 shows the usefulness of back–pressure application to improve saturation. The back–pressure consists of a controlled increase in cell pressure accompanied by a controlled increase in pore pressure. The total back–pressure, 300 kPa, is applied in steps of 100 kPa each. After each loading step a resting period of half an hour is considered. Before each step the B-factor is determined by application of a 5 kPa increase in cell pressure. The undrained pore pressure response divided by the cell pressure increase gives the B-factor.

Table 6.5: Comparison between calculated and measured B–factor

Symbol	unity	1853b ver	3963a ver	24418b hor	24418c hor
S_{ri}	[-]	0.92 ± 0.03	0.95 ± 0.02	0.94 ± 0.003	0.97 ± 0.003
β_{fgi}	[m^2/N]	9.49 $\times 10^{-7}$	6.8 $\times 10^{-7}$	8.14 $\times 10^{-7}$	5.24 $\times 10^{-7}$
β_i	[m^2/N]	1.2 $\times$ 10^{-5}	1.2 $\times$ 10^{-5}	1.2 $\times$ 10^{-5}	1.2 $\times$ 10^{-5}
B_i calculated eq. (2.3)	[-]	0.93	0.95	0.94	0.96
B_i measured	[-]	0.72	0.92	0.62	0.90
σ_{wc}	[kPa]	407	263	336	176
S_r calculated	[-]	0.99	1	0.99	1
B_{final} measured	[-]	0.99	0.99	0.95	0.99

ver = vertically retrieved sample
hor = horizontally retrieved sample

Each sample is consolidated at 10 kPa before the back–pressure is applied. In this way some effective stress is assured preventing premature failure. From this initial consolidation phase the bulk modulus, K can be estimated. For four tests β_{fgi} and σ_{wc} are derived using equation (2.4). The initial bulk modulus is on average 83 kPa, leading to $\beta_i = 1/K = 1.2 \times 10^{-5}$ m^2/N. Table 6.5 presents the results and the initial B–factor following from calculations and measurements. The values for S_{ri} and β_{fgi} are calculated for the standard values for ω, p_0, W_{vp}, σ/r_i, v and β_f used for figure 2.2.

The lower part of table 6.5 gives S_r and B after application of the back-pressure. It shows that not in each test the applied back–pressure exceeds σ_{wc}. However after application of the back–

pressure the calculated S_r equals 0.99 or larger. It can be concluded that for each of the four tests full saturation is achieved. The upper part of table 6.5 shows S_r and B for the initial conditions. For two tests, 3963a and 24418c, the measured values for B correspond well to the calculated values. However for tests 1853b and 24418b the measured B–factors for initial conditions differ from the calculated values. The exact cause for this difference is unclear possibly a local air bubble in close vicinity of the pore pressure transducer influences the measurements. After application of the back–pressure a good agreement is found between measured and calculated B–factor.

Figure 2.4 and table 2.1 indicate that for fully saturated samples including compressible solids the corresponding B–factor exceeds unity. This is not found for the four tests presented by table 6.5. Table 6.6 presents the results of 18 tests. Three of these tests show a B–factor slightly exceeding 1.0. This small deviation falls within the measurement accuracy and can be neglected. So it is concluded that compressibility of the solids, if present, does not influence pore pressure measurements.

6.6 Undrained Young's moduli and Effective Stress Paths

6.6.1 Anisotropy after an isotropic pre–consolidation

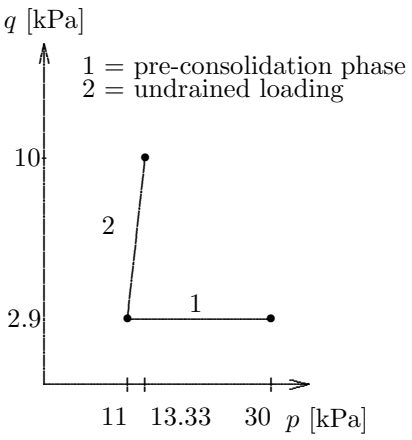

Figure 6.11: Applied loading path

Section 4.3.1 shows that the angle of an undrained effective stress path depends on the level of anisotropy for elastic material behaviour. This section presents measurements of small undrained effective stress paths (ESP). The aim of the tests is to check whether the angle of undrained ESP can be used to identify and quantify the anisotropy of peat. For this purpose horizontally and vertically retrieved samples are tested. To study the influence of pre-consolidation the loading is applied after isotropic and deviatoric pre-loading. The results of these tests also give the option to derive the undrained axial stiffness, E_v^u respectively E_h^u.

Table 6.7 presents a summary of the measurements. The samples are indicated by the number of their sampling tube followed by an a, b or c for the first, second and third sample taken from this tube. For some samples loading and unloading is repeated. This is indicated by a 1, 2 or 3 for the first, second and third loading - unloading cycle.

All samples are consolidated at a cell pressure of 10 kPa. To assure a good connection between the top cap and the sample a minimum deviator load of 5 N, 2.9 kPa, is maintained. A good connection between the top cap and sample is needed for a correct axial strain measurement. The initial isotropic pre–consolidation stress is approximately 11 kPa. Since the vertical effective stress in the field is approximately 10 kPa, this stress level is referred to as initial conditions. Section 6.2.3 discusses the axial pre-consolidation stress found in the oedometer tests. The value for σ'_{ac} for horizontal as well as vertically retrieved samples deviates from 12 to 22 kPa, which indicates that the initial OCR ranges from 1.1 to 2.0. Table 6.7 gives the ratio of p'_c/p', in which p'_c is the maximum isotropic stress at which the sample is pre–loaded and p' the effective isotropic stress at the start of the test. The lower part of table 6.7 shows the results for samples which are not pre–loaded. It should be noted that for the non pre–loaded samples some pre–consolidation is to be expected. For the non pre–loaded samples p_c relates to σ'_{ac}. Since σ'_{ac} shows a large scatter and is not measured for the individual samples no specific value is given.

The samples are loaded undrained vertically to 10 kPa (34N) under a constant cell pressure, followed by an unloading to 2.9 kPa. This loading–unloading cycle is repeated twice and for some samples three times. Figure 6.11 sketches the applied loading path. Each undrained loading probe

Table 6.6: Descriptive parameters for the conducted triaxial tests

parameter	unity	test number						
		1853a	1136c	4588a	24076	24482a	24482b	24439b
		ver	hor	ver	hor	hor	hor	hor
W_i^a	[-]	4.34 ± 0.008	6.25 ± 0.013	5.53 ± 0.006	5.54 ± 0.013	5.48 ± 0.013	6.23 ± 0.02	5.61 ± 0.012
ρ_i	[t/m^3]	1.06 ± 0.02	1.02 ± 0.02	1.03 ± 0.02	1.04 ± 0.02	1.02 ± 0.02	0.99 ± 0.02	1.02 ± 0.008
ρ_s^b	[t/m^3]	1.74 ± 0.009	1.66 ± 0.005	1.65 ± 0.003	1.64 ± 0.004	1.61 ± 0.005	1.61 ± 0.0015	1.60 ± 0.0008
e_i^c	[-]	7.7 ± 0.04	10.9 ± 0.04	9.4 ± 0.04	9.3 ± 0.04	9.3 ± 0.04	10.7 ± 0.04	9.4 ± 0.02
n_i^c	[-]	0.89 ± 0.003	0.92 ± 0.002	0.90 ± 0.002	0.90 ± 0.003	0.90 ± 0.003	0.91 ± 0.002	0.90 ± 0.001
S_{ri}^c	[-]	0.97 ± 0.01	0.96 ± 0.008	0.97 ± 0.007	0.97 ± 0.009	0.95 ± 0.009	0.93 ± 0.007	0.96 ± 0.004
B_i	[-]	0.89	0.93	0.88	0.96	0.91	0.62	0.07
B_{final}	[-]		0.99	1.03	1.00	1.00	1.01	0.79
		4590a	1853b	3963a	24418b	24418c	3963b	24482c
		ver	ver	ver	hor	hor	ver	hor
W_i^a	[-]	5.27 ± 0.005	5.56 ± 0.006	5.05 ± 0.015	4.9 ± 0.2	5.35 ± 0.02	5.6 ± 0.3	6.06 ± 0.007
ρ_i	[t/m^3]	1.01 ± 0.02	0.99 ± 0.02	1.04 ± 0.02	1.01 ± 0.002	1.03 ± 0.002	1.03 ± 0.002	1.06 ± 0.001
ρ_s^b	[t/m^3]	1.67 ± 0.004	1.67 ± 0.001	1.81 ± 0.005	1.70 ± 0.0004	1.64 ± 0.0009	1.69 ± 0.004	1.69 ± 0.004
e_i^c	[-]	9.3 ± 0.04	10.1 ± 0.3	9.6 ± 0.012	9.0 ± 0.03	9.0 ± 0.007	9.2 ± 0.01	10.28 ± 0.006
n_i^c	[-]	0.90 ± 0.002	0.91 ± 0.002	0.906 ± 0.0008	0.906 ± 0.0004	0.900 ± 0.0005	0.902 ± 0.0009	0.911 ± 0.0004
S_{ri}^c	[-]	0.94 ± 0.007	0.92 ± 0.03	0.96 ± 0.007	0.94 ± 0.003	0.97 ± 0.005	0.96 ± 0.009	1.00 ± 0.004
B_i	[-]	0.74	0.72	0.92	0.62	0.90	0.63	0.79
B_{final}	[-]	0.99	0.99	0.99	0.95	0.99	0.98	0.97
		1316a	2590a	2590b	22726a			
		ver	ver	ver	hor			
W_i^a	[-]	5.37 ± 0.007	4.06 ± 0.01	4.60 ± 0.002	4.56 ±0.008			
ρ_i	[t/m^3]	1.06 ± 0.001	1.09 ± 0.001	1.08 ± 0.001	1.05 ± 0.001			
ρ_s^b	[t/m^3]	1.64 ± 0.005	1.76 ± 0.004	1.61 ± 0.004	1.66 ± 0.003			
e_i^c	[-]	8.90 ± 0.007	7.19 ± 0.008	8.31 ± 0.01	7.81 ± 0.007			
n_i^c	[-]	0.899 ± 0.0005	0.878 ± 0.0006	0.893 ± 0.0009	0.886 ± 0.0006			
S_{ri}^c	[-]	0.99 ± 0.005	0.99 ± 0.006	1.0 ± 0.01	0.97 ± 0.004			
B_i	[-]	0.87	0.90	0.95	0.63			
B_{final}	[-]	0.98	0.98	1.04	0.98			

[a] = derived from remaining parts

[b] = measured after finalising the test

[c] = calculated by equation (6.6) under the assumption of incompressible solids

ver = vertically retrieved sample

hor = horizontally retrieved sample

allows for the determination of the undrained axial stiffness and angle of effective stress path. Using the least squares method a line is fitted through the measured q–ε_a points. The reciprocal value of the slope of the fitted line gives the E_a^u values presented in table 6.7. The least squares method is also used to find the angle of the ESP, indicated by $\Delta p'/\Delta q$. For $\Delta p'/\Delta q \approx 0$ a vertical ESP is found corresponding to $K'/J' \approx 0$. It should be noted that $\Delta p'/\Delta q < 0$ corresponds to $K'/J' > 0$ and vice versa.

Table 6.7 shows the test results in eight categories divided into vertically and horizontally retrieved samples, loading and unloading conditions and isotropically pre–loaded in triaxial device and non pre–loaded in triaxial device. Despite the over–consolidation for repeating load cycles a difference in axial stiffness is found. This might indicate some plastic behaviour. The results from test 1316a-1 and 1316a-2 strongly deviate from the other results. Table 6.7 gives the mean value, μ and standard deviation, σ, without test 1316 between brackets. When disregarding the results test 1316 for each category the average axial stiffness for vertically retrieved samples are of the same order in magnitude as found for the horizontally retrieved samples.

Except from tests 4588a-1, 1316a-1 and 1316a-2 all individual tests show that the unloading stiffness exceeds the loading stiffness. The difference in loading–unloading stiffness is more significant than the difference in axial stiffness between horizontally and vertically retrieved samples. For seven of the categories presented in table 6.7 the standard deviation for $\Delta p'/\Delta q$ exceeds the mean value. It can be concluded that the anisotropy of the tested peat is insignificant except for some individual tests like 1316a-1, 1316a-2, 2590a-1 and 24439a-1. This corresponds to the results of the $K_0 - CRS$ tests and the Simple Shear tests presented in the previous sections. For all these tests heterogeneity between the individual samples seems to be more important than differences between the horizontal and vertically retrieved samples.

Although table 6.7 shows that the tested peat samples do not show a significant anisotropic behaviour the difference between loading and unloading results can be explained by a small difference in loading and unloading stiffness. Before analysing the test results in detail it should be noted that stiffness parameters presented in table 6.7 are undrained parameters, while deviations in the reported ESP's are explained by drained elastic properties. Furthermore it should be noted, with $K'/J' = -\Delta p'/\Delta q$, that equation (4.45) relates the angle of the ESP to four drained parameters. Although K'/J' can be used to give an indication for the level of anisotropy, individual values for stiffness parameters can not be found. To relate changes in K'/J' for different test conditions to changes in E_h/E_v information on ν_{vh} and ν_{hh} is needed. Axial and volumetric strain measurements indicate that radial strain remains small, $e \approx \varepsilon_{zz}$. Small radial strain under an axial load suggests small values for ν_{hh} and ν_{vh}. For small values for ν_{vh} and ν_{hh} equation (4.45) transfers into direct relation between K'/J' and E_h/E_v. Assuming that, equivalent to the undrained stiffness parameters, the drained unloading stiffness parameter exceeds the drained stiffness parameter and that ν_{vh} and ν_{hh} are small the test results show the following:

For the vertically retrieved samples, with exception of test 1316a1, 1316a-2, 1853a-3 and 4588a-3 the $\Delta p'/\Delta q$–value for loading is smaller than for unloading conditions. This indicates a steeper slope in ESP for loading than for unloading conditions, as can be explained by equation 4.45. If the tested peat is cross–anisotropic and the axis of symmetry in the field is vertical the radial stiffness for the vertically retrieved samples corresponds to the axial stiffness of the horizontally retrieved samples. The radial stiffness of the horizontally retrieved samples corresponds to some combination of the axial stiffness of the horizontal and vertically retrieved samples. When a sample is loaded undrained in axial direction then, due to the pore pressure reaction, follows unloading in radial direction. Table 6.7 shows that the undrained axial loading stiffness for vertically retrieved samples is of the order in magnitude as the undrained unloading stiffness for the horizontally retrieved samples. Under the before mentioned assumptions this explains that $\Delta p'/\Delta q \approx 0$. For unloading the vertically retrieved samples the relatively large unloading stiffness in axial direction is combined to the relatively small loading stiffness found for the horizontally retrieved samples. This leads to the a small pore pressure reaction, $(\Delta p'/\Delta q)_{unl.} > (\Delta p'/\Delta q)_{loading}$ and $(K'/J')_{unl.} < (K'/J')_{loading}$. For the horizontally retrieved samples an equivalent reasoning can be followed.

Table 6.7: Axial stiffness and $\Delta p'/\Delta q$–values for vertically and horizontally retrieved samples, μ = mean value, σ = standard deviation

vertically retrieved samples							horizontally retrieved samples						
test	loading			unloading			test	loading			unloading		
nr	E_a^u [kPa]	$\Delta p'/\Delta q$ [-]	p'_c/p' [-]	E_a^u [kPa]	$\Delta p'/\Delta q$ [-]	p'_c/p' [-]	nr	E_a^u [kPa]	$\Delta p'/\Delta q$ [-]	p'_c/p' [-]	E_a^u [kPa]	$\Delta p'/\Delta q$ [-]	p'_c/p' [-]
4590-1	1791	-0.013	2.36	2190	0.007	2.32	24076-1	1202	-0.037	2.65	2035	-0.018	2.22
1316a-1	3419	-0.22	2.88	3612	-0.25	3.13	24076-2	1714	-0.0005	2.75	1798	-0.002	2.28
1316a-2	3504	-0.26	2.66	3470	-0.26	3.13	24076-3	1607	-0.007	2.92	1875	0.09	2.34
1853a-1	1722	0.038	2.67	2086	0.057	2.23	24439a-3	1785	-0.037	2.33	2113	-0.041	2.33
1853a-2	2123	0.040	2.65	2338	0.059	2.20							
1853a-3	1385	0.033	2.73	1691	-0.002	1.91							
4588a-1	1618	-0.065	2.19	1293	-0.014	1.76							
4588a-2	1568	-0.071	2.23	1867	-0.046	1.84							
4588a-3	1799	-0.049	2.22	2136	-0.054	1.85							
μ	2103	-0.063	2.51	2298	-0.056	2.26		1577	-0.020	2.66	1955	0.0073	2.29
	(1715)[1]	(-0.012)[1]		(1943)[1]	(0.001)[1]								
σ	796	0.11		770	0.12			261	0.019		144	0.057	
	(231)[1]	(0.05)[1]		(357)[1]	(0.044)[1]								
4590a-1	1224	0.011	-	1992	0.089	-	24439a-1	1030	0.13	-	1319	0.10	-
2590a-1	680	-0.151	-	893	-0.026	-	24482a-1	761	-0.021	-	853	0.053	-
2590a-2	792	-0.041	-	832	-0.009	-	24482b-1	743	-0.091	-	1124	0.042	-
2590b-1	1084	-0.090	-	1478	-0.010	-	24482c-1	834	-0.080	-	1109	0.041	-
2590b-2	1334	-0.016	-	1469	-0.0017	-	22726a-1	991	-0.049	-	1565	0.044	-
							22726a-2	1352	0.007	-	1591	0.031	-
μ	1023	-0.057		1333	0.0085			952	-0.017		1260	0.052	
	(1109)[2]	(-0.034)[2]											
σ	279	0.064		479	0.046			229	0.080		287	0.025	
	(235)[2]	(0.042)[2]											

[1] = without tests 1316a-1 and 1316a-2

[2] without test 2590a-1

Table 6.8: Results on isotropically pre-consolidated samples

		loading			unloading		
axial	test	E_a^u	$\Delta p'/\Delta q$	p'_0/p'	E_a^u	$\Delta p'/\Delta q$	p'_0/p'
direction	nr.	[kPa]	[-]	[-]	[kPa]	[-]	[-]
ver	4590a-1	1224	0.011	-	1992	0.089	-
	4590a-2	1983	-0.005	1.74	2809	0.091	1.71
	4590a-3	1791	-0.013	2.36	2190	0.007	2.32
hor	24439a-1	1030	0.13	-	1319	0.10	-
	24439a-2	1516	-0.032	1.64	1879	-0.031	1.64
	24439a-3	1785	-0.037	2.32	2113	-0.041	2.51
	24482b-1	743	-0.09	-	1124	0.04	-
	24482b-2	2952	-0.011	1.73	2432	0.03	1.73

For a further investigation of the load history on the anisotropy of peat 3 samples are pre–consolidated at different isotropic stress levels. The axial stiffness and $\Delta p'/\Delta q$ value is measured at $p' = 11$ kPa. First without pre–consolidation, next after isotropic pre–consolidation at $p = 20$ kPa and finally after a pre–consolidation at $p = 30$ kPa. Table 6.8 shows the results.

Table 6.8 shows a small change in $\Delta p'/\Delta q$ for each level of over–consolidation for loading and unloading conditions, with exception of 4590a-1 to 4590a-2 during unloading. This holds for the vertically retrieved samples as well as for the horizontally retrieved samples. The angle of ESP remains small.

6.6.2 Anisotropy after an anisotropic pre–consolidation

To study the influence of load history some samples are consolidated at an anisotropic stress condition, $\sigma_{hc} = 10$ kPa and $\sigma_{vc} = 65$ kPa. After reconsolidation at the same stress conditions as for the tests presented in table 6.7 the samples are loaded undrained by a small axial load to measure the undrained axial stiffness and the undrained effective stress path. Table 6.9 shows the results.

Table 6.9: E_a^u and $\Delta p'/\Delta q$ value after pre-loading up to $q = 55$ kPa

		loading			unloading		
axial	test	E_a^u	$\Delta p'/\Delta q$	σ'_{vc}/σ'_v	E_a^u	$\Delta p'/\Delta q$	σ'_{vc}/σ'_v
direction	nr	[kPa]	[-]	[-]	[kPa]	[-]	[-]
ver.	3963b-1	646	-0.46	6.3	1433	-0.29	3.7
	3963b-2	1653	-0.34	5.1	1900	-0.26	3.7
	1316a-3	2895	-0.36	4.5	3138	-0.34	3.1
	1316a-4	3255	-0.37	4.2	3081	-0.33	2.9
hor.	24482c-1	1771	-0.19	5.7	-	-	-
	22726a-6	1965	-0.25	4.9	2526	-0.35	3.8
	22726a-7	2189	-0.36	4.6	2904	-0.19	3.1

Comparison with table 6.7 shows a remarkable change in $\Delta p'/\Delta q$ value. Due to malfunctioning of the triaxial device an unloading phase could not be conducted for test 24482c-1. Despite the relatively large pre-loading the difference between loading and unloading stiffness is still considerable. The $\Delta p'/\Delta q$ value is decreased indicating a clear change in anisotropy. For the vertically retrieved samples the $\Delta p'/\Delta q$ value for loading is still larger than for unloading which can be explained by a difference in loading and unloading stiffness.

In test 22726a three levels of axial pre-loading are applied to this, horizontally retrieved, sample. Figure 6.12 sketches the loading path. After consolidation at a cell pressure of 11 kPa, the sample

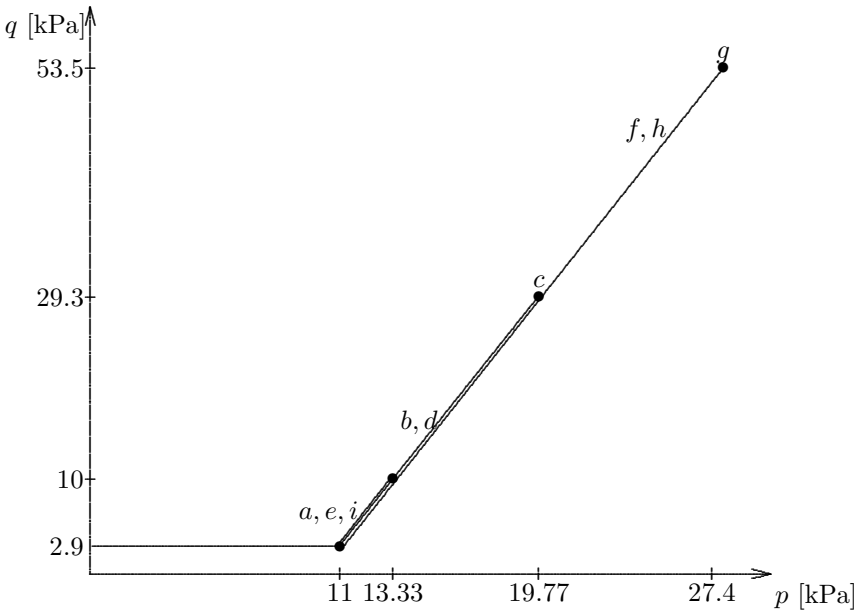

Figure 6.12: Loading path applied in test 22726a, horizontally retrieved sample

is tested at initial conditions, indicated by a in figure 6.12. After consolidation at anisotropic stress conditions indicated by b, c and d small load cycles are applied in phase e. Finally a large anisotropic pre–consolidation is applied, indicated by f, g and h and small loading cycles are applied again in phase i. Figure 6.13 gives the stress strain curve and the effective stress paths for test phases a, e and i. It should be noted that phase a consists of two undrained loading–unloading cycles without consolidation in between. Phase e consists of three loading–unloading cycles with a consolidation or swelling in between. The horizontal parts in the ESP and $q - \varepsilon_a$ shown in figure 6.13 represent the consolidation / swelling phase. Phase i consists of two undrained loading-unloading phases. The first without consolidation / swelling phase, the second includes a consolidation / swelling phase. Table 6.10 gives the results.

Table 6.10: Relation between anisotropy and loading history for test 22726a, horizontally retrieved sample

		loading			unloading		
phase	test number	σ'_{ac}/σ'_a [-]	E_h^u [kPa]	$\Delta p'/\Delta q$ [-]	σ'_{ac}/σ'_a [-]	E_h^u [kPa]	$\Delta p'/\Delta q$ [-]
a	22726a-1	1.6	991	-0.05	1.2	1565	-0.04
	22726a-2	1.7	1352	0.007	1.1	1591	0.031
	22726a-3	3.0	1873	-0.14	2.0	2073	-0.08
e	22726a-4	2.9	2234	-0.12	1.9	2602	-0.09
	22726a-5	2.8	2864	-0.10	1.9	2929	-0.10
i	22726a-6	4.9	1965	-0.25	3.8	2526	-0.35
	22726a-7	4.6	2189	-0.36	3.1	2904	-0.19

Table 6.10 clearly shows the decrease in $\Delta p'/\Delta q$ value for increasing σ'_{ac}/σ'_a. The two axial drained pre–loading cycles give the opportunity to determine the drained axial stiffness. The slope of the $q - \varepsilon_a$ diagram given in figure 6.13 gives for the unloading part of the first cycle $E_a = 1080$ kPa. The unloading part of the second cycle give $E_a = 1000$ kPa for the overall slope and $E_a = 1300$ kPa when fitting the middle part. It is remarkable that the axial stiffness shows a negligible

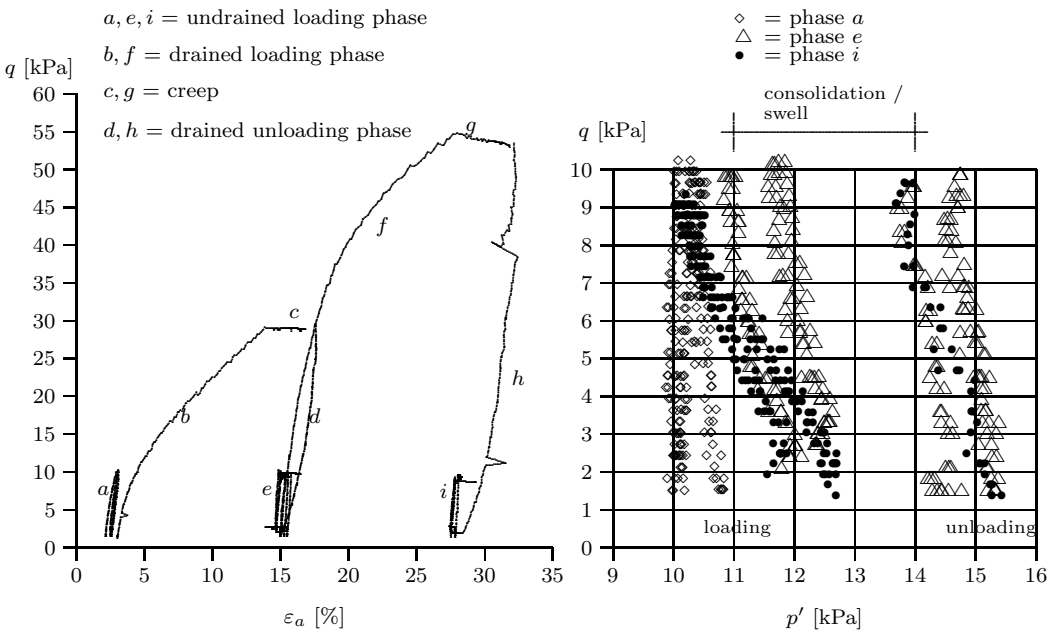

Figure 6.13: Stress–strain curve for test 22726a

increase despite considerable axial strain.

6.6.3 Conclusions

Table 6.7 shows that the tested peat initially does not behave anisotropically. This is shown by the small difference in axial undrained stiffness for horizontally and vertically retrieved samples and in the low value for $\Delta p'/\Delta q$. The results correspond to the results for the $K_0 - CRS$ tests and the Simple Shear tests. These tests show only minor differences between the horizontally and vertically retrieved samples.

Axial pre–loading causes tilting of the undrained ESP for loading and unloading in the elastic region; $\Delta p'/\Delta q$ decreases as shown by table 6.9 and 6.10. This indicates an increase in level of anisotropy. Assuming small values for ν_{hh} and ν_{vh} it can be concluded that the ratio E_r/E_a increases. This is remarkable since for a large axial pre–loading an increase in E_a and therefore a reduction in E_r/E_a is to be expected.

Axial pre–loading causes an equivalent increase in level of anisotropy for the vertically as well as for the horizontally retrieved samples. If there is initially a dominant fibre direction its influence seems small.

The test results can be explained by a pre–stressing effect of the fibres. The samples are retrieved at shallow depth underneath a horizontal surface. Initially the fibres are not pre–stressed. The samples show only a mild anisotropy. The mild anisotropy can be explained by a small difference for loading and unloading stiffness. Due to the axial pre–consolidation fibres are stretched and entangle into each other. After unloading the fibres remain entangled. When the sample is loaded undrained in axial direction due to pore pressure generation the sample is unloaded in radial direction. The entangled, pre–stressed, fibres will hardly show radial deformation leading to an increase in radial stiffness.

Concerning the pre–stressing of the fibres anisotropy (measurements on $\Delta p'/\Delta q$) is strongly influenced by the load history. It is therefore concluded that the presence of fibres in itself is not enough to explain the anisotropy of peat. Only when the fibres are pre–stressed the sample shows anisotropic behaviour. Therefore, it is to be expected that anisotropy of peat samples strongly

depends on the location at which they are retrieved. It might differ at short distances. For example, samples from underneath an embankment will show a larger degree of anisotropy than the samples retrieved from the toe of the embankment.

Since the load history plays an important role in the actual anisotropy of the tested peat samples sample disturbance becomes an important item. When during sample retrieval an axial force is applied to the samples, e.g. due to friction along the tube and the sample consolidates under this axial force the sample might show an increase in anisotropy.

The test results presented in this section show a large scatter, even for samples that come from the same sampling tube. It can be concluded that heterogeneity is an important aspect of peat behaviour.

6.7 The Mandel–Cryer effect

6.7.1 Measurements and analysis

Section 6.6 discusses the results of undrained loading and unloading tests. After some of the undrained loading or unloading phases a consolidation respectively swelling phase is included. Figure 6.14 depicts the pore pressure development during a consolidation and a swelling phase for test 1853a. The pore pressure developments shown by figure 6.14 are typical for the consolidation and swelling phases applied after undrained loading or unloading phases presented in table 6.7. The pore pressure development measured at the middle of the sample by the needle corresponds well to the pore pressure development found by the external transducer. The first measurement for each of the pore pressure developments shown by figure 6.14 corresponds to the condition before opening the drainage valve. Since $t = 0$ is not shown on a logarithmic scale the initial value, measured at $t = 0^-$ is shown at $t = 0.1$ s.

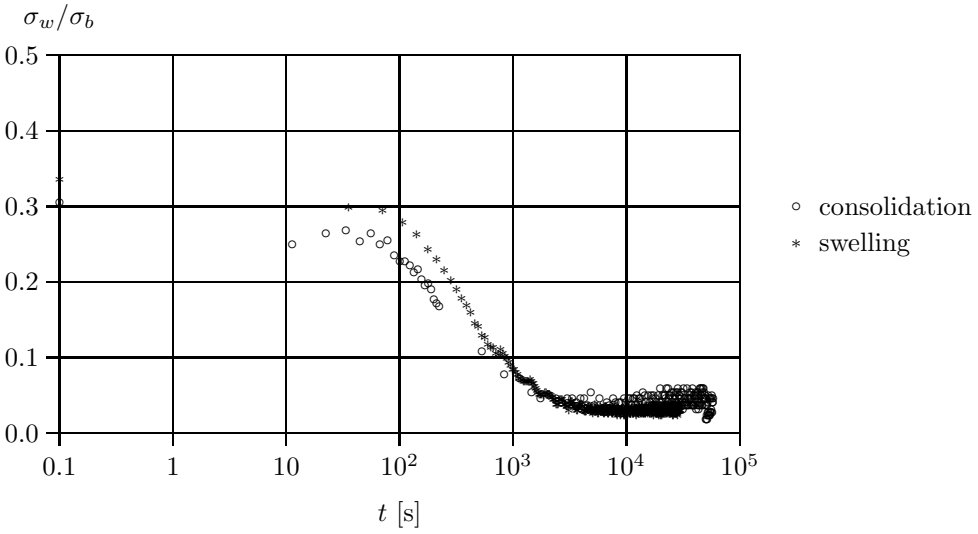

Figure 6.14: Typical pore pressure development at the middle of the sample

Figure 6.14 shows an initial $\sigma_w/\sigma_b = 0.3$ to 0.33. This corresponds to equation (4.41) for isotropic conditions, $K'/J' = 0$. Note that sign convention according to section 2.1 is used. The measurement of initial pore pressure also corresponds to results presented in table 6.7. Since for this test is found $\Delta p'/\Delta q \approx 0$. After opening the valves the pore pressure drops to $\sigma_w/\sigma_b \approx 0.25$ to 0.3. This drop in pore pressure is followed by a small pore pressure peak. The pore pressure development presented by figure 6.14 is typical for most measurements. A clear Mandel–Cryer effect as predicted by the analytical formulae is not found.

Section 6.6 shows that axial pre–loading causes tilting of the undrained ESP, which can be explained by an increase in K'/J'. Chapter 5 shows that for an increase in K'/J' a larger Mandel–Cyer effect is to be expected. The consolidation or swelling phases for axially pre–consolidated samples do not show a clear Mandel–Cryer effect. An exception is found for test 24482c.

Sample 24482c is one of the samples that are axially pre–consolidated. With $\Delta q = 55$ kPa the applied unloading is considerably larger than for the small regular loading phases discussed in section 6.6. Figure 6.15 presents the pore pressure development during this swelling phase. A small initial peak can be distinguished from the measurements using the needle. The external transducer indicates a monotonic pore pressure decay.

One of the reasons that might explain the absence of a clear Mandel–Cryer effect is found in the equipment used for the tests. Due to large deformations the cell pressure could be not kept constant in some of the tests leading to a reduction in applied loading. The same holds for the level of back–pressure. Due to the large amount of expelled pore water the stress level in the back–pressure piston rises leading to an initial increase in pore pressure in de drainage system. Although the increase in drain pressure is temporarily the test conditions no longer correspond to the boundary conditions for which the analytical solutions are derived. Especially during consolidation or swelling of isotropic loading phases the pore pressure development is influenced by the testing equipment. These phenomena were not found in each test. The measurements shown by figure 6.14 and 6.15 are found for a constant cell pressure and back–pressure.

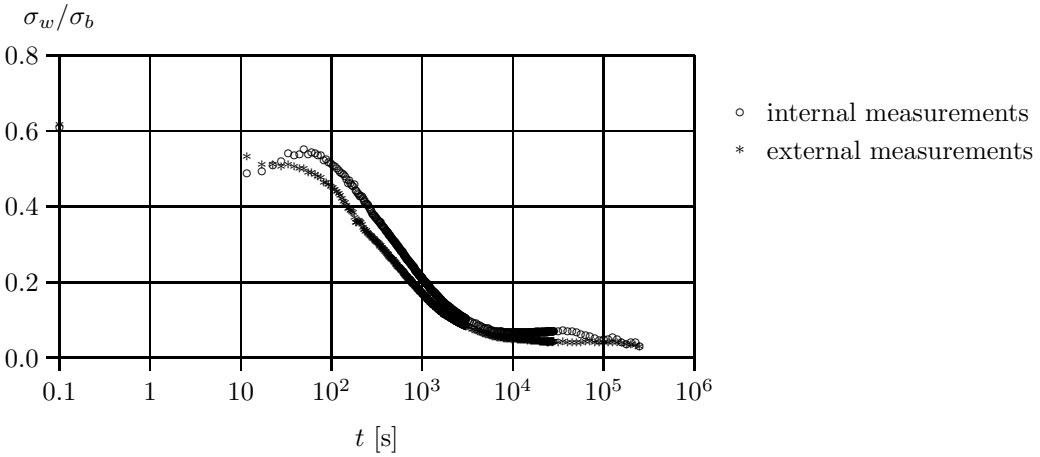

Figure 6.15: Swelling of test 24482c

Section 5.5 shows the pore pressure development for a transient drain pressure. The extent to which the peak value is still visible depends on the drain pressure decay. Section 5.5 expresses the drain pressure decay by an exponential function; $\sigma_w = \sigma_{w0} exp(-\kappa t)$. Using the measurements presented in figure 6.14 a value for κ and the permeability k can be fitted.

In section 6.6 it is concluded that the sample 1853a does not behave anisotropic. This corresponds to an initial pore pressure approximately $\sigma_w/\sigma_b = 1/3$ given in figure 6.14. The measurements can be compared to the analytical solution for isotropic conditions. The analytical solution shows that the Mandel–Cryer effect found for isotropic conditions strongly depends on the value for the Poisson's ratio. Equating the volume of expelled pore water to the total volume deformation, the average radial strain can be derived from measurements by $\varepsilon_r = 0.5 \times (e - \varepsilon_a)$. Section 3.1 shows $\nu =$ - $\varepsilon_r/\varepsilon_a$. Initially the sample behaves undrained leading to $\nu = 0.5$. When consolidation develops the ν value reaches its drained value. For the tests presented in figure 6.14 a value for ν varying from 0.10 to 0.15 is found. Figure 6.16 shows the results of the fit for isotropic material behaviour, $E = 1000$ kPa and $\nu = 0.15$.

The measurements presented by figure 6.15 can not easily be fitted. After opening the drainage

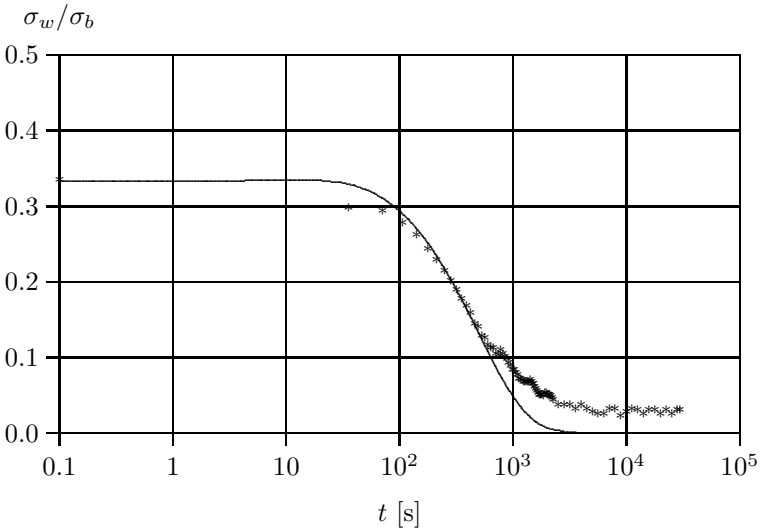

Figure 6.16: Fit for swelling phase 1853a

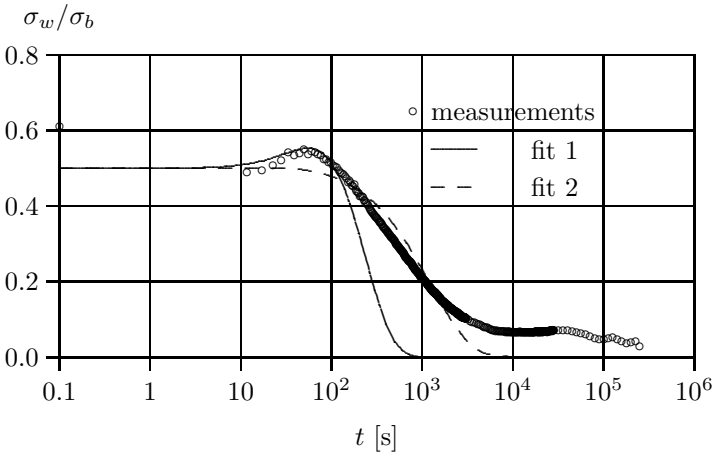

		fit 1	fit 2
E_v	[kN/m^2]	1300	800
E_h	[kN/m^2]	2210	1360
ν_{hh}	[-]	0.15	0.15
ν_{vh}	[-]	0.15	0.15
k	[m/s]	1.5×10^{-8}	1×10^{-7}
κ	[m/s]	0.01	0.0008

Figure 6.17: Fit for swelling after $\Delta q = 55$ kPa

valves the pore pressure drops from 0.61 $\times\sigma_b$ to approximately 0.53 $\times\sigma_b$ for the external transducer to 0.49 $\times\sigma_b$ for the internal measurements. Figure 6.17 shows two attempts to fit the measurement data. The first fit focuses on the peak value, which can be fitted for relatively large stiffness parameters. The second attempt focuses on the tail of the pore pressure development. The tail of the pore pressure development can be reproduced for relatively low stiffness parameters. For both cases a drain resistance is applied. The fit that predicts the peak correctly gives a too steep slope for the tail of the pore pressure development. While fits representing the tail do not correctly predict the peak value.

Gibson, Gobert & Schiffman [33] show the influence of a variable permeability. Using equation (6.7) they present the pore pressure development for spherical conditions for a material with $\chi = 4.11$. Their solution clearly shows that due to a variable permeability the initial peak is reduced while the tail of the pore pressure development is elongated. These observations correspond to the presented measurements.

6.7.2 Influence of drain resistance

To get a better understanding of a possible explanation for the difference between measurements and analytical analyses the influence of drain resistance to the consolidation of a conventional sample is further elaborated. In section 5.5 the solution for consolidation of a triaxial sample is

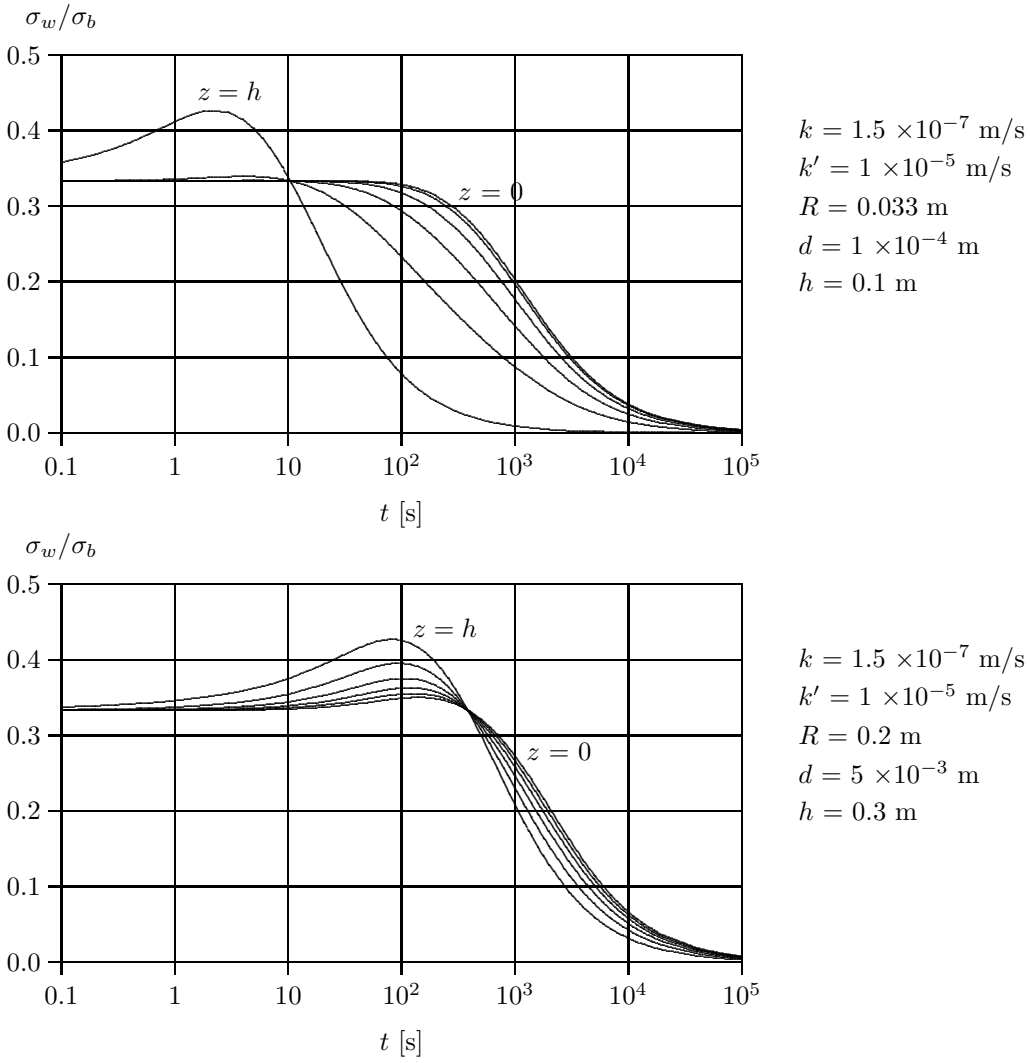

Figure 6.18: An approximation for pore pressure development at $r = 0$ including drain resistance

elaborated for a prescribed drain pressure. An improved insight on the interaction between the consolidation of the sample and drain resistance can be found when incorporating the storage conditions of the drain to the consolidation problem. With k' representing the drain resistance and d the drain thickness, the drain pressure, p_d, is given by:

$$\frac{d^2 p_d}{dz^2} = \frac{q_0 \gamma_w}{k' d}, \qquad q_0 = -\frac{k}{\gamma_w} \frac{\partial \sigma_w}{\partial r} \tag{6.12}$$

Together with boundary conditions $p_d = 0$ at $z = h$ and $\mathrm{d}p_d/\mathrm{d}z = 0$ at $z = 0$, an expression for boundary condition g_1 in appendix G is represented by p_d. Equation 6.12 represents a second order differential equation in z. Elaboration of the three dimensional consolidation problem with $g_1 =$

p_d using the Laplace transformation technique leads to an expression in transformed conditions for which the inverse transform can not be found.

Figure 6.18 shows the solution found by an approximation technique known as Direct Method. Barends [8] shows that the direct method gives the exact value at about $t = 0.5\ T$, with T the hydrodynamic period. For $t < T$ the direct method underestimates the pore pressure development and for $t > T$ the direct method over estimates the pore pressure development. Therefore this approximation will not correctly predict the Mandel–Cryer effect and can not be used to reproduce measurements. However the approximation can be used to visualise the effect of drain resistance.

Figure 6.18 shows pore pressure development for a conventional triaxial sample, $R = 0.033$ m and $h = 0.10$ m and for $R = 0.2$ m and $h = 0.3$ m. The pore pressure development is given at different levels of z. It should be noted that the pore water dissipates only in radial direction. Since at each level a different drain pressure is prescribed at $r = R$ a different pore pressure development is found at different levels of z. So the analytical solution predicts a pore pressure gradient in vertical direction. At the top of the sample $p_d = 0$ at all stages and therefore at the top of the sample the pore pressure development corresponds to the original solution presented by figure 5.3. At lower levels no Mandel–Cryer peak can be distinguished for a conventional triaxial sample size. The pore pressure development is dominated by the drain resistance. For large sample sizes in combination to a thicker drain with the same drain resistance a clear Mandel–Cryer peak is found at each level.

Figure 6.18 shows that the influence of drain resistance on the pore pressure development reduces for larger sample sizes. So in relation to drain resistance it can be concluded that the Mandel–Cryer effect is more easily aroused in large samples than in conventional triaxial tests. The next chapter discusses results of a large scale test.

6.7.3 Conclusions

Only a weak Mandel–Cryer effect is found. This is partly due to mechanical problems of the test equipment. In some tests the pistons were not able to control the cell pressure respectively the back–pressure with required accuracy. For the tests in which the cell pressure and back–pressure is controlled perfectly only a weak Mandel–Cryer effect is found. The pore pressure development including the weak Mandel–Cryer effect is hard to reproduce by the analytical solutions derived in section 5.

There are two phenomena that might explain the absence of a clear Mandel–Cryer effect in the pore pressure measurements: a variable permeability and a non constant drain pressure. Section 6.7.2 shows that size effects play a role regarding the disturbance of drain resistance. For larger samples the influence of drain resistance is small and vice versa.

Chapter 7

Large scale triaxial test

7.1 Large Scale testing

Chapter 6 discusses laboratory tests on conventional soil samples. It is concluded that for the tested samples only a minor Mandel–Cryer effect could be found. This is explained by the variable permeability of peat in combination to drain resistance. Section 6.7 shows that the influence of drain resistance on the pore pressure development depends on the consolidation characteristics of the sample. A relatively small sample, with a short drainage path leads to a relatively short consolidation period. For small samples drainage resistance influences the pore pressure development strongly. Larger samples involve a longer consolidation period, reducing the influence of drain resistance as shown by figure 6.18.

To test this conclusion a large scale triaxial test is conducted on a sample with a diameter equal to 0.4 m and height of 0.6 m. Chapter 6 shows the influence of pre–loading on anisotropy of peat, which can be explained by pre–stressing of the fibres. Since some of the fibre dimensions can be considered large, compared to conventional sample dimensions, using large scale tests the influence of size effects can be estimated.

The aim of the large scale triaxial test is therefore twofold. First, to see if the Mandel–Cryer effect can be measured when drainage length is increased. Second, to see if the conclusions drawn in section 6.6 on the influence of pre–consolidation also holds at larger dimensions. Figure 7.1 shows the applied loading path, which consists of the following phases:

phase:	description:
1	preparation and installation of the sample
2	undrained isotropic loading, 10 kPa
3	consolidation at 10 kPa isotropic load
4	application of 100 kPa back–pressure
5	undrained isotropic loading to 13 kPa
6	consolidation
7	undrained isotropic unloading to 10 kPa
8	swelling
9	undrained application of a 7.2 kPa axial load
10	consolidation
11	undrained axial unloading
12	swelling
13	drained axial loading at maximum plunger displacement
14	drained axial unloading
15	undrained isotropic loading to 14.9 kPa
16	consolidation

17 undrained application of 7.4 kPa axial load
18 consolidation

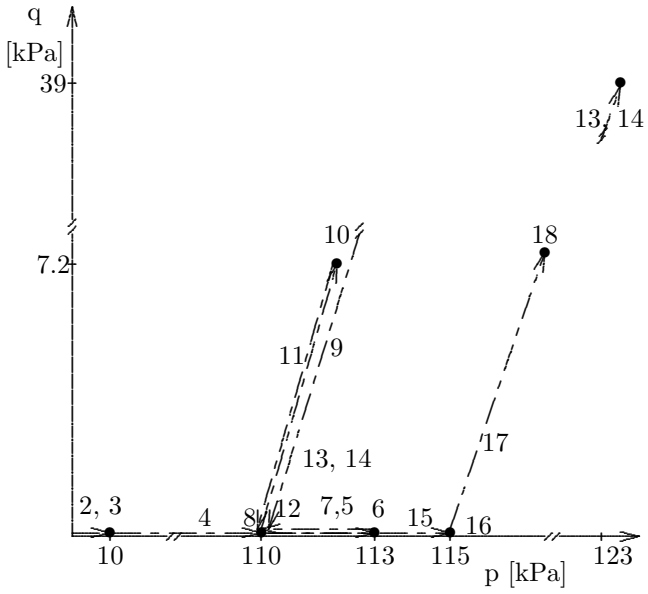

Figure 7.1: Sketch of loading path, the numbers represent the phases

The original pre–consolidation pressure of the sample can be estimated from the density of peat and the ground water levels at the location where the sample is retrieved. The pre-consolidation pressure is approximately 10 kPa. In the test phases 2 and 3 the sample is consolidated at the original, vertical, effective stress level. A back–pressure of 100 kPa is used to improve saturation of the sample. A stress level of 100 kPa is the maximum back–pressure the testing facility can handle. The degree of saturation is checked in phase 5 by calculating the Skempton B factor. The phases 5 to 12 are used to derive the level of anisotropy of peat for non pre–loading conditions, phases 15 to 18 for axial pre–loaded conditions. The total testing period lasted 12 days including a weekend that coincides to phase 12.

7.2 Testing facilities

The test is run in GeoDelft's large–scale triaxial cell. The triaxial cell was originally build to run tests on stiff soil samples like sand and gravel. Since peat is a very compressible material some minor modifications to the standard equipment was needed. Other modifications are needed to measure the Mandel–Cryer effect like a horizontal dissipation of the pore water and pore pressure measurement at the centre of the sample. The following modifications are made:

- To provide horizontal pore water dissipation, vertical strips are placed between the sample and the membrane. At top and bottom of the sample a stiff plate is placed between the sample and porous stone. The plate prevents vertical dissipation of pore water and provides a redistribution of stresses needed for the Mandel–Cryer effect. The drainage strips are folded around the stiff plate to make contact to the porous stone. In this way a horizontal drainage path is created. To reduce friction between the sample and the stiff plate a membrane is placed between the sample and the stiff plate. Silicone grease was used on the membrane to reduce friction.

- A transducer is connected at the centre of the top plate and protrudes 3 cm from the plate into the sample. This transducer is used to register the Mandel–Cryer effect.

- The plunger displacement provides the vertical deformation of the sample. Therefore contact between the plunger and the sample needs to be assured at all test phases. A minimum deviator load is maintained at each phase. Initially a minimum load of 0.07 kN (0.5 kPa) was applied. After solving some technical problems in controlling the plunger the minimum load could be increased to 0.30 kN (2.2 kPa).

- The original equipment is meant for testing stiff material. To cope with the expected relatively large deformations, a smaller sample height is chosen and the plunger is elongated by 15 cm.

- The expelled pore water is collected in a barrel, the cell water is connected to a burette. The height of the burette and barrel can be adjusted by hand. For drained conditions, the water level inside the barrel dictates the pore pressure inside the sample. The water level inside the burette provides the cell pressure. By adjusting the difference in water level between the barrel and burette an isotropic effective stress is applied on the sample. The volume of expelled pore water is measured by measuring the weight of the barrel.

- The back–pressure is applied by increasing the air pressure at the top of barrel and burette. By connecting the barrel and burette at the top deviations in air pressure in barrel and burette are prevented. The level of maximum back–pressure, 100 kPa, is dictated by the strength of the cell.

- The radial deformations are measured using a hand held laser device. Black spots were placed on the membrane. At regular interval the distance between the black spots and the cell was measured providing an estimate of the radial deformation.

7.3 The tested peat sample

The sample was taken by using a plastic tube with an inner diameter of 0.42 m and a height of 1.20 m. The sample was taken from the inner core of a secondary peat dike in Wilnis. The sample is clearly not homogeneous. The lower part consists of organic clay. The upper part has a dark colour, indicating a larger degree of humification. The middle section is selected for testing. The height of the sample is trimmed using an iron wire to cut the sample from the clayey part and the dark coloured part. The radial dimension of the sample is chosen equal to inner radius of the tube. So no trimming is needed in the radial direction. In the von Post classification [69] the sample can be described as a von Post type II peat.

Table 7.1 presents the initial and final sample dimensions and weight. The diameter is calculated using the perimeter measurements. The deviation mentioned in table 7.1 follows from the measurement accuracy.

Table 7.1: Initial and final sample dimensions

parameter	unity	initial value	final value
perimeter	[m]	1.31 ± 0.005	1.32 ± 0.005
diameter	[m]	0.42 ± 0.005	0.42 ± 0.005
height	[m]	0.61 ± 0.005	0.50 ± 0.005
weight	[kg]	77.5 ± 0.05	67.4 ± 0.05
volume	[m^3]	0.082 ± 0.0007	0.070 ± 0.0002
density	[kg/m^3]	940 ± 4	960 ± 6

Figure 7.2: a) Sample before trimming b) Drainage strips, top plate and porous stone c) Top plate and pore pressure transducer d) Complete set-up

After completion of the test, the sample is cut in vertical direction. Ten small samples are cut from the inner core. From each small sample the water content, W, the loss on ignition, N, the solid density, ρ_s, and the $CaCO_3$ content are measured. Table 7.2 presents the results. The standard deviation mentioned in table 7.2 follows from statistics.

The samples a1 to a5 and b1 to b5 represent a cross section of the large sample. Samples a1 and b1 are collected at the top while a5 and b5 are collected at the bottom. Table 7.2 shows a larger density and a lower loss on ignition for the samples b4 and b5. This corresponds to the observation that the lower part of the sample contains more clay. The last rows of table 7.2 present the average value and the standard deviation. Since the samples b4 and b5 are clearly different from the rest, the average value and standard deviation are given without the samples b4 and b5 between brackets.

The properties of table 7.2 and sample dimensions presented by the table 7.1 can be used to find the parameters like porosity and degree of saturation. By definition:

$$W = \frac{M_w}{M_s}, \quad M = M_w + M_s, \quad M_s = \frac{W+1}{M}, \quad V_s = \frac{(W+1)/M}{\rho_s}$$

Under the assumption of a constant ρ_s the initial and final values for porosity n, void ratio e and degree of saturation S_r can be found. It should be noted that the initial stage refers to the situation before the sample was placed in the cell and final stage refers to the situation in which the sample was taken from the cell. In both cases the sample will not be fully saturated.

Table 7.1 shows that the sample mainly deforms vertically and hardly any radial deformations are present. The small change in perimeter leads to a small change in diameter. For the applied accuracy the diameter change is negligible. The volume loss can be estimated from the change in height and equals 0.012 m^3. The volume reduction is mainly caused by the expelled pore

Table 7.2: Final water content, density and loss on ignition

sample	water content [-]	density [t/m^3]	Loss on ignition [%]	$CaCO_3$ [%]
a1	5.76	1.46	87.1	13.9
a2	5.67	1.46	85.8	17.1
a3	5.47	1.46	89.6	9.7
a4	5.44	1.45	91.8	4.7
a5	5.48	1.44	91.9	3.5
b1	6.39	1.42	93.0	2.0
b2	6.12	1.41	85.9	18.8
b3	5.58	1.50	73.4	16.7
b4	4.46	1.66	58.9	13.3
b5	4.01	1.84	46.8	9.7
μ_x	5.44 (5.73)^a	1.51 (1.45)^a	80 (87)^a	11
σ_x	0.67 (0.34)^a	0.14 (0.03)^a	16 (6)^a	6

^{a} = without tests b4 and b5

Table 7.3: Change in porosity, void ratio and degree of saturation

Symbol	unity	initial	final
V	[m^3]	0.082±0.0003	0.070 ± 0.0002
V_s	[m^3]	0.007±0.001	0.007±0.001
n	[-]	0.9 ± 0.02	0.9 ± 0.02
e	[-]	11 ± 2	9 ± 2
S_r	[-]	0.90 ± 3	0.90 ± 3

water. With the density of water ρ_w = 1000 kg/m^3 follows an estimated weight reduction of 12 kg. According to the tables 7.1 the difference in initial and final mass equals 10.1 kg. Table 7.3 shows that the degree of saturation equal before and after the test when the sample dimensions and weight were measured. When the exact non-rounded values are used the degree of saturation after the test is slightly larger than before the test. This difference counts for 0.5 kg of pore water. Including this difference in degree of saturation the difference sample becomes 10.6 kg (10.1 + 0.5) and is in agreement with the volume change of 0.012 m^3.

7.4 Test results

7.4.1 Skempton B–factor

Equivalent to the conventional triaxial tests as described in section 6.5 the Skempton B factor is used to check the saturation of the sample. A back–pressure of 100 kPa is applied to improve the degree of saturation. The phases 2, 5 and 15 include a cell pressure increase, phase 2 without a back–pressure and the phases 5 and 15 with the back–pressure.

Table 7.4 shows the applied cell pressure increase, $\Delta\sigma_c$ and the pore pressure reaction. In table 7.4, $\Delta\sigma_{w,in}$ indicates the pore pressure measurements inside the sample. The measurements indicated by $\Delta\sigma_{w,ex}$ refer to the drain pressure. The corresponding B–factor is indicated by B_{in} and B_{ex} respectively.

In phase 2 the isotropic load increase is applied two steps. For each step the pore pressure

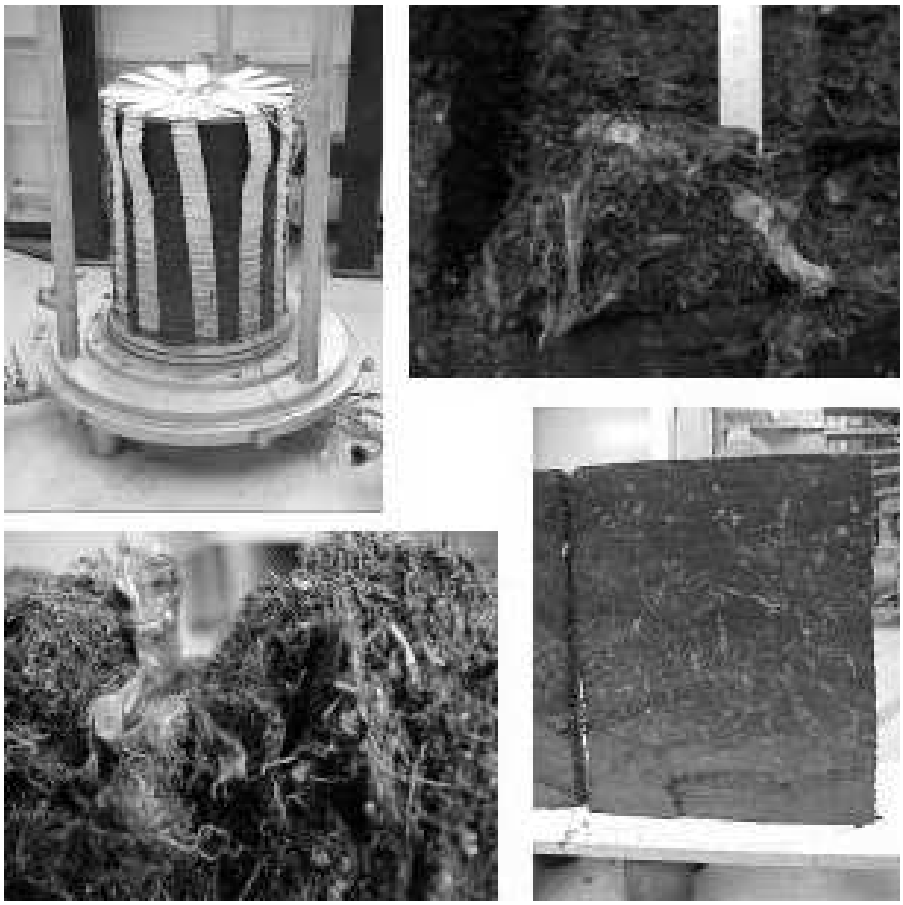

Figure 7.3: a) Sample after testing b) Indication of fibre dimension c) Impression of present fibres d) Cross-section after testing

Table 7.4: Measurement of B–factor

symbol	unity	Phase2		phase 5	phase 15
$\Delta\sigma_c$	[kPa]	4.64	4.27*	3.08	4.85
$\Delta\sigma_{w,in}$	[kPa]	3.87	4.17	3.20	4.59
B_{in}	[-]	0.83	0.98*	1.04	0.95
$\Delta\sigma_{w,ex}$	[kPa]	4.73	5.38	3.24	4.80
B_{ex}	[-]	1.02	1.26*	1.05	0.99

* = influenced by equipment modifications

reaction is measured, leading to two B–factors for this phase. The accuracy level of the used pressure transducers is, according to the manufacturer 0.2 % of maximum measurement range. The maximum measurement range is 300 kPa leading to an approximation of the absolute error in measured pore pressure of ± 0.6 kPa. Since the exact values for $\Delta\sigma_c$, $\Delta\sigma_{w,in}$ and $\Delta\sigma_{w,ex}$ follow from the subtraction of the readings before and after the justification of the cell pressure the absolute error in $\Delta\sigma_c$, $\Delta\sigma_{w,in}$ and $\Delta\sigma_{w,ex}$ becomes approximately ± 1.2 kPa. The absolute error in B follows from the summation of the relative error in $\Delta\sigma_c$ and $\Delta\sigma_{w,in}$, respectively $\Delta\sigma_{w,ex}$. The absolute error in B becomes ± 0.4 to ± 0.8. The relatively low accuracy in B–factor despite the use of accurate pressure transducers follows from the relatively small load steps. Keeping the achieved accuracy in B–factor measurement in mind it can be concluded that a reasonable degree

of saturation is achieved.

7.4.2 Volume strain

The total volume change of the sample follows from measurement of expelled pore water weight. The expelled pore water is collected in a barrel. During the test the weight of the barrel and water is measured continuously, providing the volume of expelled water. Assuming the solid particles of peat to be incompressible, the volume expelled pore water equals to the volume change of the sample. Figure 7.4 shows the volume expelled pore water during the test. Several loading and unloading phases can be distinguished. The final volume of expelled pore water equals 33 dm^3. This volume is not in agreement with the difference the initial and final sample mass (10.6 kg) and sample volume (12 dm^3) mentioned in section 7.3.

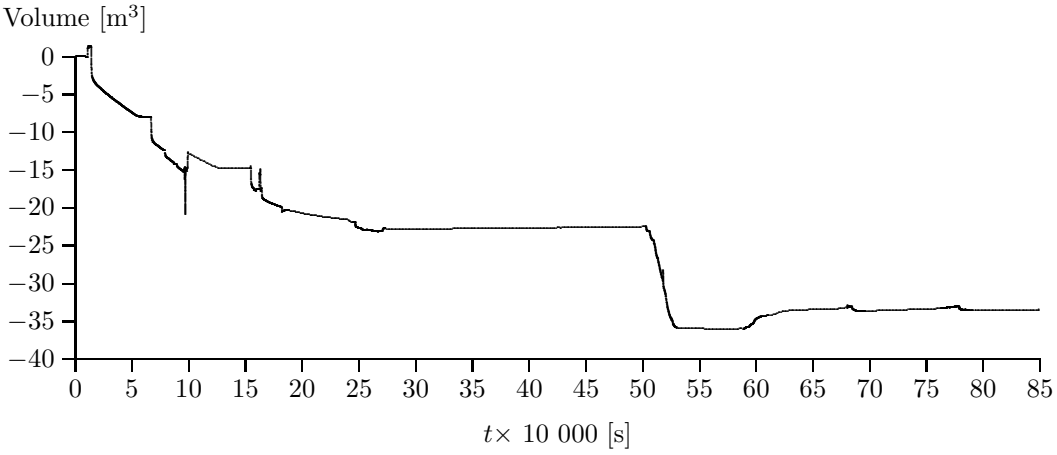

Figure 7.4: Total volume of expelled pore water

The difference between the total volume loss found by different measurements is remarkable. Leakage might be a possible explanation for the difference in weight of collected pore water and volume loss of the sample. If somehow cell water enters the drain more water is collected at the end of the drain than expelled from the sample. If leakage occurs a continuous increase in expelled water weight should be found. Figure 7.4 shows a continuous increase in expelled pore water until approximately 130 000 s. The testing period from approximately 300 000 s and 500 000 s corresponds to a weekend. During this period the cell pressure, back–pressure and vertical load was kept constant. In this period the volume of expelled pore water is constant, as shown in figure 7.4. So it seems that initially leakage occurred which was stopped during the test. The curve in graph 7.4 at 130 000 s during phase 4, the application of the back–pressure, possibly indicates the moment the leakage was stopped. The back–pressure was applied almost instantaneously followed by a resting period of approximately 15 hours. The parameters presented in this report are derived from the phases 5 to 18. There is no indication that the initial leakage did influence the measurements in the following phases. The total volume of expelled pore water up to 130 000 s is 14.7 dm^3, leading to a total volume loss during the test of 18.3 dm^3. During the application of the back–pressure the volume of expelled pore water reduces by 2.6 dm^3. This can be explained by compression of air bubbles inside the sample and by volume change of the tubes connecting the reservoir to the cell. Correcting the amount of expelled pore water for this phenomenon leads to a total volume of expelled pore water of approximately 15.7 dm^3.

7.4.3 Pore pressure development

The graphs 7.5, 7.6 and 7.7 show the pore pressure development for the phases 5 – 12 and 15 – 18. The internal pore pressure refers to the transducer that is located at the top of the sample. A second transducer is connected to the lower drain. The measurements of this transducer are referred to as the drain pressure. When the drainage valves are closed, the undrained phases, this transducer records the water pressure in the drainage system. The drainage system consists of the porous stones, the side drains and the tubes connecting the porous stones to the exterior of the cell.

After opening the drainage valve the drain transducer gives the pressure corresponding to the pressure inside the barrel almost instantaneously. It is therefore concluded that flow resistance in the tubes connecting the porous stone to the pore water collection system can be neglected. The pressure inside the drains placed between sample and membrane will be close to pressure distribution assumed in section 6.7 with $p_d = 0$ at top and bottom of the sample and $\mathrm{d}p_d\,/\mathrm{d}z = 0$ at half the sample height.

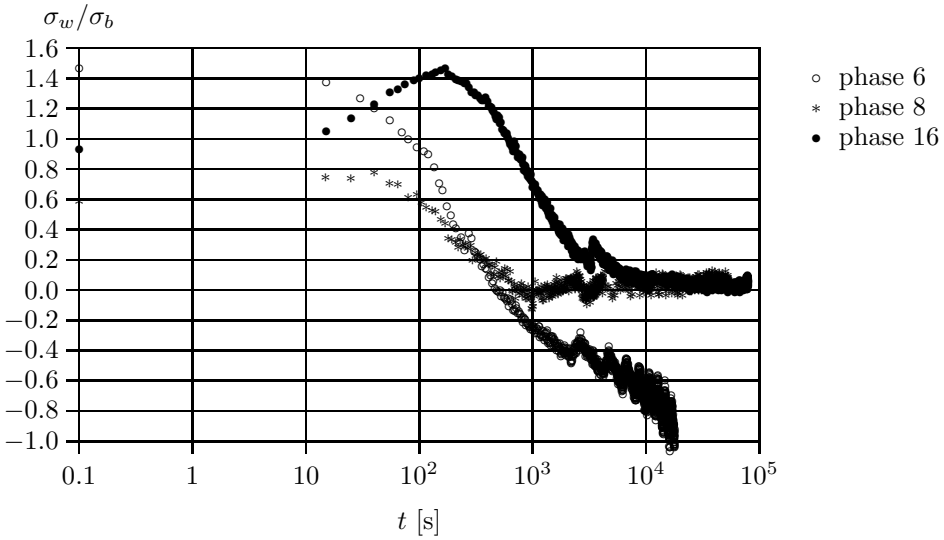

Figure 7.5: Pore pressure development at the middle of the sample during phases 6, 8 and 16

For the undrained isotropic loading phases the internal pore pressure and drain pressure development are equal. As shown in figure 7.7 an instantaneous cell pressure increase results for both transducers to an equal response. The pore pressure response remains constant until the drainage valves are opened and the consolidation process starts.

For the undrained axial loading phases however the internal and external transducers show a difference in a pressure response. Figure 7.7 shows the undrained application of approximately 7 kPa axial load and a resting period, the phases 9, 11 and 17. The resting period is approximately 10 minutes for phase 9, 1 hour for phase 11 and 4 hours for phase 17. The pore pressure found by the internal pore pressure transducer shows a more steep development reaching a peak value. During the resting period, while the drainage valves are still closed, a decay of the internal pore pressure is found. This indicates an internal consolidation process due to some pressure inhomogeneity. The drain pressure shows a less steep development during loading, reaching a smaller final value when loading is complete. During the resting period, with the drainage valves closed, the drain pressure still increases. At the end of the resting period the drain pressure equals the internal pore pressure. This can be explained by non–uniform deformation, which causes an internal consolidation process. Apparently, during the undrained resting period pore pressure in the middle of the sample consolidates by a pore water flow from the middle to the outer radius of the sample,

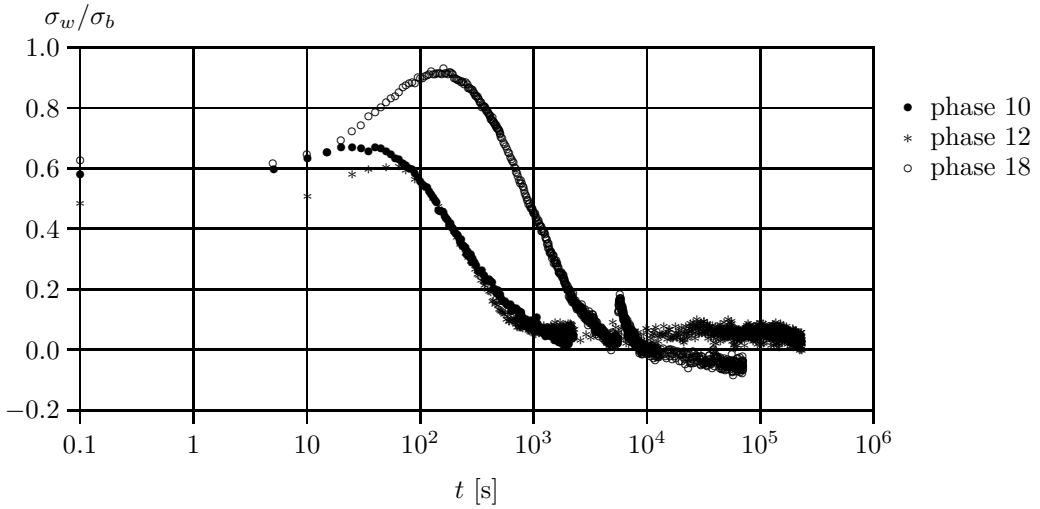

Figure 7.6: Pore pressure development at the middle of the sample during phases 10, 12 and 18

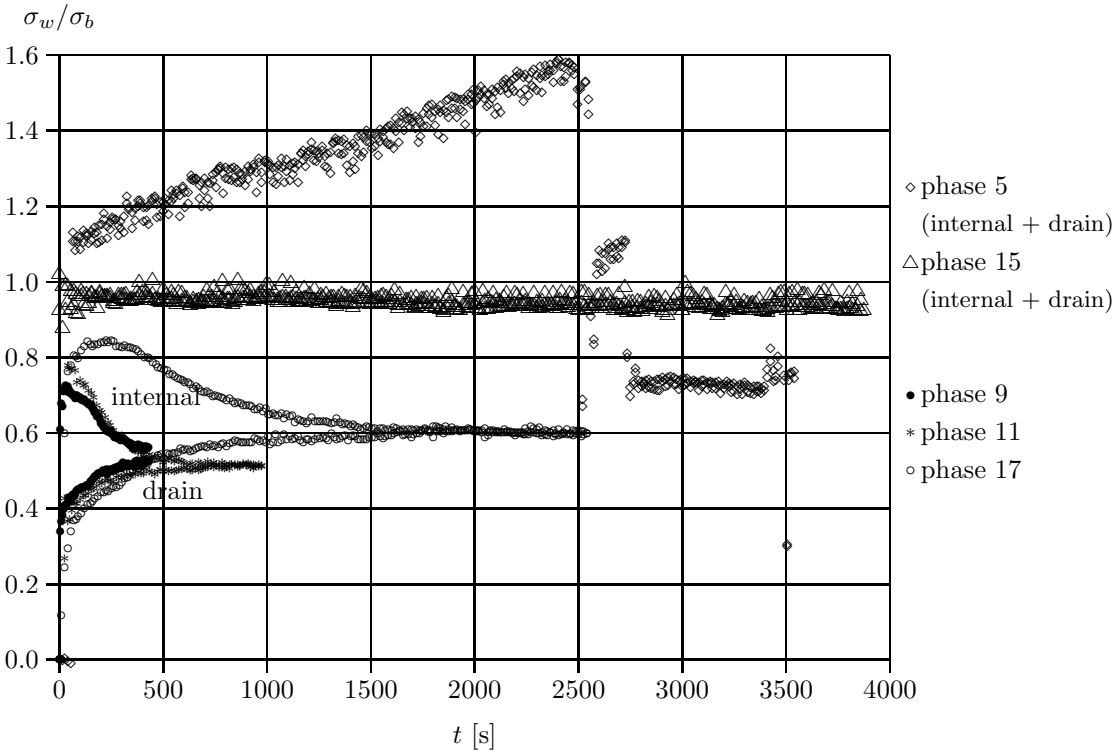

Figure 7.7: Pore pressure development during phases 5, 9, 11, 15 and 17

the drains and the porous stone.

Measurements of phase 7 are not presented by figure 7.7 since due to modifications to test equipment no clear pore pressure development is found. Figure 7.6 shows the consolidation of the sample due to an axial pre-load of approximately 7 kPa. Phases 10 and 18 represent a loading phase, while phase 12 represents an unloading phase. Figure 7.6 clearly shows the Mandel–Cryer effect.

Table 7.5 shows the exact load and pore pressure reaction. The parameters $\Delta\sigma_{w,ini}$ and

$\Delta\sigma_w/\Delta q_{ini}$ indicate the initial value which is given by the final value in the previous phase. The parameters $\Delta\sigma_{w,max}$ and $\Delta\sigma_w/\Delta q_{max}$ indicate the peak value. The minus sign in the head of table 7.5 follows from the definition for positive and negative stress. A negative value indicates a pressure reduction and refers to swelling of the sample.

Table 7.5: Consolidation development during phases 10, 12 and 18

phase	Δq [kPa]	$\Delta\sigma_{w,ini}$ [kPa]	$\Delta\sigma_{w,max}$ [kPa]	$\Delta\sigma_w/\Delta q_{ini}$ [-]	$\Delta\sigma_w/\Delta q_{max}$ [-]
10	7.15	4.11	4.82	0.58	0.67
12	-7.26	-3.46	-4.34	0.48	0.61
18	7.38	4.72	6.73	0.63	0.93

7.4.4 Effective Stress Path

Figure 4.4 shows the relation between anisotropy and the undrained effective stress path. Figure 7.8 shows the effective stress paths and the $q - \varepsilon_a$ diagram found in phases 9, 11 and 17. The curved slope of the $q - \varepsilon_a$ diagram found for phase 9 indicates the occurrence of some plasticity during this phase. For each of the three phases the effective stress path is clearly tilting backwards. Using the least squares method a line is fitted through the data. The angle of this line provides the value for $\Delta p'/\Delta q$. Table 7.6 presents the results. The parameter R^2 indicates the accuracy of the fit. A perfect fit is found for $R^2 = 1.0$.

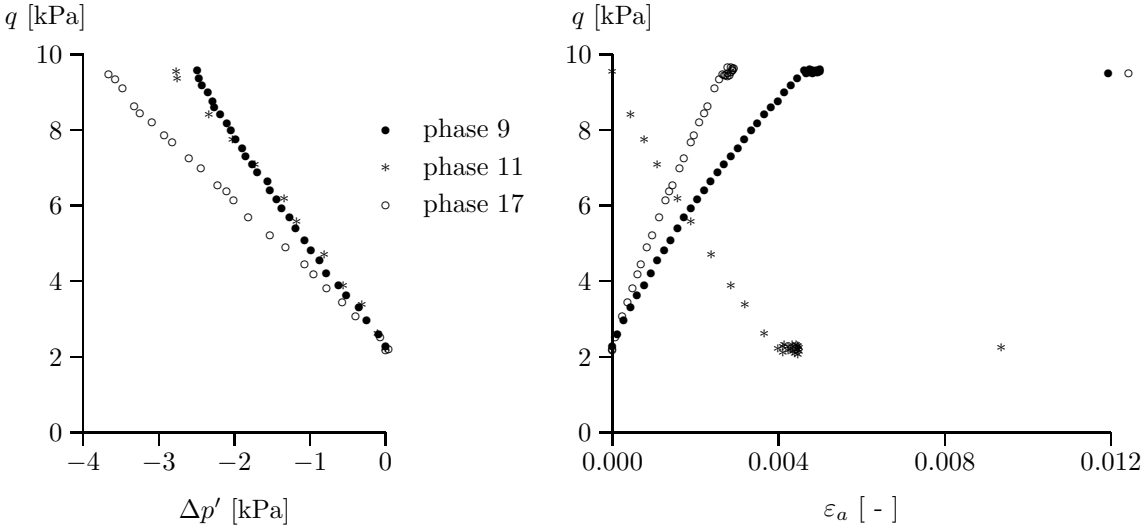

Figure 7.8: a) Undrained effective stress path, b) $q - \varepsilon_a$ diagram, for phases 9, 11 and 17

Table 7.6: The angle of effective stress path

phase	$\Delta p'/\Delta q$	R^2
9	-0.35	0.997
11	-0.38	0.999
17	-0.52	0.995

Table 7.6 shows $\Delta p'/\Delta q < 0$, indicating that the tested peat clearly behaves anisotropically.

Figure 7.7 shows the pore pressure development during the phases 9, 11 and 17. During the load application the internal pore pressure reaches a larger value than the drain pressure. In following undrained resting period the internal pore pressure decays while the drain pressure rises until equilibrium is found. Figure 7.6 shows the ratio σ_w/σ_b during the consolidation phases 10, 12 and 18. The initial value for σ_w/σ_b in these phases, shown in table 7.5, corresponds to the final value of phases 9, 11 and 17. This explains the difference in $\Delta p'/\Delta q$ value found in table 7.5 and 7.6.

The difference between internal pore pressure and the drain pressure causes an internal consolidation process even when the drainage valves are closed. The consolidation process continues until equilibrium between pore pressure and drain pressure is reached. Since the load is not applied instantaneously the internal pore pressure is influenced by the application of the load as well as by internal consolidation. The value for σ_w/σ_b during loading is therefore a combination between $(\sigma_w/\sigma_b)_{ini}$ which would be present if the load was applied instantaneously, and some increase in σ_w/σ_b caused by the Mandel-Cryer effect since the consolidation process has already started. To check this assumption $(\sigma_w/\sigma_b)_{max}$ is compared to $\Delta p'/\Delta q$ in table 7.6. It should be noted that according to equation (4.41) it is found that $\Delta p'/\Delta q = \sigma_w/\sigma_b$ - 1/3.

Table 7.7: The angle of undrained ESP

phase	from table 7.6	from $(\sigma_w/\sigma_b)_{max}$ and eq. (4.41)
9	0.35	0.34
11	0.38	0.28
17	0.52	0.60

The tables 7.6 and 7.7 show that the angle of effective stress path corresponds better to $(\sigma_w/\sigma_b)_{max}$ than $(\sigma_w/\sigma_b)_{ini}$. So it can be concluded that the relatively slow application of the load in combination to the internal consolidation increases the angle of the effective stress path and therefore seems to overestimate the value for $\Delta p'/\Delta q$.

Figure 7.7 shows the internal pore pressure and drain pressure during phase 5 and 15. In these phases the cell pressure is increased followed by an undrained resting period. During phase 5 some modifications to the test set-up were needed. This explains the strong curvature in pore pressure and drain pressure development. For the isotropic loading and unloading no internal consolidation is found. The internal pore pressure development is equivalent to the drain pressure development.

7.4.5 Radial and Axial deformations

The radial deformations are measured manually at two levels at 4 points at each level. The levels were located at 1/3 and 2/3 of the initial sample height. Black stickers affixed to the membrane indicated the points. Using a hand-held laser the distance between cell wall and membrane could be measured. The stickers were placed at opposite sides so the deformation of two lines orthogonal to each other is found. The radial displacements were measured at the beginning and end of each phase. For some long lasting phases extra measurements were taken. Table 7.8 shows the radial deformation and strain derived from the hand-held laser. A negative deformation or strain in table 7.8 indicates shrinkage of the sample while a positive deformation or strain indicates bulging of the sample.

The radial strain as presented in table 7.8 is negligible compared to the axial strain presented in table 7.1. It suggests a ν–value of almost zero. The final vertical strain is approximately -21 % while the average final radial strain is -0.49%. It is remarkable that the bulging in phase 13, the drained compression phase, counterbalances the net shrinkage in phases 1 - 7. The volume deformation of the sample during the test is dominated by the vertical deformation.

Figure 7.8 shows the $q - \varepsilon_a$ curve for the phases 9, 11 and 17. The angle of this curve provides the axial undrained vertical young's modulus. The $q - \varepsilon_a$ curve for the phases 13 and 14, figure

Table 7.8: The cumulative radial deformation and radial strain

phase	deformation[mm]				strain [%]			
	lower part		upper part		lower part		upper part	
	AC	BD	AC	BD	AC	BD	AC	BD
initial	0	0	0	0	0	0	0	0
end phase 1	1.35	0	3.37	1.35	0.32	0	0.81	0.32
end phase 2	0	0.67	3.37	1.35	0	0.16	0.81	0.32
phase 3	-2.69	-3.37	-4.04	-2.69	-0.65	-0.81	-0.97	-0.65
phase 3	-4.04	-4.04	-4.04	-4.04	-0.97	-0.97	-0.97	-0.97
end phase 3	-4.04	-4.04	-3.37	-4.71	-0.97	-0.97	-0.81	-1.13
phase 4	-0.67	-2.02	-0.67	-3.37	-0.16	-0.49	-0.16	-0.81
end phase 4	-5.39	-6.06	-4.04	-3.37	-1.3	-1.46	-0.97	-0.81
end phase 5	-4.04	-4.04	-4.71	-4.71	-0.97	-0.97	-1.13	-1.13
phase 6	-4.71	-4.71	-6.73	-5.39	-1.13	-1.13	-1.62	-1.30
end phase 6	-6.06	-5.39	-6.06	-5.39	-1.46	-1.30	-1.46	-1.30
end phase 7	-6.06	-4.71	-6.73	-5.39	-1.46	-1.13	-1.62	-1.30
phase 8	-6.06	-4.04	-5.39	-4.04	-1.46	-0.97	-1.30	-0.97
end phase 8	-5.39	-4.04	-5.39	-5.39	-1.30	-0.97	-1.30	-1.30
end phase 9	-4.71	-3.37	-4.04	-4.71	-1.13	-0.81	-0.97	-1.13
end phase 10	-4.71	-4.04	-4.71	-4.71	-1.13	-0.97	-1.13	-1.13
end phase 11	-6.06	-5.39	-6.06	-6.06	-1.46	-1.30	-1.46	-1.46
phase 12	-5.38	-4.71	-6.73	-5.39	-1.30	-1.13	-1.62	-1.30
end phase 12	-6.06	-4.04	-4.71	-4.71	-1.46	-0.97	-1.13	-1.13
phase 13	-5.39	-4.04	-4.04	-4.71	-1.30	-0.97	-0.97	-1.13
phase 13	-4.71	-4.04	-4.04	-4.71	-1.13	-0.97	-0.97	-1.13
phase 13	-1.35	0.67	1.35	-0.67	-0.32	0.16	0.32	-0.16
phase 13	-1.35	-0.67	2.02	0	-0.32	-0.16	0.49	0
phase 13	0.67	0.67	4.04	1.35	0.16	0.16	0.97	0.32
end phase 13	-0.67	0	3.37	0.67	-0.16	0	0.81	0.16
phase 14	-0.67	0	2.69	1.34	-0.16	0	0.65	0.32
phase 14	-0.67	0	2.02	0	-0.16	0	0.49	0
phase 14	-1.35	-2.02	0.67	-2.69	-0.32	-0.49	0.16	-0.65
end phase 14	-1.35	-1.35	-0.67	-1.35	-0.32	-0.32	-0.16	-0.32
end phase 15	-2.02	-1.35	0.67	-0.67	-0.49	-0.32	0.16	-0.16
end phase 16	-2.69	-2.02	-2.02	-2.02	-0.65	-0.49	-0.49	-0.49
phase 17	-2.02	-1.35	1.35	-2.02	-0.49	-0.32	0.32	-0.49
end phase 17	-1.35	-1.35	0	-1.35	-0.32	-0.32	0	-0.32
final	-2.02	-2.69	-2.02	-1.35	-0.49	-0.65	-0.49	-0.32

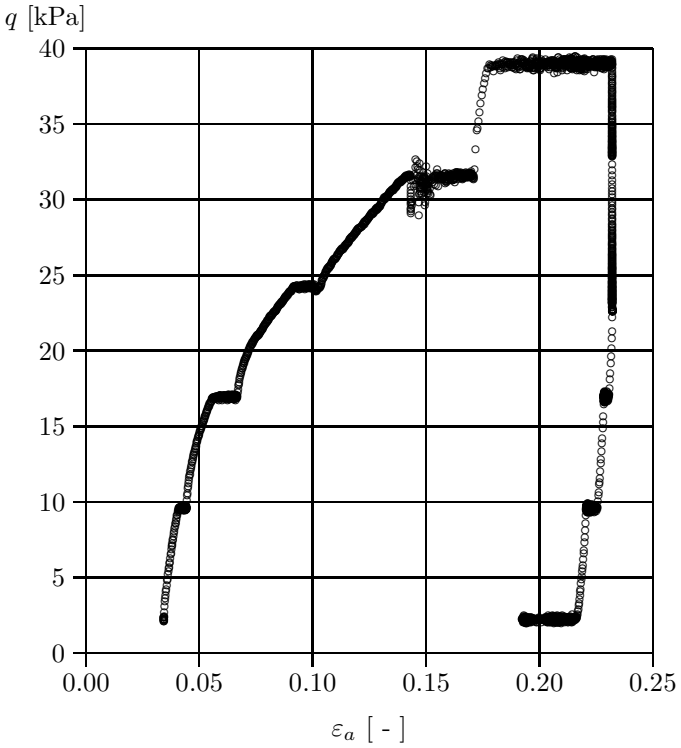

Figure 7.9: $q - \varepsilon_a$ diagram for phases 13 and 14

7.9 gives an impression of the drained axial Young's modulus. The total load is applied in 5 steps and removed in 3 steps including resting periods in between. The horizontal parts in figure 7.9 represent these resting periods. The first loading step of phase 13 and the last step of phase 14 has been used to derive E_a.

phase	E_a^u [kPa]	phase	E_a [kPa]
9	1574	13	1135
11	1673	14	1500
17	2696		

During the consolidation phases the deviator stress is constant, $\delta q = 0$. Equation (4.18) shows that for $\delta q = 0$ graphs of p' - e gives K' and p' - ε_q gives J'. Figure 7.10 shows a typical $p' - e$ and a $p' - \varepsilon_q$ development as found for phase 10. There are two options to derive the volumetric strain and deviator strain. The first uses the weight of expelled pore water, which gives the volumetric strain directly. Together with the axial strain given by the plunger displacement, the radial strain can be estimated by $\varepsilon_r = (e$ - $\varepsilon_a)/2$. The deviator strain follows from $\varepsilon_q = 2/3(\varepsilon_a$ - $\varepsilon_r)$. This option is referred to as continuous measurements in table 7.9 as the weight of expelled pore water is measured continuously during the test. This option is presented by figure 7.10. The second option uses the manually measured radial displacements. Together with the axial strain, given by the plunger displacement, the volumetric strain is found by $e = \varepsilon_a + 2\varepsilon_r$. In table 7.9 the second option is indicated by hand measurement. The parameters K' and J' involve linear elasticity. The measurements however include plastic deformation. After the excess pore pressure is dissipated the deformations continue. To derive values for K' and J' from the consolidation phases it is assumed that plastic deformations during consolidation remain relatively small. In figure 7.10 a dotted line

indicates the end of consolidation, which often corresponds to a strong curvature at the end of the consolidation period.

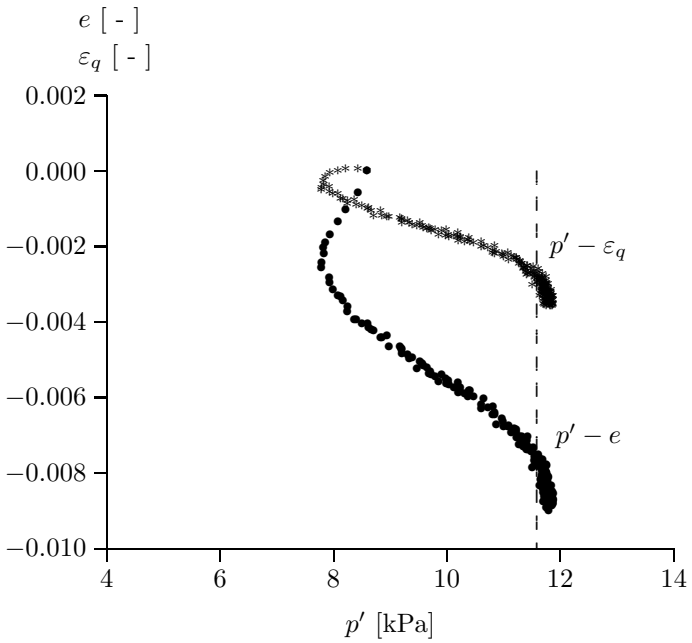

Figure 7.10: $p' - e$ and $p' - \varepsilon_q$ development for phase 10

Table 7.9 gives the values for K', J' and K'/J' found for the different consolidation phases. The phases 6, 8 and 16 gives the consolidation under an isotropic load, while the phases 10, 12 and 18 gives the consolidation under an axial stress.

Table 7.9 shows for phases 6, 8 and 10 equivalent results of both methods. For the phases 12, 16 and 18 large difference occur especially in determination of J'. Due to the axial deformations the membrane around the sample starts to buckle and curl. Since the total radial displacements are very small, buckling of the membrane induces a relatively large error. This explains that in the final phases the manual measurements indicate a larger volumetric strain and a smaller deviator strain than found by the continuous measurements

Table 7.9: Stiffness moduli K' and J' derived from the consolidation phases

phase	continuous			hand measurements		
	K' [kPa]	J' [kPa]	K'/J' [-]	K' [kPa]	J' [kPa]	K'/J' [-]
6	407	2010	0.20	452	1943	0.23
8	645	1800	0.36	898	1400	0.63
10	389	1094	0.36	407	935	0.44
12	484	1770	0.27	255	7837	0.03
16	530	1709	0.31	350	4443	0.08
18	730 - 670*	1450-1550*	0.50-0.40*	407	1207	0.13

* due to measurement noise an exact value can not be given

Table 7.9 shows a scatter in values found for K' and J'. The values for K'/J' are more consistent than the values derived by the hand held laser.

7.5 Fitting measurement data

During the consolidation phases 16 and 18 a clear Mandel–Cryer effect is found. Figure 7.11 shows a comparison between measurement data and analytical solution presented by chapter 5. The radial strain is found to be small, as shown by table 7.8. The ratio of the radial strain and the axial strain found in the drained unloading phase 13 gives an estimation of ν_{vh}, $\nu_{vh} \approx 0.1$. The previous section shows that the axial drained Young's modulus of the order of 1200 - 1500 kPa. Under the assumption $\nu_{hh} \approx \nu_{vh}$, this leaves the permeability and the radial drained Young's modulus to fit the analytical solution to the measurement data. The following parameters are found:

	phase 16	phase 18
E_a	1200 kPa	1200 kPa
E_r	3300 kPa	3300 kPa
ν_{vh}	0.1	0.1
ν_{hh}	0	0.1
$(K'/J'$	0.27	0.3)
k	8×0^{-8} m/s	6×10^{-8} m/s

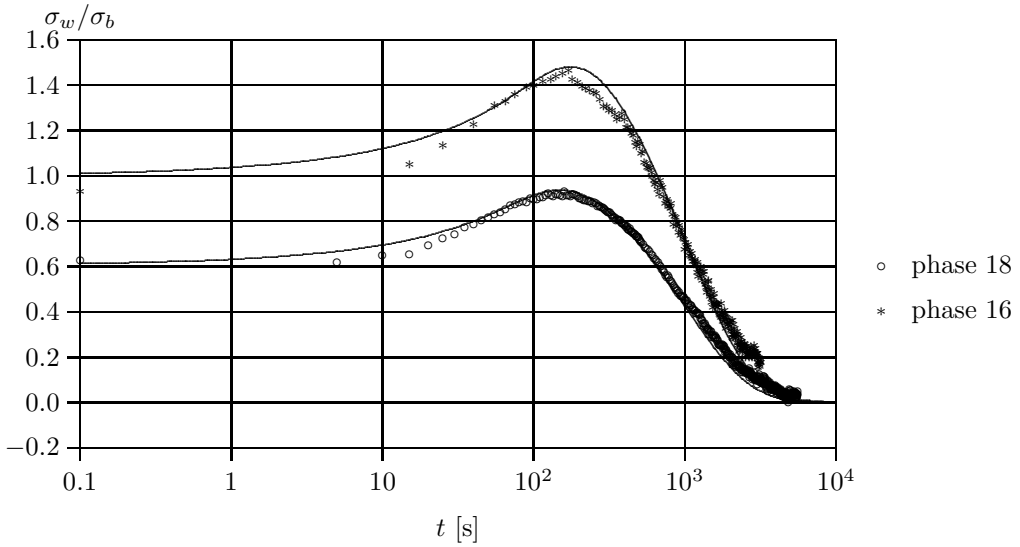

Figure 7.11: Analytical fit for measurement data phases 16 and 18

Figure 7.6 shows the pore pressure development for two axial loading phases 10 and 18 and one axial unloading phase, phase 12. The initial pore pressure in relation to the applied load, σ_b in phases 10 and 12 is in the same order of magnitude as phase 18. However as consolidation proceeds the pore pressure development shows a lower peak and a less steep slope for phases 10 and 12. The pore pressure development found in these phases can not be reproduced by the analytical formulae of chapter 5. The stiffness parameters which reproduce the initial pore pressure will predict a larger peak and vice–versa.

Section 6.7.2 explains the absence of a large Mandel–Cryer effect for the conventional triaxial testing by drain resistance. However the absence of a large peak in the phase 6, 8, 10 and 12 for large scale testing can not be explained by drain resistance. First, measurements of drain pressure, p_d, show that after opening the valves the drain pressure adjust almost instantaneously to the pressure in the pore water collection system. This indicates that $\Delta p_d = 0$, at least at the ends

of the drains. Second, a nice fit of measurement data can be found for the phases 16 and 18 disregarding drain resistance. Drain resistance is independent from loading phases. So if during phases 16 and 18 drain resistance does not influence the pore pressure development then drain resistance does not influence the pore pressure developments in the other phases.

Gibson, Gobert & Schiffmann [33] show that a non–constant permeability leads to a reduction in the Mandel–Cryer effect in combination to an increase in hydrodynamic period. The increase in hydrodynamic period is repeated by a flattening of the consolidation curve. A non constant permeability might explain the differences between the analytical solution and measurement data for phases 10 and 12.

Section 6.2.3 shows the strain dependency of the permeability of the peat used for the conventional triaxial samples. Equivalent to section 6.2.3 strain dependency is determined for the material tested in the large scale triaxial test. $K_0 - CRS$ tests are conducted on conventional samples retrieved in the vicinity of location where the large sample has been retrieved. The measurements are used to fit equation (7.1)

$$k = k_0 \times \exp\left(-\chi e\right) \tag{7.1}$$

In total 10 samples have been tested. On average is found $\chi = 8.5$ and $k_0 = 4.5 \times 10^{-8}$ m/s. Based on strain measurement equation (7.1) is used to calculate the actual permeability at the begin and end of the different consolidation phases. Equation (7.1) relates permeability to volumetric strain. Since k_0 refers to initial conditions the total volumetric strain is needed to find a proper value for the actual permeability. Section 7.4.2 shows that volumetric strain measurement in initial phases of the test is not trustworthy. Therefore an accurate development of the permeability during the test can not be given. Table 7.8 shows that the radial strain is small in comparison to the axial strain. To illustrate the development of the permeability figure 7.12 uses the total axial strain in combination to equation (7.1).

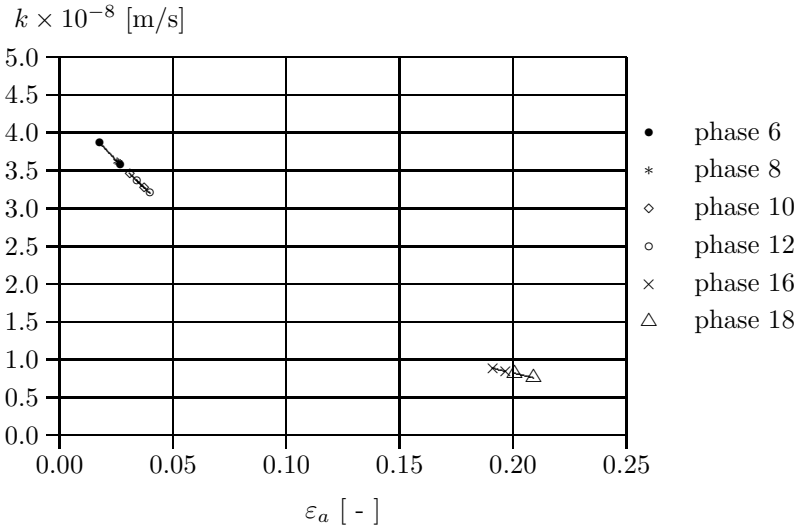

Figure 7.12: Illustration of decay in permeability during the test, based on axial strain

Figure 7.12 shows the decay in permeability when strain develops. It should be noted that the actual value for k used in figure 7.11 to fit the measurement data is larger than presented in this figure. Figure 7.12 clearly shows that the permeability decays strongly within the phases 6, 8, 10 and 12. After the large axial pre–consolidation the permeability is reduced by almost an order in magnitude. However during the phases 16 and 18 the change in permeability is small to negligible. This indicates that for the phase 6, 8, 10 and 12 the variability of the permeability might mask the Mandel–Cryer effect. While for the phases 16 and 18 a peak is found conform the analytical solution presented in chapter 5.

7.6 Conclusions

Section 7.1 discusses the aim of the large scale triaxial test, which is to study possible scale effects. Two possible scale effects are explicitly mentioned. First in relation to the Mandel–Cryer effect. Second in relation to the influence of an axial pre–consolidation.

Regarding the Mandel–Cryer it can be concluded that the measurements on the large scale triaxial test show the Mandel–Cryer effect in contrast to the conventional samples presented in section 6.7. The Mandel–Cryer effect is found during consolidation after an axial load as well as after an isotropic load. A small Mandel–Cryer effect is found for the non pre–consolidated phases and large effects are found for the axial pre–consolidated phase. The large effects can well be fitted to the analytical solutions presented in chapter 5. The small effects found in the non pre–consolidated phases can be explained by a non constant permeability. According to equation (7.1) a significant change in permeability is to be expected during the non pre–consolidated phases while for the pre–consolidated phases the change in permeability is relatively small. This is illustrated by figure 7.12. A variable permeability is also found for the peat tested in the conventional triaxial tests, see table 6.2. It is therefore concluded that absence of the Mandel–Cryer effect in the conventional triaxial tests can be explained by drain resistance in combination with a non-constant permeability. For large sample sizes the Mandel–Cryer effect is more pronounced.

To estimate the influence of an axial pre–consolidation the parameter K'/J' in different ways at different stages of the test. Table 7.10 compares the different values found for the different phases.

Table 7.10: Summary of K'/J' values found in different phases of the test

phase	$\Delta p'/\Delta q$ table 7.6	$(\Delta\sigma_w/\Delta\sigma_b)_{ini}$ table 7.5	equation 3.2 table 7.9
6	-	-	0.20
8	-	-	0.36
9	0.35	-	-
10	-	0.25	0.36
11	0.38	-	-
12	-	0.15	0.27
16	-	-	0.31
17	0.52	-	-
18	-	0.30	0.50-0.40

Despite the difference in K'/J' value found table 7.10 shows clearly the anisotropy of peat. For all phases the K'/J' value is larger than 0. Table 7.10 shows the different values for K'/J' in the range of 0.15 to 0.50. The large value 0.52 is found from the angle undrained ESP, which is influenced by internal consolidation during application of the load. Therefore it can be concluded that the angle of undrained ESP is not an appropriate parameter to indicate anisotropy for large scale testing. In contrast to the tests on conventional samples, as shown by the previous chapter, the axial pre–consolidation seems to have a limited influence on the K'/J' value. The K'/J' value is already considerable for the non pre–consolidated phases. This can be explained by a possible axial pre–consolidation in the field, which causes a large value for K'/J' for the phases 6 to 12. The sample was retrieved from a secondary dyke and it will have been axially pre–loaded.

The tested sample is retrieved such that the axial direction corresponds to the vertical direction in the field. However due to the applied loading and unloading phases the stiffness parameters derived from the test hold only for the tested sample and will probably not correspond to the original stiffness parameters in the field. Therefore the stiffness parameters are discussed in terms of E_r and E_a of the sample and not in terms of E_h and E_v in the field. To give an impression of the consequences for the values found for K'/J', equation 3.6 and table 7.11 are used to give a rough estimation for the radial stiffness. For three characteristic values for K'/J' from table 7.10

a value for E_r is estimated. The largest value for K'/J' is found in phase 17 and equals 0.52, the lowest value for K'/J' equals 0.15 and an intermediate value of $K'/J' = 0.35$. The values for the drained parameters E_a and ν_{vh} are derived from phase 13, $E_a = 1200$ kPa and $\nu_{vh} = 0.1$. For ν_{hh} the values 0 and 1/3 are used to estimate E_r.

Table 7.11: A rough estimation for E_r from measurements of K'/J' and E_a

phase	E_a [kPa]	K'/J' [-]	ν_{vh} [-]	ν_{hh} [-]	E_r [kPa]
12	1200	0.15	0.1	0	2275
				1/3	1520
9	1200	0.35	0.1	0	4210
				1/3	2800
11	1200	0.52	0.1	0	7110
				1/3	4750

Table 7.11 shows large values for E_r. It should be noted that the radial stiffness follows from radial deformations due to axial loading. The fibre structure of peat is such that an axial load leads mainly to axial deformation while radial deformation remains negligible. Therefore large to extreme values for E_r are found.

Chapter 8

Practical applications

8.1 Theory, Measurements and Engineering Practice

The chapters 3 to 7 give an answer to the question raised in chapter 1: Can redistribution of stresses during consolidation of a triaxial sample be used to determine elastic stiffness parameters? In chapter 1 it is notified that soil behaviour is not elastic. However chapter 1 states that equivalent elastic moduli, which incorporate a small amount of plasticity, can be used to describe stress and strain in soft soil for a large number of consolidation problems. The theory for linear elastic consolidation is further elaborated in the chapters 3 to 5. The theory is tested by laboratory measurements described in chapter 6 and 7. In this chapter theoretical considerations and results of the laboratory measurements are linked to engineering practice.

The practical applications of the theory described in chapters 3 to 5 and the conclusions of the laboratory measurements are illustrated by 3 examples, which are discussed in the next sections;

1 Parameter determination for anisotropy. The initial aim of this study is to find anisotropic parameters by using measurements of pore pressure development in standard triaxial testing. Section 8.2 shows an example in which the level of anisotropy can be distinguished from standard laboratory tests.

2 Lateral stress reaction. The laboratory tests described in section 6.6 show a change in level of anisotropy due to anisotropic pre–loading. A change in ratio of stiffness parameters will lead to a different deformation pattern if such a pre–loaded sample is loaded and allowed to deform. When such pre–loaded sample is not allowed to deform laterally a change in stiffness parameters will lead to different lateral stress reaction when the sample is axially loaded. Section 8.3 deals with this topic by discussing the influence of anisotropy to the K_0-value. This section also shows indicatively the influence of plasticity to the development of an anisotropic K_0.

3 Consolidation around a vertical drain. In practice vertical drains are often used to improve the consolidation behaviour of soft soil. Section 8.4 discusses the influence of anisotropy on the efficiency of vertical drains.

8.2 Parameter determination for anisotropy

Chapter 6 shows that for standard triaxial testing the Mandel–Cryer effect cannot be used to determine the level of anisotropy for peat in standard triaxial testing. This is caused by drain resistance in combination to a short hydrodynamic period for a radial drained triaxial sample. Chapter 7 shows that besides drain resistance and scale effects a variable permeability influences

the Mandel–Cryer effect strongly. For a variable permeability only a small to negligible Mandel–Cryer effect is found. Since variability in permeability in peat can only be excluded from tests after remoulding the sample severely, measurements of the Mandel–Cryer effect cannot be used to assess the level of anisotropy of peat.

Chapter 6 however shows an increase in angle of undrained effective stress path for axial pre–consolidation indicating an increase in anisotropy. So anisotropy in stiffness can be used for a better understanding of undrained ESP's for over–consolidated peat samples. This is illustrated by a series of triaxial tests run on peat samples retrieved underneath the dike around the Island of Marken. Figure 8.1 shows the results for 12 tests for OCR ≈ 2. The tests have been conducted in order to study dike stability. Six samples have been retrieved from the toe of the dike and therefore consolidated at a low pressure, approximately 10 kPa. The other six have been retrieved from underneath the dike and are therefore consolidated at a higher pressure, approximately 30-40 kPa. The water content W density, ρ and loss on ignition N are derived from remaining soil samples. On average is found a water content $W = 7.64$ and a density $\rho = 982$ kg/m^3 for the samples at the toe of the dike. For the samples collected underneath the dike is found $W = 5.03$ and $\rho = 1008$ kg/m^3. On average $N = 0.80$ is found. These values correspond well to values presented in literature, [25]. Figure 8.1 shows that all the stress paths are tilting backwards, except from test nr 167, until failure occurs.

For large values of q the horizontal effective stress reduces to 0 due to the pore pressure generation. The samples consolidated at a low pressure fail when reaching these conditions. The samples consolidated at large pressure do not fail when the horizontal stress reduces to 0. For these tests the ESP follows the line $q = 3p'$ which follow directly from the definitions of p' and q.

The upper part of figure 8.1 presents the ESP's for each test. The lower part shows the corresponding q–ε_a curve. As a reference the p'–q combination when ε_a reaches 2 % is indicated in figure 8.1 by the symbol +. The tests are ended when $\varepsilon_a = 15$ % is reached. Table 8.1 gives the angle in undrained ESP. The angle of ESP is found by application of the least squares method to the range of $q = 0$ to 4 kPa.

Table 8.1: The $\Delta p'/\Delta q$ value, between brackets the average values without test 167

at toe of dike		underneath the dike	
test nr	$\Delta p'/\Delta q$	test nr	$\Delta p'/\Delta q$
102	-0.18	47	-0.25
167	0.06	57	-0.32
135	-0.11	78	-0.29
160	-0.22	85	-0.21
175	-0.27	86	-0.24
152	-0.15	96	-0.34
average	-0.15		-0.28
	(-0.19)		

Table 8.1 shows a clear difference in $\Delta p'/\Delta q$ values for samples at the toe of the dike and underneath the dike. Soil investigation on the island of Marken shows that the peat layer is approximately 3.5 m thick at the toe of the dike, while underneath the dike the thickness is reduced to 2.1 m. This suggests that the weight of the dike has compressed the peat layer by approximately 40 %. This is of the same order in magnitude as used for the pre–consolidation in section 6.6.2.

The compression of the peat layer underneath the dike is also found in the actual values for W and ρ. As mentioned before a lower value or W is found underneath the dike, $W = 5.03$, than at the toe of the dike, $W = 7.64$. With $W = \rho_w n/\rho_s(1-n)$, the difference in W might indicate a pore volume reduction of approximately 35 %. This corresponds well to the global observation of a 40 % reduction in peat layer thickness. The difference in density also suggests a compression of

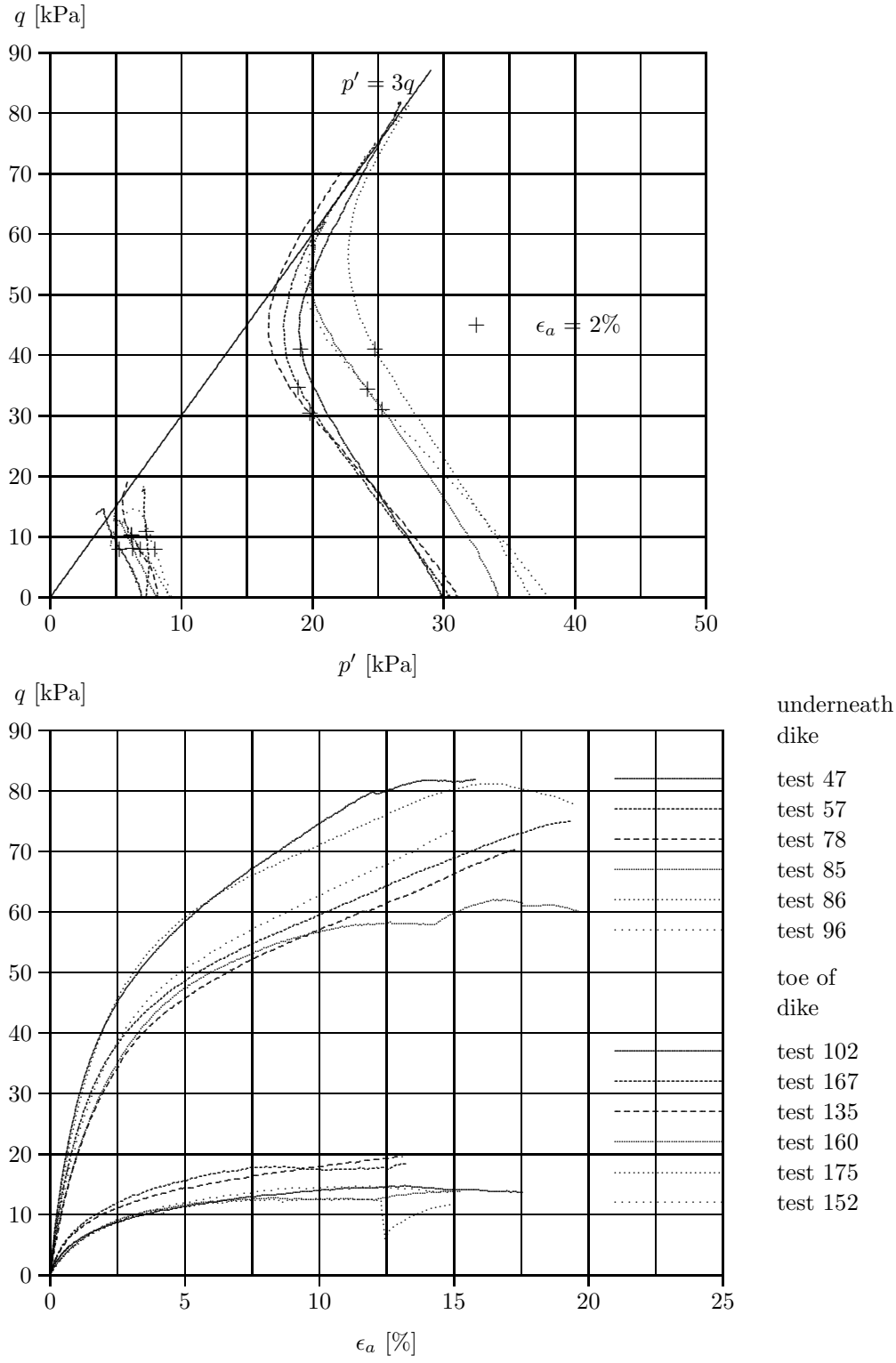

Figure 8.1: Results of triaxial tests on Marken peat, effective stress paths, ϵ_a = axial strain

the peat layer underneath the dike.

Section 6.6.2 shows an increase of $\Delta p'/\Delta q \approx 0$ for non-axial pre–consolidated samples to $\Delta p'/\Delta q \approx$ -0.2 to -0.4 pre–consolidated at $\varepsilon_a = 30$ %. The values for $\Delta p'/\Delta q$ presented by table 6.9 correspond to the values presented in table 8.1 for samples retrieved underneath the dike. The explanation for the difference in $\Delta p'/\Delta q$ found for the samples at the toe of the dike and underneath the dike can be explained by a difference in axial pre–consolidation.

Section 4.3.3 shows that -$\Delta p'/\Delta q$ corresponds directly to the K'/J' value. Chapter 7 explains the anisotropy of the large triaxial sample by the original deviator loading condition in the field. This explanation corresponds to results presented by table 8.1. The samples with a relatively large axial pre–loading due to the weight of the dike show a relatively large (negative) value while the samples with a low axial pre–loading, at the toe of the dike, show a small $\Delta p'/\Delta q$ value.

Expression (4.45) expresses the K'/J' value into E_h, E_v, ν_{vh} and ν_{hh}. A change in K'/J' value can be explained by a change in ratio E_h / E_v or a change in ν_{vh} and ν_{hh}. Chapter 6 and 7 show small values for ν_{vh}. For the Marken samples the ν_{vh} is not measured. Assuming ν_{vh} to be small for the Marken samples as well, the difference in K'/J' can be explained by a difference in ratio E_h/E_v.

8.3 Lateral stress reaction

Section 6.6.2 shows that axial pre–consolidation leads to an increase in anisotropy. The level in anisotropy changes such that radial deformation due to axial loading is reduced, indicating an increase in radial stiffness. In many soil models the stress path followed under natural compression is an important feature. The angle of this stress path is given by K_{0nc}. Conditions of natural compression are found when soil is loaded vertically while horizontal deformations are prevented. An oedometer test in which a soil sample is loaded vertically while placed in a stiff ring represents these conditions. The observation of section 6.6 that an increase in axial pre–consolidation leads to a change in level of anisotropy might influence the horizontal stress reaction. This section studies the influence of anisotropy on the development of K_{0nc}.

For linear elastic cross–anisotropic soil behaviour an expression for K_{0nc} follows from equation (3.9) and the boundary conditions $\varepsilon_{xx} = \varepsilon_{yy} = 0$.

$$K_{0nc} = \frac{\sigma'_h}{\sigma'_v} = \frac{E_h}{E_v}\frac{\nu_{vh}}{1-\nu_{hh}} \tag{8.1}$$

For isotropic conditions equation (8.1) reduces to the well known expression $K_{0nc} = \nu$ / (1 - ν). For anisotropic conditions equation (8.1) shows that an increase in ν_{vh}, ν_{hh} or E_h or a decrease in E_v leads to an increase in K_{0nc}. For a larger horizontal stiffness a larger horizontal stress reaction is needed to fulfil the boundary condition, $\varepsilon_h = 0$. Apparently the ratio ν_{vh} / (1 - ν_{hh}) represents the amount of radial strain while the ratio E_h/E_v gives the stress reaction to fulfil the boundary condition $\varepsilon_h = 0$.

For isotropic material behaviour K_{0nc} depends purely on ν. The maximum and minimum values for K_{0nc} are given by the maximum and minimum values for ν. For $\nu = 0$ is found $K_{0nc} = 0$, while $\nu = 0.5$ gives $K_{0nc} = 1$. Section 3.2 discusses the bounding values for the cross–anisotropic stiffness parameters. A minimum value for K_{0nc} is given by equation (8.1) when $\nu_{vh} = 0$. A maximum value for K_{0nc} is not found, since there is no upper boundary for E_h/E_v and the ratio ν_{vh} / (1 - ν_{hh}) has an infinite value when ν_{hh} reaches 1. Note that K_{0nc} exceeds 1 for realistic values for the stiffness parameters. If e.g. $\nu_{hh} = \nu_{vh} = 1/3$, K_{0nc} exceeds 1 for $E_h > 2E_v$.

For non pre–consolidated soil natural compression is accompanied with plasticity. To visualise the influence of anisotropy in linear elastic material behaviour on K_{0nc} the linear elastic material model described in chapter 3 is extended with a simple plastic model.

Wood [80] gives a mathematical description of the Cam–Clay model in terms of p' and q. By replacing the isotropic linear elastic part of the model by anisotropic elasticity the influence of

anisotropy on the K_{0nc} development can be estimated. It should be noted that in the description of plasticity, used in this section, no anisotropy is involved. This is found in the yield surface which is chosen symmetric around the p' axis and hardening is only given by an increase in isotropic effective stress p'_0. For reasons of simplicity the plastic deformations are expressed in terms of p' and q. With $\eta = q/p'$ and η_{nc} the angle of the natural compression line in p'–q diagram follows:

$$\eta_{nc} = \left(\frac{q}{p'}\right)_{nc} = \frac{3\,(1 - K_{0nc})}{1 + 2K_{0nc}}, \qquad K_{0nc} = \frac{3 - \eta_{nc}}{3 + 2\eta_{nc}} \tag{8.2}$$

Wood [80] shows that η_{nc} can be found from the ratio of volume and deviator strain. For axial symmetry the value for η_{nc} is found under the boundary condition $\varepsilon_r = 0$. The ratio of volumetric strain and deviator strain is then given by:

$$\frac{\delta e}{\delta \varepsilon_q} = \frac{\delta \varepsilon_a}{\frac{2}{3}\delta \varepsilon_a} = \frac{3}{2} \tag{8.3}$$

Equation (8.3) shows a constant ratio of volumetric strain and deviator strain for natural compression. The value for η which fulfils condition (8.3) represents η_{nc} and can be used to find K_{0nc} by equation (8.2). With total strain equal to the summation of elastic and plastic components it follows that:

$$\delta e = \delta e^e + \delta e^p, \qquad \delta \varepsilon_q = \delta \varepsilon_q^e + \delta \varepsilon_q^p$$

The elastic components of volume and deviator strain are given by equation (4.18), which is repeated here:

$$\begin{bmatrix} \delta e \\ \\ \delta \varepsilon_q \end{bmatrix} = \begin{bmatrix} \dfrac{1}{K'} & \dfrac{1}{J'} \\ \\ \dfrac{1}{J'} & \dfrac{1}{3G'} \end{bmatrix} \begin{bmatrix} \delta p' \\ \\ \delta q \end{bmatrix} \tag{8.4}$$

As stated before, it is assumed that anisotropy only influences the elastic part of strain. So a yield surface symmetric around the p' axis is chosen while hardening is determined by the isotropic pre–consolidation stress p'_0. Wood [80] gives for the Cam Clay model a yield surface by:

$$\frac{p'}{p'_0} = \frac{M^2}{M^2 + \eta^2} \tag{8.5}$$

The yield condition is then given by:

$$f = q^2 - M^2\left(p' p_0 - p'^2\right)$$

The assumption of an associated soil model gives for the plastic potential g, $g = f$. It is assumed that hardening is only due to a change in isotropic pre–consolidation. Equation (8.4) gives a linear relation between stress and strain. Extension to plasticity needs an extra parameter that gives the relation between volume and isotropic stress once plasticity occurs. Most soil models assume a logarithmic relation between volumetric strain and isotropic stress. The Cam–Clay model states v = - λ ln (p'), with $v = 1 + e$. In agreement with equation (8.4) a linear relation between p' and e is assumed for plasticity. This type of relation holds only for small increments of stress and strain. With the compression modulus for virgin loading equal to L the following is found:

$$\frac{\delta p'_0}{\delta e^p} = -\frac{LK'}{L - K'}, \qquad \frac{\delta p'_0}{\delta \varepsilon_q^p} = 0$$

The plastic strain is defined by the plastic multiplier χ, and the normal to the plastic potential:

$$\delta e^p = \chi \frac{\partial g}{\partial p'}, \qquad \delta \varepsilon_q^p = \chi \frac{\partial g}{\partial q}$$

χ is determined by the consistency condition $\mathrm{d}f = 0$:

$$\frac{\partial f}{\partial p'}\delta p' + \frac{\partial f}{\partial q}\delta q + \frac{\partial f}{\partial p'_0}\delta p'_0 = 0$$

and hardening rule:

$$\delta p'_0 = \frac{\partial p'_0}{\partial \varepsilon_p^p}\delta \varepsilon_p^p + \frac{\partial p'_0}{\partial \varepsilon_p^p}\delta \varepsilon_q^p$$

yields:

$$\chi = \frac{-\left(\dfrac{\partial f}{\partial p'}\delta p' + \dfrac{\partial f}{\partial q}\delta q\right)}{\dfrac{\partial f}{\partial p'_0}\left(\dfrac{\partial p'_0}{\partial e^p}\dfrac{\partial g}{\partial p'} + \dfrac{\partial p'_0}{\partial \varepsilon_q^p}\dfrac{\partial g}{\partial q}\right)}$$

Combination gives the plastic strain:

$$\begin{bmatrix} \delta e^p \\ \\ \delta \varepsilon_q^p \end{bmatrix} = \frac{-(L-K')}{M^2 L K'} \begin{bmatrix} \left(M^2-\eta^2\right) & 2\eta \\ \\ 2\eta & \dfrac{4\eta^2}{\left(M^2-\eta^2\right)} \end{bmatrix} \begin{bmatrix} \delta p' \\ \\ \delta q \end{bmatrix} \tag{8.6}$$

Summation of the elastic and plastic strain given by equations (8.4) and (8.6) in combination to condition (8.3) yields:

$$\frac{\delta e}{\delta \varepsilon_q} = \frac{\dfrac{-(L-K')}{M^2 L K'}\left(M^2-\eta_{nc}^2\right) - \dfrac{2\eta^2(L-K')}{M^2 L K'} + \dfrac{1}{K'} + \dfrac{\eta_{nc}}{J'}}{\dfrac{-(L-K')}{M^2 L K'}2\eta_{nc} - \dfrac{(L-K')}{M^2 L K'}\dfrac{4\eta_{nc}^3}{\left(M^2-\eta_{nc}^2\right)} + \dfrac{1}{J'} + \dfrac{\eta_{nc}}{3G'}} = \frac{3}{2} \tag{8.7}$$

From Equation (8.7) η_{nc} can be determined iteratively. Equation 8.7 shows that η_{nc} not only depends on the stiffness parameters, K', J', G' and L but also to the failure criteria by the parameter M. The parameter M is related to the angle of internal friction by $M = 6\ \sin(\phi')\ /(3\ -\ \sin(\phi'))$.

Figure 8.2 shows the development of K_{0nc} as a function of ϕ'. Equation (8.7) is elaborated for the seven cases explained by table 5.1, repeated by table 8.2, and three different K'/L values. Figure 8.2 shows that the influence of anisotropy in elastic parameters on the development of K_{0nc} is small. The actual value of K_{0nc} is dominated by the actual value for ϕ'. A well known relation between K_{0nc} and ϕ' is given by Jâcky as described by Wood [80]; $K_{0nc} = 1-\sin(\phi')$. This relation is given in each graph of figure 8.2.

For a reasonable value of $K'/L = 5$ equation (8.7) overestimates the value for K_{0nc} compared to the well known equation $K_{0nc} = 1\ -\ \sin(\phi')$. Wood [80] shows that this is a known feature of the Cam Clay model. For lower values of K'/L the K_{0nc} values predicted by equation (8.7) corresponds better to $K_{0nc} = 1\ -\ \sin(\phi')$. Also the differences between the cases a to g become more clear.

Chapter 5 introduces seven cases a to g to visualise the analytical solutions. Table 8.2 repeats these cases and shows the K_{0nc} value found by equation (8.1). The initial cases a to g lead to relatively small values for K_{0nc}. To illustrate that for reasonable values for E_h, E_v, ν_{hh} and ν_{vh} large values for K_{0nc} can be found, table 8.2 introduces an additional case h.

Table 8.2 and equation (8.1) shows a large influence of anisotropy on the K_{0nc} development when soil behaviour can be considered elastic. Due to anisotropy large deviations from the isotropic case are to be expected. For elastic soil behaviour the parameter ν_{vh} plays an important role. For ν_{vh} equals zero, K_{0nc} remains zero. Then K_{0nc} is independent from the values attained by ν_{hh} or the ratio E_h/E_v. For $\nu_{vh} > 0$, K_{0nc} might reach an infinite value since the ratio E_h/E_v has no upper limit and ν_{hh} might reach 1.

Equation (8.7) incorporates elastic and plastic parameters. This is a consequence of the assumption that for plastic soil behaviour the actual strain consists of a plastic and an elastic part.

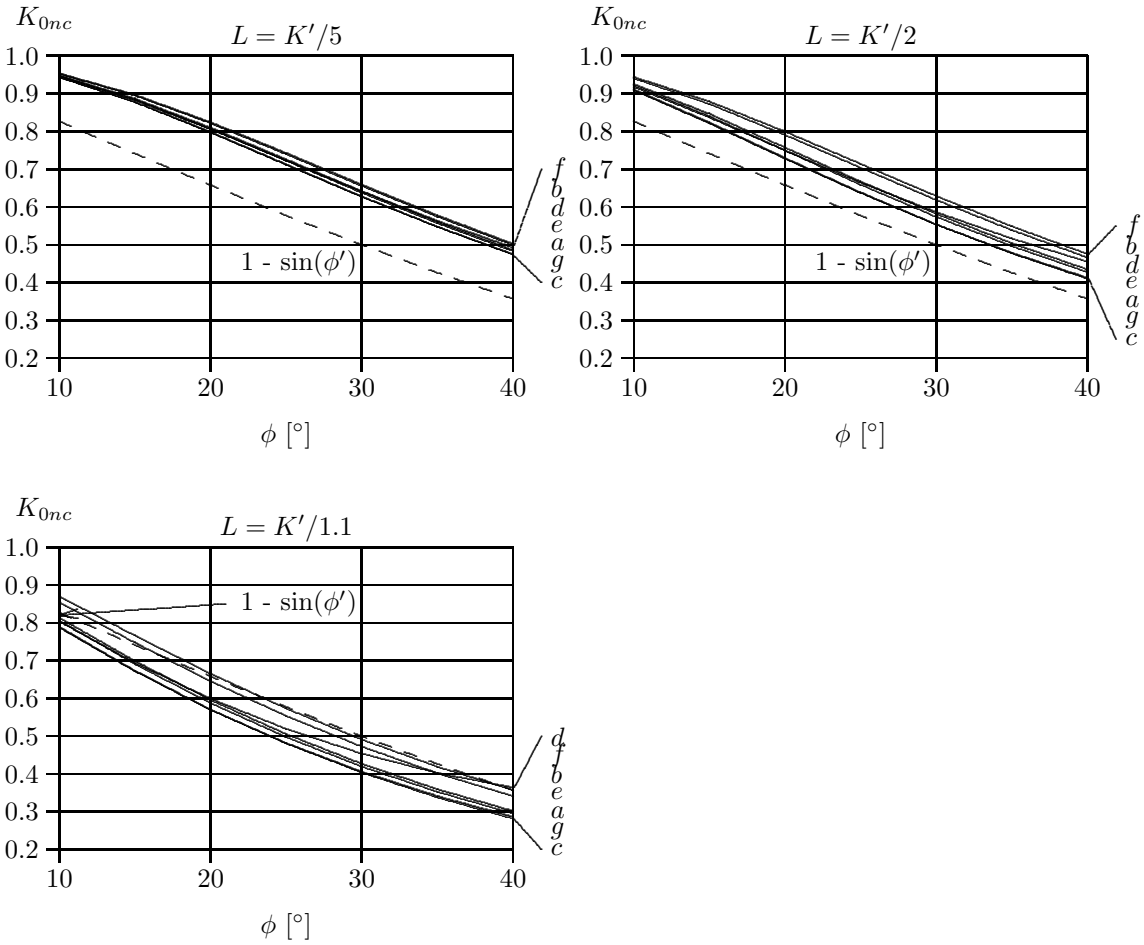

Figure 8.2: Development of K_{0nc} for different levels of anisotropy

Table 8.2: Seven cases presented by figure 8.2

case	E_h [kN/m^2]	E_v [kN/m^2]	ν_{hh} [-]	ν_{vh} [-]	K_{0nc} [-]
a (isotropic)	1000	1000	0	0	0
b	5000	1000	0	0	0
c	1000	5000	0	0	0
d	1000	1000	0	0.3	0.3
e	1000	1000	0.3	0	0
f	5000	1000	0.3	0	0
g	1000	5000	0	0.3	0.06
(h	5000	1000	0.3	0.3	2.14)

Despite this assumption figure 8.2 shows that the solution of equation (8.7) is nearly identical for the different cases a to g. So it can be concluded that as soon as plasticity is reached the parameters describing plasticity dominate the further development of K_{0nc}. Since in this section plasticity is assumed to be isotropic the differences found in figure 8.2 for the cases a to g are limited.

8.4 Consolidation around a vertical drain

To visualise the influence of anisotropy on the consolidation as observed in the field this section discusses consolidation behaviour of anisotropic soil around a vertical drain. Application of a different set of boundary conditions to the axial symmetric consolidation problem described in chapter 5 leads to the solution for the consolidation problem around vertical drains. The boundary conditions are sketched in figure 8.3, in which R represents the radius of the cylinder which is influenced by the drain. The parameter ρ represents the radius of the drain and q_r the expelled pore water flow. Equivalent to the solutions presented by chapter 5 a redistribution of stresses will occur. The surface remains flat, $\partial\varepsilon_{zz}/\partial r = 0$.

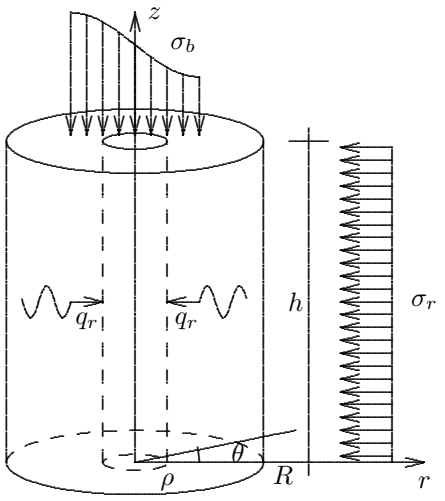

Figure 8.3: Problem definition for a vertical drain

Solutions to the consolidation problem around vertical drains for isotropic soil are given by Barron [10] and by De Leeuw [53]. Both solutions assume a flat surface. This is achieved in the Barron solution by incorporating an average pore pressure development. The De Leeuw solution is based on the Biot equations equivalent to the solution for the anisotropic case given in appendix G. In engineering practice the Barron solution is often used in combination to the average degree of consolidation U in which U is defined by:

$$U = \int_{\rho}^{R} \frac{2\pi r}{\pi\left(R^2 - \rho^2\right)} \frac{\sigma_w}{\sigma_b} \mathrm{d}r \tag{8.8}$$

Figure 8.4 shows a comparison between the Barron and the De Leeuw solution. Note that in this section the sign convention according to section 2.1 is adopted. For the average development of consolidation, (1 - U) versus T, the Barron and the De Leeuw solution predict an equivalent consolidation process. However at individual values for r and t differences occur. This is shown figure 8.4b. For the initial pore pressure reaction the Barron solution predicts a parabolic distribution of excess pore pressure in r direction. While for $t = 0^+$ on average $\sigma_w/\sigma_b = 1$, for $r = R$ the Barron solution predicts $\sigma_w/\sigma_b = 1.17$. In contrast the De Leeuw solution predicts $\sigma_w/\sigma_b = 1$ at all r except for $r = \rho$ due to the boundary condition of no excess pore pressure inside the drain, $\sigma_w/\sigma_b = 0$ at $r = \rho$.

Appendix G gives the extension of the De Leeuw solution to anisotropic conditions. Figure 8.5 shows the calculated pore pressure development found at $r = R$ for the seven cases presented by table 5.1, which is repeated by table 8.3. It should be noted that case a corresponds to the De Leeuw solution. As shown by De Leeuw [53] the isotropic solution does not show the Mandel-Cryer effect for realistic boundary conditions. Chapter 5 shows that presence of the Mandel–Cryer effect in the mathematical solution is explained by the integration coefficient $f(t)$. For $\partial f(t)/\partial t = 0$ the analytical solutions will not show a Mandel–Cryer effect. De Leeuw [53] gives for $f(t)$:

$$f(t) = -4G\frac{r\rho}{R^2 - \rho^2}\left(\frac{f_1}{\rho} - \frac{f_2}{R}\right) - f_3 - 2f_4$$

In which f_1 represents radial displacements at $r = R$, f_2 radial displacements at $r = \rho$, f_3 the load applied on top, $f_3 = \sigma_b$ and f_4 the water pressure in the drain.

Assuming enough drainage capacity f_4 remains zero during consolidation. In engineering practice the radial deformation at $r = \rho$ and $r = R$ can be disregarded. The function $f(t)$ reduces

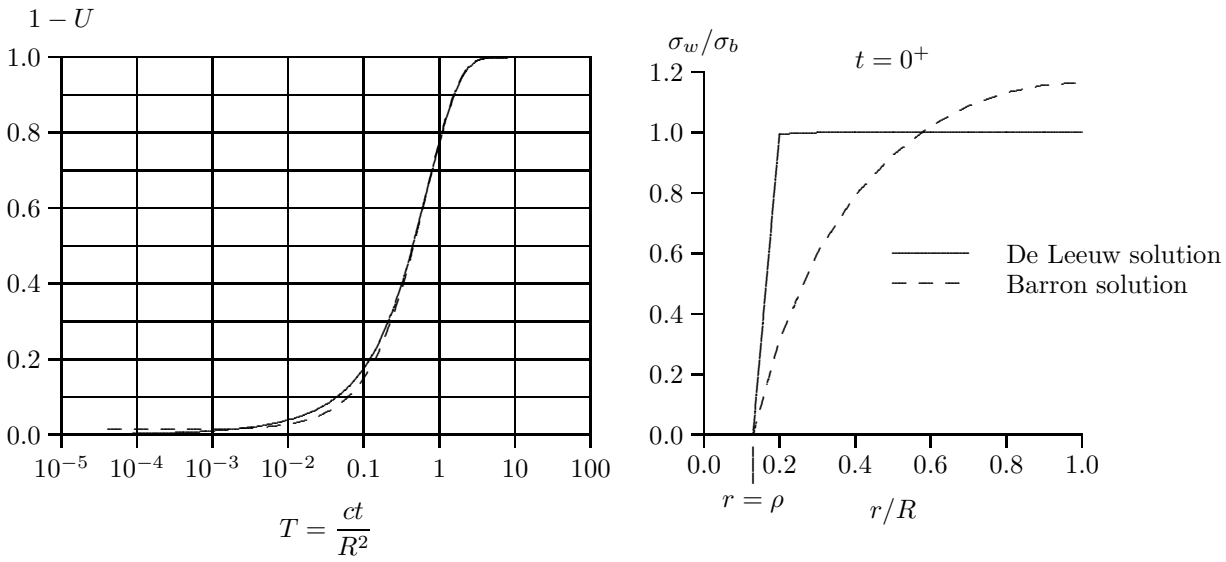

Figure 8.4: a) Development of U b) Initial pore pressure reaction

to -σ_b. After application the load remains constant and therefore $f(t)$ reduces to a constant. For anisotropic conditions $f(t)$ is expressed by equation (G.60). Equation (G.60) is a function of time even for constant boundary conditions.

Table 8.3: Seven cases for visualisation of the solutions of appendices G

case	E_h [kN/m^2]	E_v [kN/m^2]	ν_{hh} [-]	ν_{vh} [-]	$A + 2G_{hh}$ [kPa]
a (isotropic)	1000	1000	0	0	1000
b	5000	1000	0	0	5000
c	1000	5000	0	0	1000
d	1000	1000	0	0.3	1110
e	1000	1000	0.3	0	1099
f	5000	1000	0.3	0	5494.5
g	1000	5000	0	0.3	1019

Figure 8.5 clearly shows the influence of anisotropy. This influence extends beyond the influence of the coefficient of consolidation c. If the influence of anisotropy was limited to that of the coefficient of consolidation alone, the curves presented by figure 8.5 would be identical. For cases b and f a small Mandel–Cryer effect is found at $r = R$. These cases have the longest hydrodynamic period. Cases a, d and e represent the isotropic case respectively deviations in ν_{hh} and ν_{vh}. The influence of ν_{hh} and ν_{vh} appears to be small. Cases c and g show a rapid decay in excess pore pressure. The solution for case b converges badly for small values of t. This is shown by figure 8.5 by an initial $\sigma_w/\sigma_b < 1$ for case b.

Application of equation (8.8) to the anisotropic solution leads to the expression for the average degree of consolidation U for anisotropic conditions. Figure 8.6 shows the results. In the development of U the Mandel–Cryer effect is no longer visible. However the influence on the hydrodynamic period is still clearly shown. The cases c and g show a short hydrodynamic period while for b and f a relatively long period is found. Again case b converges badly for small values of t, shown in figure 8.6 by an initial (1 - U) > 0.

The coefficient of consolidation is given by $c = (A + 2G_{hh})k/\gamma_w$. The parameters k and γ_w are kept constant for each of the seven cases presented by table 8.3. Cases b and f have the largest

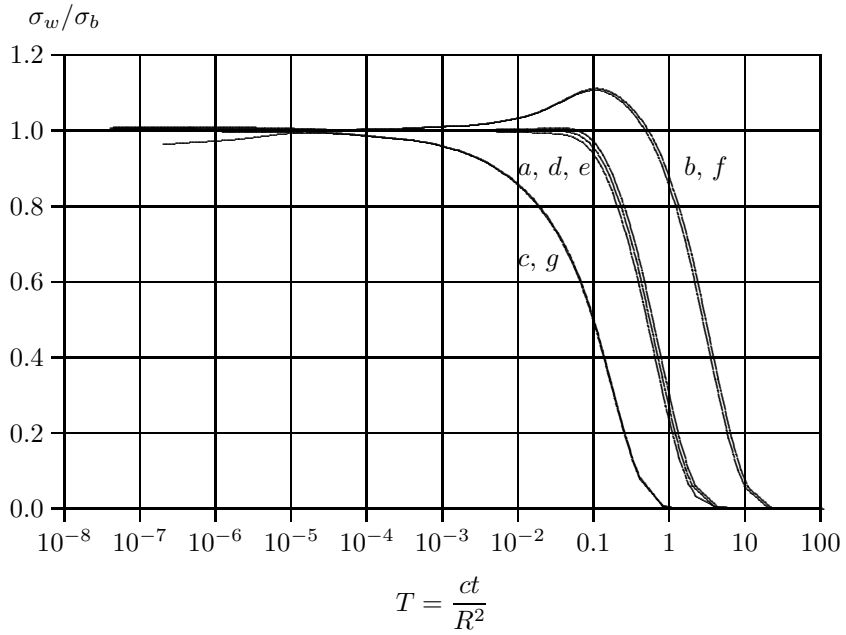

Figure 8.5: Pore pressure development for $r = R$ and $k = 1 \times 10^{-8}$ m/s

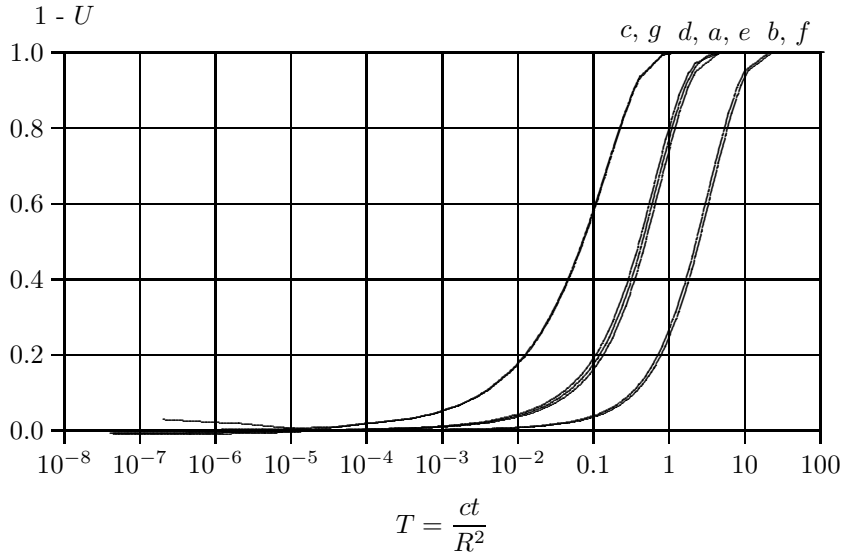

Figure 8.6: Average development of consolidation for cases a to g

value for $(A + 2G_{hh})$ and therefore the largest value for c. So a short hydrodynamic period is to be expected. In contrast figure 8.6 shows the largest hydrodynamic period for b and f. For cases c and g the value for $(A + 2G_{hh})$ is equivalent to the cases a, d and e. Nevertheless the hydrodynamic period for cases c and g is clearly shorter than found for the cases a, d and e. For the anisotropic cases the length of the hydrodynamic period is not only influenced by the coefficient of consolidation. To find the reason for the deviations in hydrodynamic period expressions for stress and strain around the vertical drain are derived.

In engineering practice deformations around vertical drains are only discussed in terms of vertical strain, settlement. With the solution presented in appendix G all stresses and strains

around a vertical drain can be derived. For two typical cases, f and g radial effective stress σ'_r, radial strain ε_r, radial displacement u_r, and volumetric strain e, are shown by figure 8.7. It should be noted that the tangential strain ε_θ, is related to the radial displacement by $\varepsilon_\theta = u_r/r$.

Figure 8.7 shows that radial deformations and radial strain are concentrated around the vertical drain. Initially the radial stress at $r = \rho$ equals the loading applied at the top while σ'_r remains unaltered at other locations along the radius. When consolidation progresses σ'_r first increases for small values for r and decreases for larger values for r. When consolidation progresses further σ'_r reduces to $K_0 \times \sigma_b$ with K_0 given by equation (8.1). For case $\nu_{vh} = 0$ and therefore K_0 and σ'_r reduce to 0. For case g $K_0 = 0.06$ and σ'_r/σ_b reduces to 0.06.

Due to the concentration of radial effective stress around the drain, radial strain is also concentrated around the drain as shown by the second part of figure 8.7. Development of ε_r is equivalent to σ'_r. Initially only at $r = \rho$ radial strain develops. As consolidation proceeds ε_r/σ_b is positive for small values for r and negative for R. For loading conditions σ_b is negative. So positive value for ε_r/σ_b gives a negative ε_r. This means that at early stages of the consolidation process the soil contracts around the drain and expands at the outer radius.

The third part of figure 8.7 shows the displacements to be expected around a vertical drain. According to the boundary conditions $u_r = 0$ at $r = \rho$ and $r = R$. The largest radial displacements are found at short distance of the drain. Initially after loading the radial displacements are negligible when consolidation progresses u_r increases first and decrease later until no radial displacements remain. The location of the maximum peak value moves from small values for r to large values for R. The location of the maximum radial displacement corresponds to the location at which ε_r changes sign.

The most remarkable difference between cases f and g is found in the development of volumetric strain. For case f is initially found $e = 0$ except at $r = \rho$. Only at $r = \rho$ the soil behaves initially drained and volumetric changes occur while the remaining soil behaves undrained and does not show any change in volume. When time progresses the volumetric strain progresses from the inner core to the outer radius until the final deformation is reached. For case g, at $r = \rho$, the initial volumetric strain exceeds its final value. When consolidation progresses the peak value reduces however the area for which the volumetric strain exceeds its final value increases. During a further development of consolidation volumetric strain develops to its final value leading to an expansion of the soil around the drain for case g. At the outer radius the soil still contracts. This expansion of the soil around the drain explains the relatively short consolidation period shown by figure 8.6.

It is therefore concluded that anisotropy in soft soil influences the consolidation behaviour of soft soil around a vertical drain. Depending on the ratio of horizontal to vertical stiffness the hydrodynamic period is longer or shorter than found for isotropic soil types. The difference in hydrodynamic period between isotropic and anisotropic soil is larger than expected from the difference in coefficient of consolidation alone, as shown by figure 8.6. If the influence of anisotropy on the consolidation behaviour did depend only on the coefficient of consolidation all graphs in figure 8.6 would be equivalent.

Anisotropy of soft soil influences the consolidation behaviour by development of the radial stress and strain that occurs around the drain. Soil tends to contract around the drain. This contraction is strongly influenced by the stiffness parameters. For $E_h/E_v < 1$ the contraction of soil around the drain is so strong that it overshoots the final volumetric strain. In a later phase of the consolidation process, for $E_h/E_v < 1$ the soil even expands around the drain leading to the considerable acceleration of pore pressure dissipation given by figure 8.6 for cases c and g.

The assumption of uniform vertical strain, $\partial\varepsilon_{zz}/\partial r = 0$, during consolidation is an important assumption. Without this assumption no redistribution of stress takes place and the phenomena discussed in this section will not be present. Measurements of a Mandel–Cryer peak inside a field of vertical drains are not known to the author. Deviations in hydrodynamic period are often found in practice. However, a large number of explanations can be found for the individual cases in which a possible redistribution of stresses in combination to anisotropy cannot be isolated.

If redistribution of stresses occurs in a field of drains and if it influences the consolidation

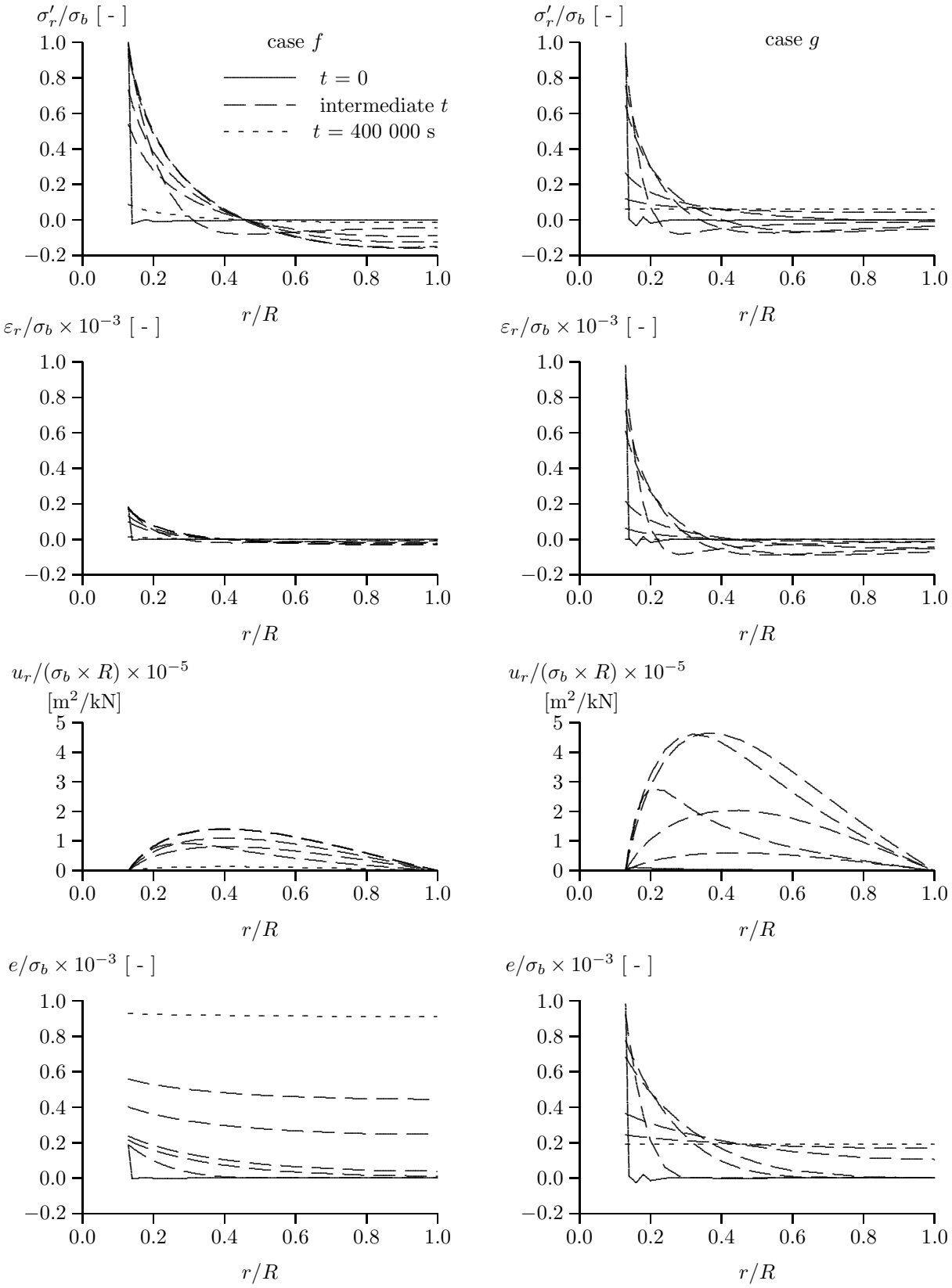

Figure 8.7: Radial effective stress and strain for cases f and g at $t = 0$, 500, 5 000, 10 000, 50 000, 100 000 and 400 000 s

development can only be established for special conditioned cases. An example of these special conditioned cases is a model test. Several model studies on the topic of consolidation around vertical drains are available.

Zwanenburg, Van & Brassinga [84] describe a centrifuge test in which consolidation around sand piles and sand walls is studied. In prototype measures the test set–up consists of 9 m thick clay layer, a 0.45 m thick sand layer on top and a 0.90 m thick sand layer underneath. The sand piles and walls are placed floating, with 0.90 m clay between sand pile or wall and lower sand layer, or non–floating when the sand pile or wall is placed on the lower sand layer. The clay consists of speswhite clay with a water content $W = 0.57$ - 0.58 and unit weight $\gamma = 16.3$ kN/m^2. The load is applied in three steps to a maximum of 100 kPa. For each configuration two pore pressure transducers are placed, one at 2.7 m below top side of the clay layer and one at 5.4 m. These locations correspond to 1/3 and 2/3 of the floating pile length. The transducers are placed at the middle between two sand piles or walls. Besides the pore pressure development settlement is measured at the original surface level at the middle between the piles or walls and at the top of the sand pile or wall.

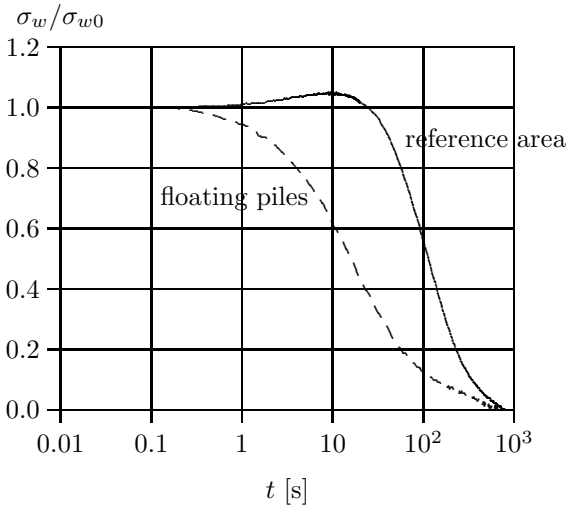

Figure 8.8: Measured pore pressure development in centrifuge test

The different configurations are tested in one test set–up. The available drainage field is separated in eight sections. Two sections involve sand walls, five sections involve sand piles. In one section no piles or walls are applied. This section is referred to as reference section. Measurements are conducted at the sand pile or wall located in the centre of the section. For the reference section measurements are conducted at the middle of the section.

The level of anisotropy of the speswhite clay is expected to be negligible. Therefore, according to the De Leeuw solution, no Mandel–Cryer peak is to be expected between the sand piles. This corresponds to figure 8.8, which shows a monotonic decay in pore pressure development in the clay in the floating drain section. In this section no Mandel–Cryer peak is found.

The reference section is connected at three sides to sections including sand piles. The horizontal distance between the pore pressure transducer in the reference section and the surrounding row of drains is of the same order in magnitude as the vertical distance to the upper and lower sand layer. It can therefore be concluded that pore water flow during consolidation will not be purely vertically.

Figure 8.8 shows the pore pressure development after the third loading phase. Despite the absence of a stiff plate on top the measurements show clearly a Mandel–Cryer peak. It can therefore be concluded that a stiff plate on top is not necessary for a redistribution of stresses. An alternative cause for a redistribution of stresses is internal friction. Friction is not considered in the analytical solutions presented by chapter 5. To which extend internal friction can be considered as a source for redistribution of stresses forms a topic a further study. So, depending on the actual geometry, influence of anisotropy in stiffness of soil that consolidates around a vertical drain is to be expected.

Appendix A

Compression of a solid sphere

In this appendix the volume loss of solid spheres due to indentation is studied. The results of this analysis are used in section 2.3.2 to determine the corresponding compressibility of solid particles. A mathematical analysis of dented spheres is presented by Timoshenko & Goodier [72].

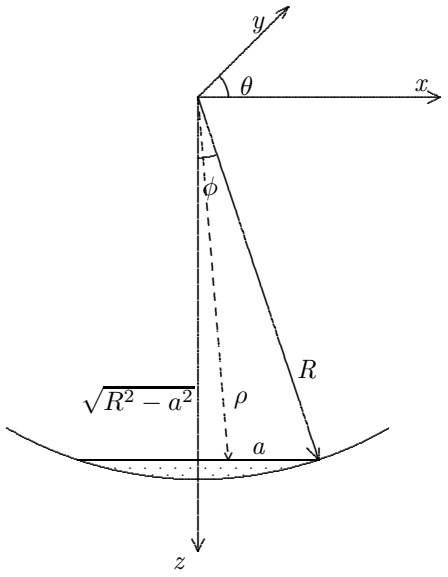

Figure A.1: Compression of a sphere, definition of parameters

Soil particles are simplified as perfect spheres. In a skeleton of spheres a specific sphere has a limited number of contact points where it touches its adjacent spheres. If the spheres are compressible they will be indented around these contact points. These indentations cause a volume loss. In figure A.1 a part of a sphere is drawn. In the centre point of the sphere the x, y and z co-ordinate system and the system in spherical co-ordinates, θ, ϕ and ρ are given. The shaded area is compressed due to the contact with a sphere below. The lower sphere does not need to be of equal size, however it still is a perfect sphere. The area of contact is a circle with a radius a. In this appendix first an expression for the radius of the dented area, a, is derived, followed by an expression for the volume of the dented area. In deriving this solution linear elastic behaviour is assumed and a is assumed to be small in comparison to radii of the individual spheres.

Consider two spheres in contact, figure A.2, the lower sphere with radius R_1 and the upper

sphere with radius R_2. If no pressure is applied there is contact in only one single point. In this contact point a plane O tangent to both spheres can be drawn. On a distance r a point M is located at the boundary of the lower sphere and a point N at the upper sphere. The distance from plane O to M is indicated by z_1 and to N by z_2. With $x_1 = R_1 - z_1$ an expression for z_1 can be found:

$$R_1 = \sqrt{r_1^2 + x^2} = z_1 + r_1$$

with:

$$z_1^2 \ll 1, \quad x_1 \simeq R_1$$

follows:

$$z_1 = \frac{r^2}{2R_1}$$

Equivalent for z_2:

$$z_2 = \frac{r^2}{2R_2}$$

The total distance between M and N becomes:

$$z_1 + z_2 = \frac{r^2}{2R_1} + \frac{r^2}{2R_2} = \frac{r^2\,(R_1 + R_2)}{2R_1R_2}$$

Compression in the direction normal to O by a force P creates a surface of contact. When holding plane O immovable the centre points of the spheres will approach each other by an amount α. The displacements w_1 and w_2 are caused by local deformation of the original contact point. The distance between M and N diminish by $\alpha - (w_1 + w_2)$. The points M and N are entering the contact surface when:

$$\alpha - (w_1 + w_2) = z_1 + z_2 = \beta r^2, \quad \beta = \frac{R_1 + R_2}{2R_2R_2} \tag{A.1}$$

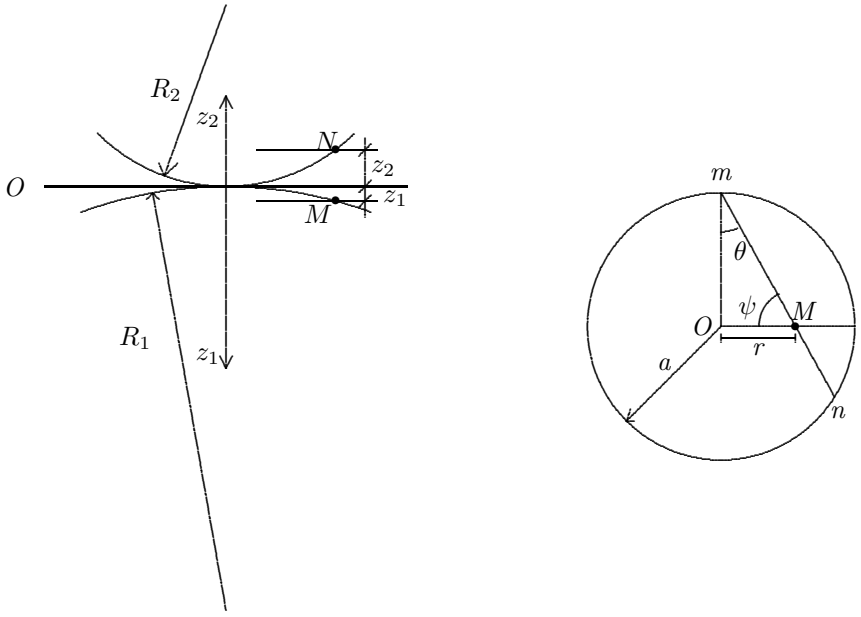

Figure A.2: Two spherical bodies in contact A) side view B) top view on contact area

When creating the area of contact, with q representing the contact pressure it is found:

$$w_1 = \frac{1-\nu_1^2}{\pi E_1} \int\int q \mathrm{d}s \mathrm{d}\psi$$

with:

$$k_1 = \frac{1-\nu_1^2}{\pi E_1}, \quad k_2 = \frac{1-\nu_2^2}{\pi E_2}$$

it holds:

$$w_1 + w_2 = (k_1 + k_2) \int\int q \mathrm{d}s \mathrm{d}\psi = \alpha - \beta r^2 \tag{A.2}$$

So the next step is to find a pressure distribution q that fulfils equation (A.2). It can be shown that a distribution of pressure q over the contact surface is represented by the ordinates of a hemisphere of radius a constructed on the surface of contact. If q_0 represents the pressure at the centre of the contact surface then

$$q_0 = ka$$

In which k is a constant factor representing the scale of the problem. So if the pressure in the centre, q_0, increases, the contact surface increases with the same amount. In figure A.2 the top view of the contact surface is presented. The contact surface has a radius a and a centre point O. The points m and n are arbitrary points on the boundary and M on the chord mn. Since the pressure distribution has the shape of a hemisphere, the pressure distribution on top of the chord mn has the shape of half a circle with radius R. The line from point O perpendicular to the line mn divides mn in two equal parts. The radius R can then be expressed by: $R = a\cos\theta$. Since q_0/a is a scale factor representing the scale of the problem the pressure active upon the chord mn is given by:

$$\int q_0 \mathrm{d}s = \frac{q_0}{a} A$$

In which A represents the area between the chord mn and the upper boundary of the pressure distribution. A is then given by:

$$A = \frac{1}{2}\pi R^2 = \frac{1}{2}\pi \left(a\cos\theta\right)^2 = \frac{1}{2}\pi a^2 \left(1 - \sin^2\theta\right)$$

From figure A.2 it is found that $a\sin\theta = r\sin\psi$:

$$A = \frac{1}{2}\pi \left(a^2 - r^2 sin^2\psi\right)$$

Application in equation (A.2) gives:

$$(w_1 + w_2) = (k_1 + k_2) \int \frac{q_0}{a} A \mathrm{d}\psi$$

$$(w_1 + w_2) = (k_1 + k_2) \int_0^{\pi} \frac{q_0}{a} \frac{1}{2}\pi \left(a^2 - r^2 sin^2\psi\right) \mathrm{d}\psi$$

$$(w_1 + w_2) = \frac{\pi q_0}{2a} (k_1 + k_2) \int_0^{\pi} \left(a^2 - r^2 sin^2\psi\right) \mathrm{d}\psi$$

With $\sin^2\psi = \frac{1}{2} - \frac{1}{2}\cos 2\psi$ it follows:

$$(w_1 + w_2) = \frac{\pi q_0}{2a} (k_1 + k_2) \left[a^2\psi - \frac{r^2\psi}{2} + \frac{1}{2}\cdot\frac{1}{2}\sin 2\psi\right]_{\psi=0}^{\psi=\pi}$$

Finally it is found that:

$$(w_1 + w_2) = \frac{\pi^2 q_0}{4a}(k_1 + k_2)\left(2a^2 - r^2\right) = \alpha - \beta r^2$$

This equation will be fulfilled for any value of r and therefore the assumed pressure distribution is the correct one if the following relations exist for α and a:

$$a = (k_1 + k_2)\frac{\pi^2 q_0}{4\beta} \tag{A.3}$$

$$\alpha = (k_1 + k_2)\frac{\pi^2 q_0 a}{2} \tag{A.4}$$

with:

$$k_1 = \frac{1 - \nu_1^2}{\pi E_1}, \qquad k_2 = \frac{1 - \nu_2^2}{\pi E_2}$$

When both spheres consist of the same material it is found that $E_1 = E_2$ and $\nu_1 = \nu_2$. The radius of contact area is then given by equation (A.5):

$$a = \frac{1 - \nu^2}{E}\frac{R_1 R_2 \pi}{R_1 + R_2} q_0 = \beta^* q_0 \tag{A.5}$$

For some value for a the volume lost by compression of one sphere, V_{sp} is found by a volume integral. According to figure A.1 this volume integral in spherical coordinates is given by equation (A.6).

$$V_{sp} = \int_{\theta=0}^{\theta=2\pi}\int_{\phi=0}^{\phi=\phi_1}\int_{\rho=\rho_1}^{\rho=R} \rho^2 \sin(\phi)\mathrm{d}\rho\,\mathrm{d}\phi\,\mathrm{d}\theta \tag{A.6}$$

with:

$$\phi_1 = \sin^{-1}\left(\frac{a}{R}\right), \quad \rho_1 = \frac{\sqrt{R^2 - a^2}}{\cos(\phi)}$$

Elaboration of this integral results in:

$$V_{sp} = 2\pi\left[\frac{1}{3}R^3 - \frac{1}{3}R^2\sqrt{R^2 - a^2} + \frac{1}{3}\left(R^2 - a^2\right)\sqrt{R^2 - a^2}\ln\left(\frac{\sqrt{R^2 - a^2}}{R}\right)\right] \tag{A.7}$$

In equation (A.7) the volume lost by denting is presented as a function of a. In equation (A.5) a is presented as a function of q_0, in which q_0 is the top of the pressure distribution. The average value of the contact pressure, q_{av} becomes:

$$q_{av} = \frac{\frac{q_0}{a}\frac{1}{2}\frac{4}{3}\pi a^2}{\pi a^2} = \frac{2}{3}q_0$$

Appendix B

Lamé constants for cross–anisotropy

A familiar way to express stress in terms volumetric strain and distortional strain for an isotropic linear elastic material is given by equation (B.1), see [72]:

$$\sigma'_{ij} = \lambda e \delta_{ij} + 2\mu\varepsilon_{ij} \tag{B.1}$$

In which λ and μ are known as Lamé constants:

$$\lambda = K + \frac{2}{3}G = \frac{\nu E}{(1+\nu)(1-2\nu)}, \quad \mu = G = \frac{E}{2(1+\nu)}$$

In this appendix Lamé - like constants are derived for cross–anisotropy. Equation 3.9, repeated below, gives the full description of Hooke's law for cross–anisotropic conditions.

$$\begin{pmatrix} \varepsilon_{xx} \\ \varepsilon_{yy} \\ \varepsilon_{zz} \\ \gamma_{xy} \\ \gamma_{yz} \\ \gamma_{zx} \end{pmatrix} = \begin{pmatrix} \frac{1}{E_h} & \frac{-\nu_{hh}}{E_h} & \frac{-\nu_{vh}}{E_v} & 0 & 0 & 0 \\ \frac{-\nu_{hh}}{E_h} & \frac{1}{E_h} & \frac{-\nu_{vh}}{E_v} & 0 & 0 & 0 \\ \frac{-\nu_{vh}}{E_v} & \frac{-\nu_{vh}}{E_v} & \frac{1}{E_v} & 0 & 0 & 0 \\ 0 & 0 & 0 & \frac{1}{G_{hh}} & 0 & 0 \\ 0 & 0 & 0 & 0 & \frac{1}{G_{vh}} & 0 \\ 0 & 0 & 0 & 0 & 0 & \frac{1}{G_{vh}} \end{pmatrix} \begin{pmatrix} \sigma'_{xx} \\ \sigma'_{yy} \\ \sigma'_{zz} \\ \tau_{xy} \\ \tau_{yz} \\ \tau_{zx} \end{pmatrix} \tag{B.2}$$

The inverse gives:

$$\begin{bmatrix} \sigma'_{xx} \\ \sigma'_{yy} \\ \sigma'_{zz} \\ \tau_{xy} \\ \tau_{yz} \\ \tau_{zx} \end{bmatrix} = \begin{bmatrix} M_{11} & M_{12} & M_{13} & 0 & 0 & 0 \\ M_{21} & M_{22} & M_{23} & 0 & 0 & 0 \\ M_{31} & M_{23} & M_{33} & 0 & 0 & 0 \\ 0 & 0 & 0 & G_{hh} & 0 & 0 \\ 0 & 0 & 0 & 0 & G_{vh} & 0 \\ 0 & 0 & 0 & 0 & 0 & G_{vh} \end{bmatrix} \begin{bmatrix} \varepsilon_{xx} \\ \varepsilon_{yy} \\ \varepsilon_{zz} \\ \gamma_{xy} \\ \gamma_{yz} \\ \gamma_{zx} \end{bmatrix}$$

with:

$$\begin{aligned} M_{11} = M_{22} &= \frac{E_h \left[E_v - E_h \nu_{vh}^2\right]}{(1+\nu_{hh}) \left[E_v (1-\nu_{hh}) - 2E_h \nu_{vh}^2\right]} \\ M_{12} = M_{21} &= \frac{E_h \left(\nu_{hh} E_v + E_h \nu_{vh}^2\right)}{(1+\nu_{hh}) \left[E_v (1-\nu_{hh}) - 2E_h \nu_{vh}^2\right]} \\ M_{13} = M_{31} = M_{32} = M_{23} &= \frac{E_h E_v \nu_{vh}}{E_v (1-\nu_{hh}) - 2E_h \nu_{vh}^2} \\ M_{33} &= \frac{E_v^2 (1-\nu_{hh})}{E_v (1-\nu_{hh}) - 2E_h \nu_{vh}^2} \end{aligned} \tag{B.3}$$

The volumetric strain is presented by:

$$e = \varepsilon_{xx} + \varepsilon_{yy} + \varepsilon_{zz}$$

Together with equation (B.2) it can be found that:

$$\begin{aligned} e &= \frac{\sigma'_{xx}}{E_h} - \frac{\nu_{hh}\sigma'_{yy}}{E_h} - \frac{\nu_{vh}\sigma'_{zz}}{E_v} - \frac{\nu_{hh}\sigma'_{xx}}{E_h} + \frac{\sigma'_{yy}}{E_h} - \frac{\nu_{vh}\sigma'_{zz}}{E_v} - \frac{\nu_{vh}\sigma'_{xx}}{E_v} - \frac{\nu_{vh}\sigma'_{yy}}{E_v} + \frac{\sigma'_{zz}}{E_v} \\ e &= \sigma'_{xx}\left[\frac{1-\nu_{hh}}{E_h} - \frac{\nu_{vh}}{E_v}\right] + \sigma'_{yy}\left[\frac{1-\nu_{hh}}{E_h} - \frac{\nu_{vh}}{E_v}\right] + \sigma'_{zz}\left[\frac{1-2\nu_{vh}}{E_v}\right] \\ \sigma'_{xx} &= e\left[\frac{E_h E_v}{E_v(1-\nu_{hh}) - E_h \nu_{vh}}\right] - \sigma'_{yy} - \sigma'_{zz}\frac{1-2\nu_{vh}}{E_v}\frac{E_h E_v}{E_v(1-\nu_{hh}) - E_h\nu_{vh}} \end{aligned} \tag{B.4}$$

The second row of equation (B.2) gives:

$$\begin{aligned} \varepsilon_{yy} &= \frac{-\nu_{hh}\sigma'_{xx}}{E_h} + \frac{\sigma'_{yy}}{E_h} - \frac{\nu_{vh}\sigma'_{zz}}{E_v} \\ -\frac{\sigma'_{yy}}{E_h} &= \frac{-\nu_{hh}\sigma'_{xx}}{E_h} - \varepsilon_{yy} - \frac{\nu_{vh}\sigma'_{zz}}{E_v} \\ \sigma'_{yy} &= \nu_{hh}\sigma'_{xx} + E_h\varepsilon_{yy} + \frac{E_h}{E_v}\nu_{vh}\sigma'_{zz} \end{aligned} \tag{B.5}$$

The third row of equation (B.2) gives:

$$\begin{aligned} \varepsilon_{zz} &= \frac{-\nu_{vh}\sigma'_{xx}}{E_v} - \frac{\nu_{vh}\sigma'_{yy}}{E_v} + \frac{\sigma'_{zz}}{E_v} \\ \frac{-\sigma'_{zz}}{E_v} &= -\varepsilon_{zz} - \frac{\nu_{vh}\sigma'_{xx}}{E_v} - \frac{\nu_{vh}\sigma'_{yy}}{E_v} \\ \sigma'_{zz} &= E_h\varepsilon_{zz} + \nu_{vh}\sigma'_{xx} + \nu_{vh}\sigma'_{yy} \end{aligned} \tag{B.6}$$

Equation (B.4) and (B.5) give:

$$\sigma'_{zz} = E_v\varepsilon_{zz} + \nu_{vh}\left[\frac{E_h E_v}{E_v(1-\nu_{hh}) - E_h\nu_{vh}}e - \sigma'_{yy} - \frac{E_h(1-2\nu_{vh})}{E_v(1-\nu_{hh}) - E_h\nu_{vh}}\sigma'_{zz}\right] + \nu_{vh}\sigma'_{yy}$$

reformulating:

$$\sigma'_{zz} = Ce + D\varepsilon_{zz} \tag{B.7}$$

with:

$$C = \frac{\nu_{vh} E_h E_v}{E_v (1 - \nu_{hh}) - 2E_h \nu_{vh}^2}$$
$$D = \frac{E_v^2 (1 - \nu_{hh}) - E_h E_v \nu_{vh}}{E_v (1 - \nu_{hh}) - 2E_h \nu_{vh}^2}$$

The first row of equation (B.2) gives:

$$\varepsilon_{xx} = \frac{\sigma'_{xx}}{E_h} - \frac{\nu_{hh}\sigma'_{yy}}{E_h} - \frac{\nu_{vh}\sigma'_{zz}}{E_v}$$

$$\sigma'_{xx} = E_h \varepsilon_{xx} + \nu_{hh}\sigma'_{yy} + \frac{E_h}{E_v}\nu_{vh}\sigma'_{zz} \tag{B.8}$$

Combination of equation (B.5) and (B.8) gives:

$$\sigma'_{yy} = \nu_{hh}\left[E_h \varepsilon_{xx} + \nu_{hh}\sigma'_{yy} + \frac{E_h}{E_v}\nu_{vh}\sigma'_{zz}\right] + E_h \varepsilon_{yy} + \frac{E_h}{E_v}\nu_{vh}\sigma'_{zz}$$
$$\sigma'_{yy}\left(1 - \nu_{hh}^2\right) = \nu_{hh} E_h \varepsilon_{xx} + E_h \varepsilon_{yy} + \frac{E_h}{E_v}\nu_{vh}\sigma'_{zz}\left(1 + \nu_{hh}\right)$$
$$\text{with } \left(1 - \nu_{hh}^2\right) = \left(1 - \nu_{hh}\right)\left(1 + \nu_{hh}\right):$$

$$\sigma'_{yy} = \frac{\nu_{hh} E_h}{1 - \nu_{hh}^2}\varepsilon_{xx} + \frac{E_h}{1 - \nu_{hh}^2}\varepsilon_{yy} + \frac{E_h}{E_v}\frac{\nu_{vh}}{1 - \nu_{hh}}\sigma'_{zz} \tag{B.9}$$

Combination of (B.7) and (B.9) gives:

$$\sigma'_{yy} = \frac{\nu_{hh} E_h}{1 - \nu_{hh}^2}\varepsilon_{xx} + \frac{E_h}{1 - \nu_{hh}^2}\varepsilon_{yy} + \frac{\nu_{vh}^2 E_h^2\left[E_v - \dfrac{E_h \nu_{vh}}{1 - \nu_{hh}}\right] e}{\left[E_v (1 - \nu_{hh}) - E_h \nu_{vh}\right]\left[E_v (1 - \nu_{hh}) - 2E_h \nu_{vh}^2\right]} + \frac{\nu_{vh} E_h E_v - \dfrac{\nu_{vh}^2 E_h^2}{1 - \nu_{hh}}}{E_v (1 - \nu_{hh}) - 2E_h \nu_{vh}^2}\varepsilon_{zz}$$

with:

$$\varepsilon_{xx} = e - \varepsilon_{yy} - \varepsilon_{zz}$$

$$\sigma'_{yy} = \frac{\nu_{hh} E_h}{1 - \nu_{hh}^2} e - \frac{\nu_{hh} E_h}{1 - \nu_{hh}^2}\varepsilon_{yy} + \frac{E_h}{1 - \nu_{hh}^2}\varepsilon_{yy} - \frac{\nu_{hh} E_h}{1 - \nu_{hh}^2}\varepsilon_{zz} + \frac{\nu_{vh} E_h E_v - \dfrac{\nu_{vh}^2 E_h^2}{1 - \nu_{hh}}}{E_v (1 - \nu_{hh}) - 2E_h \nu_{vh}^2}\varepsilon_{zz} + \frac{\nu_{vh}^2 E_h^2\left[E_v - \dfrac{E_h \nu_{vh}}{1 - \nu_{hh}}\right] e}{\left[E_v (1 - \nu_{hh}) - E_h \nu_{vh}\right]\left[E_v (1 - \nu_{hh}) - 2E_h \nu_{vh}^2\right]}$$

reformulation gives:

$$\sigma'_{yy} = Ae + 2G_{hh}\varepsilon_{yy} + B\varepsilon_{zz} \tag{B.10}$$

with:

$$
\begin{aligned}
A &= \frac{\nu_{hh}E_h}{1-\nu_{hh}^2} + \frac{\nu_{vh}^2E_h^2\left[E_v - \dfrac{E_h\nu_{vh}}{1-\nu_{hh}}\right]}{\left[E_v\left(1-\nu_{hh}\right)-E_h\nu_{vh}\right]\left[E_v\left(1-\nu_{hh}\right)-2E_h\nu_{vh}^2\right]} = \\
&= \frac{\nu_{hh}E_hE_v+\nu_{vh}^2E_h^2}{\left(1+\nu_{hh}\right)\left[E_v\left(1-\nu_{hh}\right)-2E_h\nu_{vh}^2\right]} \\
B &= \frac{\nu_{vh}E_hE_v - \dfrac{\nu_{vh}^2E_h^2}{1-\nu_{hh}}}{E_v\left(1-\nu_{hh}\right)-2E_h\nu_{vh}^2} - \frac{\nu_{hh}E_h}{1-\nu_{hh}^2} = \frac{E_hE_v\left[\nu_{vh}\left(1+\nu_{hh}\right)-\nu_{hh}\right]-E_h^2\nu_{vh}^2}{\left(1+\nu_{hh}\right)\left[E_v\left(1-\nu_{hh}\right)-2E_h\nu_{vh}^2\right]} \\
G_{hh} &= \frac{E_h}{2\left(1+\nu_{hh}\right)}
\end{aligned}
$$

The combination of equation (B.7), (B.8) and (B.10) gives:

$$
\begin{aligned}
\sigma'_{xx} &= E_h\varepsilon_{xx} + \nu_{hh}\sigma'_{yy} + \frac{E_h}{E_v}\nu_{vh}\sigma'_{zz} \\
\sigma'_{xx} &= E_h\varepsilon_{xx} + \nu_{hh}Ae + \frac{\nu_{hh}E_h}{1+\nu_{hh}}\varepsilon_{yy} + \nu_{hh}B\varepsilon_{zz} + \frac{E_h}{E_v}\nu_{vh}\left(Ce+D\varepsilon_{zz}\right)
\end{aligned}
$$

with: $\varepsilon_{yy} = e - \varepsilon_{xx} - \varepsilon_{zz}$

$$
\begin{aligned}
\sigma'_{xx} &= E_h\varepsilon_{xx} + \nu_{hh}Ae + \frac{\nu_{hh}E_h}{1+\nu_{hh}}\left(e-\varepsilon_{xx}-\varepsilon_{zz}\right) + \nu_{hh}B\varepsilon_{zz} + \frac{E_h\nu_{vh}}{E_v}Ce + \frac{E_h\nu_{vh}}{E_v}D\varepsilon_{zz} \\
\sigma'_{xx} &= \left[\nu_{hh}A + \frac{\nu_{hh}E_h}{1+\nu_{hh}} + \frac{E_h\nu_{vh}}{E_v}C\right]e + \left[E_h - \frac{\nu_{hh}E_h}{1+\nu_{hh}}\right]\varepsilon_{xx} + \\
&\left[\nu_{hh}B + \frac{E_h\nu_{vh}}{E_v}D - \frac{\nu_{hh}E_h}{1+\nu_{hh}}\right]\varepsilon_{zz}
\end{aligned}
$$

Reformulation of the individual terms gives:

$$
\begin{aligned}
&\left[\nu_{hh}A + \frac{\nu_{hh}E_h}{1+\nu_{hh}} + \frac{E_h\nu_{vh}}{E_v}C\right] = \frac{\nu_{hh}^2E_h}{1-\nu_{hh}^2} + \frac{\nu E_h\left(1-\nu_{hh}\right)}{\left(1-\nu_{hh}\right)\left(1+\nu_{hh}\right)} + \\
&\frac{\nu_{hh}\nu_{vh}^2E_h^2}{\left(1-\nu_{hh}\right)\left[E_v\left(1-\nu_{hh}\right)-2E_h\nu_{vh}^2\right]} + \frac{E_h\nu_{vh}}{E_v}\frac{\nu_{vh}E_hE_v}{E_v\left(1-\nu_{hh}\right)-2E_h\nu_{vh}^2} = \\
&\frac{\nu_{hh}E_h}{1-\nu_{hh}^2} + \frac{\nu_{hh}\nu_{vh}^2E_h^2-\nu_{hh}\nu_{vh}^2E_h^2+\nu_{vh}^2E_h^2}{\left(1-\nu_{hh}\right)\left[E_v\left(1-\nu_{hh}\right)-2E_h\nu_{vh}^2\right]} = \frac{\nu_{hh}E_h}{1-\nu_{hh}^2} + \\
&\qquad\frac{\nu_{vh}^2E_h^2}{\left(1-\nu_{hh}\right)\left[E_v\left(1-\nu_{hh}\right)-2E_h\nu_{vh}^2\right]} = \frac{\nu_{hh}E_hE_v+\nu_{vh}^2E_h^2}{\left(1+\nu_{hh}\right)\left[E_v\left(1-\nu_{hh}\right)-2E_h\nu_{vh}^2\right]} = A
\end{aligned}
$$

$$
E_h - \frac{\nu_{hh}E_h}{1+\nu_{hh}} = \frac{E_h\left(1+\nu_{hh}\right)-\nu_{hh}E_h}{1+\nu_{hh}} = \frac{E_h}{1+\nu_{hh}} = 2G_{hh}
$$

$$
\begin{aligned}
&\left[\nu_{hh}B + \frac{E_h\nu_{vh}}{E_v}D - \frac{\nu_{hh}E_h}{1+\nu_{hh}}\right] = \frac{\nu_{hh}E_hE_v\left[\nu_{vh}\left(1+\nu_{hh}\right)-\nu_{hh}\right]-\nu_{hh}\nu_{vh}^2E_h^2}{\left(1+\nu_{hh}\right)\left[E_v\left(1-\nu_{hh}\right)-2E_h\nu_{vh}^2\right]} + \\
&\frac{E_h\nu_{vh}}{E_v}\frac{E_v^2\left(1-\nu_{hh}\right)-E_hE_v\nu_{vh}}{E_v\left(1-\nu_{hh}\right)-2E_h\nu_{vh}^2} - \frac{\nu_{hh}E_h}{1+\nu_{hh}} = \\
&\qquad\frac{E_hE_v\left[\nu_{vh}\left(1+\nu_{hh}\right)-\nu_{hh}\right]-\nu_{vh}^2E_h^2}{\left(1+\nu_{hh}\right)\left[E_v\left(1-\nu_{hh}\right)-2E_h\nu_{vh}^2\right]} = B
\end{aligned}
$$

and is finally found:

$$
\sigma'_{xx} = Ae + 2G_{hh}\varepsilon_{xx} + B\varepsilon_{zz} \tag{B.11}
$$

The results can be summarised to:

$$\begin{aligned}\sigma'_{xx} &= Ae + 2G\varepsilon_{xx} + B\varepsilon_{zz}\\ \sigma'_{yy} &= Ae + 2G\varepsilon_{yy} + B\varepsilon_{zz}\\ \sigma'_{zz} &= Ce + D\varepsilon_{zz}\end{aligned} \tag{B.12}$$

with:

$$\begin{aligned}A &= \frac{\nu_{hh}E_hE_v + \nu_{vh}^2E_h^2}{(1+\nu_{hh})\left[E_v\left(1-\nu_{hh}\right) - 2E_h\nu_{vh}^2\right]}\\ B &= \frac{E_hE_v\left[\nu_{vh}\left(1+\nu_{hh}\right) - \nu_{hh}\right] - \nu_{vh}^2E_h^2}{(1+\nu_{hh})\left[E_v\left(1-\nu_{hh}\right) - 2E_h\nu_{vh}^2\right]}\\ C &= \frac{\nu_{vh}E_hE_v}{E_v\left(1-\nu_{hh}\right) - 2E_h\nu_{vh}^2}\\ D &= \frac{E_v^2\left(1-\nu_{hh}\right) - E_hE_v\nu_{vh}}{E_v\left(1-\nu_{hh}\right) - 2E_h\nu_{vh}^2}\\ 2G_{hh} &= \frac{E_h}{1+\nu_{hh}}\end{aligned}$$

After some elaboration it can be found that C = A + B:

$$\begin{aligned}A+B &= \frac{\nu_{hh}E_hE_v + \nu_{vh}^2E_h^2}{(1+\nu_{hh})\left[E_v\left(1-\nu_{hh}\right) - 2E_h\nu_{vh}^2\right]} + \frac{E_hE_v\left[\nu_{vh}\left(1+\nu_{hh}\right) - \nu_{hh}\right] - \nu_{vh}^2E_h^2}{(1+\nu_{hh})\left[E_v\left(1-\nu_{hh}\right) - 2E_h\nu_{vh}^2\right]} =\\ &\frac{\nu_{hh}E_hE_v + \nu_{vh}^2E_h^2 + \nu_{vh}E_hE_v + E_hE_v\nu_{hh}\nu_{vh} - \nu_{hh}E_hE_v - \nu_{vh}^2E_h^2}{(1+\nu_{hh})\left[E_v\left(1-\nu_{hh}\right) - 2E_h\nu_{vh}^2\right]} =\\ &\frac{\nu_{vh}E_hE_v\left(1+\nu_{hh}\right)}{(1+\nu_{hh})\left[E_v\left(1-\nu_{hh}\right) - 2E_h\nu_{vh}^2\right]} = C\end{aligned}$$

Adding shear stress and strain gives:

$$\begin{aligned}\sigma'_{xx} &= Ae + 2G_{hh}\varepsilon_{xx} + B\varepsilon_{zz}\\ \sigma'_{yy} &= Ae + 2G_{hh}\varepsilon_{yy} + B\varepsilon_{zz}\\ \sigma'_{zz} &= (A+B)\,e + D\varepsilon_{zz}\\ \tau_{xy} &= G_{hh}\gamma_{xy}\\ \tau_{yz} &= G_{vh}\gamma_{yz}\\ \tau_{zx} &= G_{vh}\gamma_{zx}\end{aligned} \tag{B.13}$$

Note that for isotropic conditions, $E_h = E_v = E$, $G_{hh} = G_{vh} = G$ and $\nu_{hh} = \nu_{vh} = \nu$ is found: $A = \nu E/[(1+\nu)(1-2\nu] = \lambda$, $B = 0$ and $D = 2G_{hh} = 2\mu$ and equation (B.13) reduces to (B.1). Equation (B.13) gives a 5 parameter model which is in agreement with the requirements for a cross–anisotropic model according to section 3.1.

Appendix C

Similarity of some irrotational linear–elastic three–parameter constitutive soil models

Not all the five independent cross–anisotropic elastic constants can be derived from standard triaxial testing. Since no shear stress and shear strain is applied to a sample the usual stress and strain in a standard triaxial test involve the top left corner of the stiffness matrix in equation (3.9). This part of the stiffness matrix involves four independent parameters, E_v, E_h ν_{vh} and ν_{hh}. A further reduction in the number of parameters to a three–parameter model as described in chapter 4 gives parameters that are some function of the four independent parameters. This appendix presents the relation between the parameters of different three–parameter models and the moduli E_v, E_h ν_{vh} and ν_{hh}. This appendix considers only increment of stress and strain (the δ–sign is omitted). For standard triaxial conditions the expressions for stress, strain and the cross–anisotropic stress–strain relationship, are presented by the equation (C.1) to (C.3). These equations refer to the horizontal plane as plane of isotropy and the axial direction perpendicular to the horizontal plane. Some of the derivations are also presented by [54].

$$\begin{bmatrix} p' \\ q \end{bmatrix} = \begin{bmatrix} 1/3 & 2/3 \\ 1 & -1 \end{bmatrix} \begin{bmatrix} \sigma'_a \\ \sigma'_r \end{bmatrix} \tag{C.1}$$

$$\begin{bmatrix} e \\ \varepsilon_q \end{bmatrix} = \begin{bmatrix} 1 & 2 \\ 2/3 & -2/3 \end{bmatrix} \begin{bmatrix} \varepsilon_a \\ \varepsilon_r \end{bmatrix} \tag{C.2}$$

$$\begin{bmatrix} \varepsilon_a \\ \varepsilon_r \end{bmatrix} = \frac{1}{E_v} \begin{bmatrix} 1 & -2\nu_{vh} \\ -\nu_{vh} & (1-\nu_{hh})/\eta \end{bmatrix} \begin{bmatrix} \sigma'_a \\ \sigma'_r \end{bmatrix}, \qquad \eta = \frac{E_h}{E_v} \tag{C.3}$$

Section 4.1 present four three-parameter models. The fourth model is expressed in E_v, ν_{vh} and F_h. With $F_h = E_h/(1-\nu_{hh})$ the relation between this model and E_v, E_h, ν_{vh} and ν_{hh} follows directly from equation (C.3).

Relation between α, ν^*, E^* and E_h, E_v, ν_{hh} and ν_{vh}
The similarity between the Graham & Houlsby model and equation (C.3) is already discussed in section 4.1. For a complete overview of the three-parameter models equation (C.4) gives the equivalent of equation (C.3) in the α, ν^*, E^* model :

$$\begin{bmatrix} \varepsilon_a \\ \varepsilon_r \end{bmatrix} = \frac{1}{\alpha^2 E^*} \begin{bmatrix} \alpha^2 & -2\alpha\nu^* \\ -\alpha\nu^* & 1-\nu^* \end{bmatrix} \begin{bmatrix} \sigma'_a \\ \sigma'_r \end{bmatrix} \tag{C.4}$$

Comparison of both first terms of the matrices in equations (C.3) to (C.4) gives $E^* = E_v$. A comparison of the off-diagonal terms gives $\nu^* = \alpha\nu_{vh}$. Both expressions were already presented in section 4.1. A comparison of the last term of both matrices gives:

$$\frac{1-\nu^*}{\alpha^2 E^*} = \frac{1-\nu_{hh}}{E_h}$$

Implementing $E^* = E_v$ and $\nu^* = \alpha\nu_{vh}$ renders this equation into:

$$(1-\nu_{hh})\frac{E_v}{E_h}\alpha^2 + \nu_{vh}\alpha - 1 = 0$$

With $\alpha^2 = E_h/E_v$ leads to $\alpha = \nu_{hh}/\nu_{vh}$. This result is also presented in section 4.1 by equation (4.17).

Relation K^*, G^*, J and E_v, E_h, ν_{hh} and ν_{vh}
In the G^*, K^*, J model the stress–strain relationship is given by:

$$\begin{bmatrix} p' \\ q \end{bmatrix} = \begin{bmatrix} K^* & J \\ J & 3G^* \end{bmatrix} \begin{bmatrix} e \\ \varepsilon_q \end{bmatrix} \tag{C.5}$$

An expression for G^* can be found under the condition $e = 0$:

$$G^* = \frac{1}{3}\left(\frac{q}{\varepsilon_q}\right)_{e=0}$$

With $e = 0$, it follows from equation (C.2) that $\varepsilon_a = -2\varepsilon_r$. Application to equation (C.3) gives:

$$\frac{\sigma'_r}{\sigma'_a} = -\frac{1}{2}\frac{(1-2\nu_{vh})E_h}{(1-\nu_{hh})E_v - \nu_{vh}E_h} \tag{C.6}$$

From equation (C.1):

$$q = \sigma'_a - \sigma'_r = \sigma'_a\left(1 - \frac{\sigma'_r}{\sigma'_a}\right)$$

is found with equation (C.6) for q:

$$q = \frac{\sigma'_a}{2}\left[\frac{2(1-\nu_{hh})E_v + (1-4\nu_{vh})E_h}{(1-\nu_{hh})E_v - \nu_{vh}E_h}\right]$$

For $e = 0$ it is found from equation (C.2) that $\varepsilon_q = \varepsilon_a = -2\varepsilon_r$, with equation (C.3) and (C.6) is found:

$$\varepsilon_q = \sigma'_a\left[\frac{1}{E_v} + \frac{\nu_{vh}}{E_v}\frac{(1-2\nu_{vh})E_h}{(1-\nu_{hh})E_v - \nu_{vh}E_h}\right]$$

For G^* it is then found that:

$$G^* = \frac{E_v}{6}\left[\frac{2(1-\nu_{hh})E_v + (1-4\nu_{vh})E_h}{(1-\nu_{hh})E_v - 2\nu_{vh}^2 E_h}\right] \tag{C.7}$$

An expression for K^* is found for the condition $\varepsilon_q = 0$:

$$K^* = \left(\frac{p}{e}\right)_{\varepsilon_q=0}$$

For $\varepsilon_q = 0$ equation (C.2) gives $\varepsilon_a = \varepsilon_r$ in combination with equation (C.3) is found:

$$\frac{\sigma'_r}{\sigma'_a} = \frac{(1+\nu_{vh})\,E_h}{(1-\nu_{hh})\,E_v + 2\nu_{vh}E_h} \tag{C.8}$$

From equation (C.1):

$$p' = \frac{1}{3}\sigma'_a + \frac{2}{3}\sigma'_r = \sigma'_a\left(\frac{1}{3} + \frac{2}{3}\frac{\sigma'_r}{\sigma'_a}\right)$$

Combination with equation (C.8) yields:

$$p' = \frac{\sigma'_a}{3}\left[\frac{(1-\nu_{hh})\,E_v + 2\,(1+2\nu_{vh})\,E_h}{(1-\nu_{hh})\,E_v + 2\nu_{vh}E_h}\right]$$

With $\varepsilon_a = \varepsilon_r$ equation (C.2) and (C.3) yields:

$$e = 3\sigma'_a\left[\frac{(1-\nu_{hh})\,E_v - 2\nu_{vh}^2E_h}{E_v\,((1-\nu_{hh})\,E_v + 2\nu_{vh}E_h)}\right]$$

The expression for K^* is given by:

$$K^* = \frac{E_v}{9}\left[\frac{(1-\nu_{hh})\,E_v + 2\,(1+2\nu_{vh})\,E_h}{(1-\nu_{hh})\,E_v - 2\nu_{vh}^2E_h}\right] \tag{C.9}$$

An expression for J can be found for $e = 0$ or $\varepsilon_q = 0$. Here the option for $e = 0$ is elaborated:

$$J = \left(\frac{p'}{\varepsilon_q}\right)_{e=0}$$

Equation (C.2) indicates that for $e = 0$, $\varepsilon_q = \varepsilon_a = -2\varepsilon_r$. In combination to equation(C.3) and (C.6) it is found that:

$$\varepsilon_q = \sigma'_a\left[\frac{1}{E_v} + \frac{\nu_{vh}}{E_v}\frac{(1-2\nu_{vh})\,E_h}{(1-\nu_{hh})\,E_v - \nu_{vh}E_h}\right] = \frac{\sigma'_a}{E_v}\frac{(1-\nu_{hh})\,E_v - 2\nu_{vh}^2E_h}{(1-\nu_{hh})\,E_v - \nu_{vh}E_h}$$

From equation (C.1):

$$p' = \frac{\sigma'_a}{3}\left(1 + 2\frac{\sigma'_r}{\sigma'_a}\right)$$

in combination with equation (C.6):

$$p' = \frac{\sigma'_a}{3}\left[\frac{(1-\nu_{hh})\,E_v - (1-\nu_{vh})\,E_h}{(1-\nu_{hh})\,E_v - \nu_{vh}E_h}\right]$$

Finally, J is given by:

$$J = \frac{E_v}{3}\left[\frac{(1-\nu_{hh})\,E_v - (1-\nu_{vh})\,E_h}{(1-\nu_{hh})\,E_v - 2\nu_{vh}^2E_h}\right] \tag{C.10}$$

Relation between K', G', J' and E_v, E_h, ν_{vh} and ν_{hh}
In the K', G', J' model equation (C.3) is replaced by equation (C.11):

$$\begin{bmatrix} e \\ \\ \varepsilon_q \end{bmatrix} = \begin{bmatrix} \frac{1}{K'} & \frac{1}{J'} \\ \\ \frac{1}{J'} & \frac{1}{3G'} \end{bmatrix} \begin{bmatrix} p' \\ \\ q \end{bmatrix} \tag{C.11}$$

For $p' = 0$ an expression for G' can be found from equation (C.11):

$$G' = \frac{1}{3}\left(\frac{q}{\varepsilon_q}\right)_{p'=0}$$

Equation (C.1) and the condition $p' = 0$ gives $\sigma'_a = -2\sigma'_r$. Application to the equations (C.2) and (C.3) gives:

$$\varepsilon_q = \frac{2}{3}\left(\varepsilon_a - \varepsilon_r\right) = \frac{2}{3}\left(\frac{1+2\nu_{vh}}{E_v} + \frac{1-\nu_{hh}}{2E_h}\right)\sigma'_a$$

Since $\sigma'_a = -2\sigma'_r$ equation (C.1) yields $\sigma'_a = 2/3q$ and consequently ε_q becomes:

$$\varepsilon_q = \frac{4}{9}\left(\frac{1+2\nu_{vh}}{E_v} + \frac{1-\nu_{hh}}{2E_h}\right)q \tag{C.12}$$

G' is expressed by:

$$G' = \frac{3}{4\left(\dfrac{1+2\nu_{vh}}{E_v} + \dfrac{1-\nu_{hh}}{2E_h}\right)} \tag{C.13}$$

Equation (C.11) and $q = 0$ gives an expression for K'

$$K' = \left(\frac{p'}{e}\right)_{q=0}$$

With $q = 0$ it follows from equation (C.1) that $\sigma'_r = \sigma'_a$ and further $p' = \sigma'_a$, in combination to equations (C.2) and (C.3) gives:

$$e = \varepsilon_a + 2\varepsilon_r = \left[\frac{1-4\nu_{vh}}{E_v} + \frac{2\left(1-\nu_{hh}\right)}{E_h}\right]p'$$

and for K':

$$K' = \frac{1}{\dfrac{1-4\nu_{vh}}{E_v} + \dfrac{2\left(1-\nu_{hh}\right)}{E_h}} \tag{C.14}$$

The expression for J' can be found from the condition $p' = 0$ or $q = 0$. Here, condition $p' = 0$ is applied:

$$J' = \left(\frac{q}{e}\right)_{p'=0}$$

From equation (C.1) it follows for $p' = 0$ that $\sigma'_a = -2\sigma'_r$, with combination of equations (C.2) and (C.3) it is found that:

$$e = \varepsilon_a + 2\varepsilon_r = \frac{1-\nu_{vh}}{E_v}\sigma'_a - \frac{1-\nu_{hh}}{E_h}\sigma'_a$$

Equation (C.1) with $p' = 0$ and $\sigma'_a = 2/3q$ give for e:

$$e = \frac{2}{3}\left(\frac{1-\nu_v h}{E_v} - \frac{1-\nu_{hh}}{E_h}\right)q$$

For J' it is found that:

$$J' = \frac{3}{2\left(\dfrac{1-\nu_{vh}}{E_v} - \dfrac{1-\nu_{hh}}{E_h}\right)} \tag{C.15}$$

So far the axis of symmetry is assumed to be aligned in axial direction. If the axis of symmetry is aligned in radial direction equations (C.2) and (C.3) are no longer valid. The deformations of the sample are no longer axial symmetric since in radial direction both the horizontal E_h and vertical stiffness E_v are active. For this condition expressions for K', J' and G' can be found. With ε_{r1} radial strain in the direction parallel to E_h and ε_{r2} parallel to E_v, the corresponding stress–strain state is described by:

$$\begin{pmatrix} \varepsilon_a \\ \\ \varepsilon_{r1} \\ \\ \varepsilon_{r2} \end{pmatrix} = \begin{pmatrix} \frac{1}{E_h} & \frac{-\nu_{hh}}{E_h} & \frac{-\nu_{vh}}{E_v} \\ \frac{-\nu_{hh}}{E_h} & \frac{1}{E_h} & \frac{-\nu_{vh}}{E_v} \\ \frac{-\nu_{vh}}{E_v} & \frac{-\nu_{vh}}{E_v} & \frac{1}{E_v} \end{pmatrix} \begin{pmatrix} \sigma'_a \\ \\ \sigma'_r \\ \\ \sigma'_r \end{pmatrix} \tag{C.16}$$

The volumetric strain is now presented by:

$$e = \varepsilon_a + \varepsilon_{r1} + \varepsilon_{r2} = \left(\frac{1-\nu_{hh}}{E_h} - \frac{\nu_{vh}}{E_v} \right) \sigma'_a + \left(\frac{1-\nu_{hh}}{E_h} + \frac{1-3\nu_{vh}}{E_v} \right) \sigma'_r \tag{C.17}$$

With $q = 0$, which gives $\sigma'_a = \sigma'_r = \sigma$, it follows that:

$$e = \left[\frac{2\left(1-\nu_{hh}\right)}{E_h} + \frac{1-4\nu_{vh}}{E_v} \right] \sigma$$

and:

$$K' = \frac{1}{\frac{1-4\nu_{vh}}{E_v} + \frac{2\left(1-\nu_{hh}\right)}{E_h}} \tag{C.18}$$

Note that equation (C.18) equals (C.14). Obviously the parameter K' is independent of the alignment of the axial axis in relation to the axis of symmetry in the soil. Again for $p' = 0$ leads to $\sigma'_a = -2\sigma'_r$ and $\sigma'_a = 2/3q$ equation (C.17) reduces to:

$$e = \frac{q}{3} \left(\frac{1-\nu_{hh}}{E_h} - \frac{1-\nu_{vh}}{E_v} \right)$$

and:

$$J' = \frac{3}{\frac{1-\nu_{hh}}{E_h} - \frac{1-\nu_{vh}}{E_v}} \tag{C.19}$$

Finally G' is given by:

$$G' = \frac{1}{3} \left(\frac{q}{\varepsilon_q} \right)_{p'=0}$$

Since strain is no longer axial symmetric in absence of shear strain ε_q is defined by:

$$\varepsilon_q = \frac{1}{3} \sqrt{2 \left[\left(\varepsilon_{r1} - \varepsilon_{r2}\right)^2 + \left(\varepsilon_{r2} - \varepsilon_a\right)^2 + \left(\varepsilon_a - \varepsilon_{r1}\right)^2 \right]} \tag{C.20}$$

Application of equation (C.16) to (C.20) for p'= 0 ($\sigma'_a = -2\sigma'_r$) gives:

$$\varepsilon_q = \sqrt{\frac{E_h^2\left(1+2\nu_{vh}\right)^2 + E_v E_h \left(1-\nu_{hh}\right)\left(1+2\nu_{vh}\right) + E_v^2\left(7+13\nu_{hh}+7\nu_{hh}^2\right)}{E_h^2 E_v^2}} \times \frac{\sigma'_a}{3}$$

With $q = \sigma'_a - \sigma'_r = 3/2\sigma'_a$, G' becomes:

$$G' = \frac{3E_v E_h}{2\sqrt{E_h^2\left(1+2\nu_{vh}\right)^2 + E_v E_h \left(1-\nu_{hh}\right)\left(1+2\nu_{vh}\right) + E_v^2\left(7+13\nu_{hh}+7\nu_{vh}^2\right)}} \tag{C.21}$$

Application of isotropic conditions gives a simple validity check of equation (C.21). For isotropic conditions equation (C.21) reduces to:

$$G' = \frac{E}{2\,(1+\nu)}$$

Appendix D

Relation between Drained and Undrained parameters

A total stress analysis for undrained conditions uses undrained stiffness parameters. As shown in section 4.3.2 the undrained parameters can be expressed into drained parameters, but drained parameters can not be uniquely expressed into undrained parameters. The relation between drained and undrained parameters for isotropic conditions is given by Bishop & Hight [15]. The derivation is straight forward. For principal stress and strain, with $\sigma_i' = \sigma_i - \sigma_w$ and i, j, k a cyclic permutation of 1, 2, 3, Hooke's law is represented by:

$$\varepsilon_i = \frac{1}{E}\left[\sigma_i - \sigma_w - \nu\left(\sigma_j + \sigma_k - 2\sigma_w\right)\right]$$

$$e = \varepsilon_i + \varepsilon_j + \varepsilon_k = \frac{1-2\nu}{E}\left(\sigma_i + \sigma_j + \sigma_k\right) - 3\frac{1-2\nu}{E}\sigma_w$$

$$\sigma_w = Bp, \qquad p = \frac{\sigma_i + \sigma_j + \sigma_k}{3}$$

Rewriting yields:

$$\varepsilon_i = \frac{1}{E}\left[\sigma_i - \nu\left(\sigma_j + \sigma_k\right) - \left(1-2\nu\right)Bp\right]$$

$$\varepsilon_i = \frac{3-\left(1-2\nu\right)B}{3E}\left[\sigma_i - \frac{3\nu + \left(1-2\nu\right)B}{3-\left(1-2\nu\right)B}\left(\sigma_j + \sigma_k\right)\right] \tag{D.1}$$

For undrained conditions Hooke's law for principal stress and strain is given by:

$$\varepsilon_i = \frac{1}{E^u}\left[\sigma_i - \nu^u\left(\sigma_j + \sigma_k\right)\right] \tag{D.2}$$

Comparison of equation (D.1) and (D.2) gives:

$$E^u = \frac{3E}{3-\left(1-2\nu\right)B}; \qquad \nu^u = \frac{3\nu + \left(1-2\nu\right)B}{3-\left(1-2\nu\right)B} \tag{D.3}$$

Section 4.3.1 explains the relation undrained pore pressure response and isotropic loading;

$$\sigma_w = Bp \tag{D.4}$$

This relation is based on the assumption that undrained conditions are represented by equating the total volumetric strain to the pore fluid compression. This assumption only holds when the pore fluid can be considered as a continuous phase. Section 2.2 states that a continuous pore

fluid phase is present for $S_r > 0.85$. Therefore it should be noted that the validity of equation (D.3) is restricted to $S_r > 0.85$.
Completely saturated soil, $B = 1$, equation (D.3) leads to $E^u > E$ and $\nu^u > \nu$. The maximum value for E^u ν^u is found when $\nu = 0$; $E^u = 3E/2$. For $B = 1$ gives $\nu^u = 1/2$.
Lings [55] gives the relation between drained and undrained stiffness parameters for a cross–anisotropic material and for $B = 1$. Using the same method as Bishop & Hight a relation between drained and undrained stiffness parameters including the B–factor can be derived.
With the axis of symmetry in vertical direction and aligned in axial direction Hooke's law for principal stress and strain is given by (C.3):

$$\varepsilon_a = -\frac{2\nu_{vh}}{E_v}\sigma'_r + \frac{1}{E_v}\sigma'_a$$
$$\varepsilon_r = \frac{1-\nu_{hh}}{E_h}\sigma'_r - \frac{\nu_{vh}}{E_v}\sigma'_a$$

With (C.1) $p' = \sigma'_a/3 + 2\sigma'_r/3$ and $q = \sigma_a - \sigma_r$ equation (4.40) can be rewritten into:

$$\sigma_{w0} = B\left[\left(\frac{1}{3} + \frac{K'}{J'}\right)\sigma_a + \left(\frac{2}{3} - \frac{K'}{J'}\right)\sigma_r\right] \tag{D.5}$$

Equation (D.5) is derived in section 4.3.1. Again the undrained material behaviour is modeled by equating volumetric strain to the pore fluid compression. As stated before this only holds for $S_r > 0.85$.
With $\sigma' = \sigma - \sigma_{w0}$ the following is found:

$$\begin{aligned}
\varepsilon_a &= \left[-\frac{2\nu_{vh}}{E_v} + B\frac{2\nu_{vh}-1}{E_v}\left(\frac{2}{3} - \frac{K'}{J'}\right)\right]\sigma_r + \left[\frac{1}{E_v} + B\frac{2\nu_{vh}-1}{E_v}\left(\frac{1}{3} + \frac{K'}{J'}\right)\right]\sigma_a \\
\varepsilon_r &= \left[\frac{1-\nu_{hh}}{E_h} + \left(\frac{\nu_{vh}}{E_v} - \frac{1-\nu_{hh}}{E_h}\right)\left(\frac{2}{3} - \frac{K'}{J'}\right)B\right]\sigma_r \\
&\quad + \left[\left(\frac{\nu_{vh}}{E_v} - \frac{1-\nu_{hh}}{E_h}\right)\left(\frac{1}{3} + \frac{K'}{J'}\right)B - \frac{\nu_{vh}}{E_v}\right]\sigma_a
\end{aligned} \tag{D.6}$$

Undrained triaxial conditions in which the axis of symmetry corresponds to the axial direction are also presented by:

$$\varepsilon_a = -\frac{2\nu^u_{vh}}{E^u_v}\sigma_r + \frac{1}{E^u_v}\sigma_a$$
$$\varepsilon_r = \frac{1-\nu^u_{hh}}{E^u_h}\sigma_r - \frac{\nu^u_{vh}}{E^u_v}\sigma_a \tag{D.7}$$

Similarity of equations (D.6) and (D.7) gives:

$$-\frac{2\nu^u_{vh}}{E^u_v} = -\frac{2\nu_{vh}}{E_v} + B\frac{2\nu_{vh}-1}{E_v}\left(\frac{2}{3} - \frac{K'}{J'}\right) \tag{D.8}$$

$$\frac{1}{E^u_v} = \frac{1}{E_v} + B\frac{2\nu_{vh}-1}{E_v}\left(\frac{1}{3} + \frac{K'}{J'}\right) \tag{D.9}$$

$$\frac{1-\nu^u_{hh}}{E^u_h}\left(=\frac{1}{F^u_h}\right) = \frac{1-\nu_{hh}}{E_h} + \left(\frac{\nu_{vh}}{E_v} - \frac{1-\nu_{hh}}{E_h}\right)\left(\frac{2}{3} - \frac{K'}{J'}\right)B \tag{D.10}$$

$$-\frac{\nu^u_{vh}}{E^u_v} = \left(\frac{\nu_{vh}}{E_v} - \frac{1-\nu_{hh}}{E_h}\right)\left(\frac{1}{3} + \frac{K'}{J'}\right)B - \frac{\nu_{vh}}{E_v} \tag{D.11}$$

With expressions (C.14) and (C.15) equation (D.9) can be rewritten into:

$$\frac{1}{E^u_v} = \frac{1}{E_v} - B\left[\frac{(1-2\nu_{vh})^2 E_h}{E_v\left[(1-4\nu_{vh})E_h + 2(1-\nu_{hh})E_v\right]}\right] \tag{D.12}$$

leading to:

$$E_v^u = \frac{E_v\left[\left(1-4\nu_{vh}\right)E_h + 2\left(1-\nu_{hh}\right)E_v\right]}{E_h\left[\left(1-4\nu_{vh}\right) - B\left(1-2\nu_{vh}\right)^2\right] + 2\left(1-\nu_{hh}\right)E_v} \tag{D.13}$$

Application of the equations (C.14) and (C.15) to (D.11) gives:

$$\frac{\nu_{vh}}{E_v^u} = \frac{\nu_{vh}}{E_v} - B\left[\frac{\left[\nu_{vh}E_h - E_v\left(1-\nu_{hh}\right)\right]\left(1-2\nu_{vh}\right)}{E_v\left[\left(1-4\nu_{vh}\right)E_h + 2\left(1-\nu_{hh}\right)E_v\right]}\right] \tag{D.14}$$

Introducing equation (D.13) gives after rewriting:

$$\nu_{vh}^u = \frac{\nu_{vh}E_h\left[\left(1-4\nu_{vh}\right) - B\left(1-2\nu_{vh}\right)\right] + \left(1-\nu_{hh}\right)E_v\left[2\nu_{vh} + B\left(1-2\nu_{vh}\right)\right]}{E_h\left[\left(1-4\nu_{vh}\right) - B\left(1-2\nu_{vh}\right)^2\right] + 2\left(1-\nu_{hh}\right)E_v} \tag{D.15}$$

In the equation (D.10) the parameters ν_{hh}^u and E_h^u can not be separated. Since the subscripts h and v refer to the conditions in the field, E_h^u and E_v^u are independent from sample orientation. In order to derive individual expressions for ν_{hh}^u and E_h^u an other configuration is considered in which the axis symmetry corresponds to one of the radial directions of the sample. This configuration is also discussed in appendix C.
Equation (C.16) gives the stress–strain relationship for these conditions. The axis of symmetry is now considered to be aligned in radial direction while E_h^u now dominates the axial strain. The first row of equation (C.16) in combination to equation (D.5) gives:

$$\begin{aligned}\varepsilon_a = &\left[\frac{1}{E_h} + \left(\frac{\nu_{hh}-1}{E_h} + \frac{\nu_{vh}}{E_v}\right)\left(\frac{1}{3} + \frac{K'}{J'}\right)B\right]\sigma_a + \\ &\left[-\frac{\nu_{hh}}{E_h} - \frac{\nu_{vh}}{E_v} + \left(\frac{\nu_{hh}-1}{E_h} + \frac{\nu_{vh}}{E_v}\right)\left(\frac{2}{3} - \frac{K'}{J'}\right)B\right]\sigma_r\end{aligned} \tag{D.16}$$

For undrained condition the following holds:

$$\varepsilon_a = \frac{1}{E_h^u}\sigma_a - \left(\frac{\nu_{hh}^u}{E_h^u} + \frac{\nu_{vh}^u}{E_v^u}\right)\sigma_r$$

Similarity with equation (D.16) yields:

$$\frac{1}{E_h^u} = \frac{1}{E_h} + \left(\frac{\nu_{hh}-1}{E_h} + \frac{\nu_{vh}}{E_v}\right)\left(\frac{1}{3} + \frac{K'}{J'}\right)B \tag{D.17}$$

It should be noted that for the relevant conditions equations (C.18) and (C.19) give the relation between K' and J' for the specific sample orientation. Application of these equations to expression (D.17) gives after elaboration:

$$\frac{1}{E_h^u} = \frac{1}{E_h} - B\left[\frac{E_v^2\left(1-\nu_{hh}\right)^2 - 2E_vE_h\nu_{vh}\left(1-\nu_{hh}\right) + \nu_{vh}^2E_h^2}{E_vE_h\left[\left(1-4\nu_{vh}\right)E_h + 2\left(1-\nu_{hh}\right)E_v\right]}\right] \tag{D.18}$$

and finally:

$$E_h^u = \frac{E_vE_h\left[\left(1-4\nu_{vh}\right)E_h + 2\left(1-\nu_{hh}\right)E_v\right]}{E_v\left[\left(1-4\nu_{vh}\right)E_h + 2\left(1-\nu_{hh}\right)E_v\right] - B\left[E_v^2\left(1-\nu_{hh}\right)^2 - 2E_vE_h\nu_{vh}\left(1-\nu_{hh}\right) + \nu_{vh}^2E_h^2\right]} \tag{D.19}$$

The last parameter to solve is ν_{hh}^u, rewriting equation (D.10) gives:

$$\nu_{hh}^u = 1 - \left(1-\nu_{hh}\right)\frac{E_h^u}{E_h} - \left(\frac{\nu_{vh}}{E_v} - \frac{1-\nu_{hh}}{E_h}\right)\left(\frac{2}{3} - \frac{K'}{J'}\right)BE_h^u \tag{D.20}$$

Application of equation (D.19) to (D.20) yields:

$$\nu_{hh}^{u} = \frac{\nu_{hh}E_v d + B\left[E_v^2\left(1-\nu_{hh}\right)^2 + E_h^2\nu_{vh}^2 - 2E_hE_v\nu_{vh}\left(1-\nu_h\right)\right]}{E_v d + B\left[2E_vE_h\nu_{vh}\left(1-\nu_{hh}\right) - E_v^2\left(1-\nu_{hh}\right)^2 - \nu_{vh}^2E_h^2\right]} \tag{D.21}$$

with

$$d = \left(1-4\nu_{vh}\right)E_h + 2\left(1-\nu_{hh}\right)E_v$$

The expressions (D.13), (D.15), (D.19) and (D.21) relates the drained stiffness parameters to the undrained stiffness parameters using the Skempton B–factor. Lings [55] presents expressions for the undrained stiffness parameters for $B = 1$. Elaboration for $B = 1$ shows that equations (D.13), (D.15), (D.19) and (D.21) are equal to the expressions given by Lings [55]:

$$\begin{aligned}
E_v^u &= \frac{E_v\left[\left(1-4\nu_v h\right)E_h + 2\left(1-\nu_{hh}\right)E_v\right]}{2\left(1-\nu_{hh}\right)E_v - 4\nu_{vh}^2E_h} \\
\nu_{vh}^u &= \frac{1}{2} \\
E_h^u &= \frac{E_vE_h\left[\left(1-4\nu_{vh}\right)E_h + 2\left(1-\nu_{hh}\right)E_v\right]}{E_v^2\left(1-\nu_{hh}^2\right) + E_vE_h\left(1-2\nu_{vh}-2\nu_{hh}\nu_{vh}\right) - \nu_{vh}^2E_h^2} \\
\nu_{hh}^u &= \frac{E_h^2\nu_{vh}^2 + E_hE_v\left(\nu_{hh}-2\nu_{vh}-2\nu_{hh}\nu_{vh}\right) + E_v^2\left(1-\nu_{hh}^2\right)}{E_v^2\left(1-\nu_{hh}^2\right) + E_hE_v\left(1-2\nu_{vh}-2\nu_{vh}\nu_{hh}\right) - \nu_{vh}^2E_h^2}
\end{aligned} \tag{D.22}$$

Although equations (D.4) and (D.5) and therefore equations (D.13), (D.15), (D.19) and (D.21) only hold for $S_r > 0.85$. It is interesting to note that according equations (D.13), (D.15), (D.19) and (D.21) the undrained stiffness parameters reduce to their drained values for $B = 0$:

$$\begin{aligned}
E_v^u &= E_v \\
E_h^u &= E_h \\
\nu_{vh}^u &= \nu_{vh} \\
\nu_{hh}^u &= \nu_{hh}
\end{aligned} \tag{D.23}$$

Appendix E

Consolidation for axial symmetric isotropic conditions

This appendix discusses the derivation of the expressions for stress and strain for the axial symmetric consolidation problem. The solution for the pore pressure development is also presented in [52]. The consolidation problem is solved following 4 steps:

1 gathering the relevant expressions

2 application of the Laplace transformation

3 solving the transformed equation for imposed boundary conditions

4 finding the inverse transform

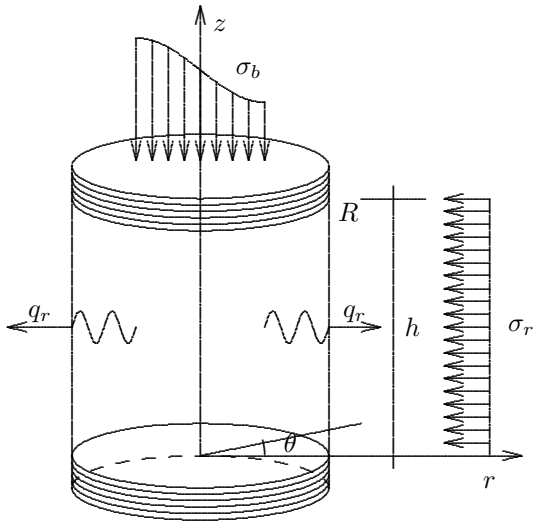

Figure E.1: Axial symmetric conditions

step 1, the relevant expressions
For axial symmetry, stress and strain is conveniently expressed in cylindrical co–ordinates as shown in figure E.1. Strain is then expressed by (see also [72]):

$$\begin{aligned} &\text{radial strain:} && \varepsilon_r = \frac{\partial u_r}{\partial r} \\ &\text{tangential strain:} && \varepsilon_\theta = \frac{u_r}{r} + \frac{1}{r}\frac{\partial u_\theta}{\partial \theta} \\ &\text{axial strain:} && \varepsilon_{zz} = \frac{\partial u_{zz}}{\partial z} \end{aligned} \tag{E.1}$$

Shear strain is defined by:

$$\begin{aligned} \gamma_{\theta z} &= \frac{\partial u_\theta}{\partial z} + \frac{\partial u_{zz}}{\partial \theta} \\ \gamma_{rz} &= \frac{\partial u_r}{\partial z} + \frac{\partial u_{zz}}{\partial r} \\ \gamma_{r\theta} &= \frac{1}{r}\frac{\partial u_r}{\partial \theta} + \frac{\partial u_\theta}{\partial r} - \frac{u_\theta}{r} \end{aligned} \tag{E.2}$$

Since the purpose of the mathematical analysis is to model triaxial tests, the following simplifications are used:

$$\begin{aligned} &\text{axial symmetry:} && \frac{\partial}{\partial \theta} = 0 \\ &\text{stiff plate on top:} && \frac{\partial \varepsilon_{zz}}{\partial z} = \frac{\partial \varepsilon_{zz}}{\partial r} = 0 \\ &\text{no shear stress and strain:} && \gamma_{\theta z} = \ \gamma_{r\theta} = \gamma_{rz} = \tau_{\theta z} = \ \tau_{r\theta} = \tau_{rz} = 0 \end{aligned}$$

Application of the assumptions to definition (E.1) gives:

$$\begin{aligned} \varepsilon_r &= \frac{\partial u_r}{\partial r} \\ \varepsilon_\theta &= \frac{u_r}{r} \\ \varepsilon_{zz} &= \frac{\partial u_{zz}}{\partial z} \\ e &= \frac{\partial u_r}{\partial r} + \frac{u_r}{r} + \frac{\partial u_{zz}}{\partial z} = \frac{1}{r}\frac{\partial (r\, u_r)}{\partial r} + \frac{\partial u_{zz}}{\partial z} \end{aligned} \tag{E.3}$$

The relation between stress and strain, the constitutive relation, becomes:

$$\begin{aligned} \sigma'_r &= 2G\left[\frac{\partial u_r}{\partial r} + \frac{\nu}{1-2\nu}e\right] \\ \sigma'_\theta &= 2G\left[\frac{u_r}{r} + \frac{\nu}{1-2\nu}e\right] \\ \sigma'_{zz} &= 2G\left[\frac{\partial u_{zz}}{\partial z} + \frac{\nu}{1-2\nu}e\right] \end{aligned} \tag{E.4}$$

Different textbooks present the storage equation, e.q Barends [7] or Verruijt [76] give:

$$\frac{k}{\gamma_w}\nabla^2 \sigma_w = \frac{\partial e}{\partial t} \tag{E.5}$$

and equilibrium of forces gives, see e.g. [7] and [76]:

$$\left(K + \frac{4}{3}G\right)\nabla^2 e = \nabla^2 \sigma_w \tag{E.6}$$

Combination of equation (E.6) and (E.5) gives:

$$\nabla^2 e = \frac{1}{c}\frac{\partial e}{\partial t}, \quad c = \frac{k}{\gamma_w}\left[K + \frac{4}{3}G\right] \tag{E.7}$$

step 2, the Laplace transformation
Application of the Laplace transformation to equation (E.7) gives:

$$\int_0^\infty \nabla^2 e \, \exp(-st)\, dt = \frac{1}{c}\int_0^\infty \frac{\partial e}{\partial t}\exp(-st)\, dt$$

$$\nabla^2 \overline{e} = \frac{1}{c}\left(s\overline{e} - e_0\right)$$

In which e_0 is the initial volumetric strain at $t = 0$. Since initially the soil behaves undrained, $e_0 = 0$.

$$\nabla^2 \overline{e} = \frac{s}{c}\overline{e}$$

$$\frac{\partial^2 \overline{e}}{\partial r^2} + \frac{1}{r}\frac{\partial \overline{e}}{\partial r} - \frac{s}{c}\overline{e} = 0$$

$$r^2\frac{\partial^2 \overline{e}}{\partial r^2} + r\frac{\partial \overline{e}}{\partial r} - r^2\frac{s}{c}\overline{e} = 0 \tag{E.8}$$

In which the overbar indicates the transformed quantities. A standard solution of equation (E.8) can be found by using Bessel functions:

$$\overline{e} = C_1 J_0(\lambda r) + C_2 Y_0(\lambda r) \tag{E.9}$$

with:

λ $= \sqrt{\frac{-s}{c}}$
J_0 = The Bessel function of the first kind
Y_0 = The Bessel function of the second kind

Equation (E.6) can be rewritten into:

$$\nabla^2 e = \frac{1}{4mG}\nabla^2 \sigma_w$$

$$\text{with } m = \frac{K + \frac{4}{3}G}{4G} = \frac{\frac{E}{3(1-2\nu)} + \frac{4}{3}\frac{E}{2(1+\nu)}}{\frac{4E}{2(1+\nu)}} = \frac{2(1+\nu)}{12(1-2\nu)} + \frac{1}{3}\frac{4(1-2\nu)}{4(1-2\nu)}$$

$$m = \frac{1-\nu}{2(1-2\nu)}$$

Application of the Laplace transform and integration of (E.6) gives:

$$\nabla^2 \overline{e} = \frac{1}{4mG}\nabla^2 \overline{\sigma}_w$$

$$\overline{e} = \frac{1}{4mG}\overline{\sigma}_w + C_3, \quad \text{with} \quad \nabla^2 C_3 = 0 \tag{E.10}$$

Combination of equation (E.10) and (E.9) gives:

$$\overline{\sigma}_w = 4mG\left[C_1 J_0(\lambda r) + C_2 Y_0(\lambda r) - C_3\right] \tag{E.11}$$

The definition of volumetric strain, equation (G.1), in the Laplace transform results in:

$$\overline{e} = \frac{1}{r}\frac{\partial(r\overline{u}_r)}{\partial r} + \frac{\partial \overline{u}_{zz}}{\partial z}$$

In combination with equation (E.9):

$$\frac{1}{r}\frac{\partial(r\overline{u}_r)}{\partial r} = C_1 J_0(\lambda r) + C_2 Y_0(\lambda r) - \frac{\partial \overline{u}_{zz}}{\partial z}$$
$$\frac{\partial(r\overline{u}_r)}{\partial r} = r\,C_1 J_0(\lambda r) + r\,C_2 Y_0(\lambda r) - r\frac{\partial \overline{u}_{zz}}{\partial z}$$

To find a expression for $\overline{u}_r$ integration of Bessel functions is needed.

$$\int r\,J_0(\lambda r)\,\mathrm{d}r \quad \rightarrow \quad \text{with } w = \lambda r, \quad \mathrm{d}w = \mathrm{d}(\lambda r) = \lambda \mathrm{d}r \quad \text{then}$$
$$\int \frac{w}{\lambda^2} J_0(w)\,\mathrm{d}w = \frac{w}{\lambda^2} J_1(w) = \frac{r}{\lambda} J_1(\lambda r)$$

The same holds for the Bessel function of the second kind. For $\overline{u}_r$ is found:

$$r\overline{u}_r = \frac{r}{\lambda} C_1 J_1(\lambda r) + \frac{r}{\lambda} C_2 Y_1(\lambda r) - \frac{1}{2} r^2 \frac{\partial \overline{u}_{zz}}{\partial z} + C_4$$
$$\frac{\overline{u}_r}{R} = \frac{1}{\lambda R} C_1 J_1(\lambda r) + \frac{1}{\lambda R} C_2 Y_1(\lambda r) - \frac{r}{2R}\frac{\partial \overline{u}_{zz}}{\partial z} + \frac{C_4}{rR} \tag{E.12}$$

Differentiation of equation (E.12) gives:

$$\frac{\partial \overline{u}_r}{\partial r} = C_1\left[J_0(\lambda r) - \frac{J_1(\lambda r)}{\lambda r}\right] + C_2\left[Y_0(\lambda r) - \frac{Y_1(\lambda r)}{\lambda r}\right] - \frac{1}{2}\frac{\partial \overline{u}_{zz}}{\partial z} - \frac{C_4}{r^2} \tag{E.13}$$

Combination of equations (E.4), (E.9) and (E.13) gives the expression for the stresses in transformed conditions:

$$\overline{\sigma}'_r = 2G\left[\begin{array}{l} C_1 J_0(\lambda r)\left(1 + \dfrac{\nu}{1-2\nu}\right) - C_1\dfrac{J_1(\lambda r)}{\lambda r} + C_2 Y_0(\lambda r)\left(1 + \dfrac{\nu}{1-2\nu}\right) - \\ C_2\dfrac{Y_1(\lambda r)}{\lambda r} - \dfrac{1}{2}\dfrac{\partial \overline{u}_{zz}}{\partial z} - \dfrac{C_4}{r^2} \end{array}\right] \tag{E.14}$$

$$\text{with: } \left(1 + \frac{\nu}{1-2\nu}\right) = \frac{1-2\nu}{1-2\nu} + \frac{\nu}{1-2\nu} = \frac{1-\nu}{1-2\nu} = 2m$$

$$\overline{\sigma}'_r = 2G\left[2mC_1 J_0(\lambda r) - C_1\frac{J_1(\lambda r)}{\lambda r} + 2mC_2 Y_0(\lambda r) - C_2\frac{Y_1(\lambda r)}{\lambda r} - \frac{1}{2}\frac{\partial \overline{u}_{zz}}{\partial z} - \frac{C_4}{r^2}\right] \tag{E.15}$$

For $r = 0$, $Y_1(\lambda r) \rightarrow \infty$ since $\overline{\sigma}'_r$ has a limited value at r =0 it follows that $C_2 = 0$. The same holds for C_4, since for $r = 0$ $C_4/r^2 \rightarrow \infty$, so $C_4 = 0$. The expressions for tangential and axial stress can be found equivalent to the derivation of equation (E.15). The summation of effective stress and pore pressure results in an expression for total stress. Since effective and total stress are defined positive for tension while the pore pressure is defined positive for pressure, the sign convention introduced in section 5.3.1, it follows:

$$\overline{\sigma}_r = \overline{\sigma}'_r - \overline{\sigma}_w$$
$$\overline{\sigma}_\theta = \overline{\sigma}'_\theta - \overline{\sigma}_w$$
$$\overline{\sigma}_{zz} = \overline{\sigma}'_{zz} - \overline{\sigma}_w$$

The following set of equations is found:

$$\overline{e} = C_1 J_0(\lambda r) \tag{E.16}$$

$$\overline{\sigma}_w = 4mG\left[C_1 J_0(\lambda r) - C_3\right] \tag{E.17}$$

$$\frac{\overline{u}_r}{R} = C_1 \frac{J_1(\lambda r)}{\lambda R} - \frac{r}{2R}\frac{\partial \overline{u}_{zz}}{\partial z} \tag{E.18}$$

$$\overline{\sigma}'_r = 2GC_1\left[2mJ_0(\lambda r) - \frac{J_1(\lambda r)}{\lambda r}\right] - G\frac{\partial \overline{u}_{zz}}{\partial z} \tag{E.19}$$

$$\overline{\sigma}'_\theta = 2GC_1\left[\frac{\nu}{1-2\nu}J_0(\lambda r) + \frac{J_1(\lambda r)}{\lambda r}\right] - G\frac{\partial \overline{u}_{zz}}{\partial z} \tag{E.20}$$

$$\overline{\sigma}'_{zz} = 2GC_1\left[\frac{\nu}{1-2\nu}J_0(\lambda r)\right] + 2G\frac{\partial \overline{u}_{zz}}{\partial z} \tag{E.21}$$

$$\overline{\sigma}_r = 2GC_1\left[\frac{-J_1(\lambda r)}{\lambda r}\right] - G\frac{\partial \overline{u}_{zz}}{\partial z} + 4mGC_3 \tag{E.22}$$

$$\overline{\sigma}_\theta = 2GC_1\left[-J_0(\lambda r) + \frac{J_1(\lambda r)}{\lambda r}\right] - G\frac{\partial \overline{u}_{zz}}{\partial z} + 4mGC_3 \tag{E.23}$$

$$\overline{\sigma}_{zz} = -2GC_1 J_0(\lambda r) + 2G\frac{\partial \overline{u}_{zz}}{\partial z} + 4mGC_3 \tag{E.24}$$

step 3, solving for boundary conditions
The equations (E.16) to (E.24) contain 3 unknown coefficients; C_1, C_3 and $\partial\overline{u}_{zz}/\partial z$. These coefficients are defined by the following boundary conditions:

a) at $r = R \quad \sigma_w = g_1, \quad \rightarrow \quad \overline{\sigma}_w = \overline{g}_1$

b) at $r = R \quad \sigma_r = g_2, \quad \rightarrow \quad \overline{\sigma}_r = \overline{g}_2$

c) at $z = h \quad 1/A\int 2\pi r\sigma_{zz}\mathrm{d}r = g_3, \quad \rightarrow \quad 1/A\int 2\pi r\overline{\sigma}_{zz}\mathrm{d}r = \overline{g}_3$

Boundary condition a combined to equation (E.17) and rewriting for m give:

$$\overline{g}_1 = \left(K + \frac{4}{3}G\right)\left[C_1 J_0(\lambda R) - C_3\right]$$

$$C_3 = \frac{-\overline{g}_1}{K + \frac{4}{3}G} + C_1 J_0(\lambda R) \tag{E.25}$$

Boundary condition b and equation (E.22) give:

$$\overline{g}_2 = 2C_1 G\left[\frac{-J_1(\lambda R)}{\lambda R} + 2mJ_0(\lambda R)\right] - G\frac{\partial \overline{u}_{zz}}{\partial z} - 4mG\frac{\overline{g}_1}{K + \frac{4}{3}G}$$

$$G\frac{\partial \overline{u}_{zz}}{\partial z} = 2C_1 G\left[\frac{-J_1(\lambda R)}{\lambda R} + 2mJ_0(\lambda R)\right] - \overline{g}_1 - \overline{g}_2 \tag{E.26}$$

Boundary condition c and equation (E.24) give :

$$\overline{g}_3 = \int_0^R \frac{2r}{R^2}\left[-2GC_1 J_0(\lambda r) + 2G\frac{\partial \overline{u}_{zz}}{\partial z} + 4mGC_1 J_0(\lambda R) - \overline{g}_1\right] dr$$

Integration of the individual parts and summation of the results gives

$$\int_0^R \frac{-4}{R^2} GC_1 \frac{\lambda}{\lambda} r\ J_0(\lambda r)\, dr = \left[\frac{-4GC_1}{\lambda R^2} r\ J_1(\lambda r)\right]_0^R = -4GC_1 \frac{J_1(\lambda R)}{\lambda R}$$

$$\int_0^R \frac{4r}{R^2} G \frac{\partial \overline{u}_{zz}}{\partial z} dr = \left[\frac{2r^2}{R^2} G \frac{\partial \overline{u}_{zz}}{\partial z}\right]_0^R = 2G \frac{\partial \overline{u}_{zz}}{\partial z}$$

$$\int_0^R \frac{8mGC_1 J_0(\lambda R)}{R^2} r\, dr = \left[\frac{4mGC_1 J_0(\lambda R)}{R^2} r^2\right]_0^R = 4mGC_1 J_0(\lambda R)$$

$$\int_0^R \frac{2r}{R^2} \overline{g}_1 dr = \left[\frac{r^2}{R^2} \overline{g}_1\right]_0^R = \overline{g}_1$$

$$\overline{g}_3 = -4GC_1 \frac{J_1(\lambda R)}{\lambda R} + 2G \frac{\partial \overline{u}_{zz}}{\partial z} + 4mGC_1 J_0(\lambda R) - \overline{g}_1 \tag{E.27}$$

The combination of equations (E.26) and (E.27) gives C_1:

$$C_1 = \frac{\overline{g}_3 + 3\overline{g}_1 + 2\overline{g}_2}{4G\left[3mJ_0(\lambda R) - \dfrac{2J_1(\lambda R)}{\lambda R}\right]} \tag{E.28}$$

The expression for $\partial \overline{u}_{zz}/\partial z$ can be found by combination of (E.28) and (E.26):

$$G \frac{\partial \overline{u}_{zz}}{\partial z} = \frac{\overline{g}_3 \left[mJ_0(\lambda R) - \dfrac{J_1(\lambda R)}{2\lambda R}\right] + \overline{g}_1 \dfrac{J_1(\lambda R)}{2\lambda R} - \overline{g}_2 \left[mJ_0(\lambda R) - \dfrac{J_1(\lambda R)}{\lambda R}\right]}{3mJ_0(\lambda R) - 2\dfrac{J_1(\lambda R)}{\lambda R}} \tag{E.29}$$

Combination of (E.28) and (E.25)

$$C_3 = \frac{(\overline{g}_3 + 3\overline{g}_1 + 2\overline{g}_2) J_0(\lambda R) - \overline{g}_1 \left[3J_0(\lambda R) - \dfrac{2}{m} \dfrac{J_1(\lambda R)}{\lambda R}\right]}{\left(K + \dfrac{4}{3}G\right)\left[3J_0(\lambda R) - \dfrac{2J_1(\lambda R)}{m\lambda R}\right]} \tag{E.30}$$

The equations (E.28), (E.29) and (E.30) complete the expressions (E.16) to (E.24) for transformed conditions.

step 4, inverse transformation
The inverse transformation starts with finding an expression for the boundary conditions $\overline{g}_1$, $\overline{g}_2$ and $\overline{g}_3$. Standard triaxial testing with a radial pore pressure dissipation is modelled by $g_1 = g_2 = 0$, $g_3 = \sigma_b$, a jump load at $t = 0$. The boundary conditions in transformed conditions is then given by:

$$\overline{g}_1 = 0$$
$$\overline{g}_2 = 0$$
$$\overline{g}_3 = \int_0^\infty \sigma_b \exp(-st)\, \mathrm{d}t = \frac{\sigma_b}{s}$$

First the inverse transform of the pore pressure expression is derived. Combining the equations (E.17), (E.28) and (E.30) leads to:

$$\overline{\sigma}_w = 4mG\left[C_1 J_0\left(\lambda R\right) - C_3\right] \tag{E.31}$$

$$\frac{\overline{\sigma}_w}{\sigma_b} = \frac{J_0\left(\lambda r\right) - J_0\left(\lambda R\right)}{s\left[3J_0\left(\lambda R\right) - \dfrac{2}{m}\dfrac{J_1\left(\lambda R\right)}{\lambda R}\right]} \tag{E.32}$$

The inverse transform of equation (E.32) can be found by the Heaviside expansion theorem. This theorem states that:

$$\text{for } \overline{\sigma}_w = \frac{t\left(s\right)}{n\left(s\right)}, \quad \text{then } \sigma_w = \sum_{j=1}^{\infty} \frac{t\left(a_j\right)}{\dfrac{d}{ds}n\left(a_j\right)} \exp(a_j t), \quad \text{with } a_j \text{ the roots of } n(s)$$

The roots of $n(s)$ are given by:

$$s = 0 \quad \vee \quad 3\,J_0\left(\lambda R\right) - \frac{2}{m}\frac{J_1\left(\lambda R\right)}{\lambda R} = 0$$

For $s = 0$ the nominator in the Heaviside expansion theorem, $t(a_j)$, turns to 0. So since $s = 0$ does not give any contribution to the inverse transform of equation (E.32), $s = 0$ is a removable root. The other roots are found for:

$$\frac{J_1\left(\lambda R\right)}{J_0\left(\lambda R\right)} = \frac{3}{2}m\lambda R, \quad \lambda = \sqrt{\frac{-s}{c}} \tag{E.33}$$

Since there is an infinite number of values for s that fulfil condition (E.33) the roots of equation (E.32) are now indicated by s_j and as a consequence the values for λ are now indicated by λ_j. The inverse transform of the pore pressure development is then found:

$$\frac{\sigma_w}{\sigma_b} = \sum_{j=1}^{\infty} \frac{\left(J_0\left(\lambda_j r\right) - J_0\left(\lambda_j R\right)\right) e^{s_j t}}{\dfrac{\partial}{\partial s}\left[s\left(3J_0\left(\lambda_j R\right) - \dfrac{2}{m}\dfrac{J_1\left(\lambda_j R\right)}{\lambda_j R}\right)\right]} \tag{E.34}$$

In order to find the derivative of the denominator as indicated in expression (E.34) the derivatives of the individual terms are derived first:

$$\frac{\partial}{\partial s}\left(\lambda_j R\right) = \frac{R}{2\sqrt{\dfrac{-s_j}{c}}}\frac{1}{c} = \frac{R}{2\sqrt{-s_j}\sqrt{c}}\frac{\sqrt{-s_j}}{\sqrt{-s_j}} = \frac{\lambda_j R}{2s_j}$$

$$\frac{\partial}{\partial s}\left(\frac{1}{\lambda R}\right) = \frac{\partial}{\partial s}\left(\frac{1}{R\sqrt{\dfrac{-s_j}{c}}}\right) = \frac{-1}{2R\left(\dfrac{-s_j}{c}\right)^{3/2}}\frac{1}{c} = \frac{-1}{2\lambda_j R s_j}$$

$$\frac{\partial}{\partial s}\left(J_0\left(\lambda_j R\right)\right) = -J_1\left(\lambda_j R\right)\frac{\partial}{\partial s}\left(\lambda_j R\right) = \frac{-J_1\left(\lambda_j R\right)\,\lambda_j R}{2s_j}$$

$$\frac{\partial}{\partial s}\left(\frac{J_1\left(\lambda_j R\right)}{\lambda_j R}\right) = J_1\left(\lambda_j R\right)\,\frac{\partial}{\partial s}\left(\frac{1}{\lambda_j R}\right) + \frac{1}{\lambda_j R}\frac{\partial}{\partial s}\left(J_1\left(\lambda_j R\right)\right) = \frac{-J_1\left(\lambda_j R\right)}{2\lambda_j R s_j} +$$

$$\frac{1}{\lambda_j R}\left[\frac{\lambda_j R}{2s_j}J_0\left(\lambda_j R\right) - \frac{1}{2s_j}J_1\left(\lambda_j R\right)\right] = \frac{-2J_1\left(\lambda_j R\right)}{2\lambda_j R s_j} + \frac{1}{2s_j}J_0\left(\lambda_j R\right)$$

$$\frac{\partial}{\partial s}\left[s\left(3J_0\left(\lambda_j R\right)-\frac{2}{m}\frac{J_1\left(\lambda_j R\right)}{\lambda_j R}\right)\right]=$$
$$1\left[3J_0\left(\lambda_j R\right)-\frac{2}{m}\frac{J_1\left(\lambda_j R\right)}{\lambda_j R}\right]+s\left[3\frac{-J_1\left(\lambda_j R\right)\lambda_j R}{2s_j}-\frac{2}{m}\left[\frac{-2J_1\left(\lambda_j R\right)}{2\lambda_j R s_j}+\frac{1}{2s_j}J_0\left(\lambda_j R\right)\right]\right]$$

The first term at the right hand side of the presented derivative of the denominator reduces to 0 for the values of s_j found to fulfil condition (E.33). This gives

$$s\frac{1}{s}\left[\frac{-3J_1\left(\lambda_j R\right)}{2}\lambda_j R+\frac{2J_1\left(\lambda_j R\right)}{\lambda_j mR}-\frac{1}{m}J_0\left(\lambda_j R\right)\right]=$$
$$\frac{-1}{m}J_0\left(\lambda_j R\right)+J_1\left(\lambda_j R\right)\left[\frac{2}{\lambda_j mR}-\frac{3}{2}\lambda_j R\right]$$

Equation (E.34) can now be rewritten:

$$\frac{\sigma_w}{\sigma_b}=\sum_{j=1}^{\infty}\frac{\left[J_0\left(\lambda_j r\right)-J_0\left(\lambda_j R\right)\right]e^{s_j t}}{\frac{-1}{m}J_0\left(\lambda_j R\right)+J_1\left(\lambda_j R\right)\left[\frac{2}{\lambda_j mR}-\frac{3}{2}\lambda_j R\right]}$$
$$\frac{\sigma_w}{\sigma_b}=\sum_{j=1}^{\infty}\frac{\left[\frac{J_0\left(\lambda_j r\right)}{J_0\left(\lambda_j R\right)}-1\right]e^{s_j t}}{\frac{-1}{m}+\frac{J_1\left(\lambda_j R\right)}{J_0\left(\lambda_j R\right)}\left[\frac{2}{\lambda_j mR}-\frac{3}{2}\lambda_j R\right]}$$
$$\text{with }\frac{J_1\left(\lambda_j R\right)}{J_0\left(\lambda_j R\right)}=\frac{3}{2}m\lambda_j R$$

$$\frac{\sigma_w}{\sigma_b}=\sum_{j=1}^{\infty}\frac{e^{s_j t}}{\frac{-1}{m}+3-\frac{9}{4}m\left(\lambda_j R\right)^2}\left[\frac{J_0\left(\lambda_j r\right)}{J_0\left(\lambda_j R\right)}-1\right] \tag{E.35}$$

In similar way the inverse transforms of the equations (E.16) to (E.24) can be found. The radial effective stress, equation E.19 is rewritten into:

$$\frac{\overline{\sigma}'_r}{\sigma_b}=\frac{\left[J_0\left(\lambda r\right)-J_0\left(\lambda R\right)\right]-\frac{1}{2m}\left[\frac{J_1\left(\lambda r\right)}{\lambda r}-\frac{J_1\left(\lambda R\right)}{\lambda R}\right]}{s\left[3\,J_0\left(\lambda R\right)-\frac{2}{m}\frac{J_1\left(\lambda R\right)}{\lambda R}\right]} \tag{E.36}$$

The denominator of equation (E.36) equals the denominator of (E.32). So both equations have the same roots. Again $s=0$ results in a removable root as:

$$\lim_{s_j\to 0}\left(\frac{J_1\left(\lambda_j r\right)}{\lambda_j r}\right)=\lim_{s_j\to 0}\left(\frac{J_1\left(\lambda_j R\right)}{\lambda_j R}\right)=\frac{1}{2} \tag{E.37}$$

The remaining roots are found by the values for s_j that fulfil condition (E.33). The inverse transform can then be found:

$$\frac{\sigma'_r}{\sigma_b}=\sum_{j=1}^{\infty}\left[\frac{\frac{J_0\left(\lambda_j r\right)}{J_0\left(\lambda_j R\right)}-\frac{1}{2m\lambda_j r}\frac{J_1\left(\lambda_j r\right)}{J_0\left(\lambda_j R\right)}-\frac{1}{4}}{\frac{-1}{m}+3-\frac{9}{4}m\left(\lambda_j R\right)^2}\right]e^{s_j t} \tag{E.38}$$

Note that the nominator of (E.38) still has a finite value for $r = 0$ by the condition (E.37). For the tangential effective stress:

$$\frac{\overline{\sigma}'_\theta}{\sigma_b} = \frac{\dfrac{\nu}{1-\nu} J_0(\lambda r) - J_0(\lambda R) + \dfrac{J_1(\lambda r)}{2m\lambda r} + \dfrac{J_1(\lambda R)}{2m\lambda R}}{s\left[3J_0(\lambda R) - \dfrac{2}{m}\dfrac{J_1(\lambda R)}{\lambda R}\right]}$$

and the inverse transform with the roots defined by (E.33):

$$\frac{\sigma'_\theta}{\sigma_b} = \sum_{j=1}^{\infty} \frac{\left[\dfrac{\nu}{1-\nu}\dfrac{J_0(\lambda_j r)}{J_0(\lambda_j R)} - \dfrac{1}{4} + \dfrac{J_1(\lambda_j r)}{2m\lambda_j r J_0(\lambda_j R)}\right] e^{s_j t}}{\dfrac{-1}{m} + 3 - \dfrac{9}{4} m (\lambda_j R)^2} \tag{E.39}$$

The effective vertical stress, equation (E.21) gives after rewriting :

$$\frac{\overline{\sigma}'_{zz}}{\sigma_b} = \frac{\dfrac{\nu}{1-\nu} J_0(\lambda r) + 2J_0(\lambda R) - \dfrac{J_1(\lambda R)}{m\lambda R}}{s\left[3J_0(\lambda R) - \dfrac{2J_1(\lambda R)}{m\lambda R}\right]} \tag{E.40}$$

The roots of (E.40) are defined by (E.33). Application of the root $s = 0$ to equation (E.40) gives:

$$\left(\frac{\sigma'_{zz}}{\sigma_b}\right)_{s=0} = \frac{\dfrac{\nu}{1-\nu} + 2 - \dfrac{1}{2m}}{3 - \dfrac{1}{m}} e^0 = 1, \qquad m = \frac{1-\nu}{2(1-2\nu)} \tag{E.41}$$

The other roots are found by condition (E.33). Together with (E.41) the inverse transform of the vertical effective stress is given by:

$$\frac{\sigma'_{zz}}{\sigma_b} = 1 + \sum_{j=1}^{\infty} \frac{\left[\dfrac{\nu}{1-\nu}\dfrac{J_0(\lambda_j r)}{J_0(\lambda_j R)} + \dfrac{1}{2}\right] e^{s_j t}}{\dfrac{-1}{m} + 3 - \dfrac{9}{4} m (\lambda_j R)^2} \tag{E.42}$$

The expressions for total stress can either be found by deriving the inverse transform of equations (E.22) to (E.24) or by a summation of the expressions for pore pressure development (E.35) and effective stress (E.38), (E.39) and (E.42). Both give the following results:

$$\frac{\sigma_r}{\sigma_b} = \sum_{j=1}^{\infty} \frac{\left[\dfrac{3}{4} - \dfrac{1}{2m\lambda_j r}\dfrac{J_1(\lambda_j r)}{J_0(\lambda_j R)}\right] e^{s_j t}}{\dfrac{-1}{m} + 3 - \dfrac{9}{4} m (\lambda_j R)^2} \tag{E.43}$$

$$\frac{\sigma_\theta}{\sigma_b} = \sum_{j=1}^{\infty} \frac{\left[\dfrac{\dfrac{J_1(\lambda_j r)}{\lambda_j r} - J_0(\lambda_j r)}{2mJ_0(\lambda_j R)} + \dfrac{3}{4}\right] e^{s_j t}}{\dfrac{-1}{m} + 3 - \dfrac{9}{4} m (\lambda_j R)^2} \tag{E.44}$$

$$\frac{\sigma_{zz}}{\sigma_b} = 1 + \sum_{j=1}^{\infty} \frac{\left[\dfrac{-1}{2m}\dfrac{J_0(\lambda_j r)}{J_0(\lambda_j R)} + \dfrac{3}{2}\right] e^{s_j t}}{\dfrac{-1}{m} + 3 - \dfrac{9}{4} m (\lambda_j R)^2} \tag{E.45}$$

The expression for vertical strain, ε_{zz} can be found by deriving the inverse transform of (E.29). Rewriting (E.29) gives:

$$\frac{\partial \overline{u}_{zz}}{\partial z} = \frac{\frac{\sigma_b}{G}\left[J_0(\lambda R) - \frac{1}{2m}\frac{J_1(\lambda R)}{\lambda R}\right]}{s\left[3J_0(\lambda R) - \frac{2}{m}\frac{J_1(\lambda R)}{\lambda R}\right]} \tag{E.46}$$

Application of the Heaviside theorem for the root $s = 0$ and condition (E.37) gives:

$$\frac{\frac{\sigma_b}{G}\left[1 - \frac{1}{2m}\frac{1}{2}\right]e^{0t}}{3 - \frac{1}{m}} = \frac{\sigma_b}{\frac{E}{2(1+\nu)}}\frac{1}{2(1+\nu)} = \frac{\sigma_b}{E} \tag{E.47}$$

The other roots are defined by condition (E.33). With (E.47) this results in :

$$\varepsilon_{zz} = \frac{\partial u_{zz}}{\partial z} = \frac{\sigma_b}{E}\left[1 + \sum_{j=1}^{\infty}\frac{\frac{1}{2}(1+\nu)\,e^{s_j t}}{\frac{-1}{m} + 3 - \frac{9}{4}m(\lambda_j R)^2}\right] \tag{E.48}$$

The expression for tangential strain can be found after rewriting the inverse transforms of either (E.18) or (E.13) and rewriting the found expression. Both give:

$$\varepsilon_\theta = \frac{u_r}{r} = \frac{\sigma_b}{E}\left[-\nu + 2(1+\nu)\sum_{j=1}^{\infty}\frac{\frac{J_1(\lambda_j r)/J_0(\lambda_j R)}{4m\lambda_j r} - \frac{1}{8}}{\frac{-1}{m} + 3 - \frac{9}{4}m(\lambda_j R)^2}e^{s_j t}\right] \tag{E.49}$$

The radial strain is found by the inverse transform of (E.13):

$$\varepsilon_r = \frac{\partial u_r}{\partial r} = \frac{\sigma_b}{E}\left[-\nu + 2(1+\nu)\sum_{j=1}^{\infty}\frac{\left(\frac{\lambda_j J_0(\lambda_j r) - \frac{1}{r}J_1(\lambda_j r)}{4m\lambda_j J_0(\lambda_j R)} - \frac{1}{8}\right)e^{s_j t}}{\frac{-1}{m} + 3 - \frac{9}{4}m(\lambda_j R)^2}\right] \tag{E.50}$$

Finally an expression for volumetric strain can be found either by deriving the inverse transform of (E.16) or by a summation of (E.48), (E.49) and (E.50). Both lead to:

$$e = \frac{\sigma_b}{E}\left[(1-2\nu) + \frac{1}{K + \frac{4}{3}G}\sum_{j=1}^{\infty}\frac{\frac{2(1+\nu)\,J_0(\lambda_j r)}{J_0(\lambda_j R)}\,e^{s_j t}}{\frac{-1}{m} + 3 - \frac{9}{4}m(\lambda_j R)^2}\right] \tag{E.51}$$

Function f(t)

Section 5.2 explains the difference between the Biot equations and the Terzaghi–Rendulic solution for three dimensional consolidation, which is found in equation (E.6). Double integration of equation (E.6) gives:

$$\left(K + \frac{4}{3}G\right)e = \sigma_w + f(x, y, z, t)$$

In the Terzaghi–Rendulic solution a direct relation between e and σ_w is assumed, leading to $f(x, y, z, t) = 0$. De Josselin de Jong [41] shows that in absence of rotations $f(x, y, z, t)$ reduces to

$f(t)$ but not necessarily to 0. With the solutions found for e and σ_w an expression for $f(t)$ can be found. The Laplace transformation of equation (E.6) gives:

$$\left(K + \frac{4}{3}G\right)\overline{e} = \overline{\sigma}_w + \overline{f}(t) \tag{E.52}$$

With the equations (E.9) and (E.17)

$$\overline{f}(t) = C_3\left(K + \frac{4}{3}G\right) \tag{E.53}$$

With C_3 expressed by equation (E.30) gives:

$$\overline{f}(t) = \frac{\left(\overline{g}_3 + 2\overline{g}_2\right) J_0(\lambda R) + \dfrac{2\overline{g}_1}{m}\dfrac{J_1(\lambda R)}{\lambda R}}{3J_0(\lambda R) - \dfrac{2}{m}\dfrac{J_1(\lambda R)}{\lambda R}} \tag{E.54}$$

The inverse transformation is found equivalent to the previous given inverse transformations of stresses and strains, with $g_1 = g_2 = 0$ and $g_3 = \sigma_b$ and condition (E.37):

$$f(t) = \frac{\sigma_b}{3 - \dfrac{1}{m}} + \sum_{j=1}^{\infty} \frac{\sigma_b e^{s_j t}}{3 - \dfrac{1}{m} + \dfrac{9}{4}m(\lambda R)^2} \tag{E.55}$$

Non–perfect drainage

Due to hydraulic resistance in the drains, porous stone and the pore water collection system boundary condition a might not hold in practice. To study the influence of a non–perfect drainage system boundary condition a is replace by a time depending boundary condition. Section 5.5 suggest the following boundary condition:

$$g_1 = -\frac{1}{3}\sigma_b e^{-\kappa t}$$

In which the parameters κ controls the drain pressure decay. The complete set of boundary conditions becomes:

$$\begin{aligned} g_1 &= -\frac{1}{3}\sigma_b e^{-\kappa t}, \quad \rightarrow \quad \overline{g}_1 = -\frac{1}{3}\frac{\sigma_b}{\kappa + s} \\ g_2 &= 0 \qquad \rightarrow \qquad \overline{g}_2 = 0 \\ g_3 &= \sigma_b \qquad \rightarrow \qquad \overline{g}_3 = \frac{\sigma_b}{s} \end{aligned}$$

Application of this set of boundary conditions to equation (E.31) gives:

$$\begin{aligned} \overline{\sigma}_w = &\frac{\left(J_0(\lambda r) - J_0(\lambda R)\right)\sigma_b}{s\left[3J_0(\lambda R) - \dfrac{2}{m}\dfrac{J_1(\lambda R)}{\lambda R}\right]} - \frac{\left(J_0(\lambda r) - J_0(\lambda R)\right)\sigma_b}{(\kappa + s)\left[3J_0(\lambda R) - \dfrac{2}{m}\dfrac{J_1(\lambda R)}{\lambda R}\right]} \\ &-\frac{1}{3}\frac{\sigma_b}{\kappa + s} \end{aligned} \tag{E.56}$$

The right hand side of equation (E.56) consists of three parts. The inverse transform is found after summation of the inverse transforms of each individual parts. The inverse transformation of the first part has already been given by equation (E.35). The inverse transform of the third part follows directly from the boundary conditions:

$$\mathscr{L}^{-1}\left(-\frac{1}{3}\frac{\sigma_b}{\kappa + s}\right) = -\frac{1}{3}\sigma_b e^{-\kappa t}$$

For finding the inverse transform of the second part the Heaviside expansion theorem is used. The roots of the second term are given by:

$$s = -\kappa \quad \vee \quad 3\,J_0\left(\lambda R\right) - \frac{2}{m}\frac{J_1\left(\lambda R\right)}{\lambda R} = 0$$

The second group of roots are given by equation (E.33). The derivative of the denominator of the second term in equation (E.56) is given by:

$$\left(\kappa + s\right)\frac{\partial}{\partial s}\left[3J_0\left(\lambda R\right) - \frac{2J_1\left(\lambda R\right)}{m\lambda R}\right] + \left[3J_0\left(\lambda R\right) - \frac{2J_1\left(\lambda R\right)}{m\lambda R}\right]\frac{\partial}{\partial s}\left(\kappa + s\right) =$$
$$\frac{\kappa + s}{s}\left[\frac{-1}{m}J_0\left(\lambda R\right) + J_1\left(\lambda R\right)\left(\frac{2}{\lambda R m} - \frac{3}{2}\lambda R\right)\right] + \left[3J_0\left(\lambda R\right) - \frac{2J_1\left(\lambda R\right)}{m\lambda R}\right]$$

Application of the roots gives the inverse transform of the second term of equation (E.56):

$$\sum_{j=1}^{\infty}\frac{\left[J_0\left(\lambda_j r\right) - J_0\left(\lambda_j R\right)\right]\sigma_b e^{s_j t}}{\frac{\kappa + s_j}{s_j}\left[\frac{-1}{m}J_0\left(\lambda_j R\right) + J_1\left(\lambda_j R\right)\left(\frac{2}{\lambda_j R m} - \frac{3}{2}\lambda_j R\right)\right]} + \frac{\left[J_0\left(\sqrt{\frac{\kappa}{c}}r\right) - J_0\left(\sqrt{\frac{\kappa}{c}}R\right)\right]\sigma_b e^{-\kappa t}}{3J_0\left(\sqrt{\frac{\kappa}{c}}R\right) - \frac{2J_1\left(\sqrt{\frac{\kappa}{c}}R\right)}{m\sqrt{\frac{\kappa}{c}}R}}$$

Combining the inverse transforms of the parts together gives the final solution for the pore pressure development:

$$\frac{\sigma_w}{\sigma_b} = \sum_{j=1}^{\infty}\frac{\left[\frac{J_0\left(\lambda_j r\right)}{J_0\left(\lambda_j R\right)} - 1\right]e^{s_j t}}{3 - \frac{1}{m} - \frac{9}{4}m\left(\lambda_j R\right)^2} - \sum_{j=1}^{\infty}\frac{\left[\frac{J_0\left(\lambda_j r\right)}{J_0\left(\lambda_j R\right)} - 1\right]e^{s_j t}}{\frac{\kappa + s_j}{s_j}\left[3 - \frac{1}{m} - \frac{9}{4}m\left(\lambda_j R\right)^2\right]} -$$
$$\frac{\left[J_0\left(\sqrt{\frac{\kappa}{c}}r\right) - J_0\left(\sqrt{\frac{\kappa}{c}}R\right)\right]e^{-\kappa t}}{3J_0\left(\sqrt{\frac{\kappa}{c}}R\right) - \frac{2J_1\left(\sqrt{\frac{\kappa}{c}}R\right)}{m\sqrt{\frac{\kappa}{c}}R}} - \frac{1}{3}e^{-\kappa t} \tag{E.57}$$

Graphs of stress and strain

To illustrate the results this section presents graphs of the derived expressions for stress and strain. The graphs present the stress and strain for $\nu = 0$, 1/3 and 0.45, $c = 1 \times 10^{-6}$ m^2/s and $R = 0.5$ m.

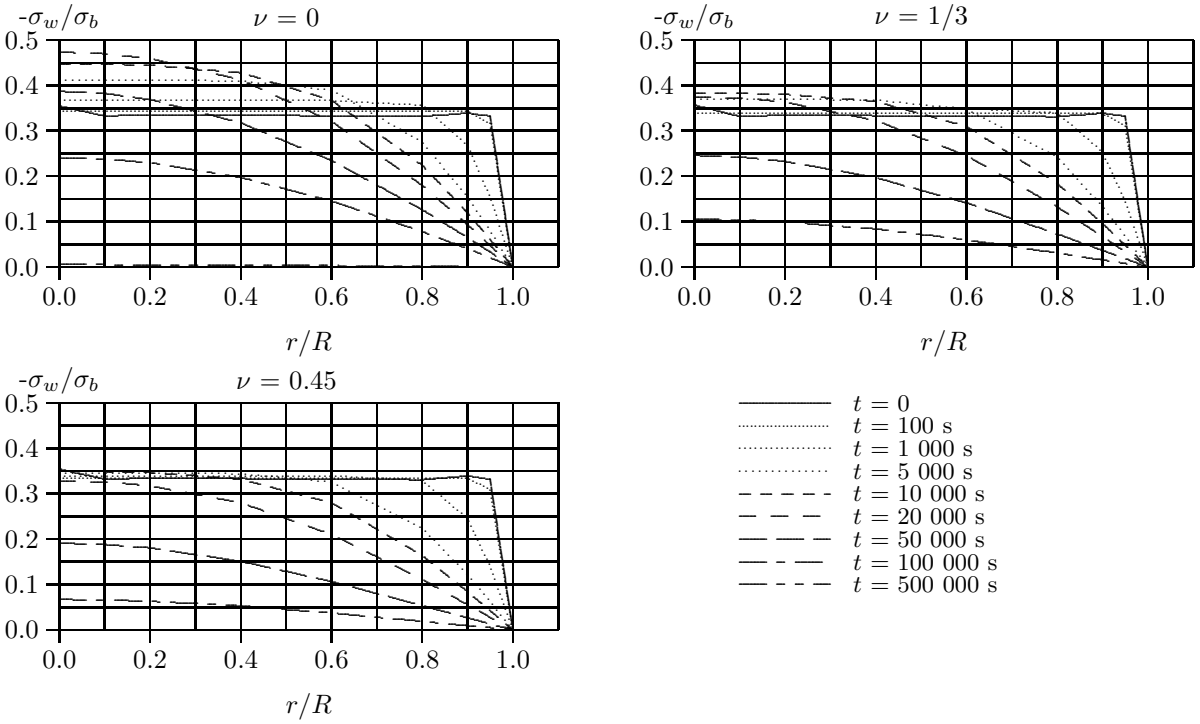

Figure E.2: Pore pressure development for isotropic linear elasticity and axial symmetric conditions

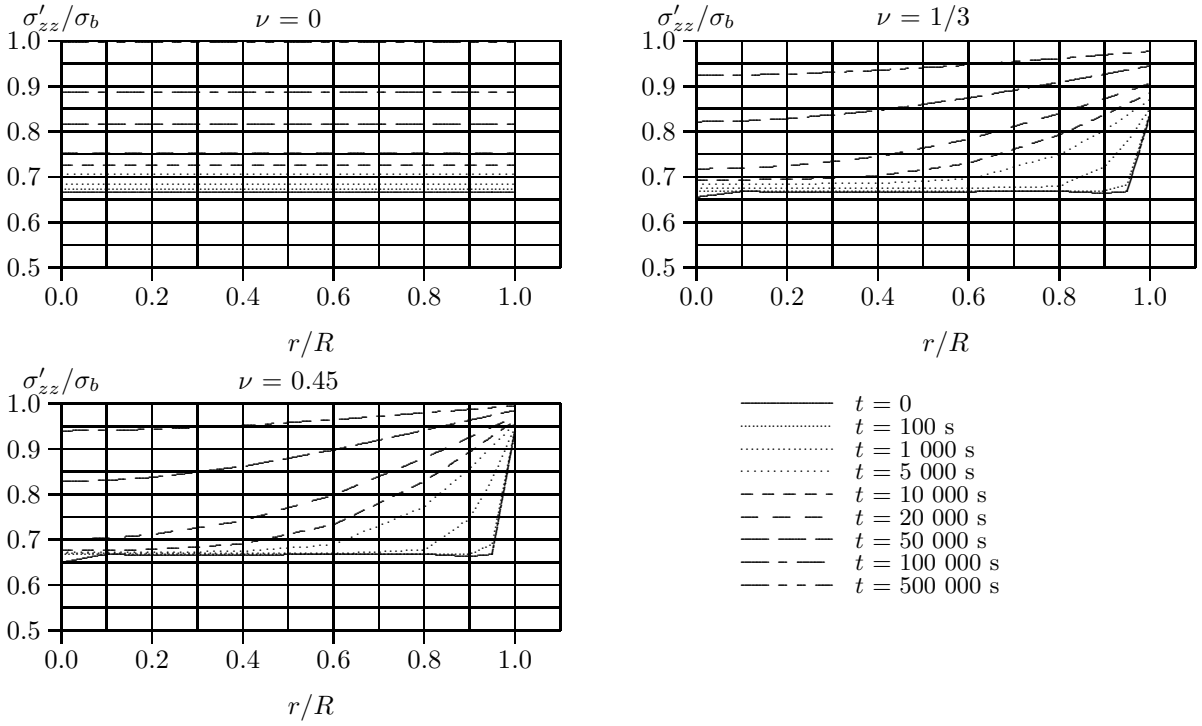

Figure E.3: Development of vertical effective stress for isotropic linear elasticity and axial symmetric conditions

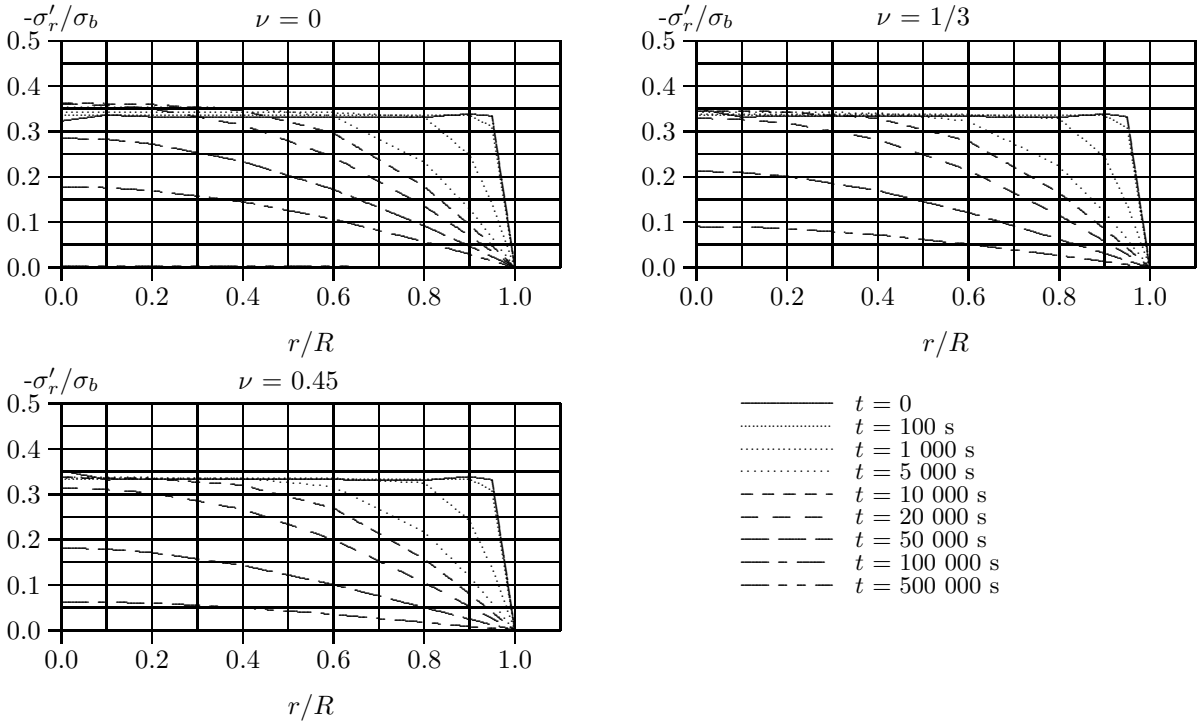

Figure E.4: Development of radial effective stress for isotropic linear elasticity and axial symmetric conditions

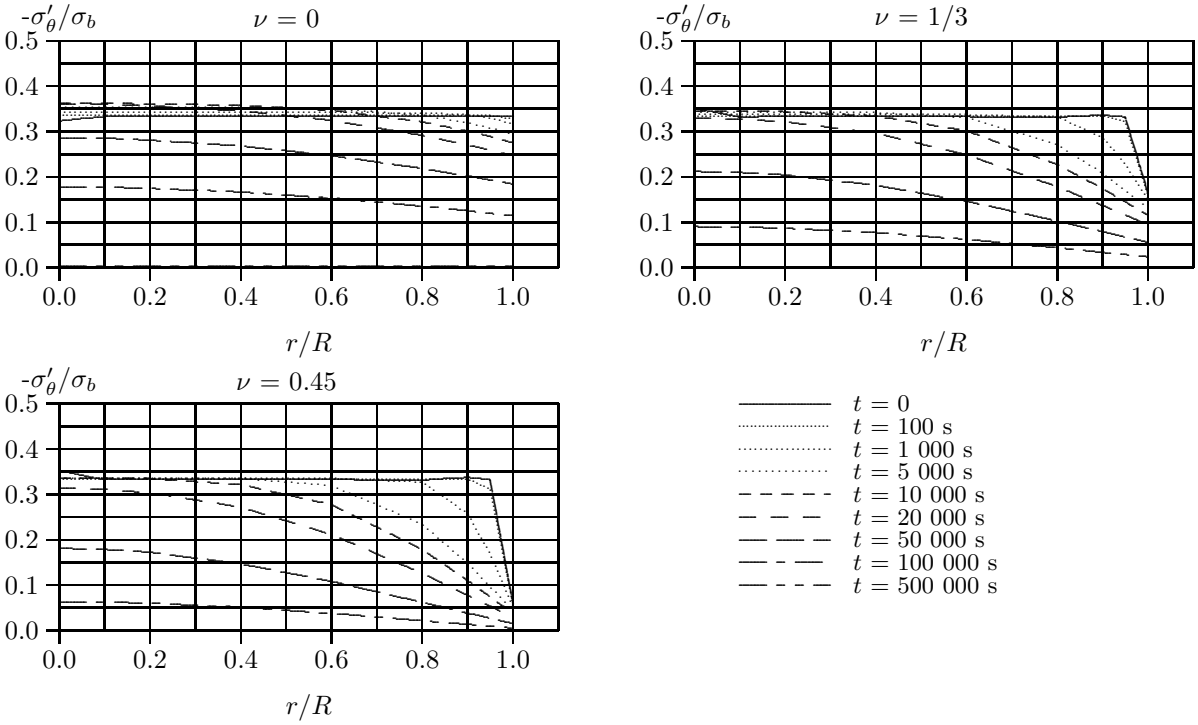

Figure E.5: Development of tangential effective stress for isotropic linear elasticity and axial symmetric conditions

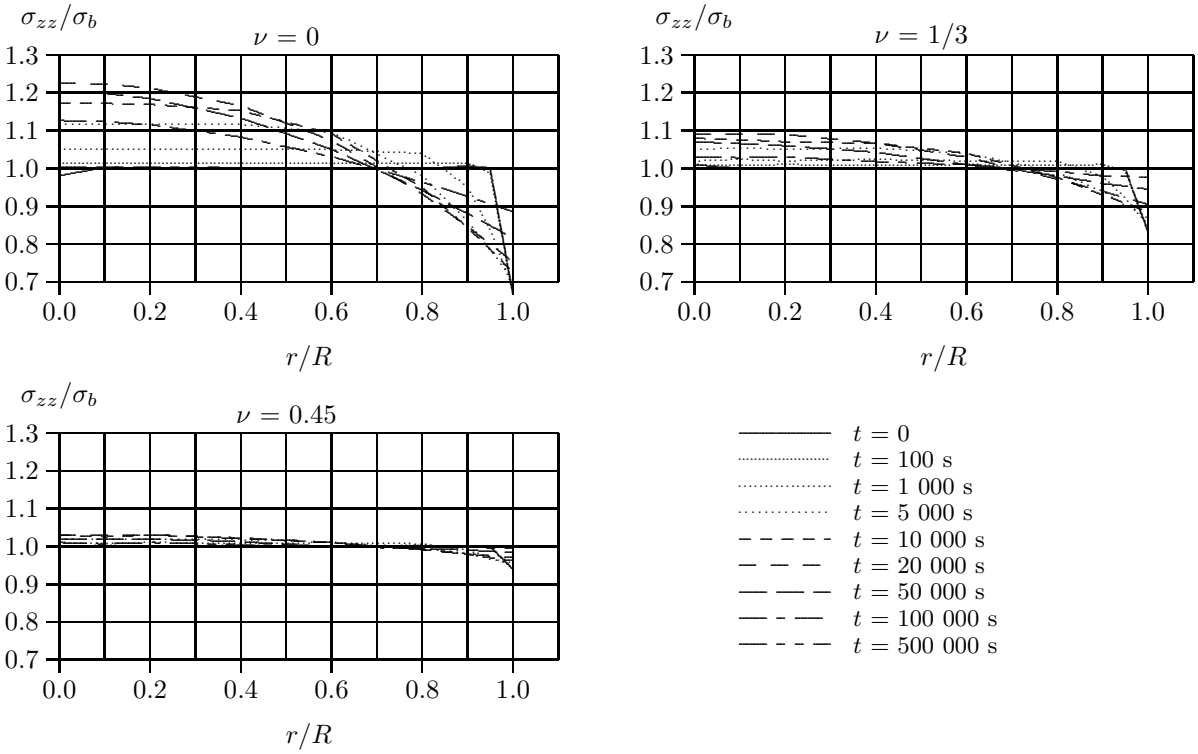

Figure E.6: Development of vertical total stress for isotropic linear elasticity and axial symmetric conditions

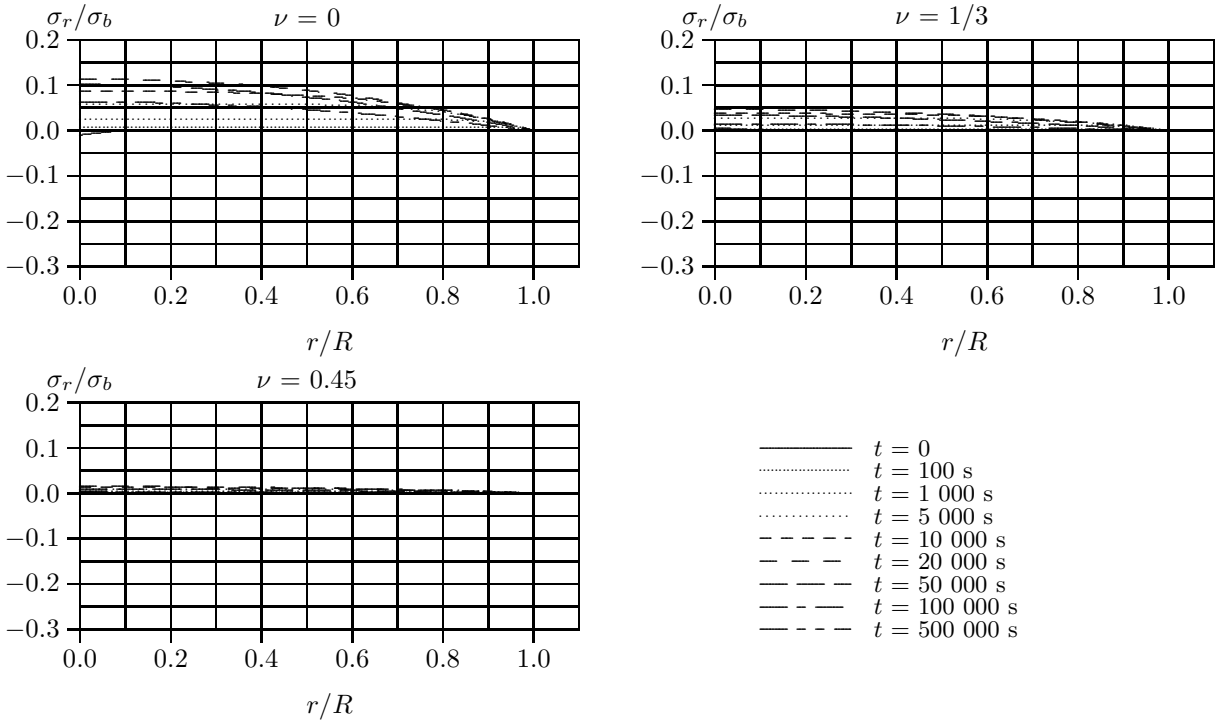

Figure E.7: Development of radial total stress for isotropic linear elasticity and axial symmetric conditions

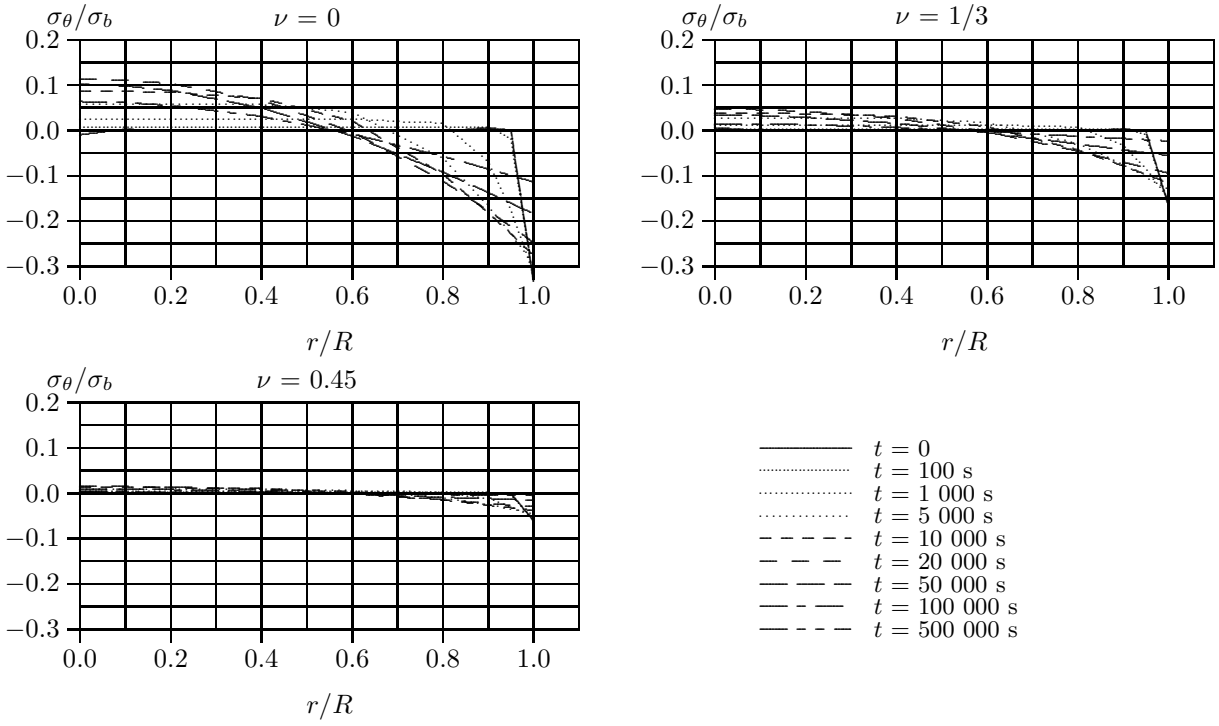

Figure E.8: Development of tangential total stress for isotropic linear elasticity and axial symmetric conditions

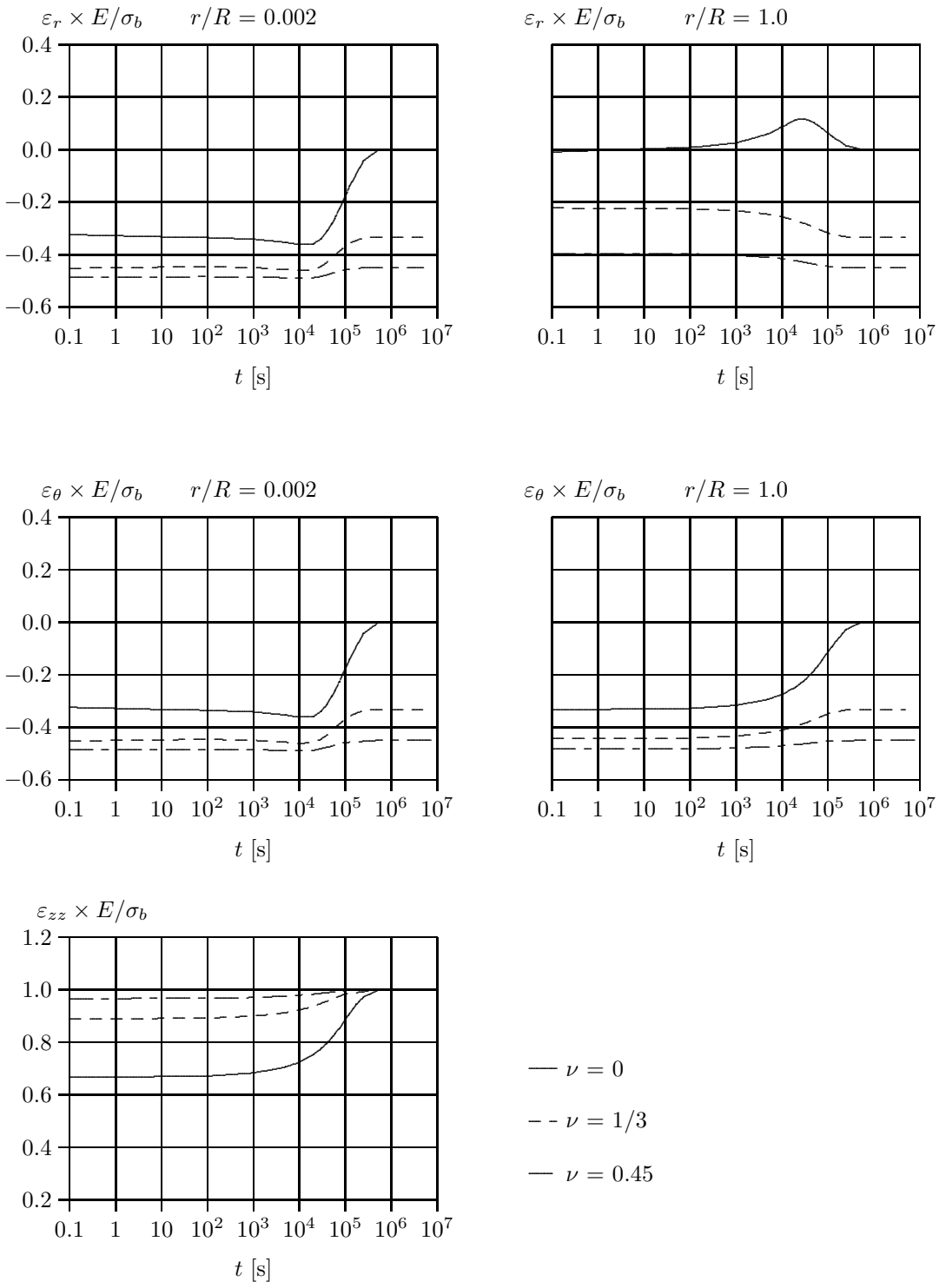

Figure E.9: Development of vertical, radial and tangential strain for isotropic linear elasticity and axial symmetric conditions

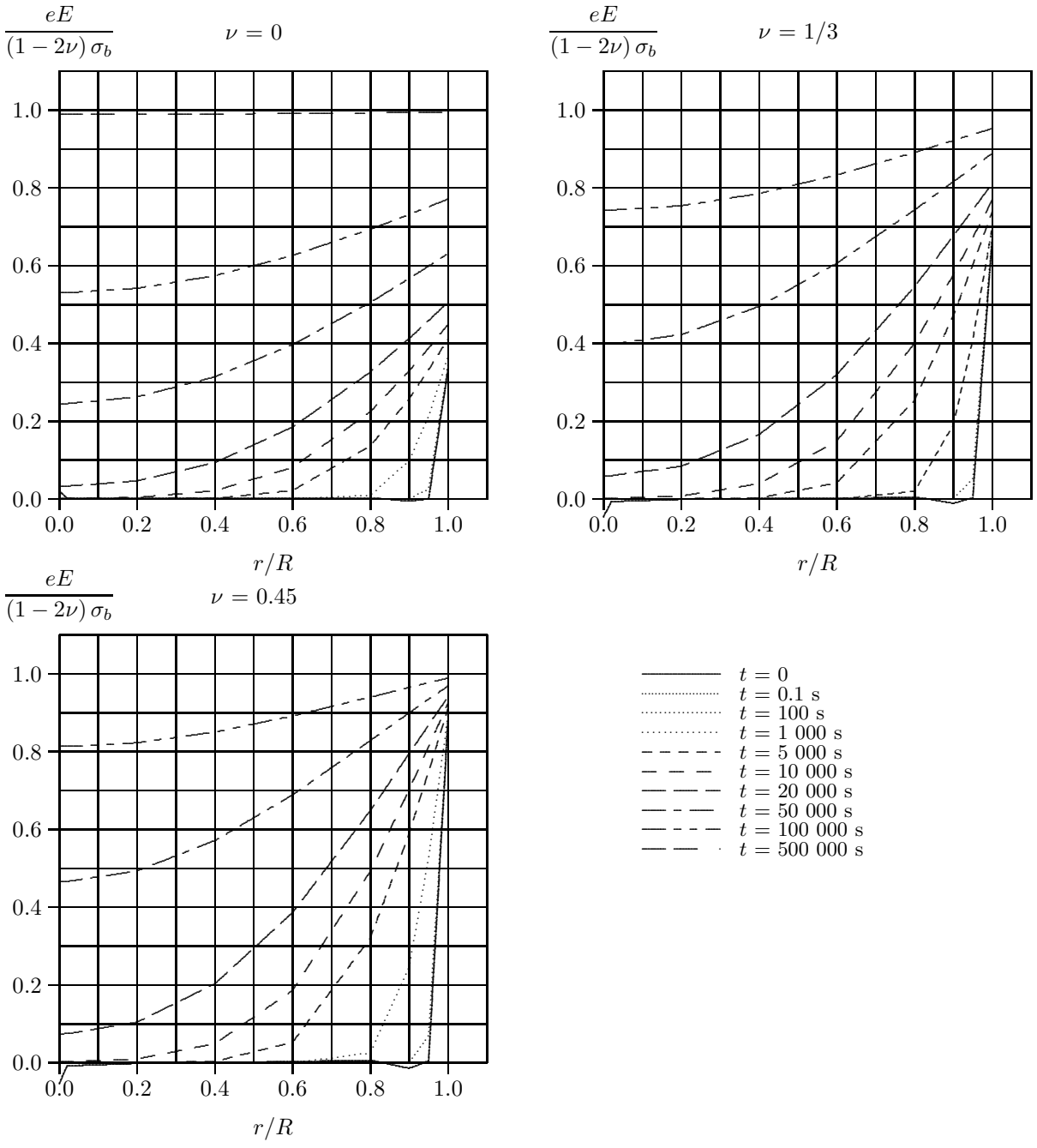

Figure E.10: Development volume strain for isotropic linear elasticity and axial symmetric conditions

Appendix F

Consolidation for isotropic plane–strain conditions

In the previous appendix a solution is found for the axial-symmetric consolidation problem. In this appendix the consolidation problem is solved for plane–strain conditions. Figure F.1 shows the plane–strain conditions. Again 4 steps are taken.

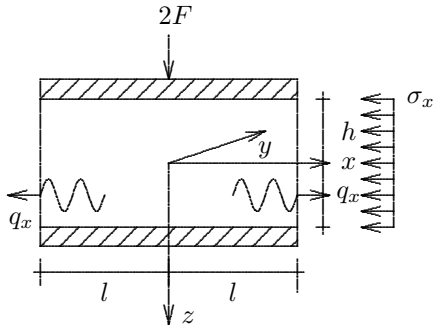

Figure F.1: Plane strain conditions

step 1, the relevant equations
For plane–strain conditions the stress–strain relation is given by:

$$\begin{aligned} \sigma'_{xx} &= 2G\left[\frac{\nu}{1-2\nu}e + \varepsilon_{xx}\right] \\ \sigma'_{yy} &= 2G\left[\frac{\nu}{1-2\nu}e + \varepsilon_{yy}\right] \\ \sigma'_{zz} &= 2G\left[\frac{\nu}{1-2\nu}e + \varepsilon_{zz}\right] \end{aligned} \tag{F.1}$$

The relation between strain and deformation:

$$\varepsilon_{xx} = \frac{\partial u_{xx}}{\partial x}, \quad \varepsilon_{yy} = 0, \quad \varepsilon_{zz} = \frac{\partial u_{zz}}{\partial z} \tag{F.2}$$

Equation (F.2) reduces (F.1) to:

$$\begin{aligned}\sigma'_{xx} &= 2G\left[\frac{\nu}{1-2\nu}e + \frac{\partial u_{xx}}{\partial x}\right]\\ \sigma'_{yy} &= 2G\left[\frac{\nu}{1-2\nu}e\right]\\ \sigma'_{zz} &= 2G\left[\frac{\nu}{1-2\nu}e + \frac{\partial u_{zz}}{\partial z}\right]\end{aligned} \tag{F.3}$$

The storage equation is given by:

$$\frac{k}{\gamma_w}\nabla^2\sigma_w = \frac{\partial e}{\partial t} \tag{F.4}$$

Equilibrium of forces gives :

$$\left(K + \frac{4}{3}G\right)\nabla^2 e = \nabla^2\sigma_w \tag{F.5}$$

Combination of equations (F.4) and (F.5):

$$\nabla^2 e = \frac{1}{c}\frac{\partial e}{\partial t}, \quad \text{with } c = \frac{k}{\gamma_w}\left(K + \frac{4}{3}G\right) \tag{F.6}$$

step 2, the Laplace transformation
Equation (F.6) is solved by the use of the Laplace transformation. Application of the Laplace transformation to (F.6) gives:

$$\nabla^2\overline{e} = \frac{1}{c}\left(s\overline{e} - e_0\right) \tag{F.7}$$

In which e_0 represents the initial volumetric strain. Since initially the soil behaves undrained it follows that $e_0 = 0$. For plane–strain condition, $\varepsilon_y = 0$ and ε_z is constant in depth:

$$\begin{aligned}&e = \varepsilon_{xx} + \varepsilon_{zz}\\ &\frac{\partial^2\varepsilon_{zz}}{\partial z^2} = 0, \quad \nabla^2 e = \frac{\partial^2\varepsilon_{xx}}{\partial x^2} = \frac{\partial^2 e}{\partial x^2}, \quad \rightarrow \nabla^2\overline{e} = \frac{\partial^2\overline{e}}{\partial x^2}\end{aligned} \tag{F.8}$$

For equation (F.7) is found:

$$\frac{\partial^2\overline{e}}{\partial x^2} - \frac{s}{c}\overline{e} = 0$$

standard solution:

$$\overline{e} = C_1\exp\left(\sqrt{\frac{s}{c}}x\right) + C_2\exp\left(-\sqrt{\frac{s}{c}}x\right)$$

or:

$$\overline{e} = C_1\cosh\left(\sqrt{\frac{s}{c}}x\right) + C_2\sinh\left(\sqrt{\frac{s}{c}}x\right) \tag{F.9}$$

Equations (F.8) and (F.9) gives:

$$\overline{e} = C_1\cosh\left(\sqrt{\frac{s}{c}}x\right) + C_2\sinh\left(\sqrt{\frac{s}{c}}x\right) = \frac{\partial\overline{u}_{xx}}{\partial x} + \frac{\partial\overline{u}_{zz}}{\partial z}$$

$$\frac{\partial\overline{u}_{xx}}{\partial x} = C_1\cosh\left(\sqrt{\frac{s}{c}}x\right) + C_2\sinh\left(\sqrt{\frac{s}{c}}x\right) - \frac{\partial\overline{u}_{zz}}{\partial z} \tag{F.10}$$

Application of the Laplace transformation to equation (F.5) gives:

$$\nabla^2\overline{e} = \frac{1}{4mG}\nabla^2\overline{\sigma}_w, \quad m = \frac{K + \frac{4}{3}G}{4G} = \frac{1-\nu}{2\left(1-2\nu\right)} \tag{F.11}$$

Integration of equation (F.11) gives :

$$\overline{e} = \frac{1}{4mG}\overline{\sigma}_w + C_3, \quad \text{with } \nabla^2 C_3 = 0 \tag{F.12}$$

Equation (F.9) and (F.12) give the expression for the pore pressure development in transformed conditions:

$$\overline{\sigma}_w = 4mG\left[C_1 \cosh\left(\sqrt{\frac{s}{c}}x\right) + C_2 \sinh\left(\sqrt{\frac{s}{c}}x\right) - C_3\right] \tag{F.13}$$

Combination of equations (F.9), (F.10) and (F.3) gives the effective stress in transformed conditions. The summation of effective stress and pore pressure, equation (F.13), gives the expressions for total stress. Note the sign convention in which effective and total stress is defined positive for tension while pore pressure is defined positive for pressure. The total stress is given by:

$$\sigma = \sigma' - \sigma_w, \quad \rightarrow \overline{\sigma} = \overline{\sigma}' - \overline{\sigma}_w$$

The expressions for stress and strain for transformed conditions become:

$$\overline{e} = C_1 \cosh\left(\sqrt{\frac{s}{c}}x\right) + C_2 \sinh\left(\sqrt{\frac{s}{c}}x\right) \tag{F.14}$$

$$\frac{\partial \overline{u}_{xx}}{\partial x} = C_1 \cosh\left(\sqrt{\frac{s}{c}}x\right) + C_2 \sinh\left(\sqrt{\frac{s}{c}}x\right) - \frac{\partial \overline{u}_{zz}}{\partial z} \tag{F.15}$$

$$\overline{\sigma}_w = 4mG\left[C_1 \cosh\left(\sqrt{\frac{s}{c}}x\right) + C_2 \sinh\left(\sqrt{\frac{s}{c}}x\right) - C_3\right] \tag{F.16}$$

$$\overline{\sigma}'_{xx} = 2G\left[\begin{array}{l}\dfrac{\nu}{1-2\nu}\left(C_1 \cosh\left(\sqrt{\dfrac{s}{c}}x\right) + C_2 \sinh\left(\sqrt{\dfrac{s}{c}}x\right)\right) + C_1 \cosh\left(\sqrt{\dfrac{s}{c}}x\right) + \\ C_2 \sinh\left(\sqrt{\dfrac{s}{c}}x\right) - \dfrac{\partial \overline{u}_{zz}}{\partial z}\end{array}\right] \tag{F.17}$$

$$\overline{\sigma}'_{yy} = 2G\left[\frac{\nu}{1-2\nu}\left(C_1 \cosh\left(\sqrt{\frac{s}{c}}x\right) + C_2 \sinh\left(\sqrt{\frac{s}{c}}x\right)\right)\right] \tag{F.18}$$

$$\overline{\sigma}'_{zz} = 2G\left[\frac{\nu}{1-2\nu}\left(C_1 \cosh\left(\sqrt{\frac{s}{c}}x\right) + C_2 \sinh\left(\sqrt{\frac{s}{c}}x\right)\right) + \frac{\partial \overline{u}_{zz}}{\partial z}\right] \tag{F.19}$$

$$\begin{aligned}\overline{\sigma}_{xx} = {} & 2GC_1\left[\frac{\nu}{1-2\nu} + 1 - 2m\right]\cosh\left(\sqrt{\frac{s}{c}}x\right) + 2GC_2 \\ & \left[\frac{\nu}{1-2\nu} + 1 - 2m\right]\sinh\left(\sqrt{\frac{s}{c}}x\right) - 2G\frac{\partial \overline{u}_{zz}}{\partial z} + 4mGC_3\end{aligned} \tag{F.20}$$

$$\overline{\sigma}_{yy} = 2GC_1\left[\frac{\nu}{1-2\nu} - 2m\right]\cosh\left(\sqrt{\frac{s}{c}}x\right) + 2GC_2\left[\frac{\nu}{1-2\nu} - 2m\right]\sinh\left(\sqrt{\frac{s}{c}}x\right) + 4mGC_3 \tag{F.21}$$

$$\overline{\sigma}_{zz} = 2GC_1\left[\frac{\nu}{1-2\nu} - 2m\right]\cosh\left(\sqrt{\frac{s}{c}}x\right) + 2GC_2\left[\frac{\nu}{1-2\nu} - 2m\right]\sinh\left(\sqrt{\frac{s}{c}}x\right) + 2G\frac{\partial \overline{u}_{zz}}{\partial z} + 4mGC_3 \tag{F.22}$$

step 3, solving for the boundary conditions
The set of equations (F.14) to (F.22) contains 4 unknown coefficients; C_1, C_2, C_3 and $\partial \overline{u}_{zz}/\partial z$. These coefficients are to be determined by the boundary conditions:

a) at $x = 0$, $\quad \dfrac{\partial \sigma_w}{\partial x} = 0, \rightarrow \dfrac{\partial \overline{\sigma}_w}{\partial x} = 0$

b) at $x = l$, $\quad \sigma_w = 0, \rightarrow \overline{\sigma}_w = 0$

c) at $x = l$, $\quad \sigma_x = 0, \rightarrow \overline{\sigma}_{xx} = 0$

d) $\int\limits_{-l}^{l} \dfrac{\sigma_{zz}}{2l} dx = \dfrac{2F}{2l}, \rightarrow \int\limits_{-l}^{l} \dfrac{\overline{\sigma}_{zz}}{2l} dx = \dfrac{\overline{F}}{l}, \quad \overline{F} = \int\limits_{0}^{l} \overline{\sigma}_{zz} dx$

Boundary condition a and the derivative of equation (F.16) gives:

$$\frac{\partial \overline{\sigma}_w}{\partial x} = 4mG \left[C_1 \sqrt{\frac{s}{c}} \sinh\left(\sqrt{\frac{s}{c}} x \right) + C_2 \sqrt{\frac{s}{c}} \cosh\left(\sqrt{\frac{s}{c}} x \right) \right]$$

for $x = 0$:

$$4mG \left[C_1 \times 0 + C_2 \times 1 \right] = 0, \qquad C_2 = 0 \tag{F.23}$$

Boundary condition b in combination with equation (F.16) and (F.23) results in:

$$C_3 = C_1 \cosh\left(\sqrt{\frac{s}{c}} l \right) \tag{F.24}$$

Equation (F.16) can now be rewritten in:

$$\overline{\sigma}_w = 4mGC_1 \left[\cosh\left(\sqrt{\frac{s}{c}} x \right) - \cosh\left(\sqrt{\frac{s}{c}} l \right) \right] \tag{F.25}$$

Before application of boundary condition c expression (F.20) can now be rewritten:

$$\overline{\sigma}_{xx} = 2GC_1 \left[\frac{\nu}{1-2\nu} + 1 - 2m \right] \cosh\left(\sqrt{\frac{s}{c}} x \right) - 2G \frac{\partial \overline{u}_{zz}}{\partial z} + 4mGC_1 \cosh\left(\sqrt{\frac{s}{c}} l \right)$$

$$\text{with } \left[\frac{\nu}{1-2\nu} + 1 - 2m \right] = \left[\frac{\nu}{1-2\nu} + \frac{(1-2\nu)}{(1-2\nu)} - \frac{2(1-\nu)}{2(1-2\nu)} \right] = 0$$

$$\overline{\sigma}_{xx} = -2G \frac{\partial \overline{u}_{zz}}{\partial z} + 4mGC_1 \cosh\left(\sqrt{\frac{s}{c}} l \right)$$

with boundary condition c this leads to:

$$C_1 = \frac{\dfrac{\partial \overline{u}_{zz}}{\partial z}}{2m \cosh\left(\sqrt{\frac{s}{c}} l \right)} \tag{F.26}$$

boundary condition d gives with the equations (F.22), (F.23), (F.24) and (F.26):

$$\overline{F} = \int\limits_{0}^{l} \left[\begin{array}{l} 2G \dfrac{\partial \overline{u}_{zz}/\partial z}{2m \cosh\left(\sqrt{\frac{s}{c}} l \right)} \left[\dfrac{\nu}{1-2\nu} - 2m \right] \cosh\left(\sqrt{\dfrac{s}{c}} x \right) + 2G \dfrac{\partial \overline{u}_{zz}}{\partial z} \\ 4mG \dfrac{\partial \overline{u}_{zz}/\partial z}{2m \cosh\left(\sqrt{\dfrac{s}{c}} l \right)} \cosh\left(\sqrt{\dfrac{s}{c}} l \right) \end{array} \right] dx$$

$$\overline{F} = \int\limits_{0}^{l} \left[2G \frac{\partial \overline{u}_{zz}/\partial z}{2m \cosh\left(\sqrt{\frac{s}{c}} l \right)} \left[\frac{\nu}{1-2\nu} - \frac{2(1-\nu)}{2(1-2\nu)} \right] \cosh\left(\sqrt{\frac{s}{c}} x \right) + 4G \frac{\partial \overline{u}_{zz}}{\partial z} \right] dx$$

$$\overline{F} = \int\limits_{0}^{l} \left[-2G \frac{\dfrac{\partial \overline{u}_{zz}}{\partial z} \cosh\left(\sqrt{\frac{s}{c}} x \right)}{2m \cosh\left(\sqrt{\frac{s}{c}} l \right)} + 4G \frac{\partial \overline{u}_{zz}}{\partial z} \right] dx$$

Since $\partial\overline{u}_{zz}/\partial z$ is independent from x it follows:

$$\overline{F} = \left[-2G\frac{\frac{\partial\overline{u}_{zz}}{\partial z}\sinh\left(\sqrt{\frac{s}{c}}x\right)}{2m\sqrt{\frac{s}{c}}\cosh\left(\sqrt{\frac{s}{c}}l\right)} + 4G\frac{\partial\overline{u}_{zz}}{\partial z}x \right]_0^l$$

$$\overline{F} = \frac{\partial\overline{u}_{zz}}{\partial z}\left[4Gl - \frac{G\sinh\left(\sqrt{\frac{s}{c}}x\right)}{m\sqrt{\frac{s}{c}}\cosh\left(\sqrt{\frac{s}{c}}l\right)} \right]$$

$$\frac{\partial\overline{u}_{zz}}{\partial z} = \frac{\overline{F}}{4Gl - G\sinh\left(\sqrt{\frac{s}{c}}x\right)\Big/ m\sqrt{\frac{s}{c}}\cosh\left(\sqrt{\frac{s}{c}}l\right)}$$

$$\overline{F} = \int_0^\infty F e^{-st}dt \; = \frac{1}{s}F$$

$$\frac{\partial\overline{u}_{zz}}{\partial z} = \frac{F}{s\left[4Gl - G\sinh\left(\sqrt{\frac{s}{c}}x\right)\Big/ m\sqrt{\frac{s}{c}}\cosh\left(\sqrt{\frac{s}{c}}l\right)\right]} \tag{F.27}$$

By the expressions (F.23), (F.24), (F.26) and (F.27) the expression of the stresses and strains for the transformed conditions are determined. The equation (F.14) to (F.22) can now be rewritten in:

$$\overline{e} = \frac{\frac{F}{2mG}\cosh\left(\sqrt{\frac{s}{c}}x\right)}{s\left[4l - \tanh\left(\sqrt{\frac{s}{c}}l\right)/\left(\sqrt{\frac{s}{c}}m\right)\right]\cosh\left(\sqrt{\frac{s}{c}}l\right)} \tag{F.28}$$

$$\frac{\partial\overline{u}_{xx}}{\partial x} = \frac{\frac{1}{G}\left[\frac{F}{2m}\cosh\left(\sqrt{\frac{s}{c}}x\right) - F\cosh\left(\sqrt{\frac{s}{c}}l\right)\right]}{s\left[4l - \tanh\left(\sqrt{\frac{s}{c}}l\right)\Big/\left(\sqrt{\frac{s}{c}}m\right)\right]\cosh\left(\sqrt{\frac{s}{c}}l\right)} \tag{F.29}$$

$$\overline{\sigma}_w = \frac{2F\left[\cosh\left(\sqrt{\frac{s}{c}}x\right) - \cosh\left(\sqrt{\frac{s}{c}}l\right)\right]}{s\left[4l - \tanh\left(\sqrt{\frac{s}{c}}l\right)\Big/\left(\sqrt{\frac{s}{c}}m\right)\right]\cosh\left(\sqrt{\frac{s}{c}}l\right)} \tag{F.30}$$

$$\overline{\sigma}'_{xx} = \frac{2F\left[\cosh\left(\sqrt{\frac{s}{c}}x\right) - \cosh\left(\sqrt{\frac{s}{c}}l\right)\right]}{s\left[4l - \tanh\left(\sqrt{\frac{s}{c}}l\right)\Big/\left(\sqrt{\frac{s}{c}}m\right)\right]\cosh\left(\sqrt{\frac{s}{c}}l\right)} \tag{F.31}$$

$$\overline{\sigma}'_{yy} = \frac{\frac{2\nu}{1-\nu}F\cosh\left(\sqrt{\frac{s}{c}}x\right)}{s\left[4l - \tanh\left(\sqrt{\frac{s}{c}}l\right)\Big/\left(\sqrt{\frac{s}{c}}m\right)\right]\cosh\left(\sqrt{\frac{s}{c}}l\right)} \tag{F.32}$$

$$\overline{\sigma}'_{zz} = \frac{F\left[\frac{2\nu}{1-\nu}\cosh\left(\sqrt{\frac{s}{c}}x\right) + 2\cosh\left(\sqrt{\frac{s}{c}}l\right)\right]}{s\left[4l - \tanh\left(\sqrt{\frac{s}{c}}l\right)\Big/\left(\sqrt{\frac{s}{c}}m\right)\right]\cosh\left(\sqrt{\frac{s}{c}}l\right)} \tag{F.33}$$

$$\overline{\sigma}_{xx} = \frac{-2F}{s\left[4l - \tanh\left(\sqrt{\frac{s}{c}}l\right)\Big/\left(m\sqrt{\frac{s}{c}}\right)\right]} + \frac{2F}{s\left[4l - \tanh\left(\sqrt{\frac{s}{c}}l\right)\Big/\left(m\sqrt{\frac{s}{c}}\right)\right]} = 0 \tag{F.34}$$

$$\overline{\sigma}_{yy} = \frac{F\left[2\cosh\left(\sqrt{\frac{s}{c}}l\right) - \frac{1}{m}\cosh\left(\sqrt{\frac{s}{c}}x\right)\right]}{s\left[4l - \tanh\left(\sqrt{\frac{s}{c}}l\right)\Big/\left(\sqrt{\frac{s}{c}}m\right)\right]\cosh\left(\sqrt{\frac{s}{c}}l\right)} \tag{F.35}$$

$$\overline{\sigma}_{zz} = \frac{F\left[4\cosh\left(\sqrt{\frac{s}{c}}l\right) - \frac{1}{m}\cosh\left(\sqrt{\frac{s}{c}}x\right)\right]}{s\left[4l - \tanh\left(\sqrt{\frac{s}{c}}l\right)\Big/\left(\sqrt{\frac{s}{c}}m\right)\right]\cosh\left(\sqrt{\frac{s}{c}}l\right)} \tag{F.36}$$

step 4, inverse transformation
Finding the inverse transforms of the equations above finalises the solution of plane–strain consolidation problem. The inverse transform is found by using the Heaviside expansion theorem. When elaborating this theorem for the pore pressure development, equation (F.30), it is found:

$$\sigma_w = \sum_{j=1}^{m} \frac{t\left(a_j\right)}{\frac{d}{ds}n\left(a_j\right)} e^{a_j t}$$

In which:
a_j = the roots of equation (F.30)
t = nominator of equation (F.30)
n = denominator of equation (F.30)

The roots of equation (F.30) can be found by:

$$s = 0 \quad \vee \quad 4l\cosh\left(\sqrt{\frac{s}{c}}l\right) - \frac{\sinh\left(\sqrt{\frac{s}{c}}l\right)}{\sqrt{\frac{s}{c}}m} = 0$$

For $s = 0$ also the nominator of (F.30) turns to 0. So $s = 0$ does not contribute to the inverse transform and is therefore a removable root. The other roots are found by:

$$4l\cosh\left(\sqrt{\frac{s}{c}}l\right) = \frac{\sinh\left(\sqrt{\frac{s}{c}}l\right)}{m\sqrt{\frac{s}{c}}}$$
$$m4l\sqrt{\frac{s}{c}} = \tanh\left(\sqrt{\frac{s}{c}}l\right)$$

Only for $s = 0$ a real root is found. For imaginary values trigonometric functions can be written

as:

$$\cos(iy) = \frac{e^{i(iy)} + e^{-i(iy)}}{2} = \frac{e^{-y} + e^{y}}{2} = \cosh(y)$$
$$\sin(iy) = \frac{e^{i(iy)} - e^{-i(iy)}}{2i} = \frac{e^{-y} - e^{y}}{2i}\frac{i}{i} = i\frac{e^{y} - e^{-y}}{2} = i\sinh(y)$$
$$\sin(iy) = i\sinh(y) \;\rightarrow\; \sinh(y) = \frac{\sin(iy)}{i}\frac{i}{i} = -i\sin(iy)$$

So:

$$\cosh\left(\sqrt{\frac{s}{c}}l\right) = \cos\left(i\sqrt{\frac{s}{c}}l\right)$$
$$\sinh\left(\sqrt{\frac{s}{c}}l\right) = -i\sin\left(i\sqrt{\frac{s}{c}}l\right)$$

The roots of (F.30) can now be found:

$$4l\cos\left(i\sqrt{\frac{s}{c}}l\right) = \frac{-i}{\sqrt{\frac{s}{c}}m}\sin\left(i\sqrt{\frac{s}{c}}l\right)$$
$$\frac{4m\sqrt{\frac{s}{c}}l}{-i}\frac{i}{i} = \frac{\sin\left(i\sqrt{\frac{s}{c}}l\right)}{\cos\left(i\sqrt{\frac{s}{c}}l\right)}$$
$$4mi\sqrt{\frac{s}{c}}l = \tan\left(i\sqrt{\frac{s}{c}}l\right)$$
$$\text{with } \alpha = i\sqrt{\frac{s}{c}}l$$

$$4m\alpha = \tan(\alpha) \tag{F.37}$$

The values of s that fulfil condition (F.37) are the roots of equation (F.30). Since an infinite number of values for s, which fulfil (F.37) can be found, the roots are now indicated by s_j and α_j. The next step in deriving the inverse transform of (F.30) is finding the derivative of the denominator. The derivatives of the individual parts of the denominator are:

$$\frac{d}{ds}\left(\sqrt{\frac{s}{c}}l\right) = \frac{l}{2\sqrt{\frac{s}{c}}c}$$
$$\frac{d}{ds}\cosh\left(\sqrt{\frac{s}{c}}l\right) = \sinh\left(\sqrt{\frac{s}{c}}l\right)\frac{l}{2\sqrt{\frac{s}{c}}c}$$
$$\frac{d}{ds}\left(\frac{1}{\sqrt{\frac{s}{c}}m}\right) = \frac{-1}{2cm\left(\frac{s}{c}\right)^{1\frac{1}{2}}}$$
$$\frac{d}{ds}\left(\frac{\sinh\left(\sqrt{\frac{s}{c}}l\right)}{\sqrt{\frac{s}{c}}m}\right) = \sinh\left(\sqrt{\frac{s}{c}}l\right)\frac{d}{ds}\left(\frac{1}{\sqrt{\frac{s}{c}}m}\right) + \frac{1}{\sqrt{\frac{s}{c}}m}\frac{d}{ds}\left(\sinh\left(\sqrt{\frac{s}{c}}l\right)\right) =$$
$$\frac{-\sinh\left(\sqrt{\frac{s}{c}}l\right)}{2cm\left(\frac{s}{c}\right)^{1\frac{1}{2}}} + \frac{1}{\sqrt{\frac{s}{c}}m}\cosh\left(\sqrt{\frac{s}{c}}l\right)\frac{l}{2\sqrt{\frac{s}{c}}c}$$

The derivative of the denominator of (F.30) becomes:

$$\frac{d}{ds}\left[s\left(4l\cosh\left(\sqrt{\frac{s}{c}}l\right)-\frac{1}{m\sqrt{\frac{s}{c}}}\sinh\left(\sqrt{\frac{s}{c}}l\right)\right)\right]=$$

$$\left[4l\cosh\left(\sqrt{\frac{s}{c}}l\right)-\frac{1}{m\sqrt{\frac{s}{c}}}\sinh\left(\sqrt{\frac{s}{c}}l\right)\right]\frac{d}{ds}(s)+s\frac{d}{ds}\left[4l\cosh\left(\sqrt{\frac{s}{c}}l\right)-\frac{1}{m\sqrt{\frac{s}{c}}}\sinh\left(\sqrt{\frac{s}{c}}l\right)\right]=$$

$$\begin{aligned}&\left[4l\cosh\left(\sqrt{\frac{s}{c}}l\right)-\frac{1}{m\sqrt{\frac{s}{c}}}\sinh\left(\sqrt{\frac{s}{c}}l\right)\right]+\\&\quad s\left(4l\sinh\left(\sqrt{\frac{s}{c}}l\right)\frac{l}{\sqrt{\frac{s}{c}}2c}+\frac{\sinh\left(\sqrt{\frac{s}{c}}l\right)}{2cm\left(\frac{s}{c}\right)^{1\frac{1}{2}}}-\frac{l\cosh\left(\sqrt{\frac{s}{c}}l\right)}{2c\frac{s}{c}}\right)\end{aligned}\tag{F.38}$$

When roots derived by condition (F.37) are applied to (F.38) the first term reduces to zero. Rewriting the second term gives:

$$2l^2\sinh\left(\sqrt{\frac{s_j}{c}}l\right)\sqrt{\frac{s_j}{c}}+\frac{\sinh\left(\sqrt{\frac{s_j}{c}}l\right)}{2m\sqrt{\frac{s_j}{c}}}-\frac{l\cosh\left(\sqrt{\frac{s_j}{c}}l\right)}{2m}$$

$$2l\left(\sqrt{\frac{s_j}{c}}l\right)\sinh\left(\sqrt{\frac{s_j}{c}}l\right)+\frac{l\sinh\left(\sqrt{\frac{s_j}{c}}l\right)}{2m\sqrt{\frac{s_j}{c}}l}-\frac{l}{2m}\cosh\left(\sqrt{\frac{s_j}{c}}l\right)$$

with: $i\sqrt{\frac{s_j}{c}}l=\alpha_j,\quad\rightarrow\quad\sqrt{\frac{s_j}{c}}l=-\alpha_j i$

$$-2l\alpha_j i\sinh(-\alpha_j i)+\frac{l\sinh(-\alpha_j i)}{2m(-\alpha_j i)}-\frac{l}{2m}\cosh(-\alpha_j i)$$

with: $\sinh(-\alpha_j i)=i\sin(-\alpha_j)$ and
$\cosh(-\alpha_j i)=\cos(-\alpha_j)$

$$-2l\alpha_j i\; i\sin(-\alpha_j)-\frac{li\sin(-\alpha_j)}{2m\alpha_j i}-\frac{l}{2m}\cos(-\alpha_j)=$$

$$2l\alpha_j\sin(-\alpha_j)-\frac{l}{2m\alpha_j}\sin(-\alpha_j)-\frac{l}{2m}\cos(-\alpha_j)=$$

$$-2l\alpha_j\sin(\alpha_j)+\frac{l}{2m\alpha_j}\sin(\alpha_j)-\frac{l}{2m}\cos(\alpha_j)$$

$$l\sin(\alpha_j)\left(\frac{1}{2m\alpha_j}-2\alpha_j\right)-\frac{l}{2m}\cos(\alpha_j)\tag{F.39}$$

The inverse transform of (F.30) can now be found with:

$$\cosh\left(\sqrt{\frac{s_j}{c}}x\right) = \cosh\left(-\alpha_j i\frac{x}{l}\right) = \cos\left(\alpha_j\frac{x}{l}\right)$$

$$\cosh\left(\sqrt{\frac{s_j}{c}}l\right) = \cosh\left(-\alpha_j i\right) = \cos\left(\alpha_j\right)$$

$$s_j = -\frac{\alpha_j^2 c}{l^2}, \quad \rightarrow \quad e^{s_j t} = e^{-\frac{\alpha_j^2 ct}{l^2}}$$

it follows that:

$$\sigma_w = \frac{F}{l}\sum_{j=1}^{\infty}\left[\frac{2\left(\cos\left(\alpha_j\frac{x}{l}\right)-\cos\left(\alpha_j\right)\right)e^{-\frac{\alpha_j^2 ct}{l^2}}}{\sin\left(\alpha_j\right)\left(\frac{1}{2m\alpha_j}-2\alpha_j\right)-\frac{\cos\left(\alpha_j\right)}{2m}}\right] \tag{F.40}$$

The inverse transforms of the equations (F.28) to (F.36) can be found in the same way. Since all these equations have the same denominator the values for s that fulfil condition (F.37) are the roots for all the expressions. It should be noted however that $s = 0$ is not a removable root for all the expressions. Elaborating the Heaviside expansion theorem to the equations (F.28) to (F.36) gives:

$$e = \frac{F}{l}\frac{(1+\nu)(1-2\nu)}{E}\left[1+\sum_{j=1}^{\infty}\frac{\frac{2}{1-\nu}\cos\left(\alpha_j\frac{x}{l}\right)e^{\frac{-\alpha_j^2 ct}{l^2}}}{\sin\left(\alpha_j\right)\left(\frac{1}{2m\alpha_j}-2\alpha_j\right)-\frac{\cos\left(\alpha_j\right)}{2m}}\right] \tag{F.41}$$

$$\frac{\partial u_{xx}}{\partial x} = \frac{F}{l}\frac{(1+\nu)}{E}\left[-\nu+\sum_{j=1}^{\infty}\frac{\left(\frac{\cos\left(\alpha_j\frac{x}{l}\right)}{m}-2\cos\left(\alpha_j\right)\right)e^{\frac{-\alpha_j^2 ct}{l^2}}}{\sin\left(\alpha_j\right)\left(\frac{1}{2m\alpha_j}-2\alpha_j\right)-\frac{\cos\left(\alpha_j\right)}{2m}}\right] \tag{F.42}$$

$$\frac{\partial u_{zz}}{\partial z} = \frac{F}{El}\left[\left(1-\nu^2\right)+\sum_{j=1}^{\infty}\frac{2(1+\nu)\cos\left(\alpha_j\right)e^{\frac{-\alpha_j^2 ct}{l^2}}}{\sin\left(\alpha_j\right)\left(\frac{1}{2m\alpha_j}-2\alpha_j\right)-\frac{\cos\left(\alpha_j\right)}{2m}}\right] \tag{F.43}$$

$$\sigma_w = \frac{F}{l}\sum_{j=1}^{\infty}\left[\frac{2\left(\cos\left(\alpha_j\frac{x}{l}\right)-\cos\left(\alpha_j\right)\right)e^{-\frac{\alpha_j^2 ct}{l^2}}}{\sin\left(\alpha_j\right)\left(\frac{1}{2m\alpha_j}-2\alpha_j\right)-\frac{\cos\left(\alpha_j\right)}{2m}}\right] \tag{F.44}$$

$$\sigma'_{xx} = \frac{F}{l}\sum_{j=1}^{\infty}\left[\frac{2\left(\cos\left(\alpha_j\frac{x}{l}\right)-\cos\left(\alpha_j\right)\right)e^{-\frac{\alpha_j^2 ct}{l^2}}}{\sin\left(\alpha_j\right)\left(\frac{1}{2m\alpha_j}-2\alpha_j\right)-\frac{\cos\left(\alpha_j\right)}{2m}}\right] \tag{F.45}$$

$$\sigma'_{yy} = \frac{F}{l}\left[\nu+\sum_{j=1}^{\infty}\left[\frac{\frac{2\nu}{1-\nu}\cos\left(\alpha_j\frac{x}{l}\right)e^{-\frac{\alpha_j^2 ct}{l^2}}}{\sin\left(\alpha_j\right)\left(\frac{1}{2m\alpha_j}-2\alpha_j\right)-\frac{\cos\left(\alpha_j\right)}{2m}}\right]\right] \tag{F.46}$$

$$\sigma'_{zz} = \frac{F}{l}\left[1 + \sum_{j=1}^{\infty}\left[\frac{2\left(\frac{\nu}{1-\nu}\cos\left(\alpha_j\frac{x}{l}\right) + \cos\left(\alpha_j\right)\right)e^{-\frac{\alpha_j^2 ct}{l^2}}}{\sin\left(\alpha_j\right)\left(\frac{1}{2m\alpha_j} - 2\alpha_j\right) - \frac{\cos\left(\alpha_j\right)}{2m}}\right]\right] \tag{F.47}$$

$$\sigma_{xx} = 0 \tag{F.48}$$

$$\sigma_{yy} = \frac{F}{l}\left[\nu + \sum_{j=1}^{\infty}\left[\frac{\left(2\cos\left(\alpha_j\right) - \frac{1}{m}\cos\left(\alpha_j\frac{x}{l}\right)\right)e^{-\frac{\alpha_j^2 ct}{l^2}}}{\sin\left(\alpha_j\right)\left(\frac{1}{2m\alpha_j} - 2\alpha_j\right) - \frac{\cos\left(\alpha_j\right)}{2m}}\right]\right] \tag{F.49}$$

$$\sigma_{zz} = \frac{F}{l}\left[1 + \sum_{j=1}^{\infty}\left[\frac{\left(4\cos\left(\alpha_j\right) - \frac{1}{m}\cos\left(\alpha_j\frac{x}{l}\right)\right)e^{-\frac{\alpha_j^2 ct}{l^2}}}{\sin\left(\alpha_j\right)\left(\frac{1}{2m\alpha_j} - 2\alpha_j\right) - \frac{\cos\left(\alpha_j\right)}{2m}}\right]\right] \tag{F.50}$$

As is to be expected, the derivation of the inverse transforms of the expressions for total stress leads to the same results as the summation of the expressions for effective stress (F.45) to (F.47) and the expression for the pore pressure development (F.44). The same holds for the expression of the volumetric strain, which can either be found by the inverse transform of (F.28) or by the summation of (F.42) and (F.43).

Function f(t)

Equivalent to appendix E an expression for the function f(t) can be derived. With equations (F.5), (F.12) and (F.13) the following is found:

$$f(t) = \frac{F}{l} + \frac{F}{l}\sum_{j=1}^{\infty}\frac{2\cos(\alpha_j)e^{\frac{-\alpha_j^2 ct}{l^2}}}{\sin(\alpha_j)\left(\frac{1}{2m\alpha_j} - 2\alpha_j\right) - \frac{l}{2m}\cos(\alpha_j)} \tag{F.51}$$

Graphs of stress and strain

To illustrate the results this section presents graphs of the derived expressions for stress and strain. The graphs present the stress and strain for $c = 1 \times 10^{-6}$ m^2/s and $L = 1.0$ m.

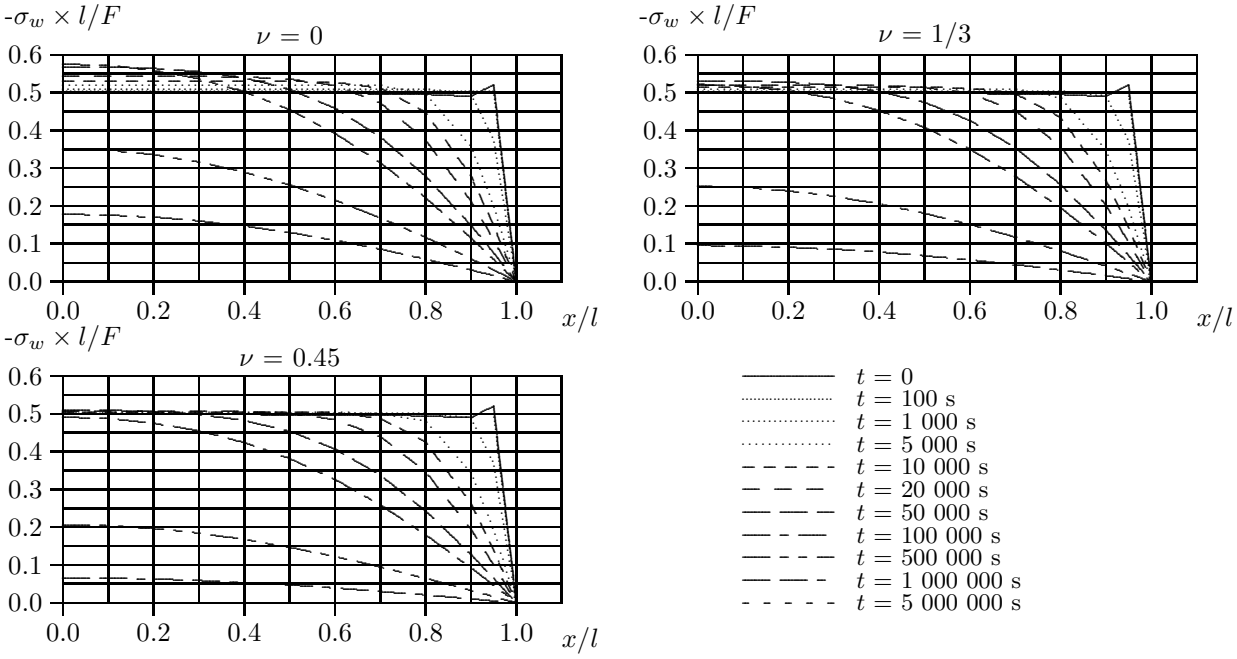

Figure F.2: Pore pressure development for plane strain conditions and isotropic linear elasticity

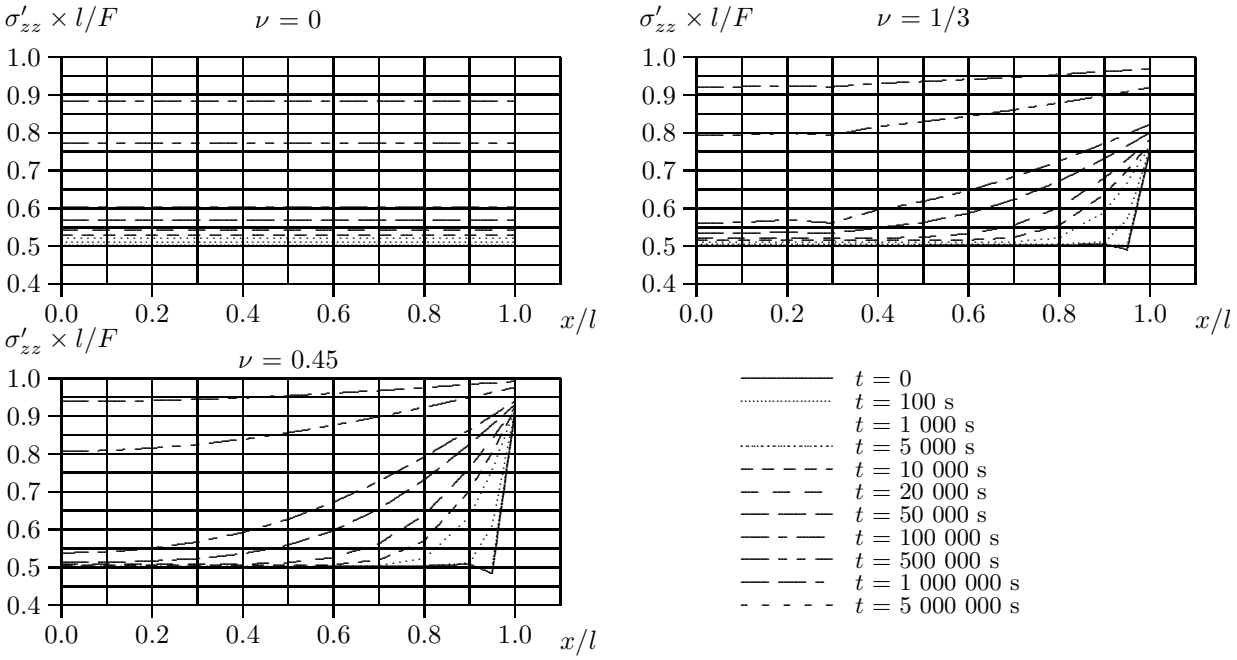

Figure F.3: Development of vertical effective stress for plane strain conditions and isotropic linear elasticity

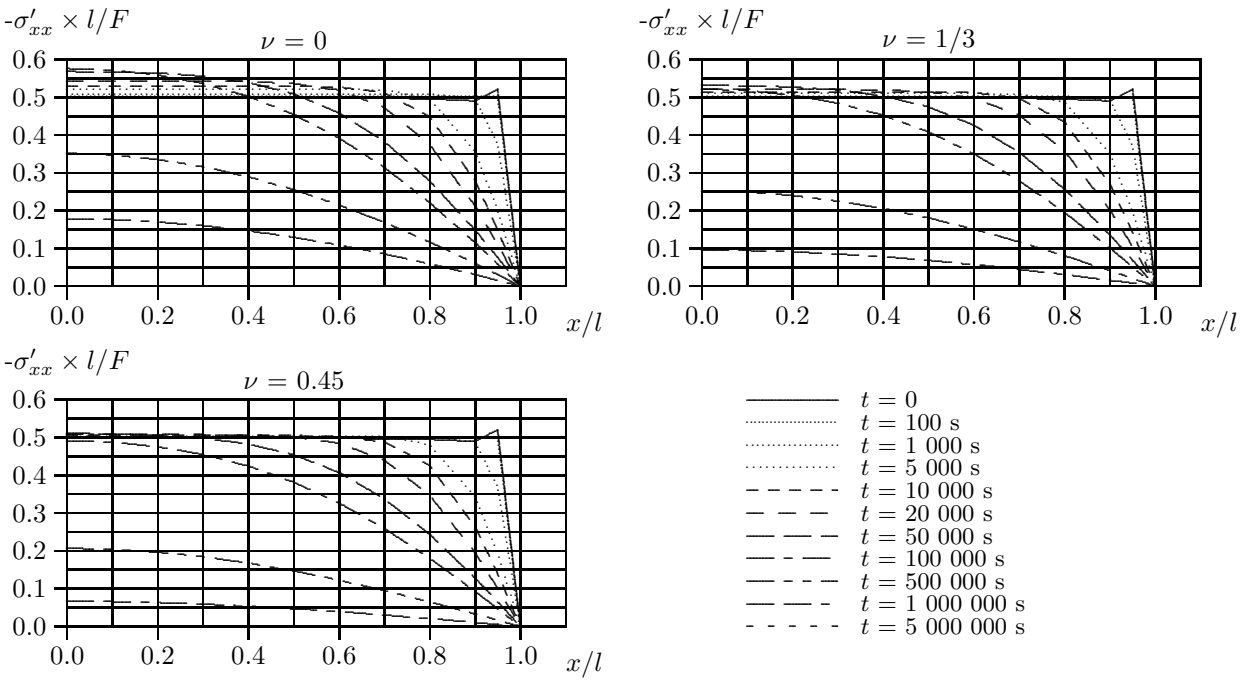

Figure F.4: Development effective stress in x-direction for plane strain conditions and isotropic linear elasticity

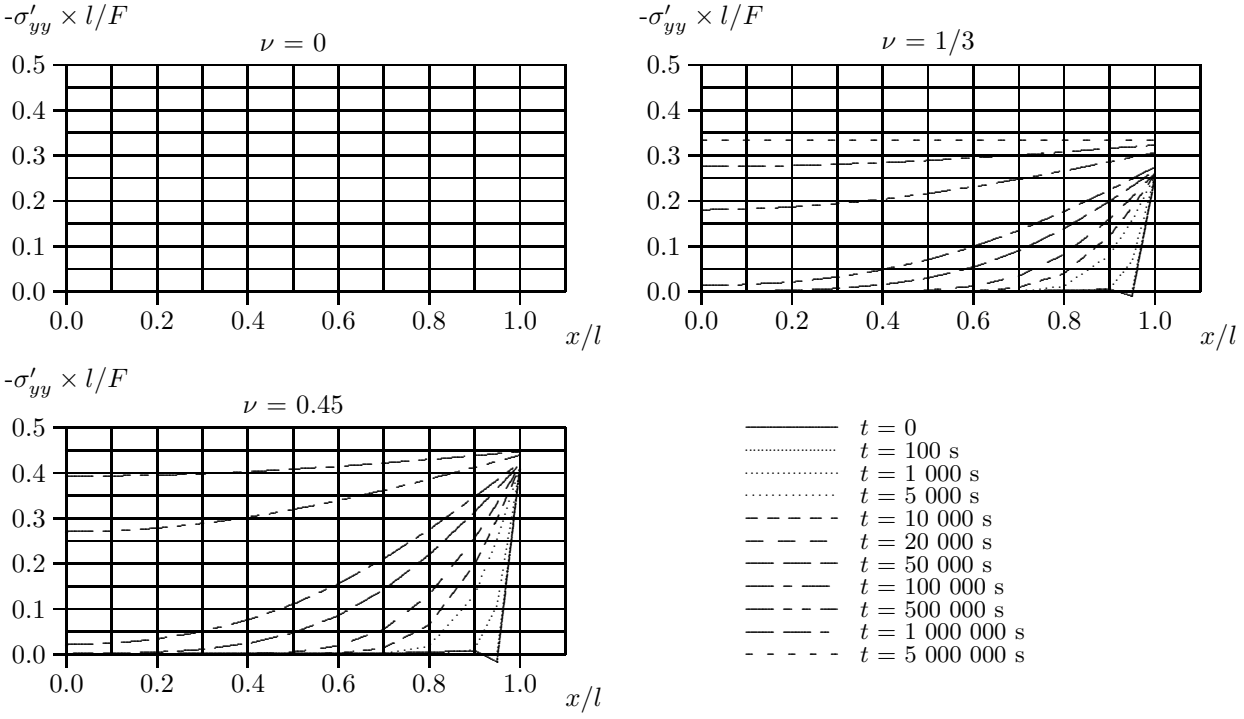

Figure F.5: Development effective stress in y-direction for plane strain conditions and isotropic linear elasticity

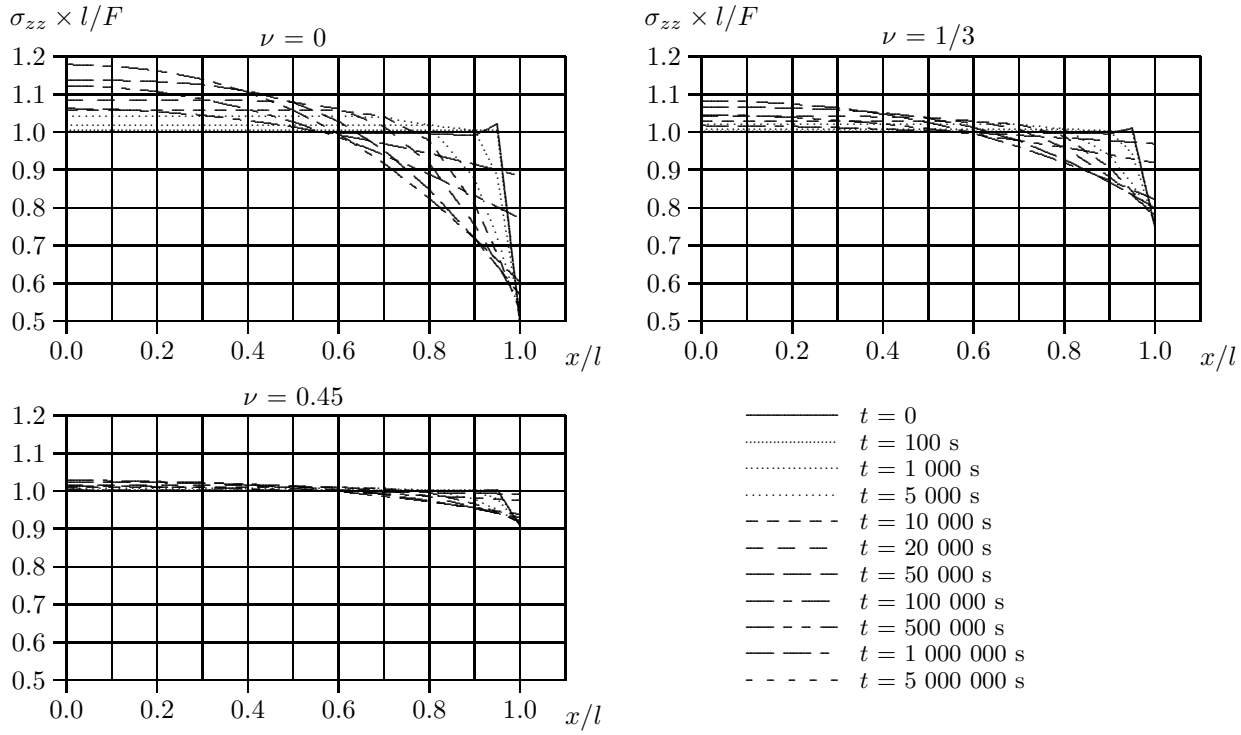

Figure F.6: Development of vertical total stress for plane strain conditions and isotropic linear elasticity

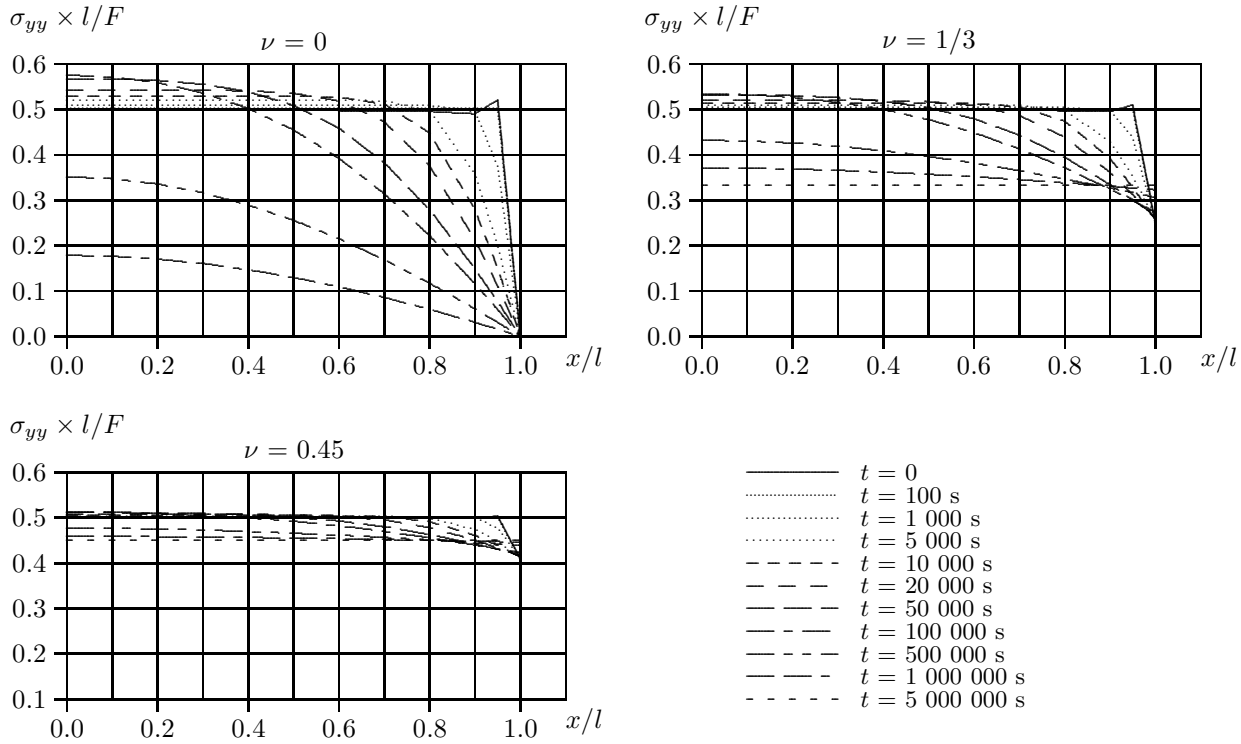

Figure F.7: Development total stress in y-direction for plane strain conditions and isotropic linear elasticity

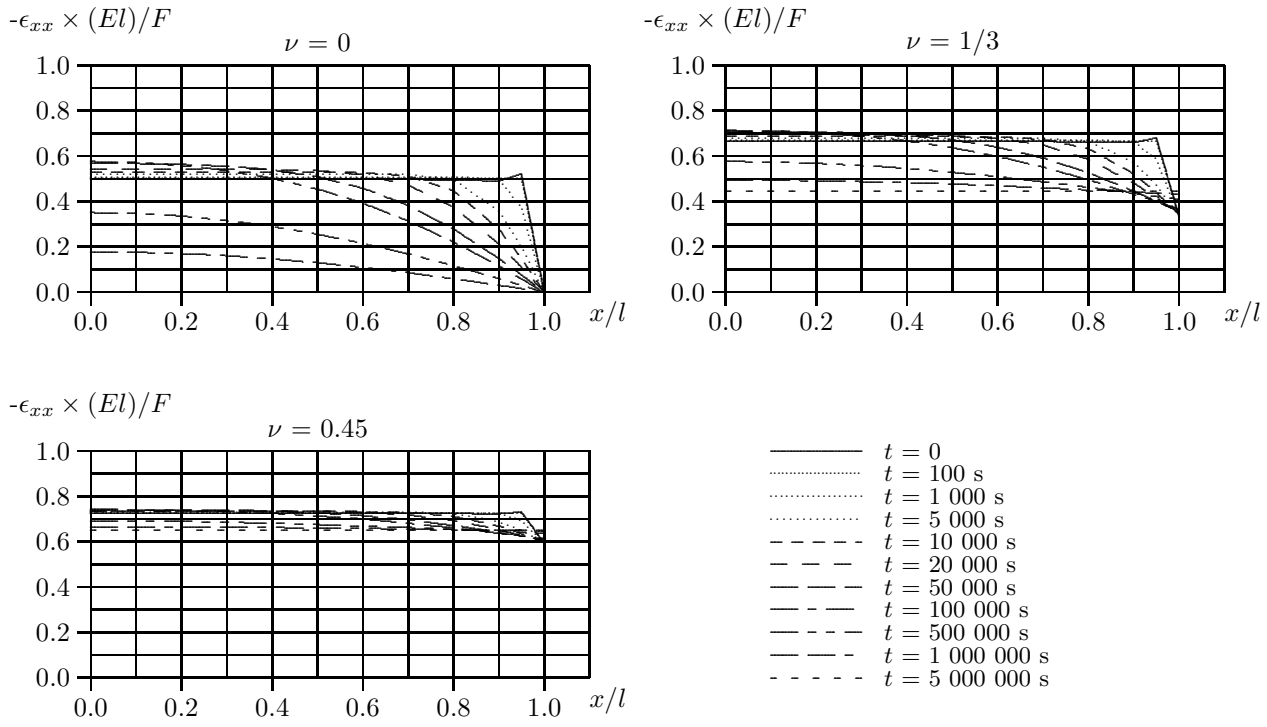

Figure F.8: Development strain in x-direction for plane strain conditions and isotropic linear elasticity

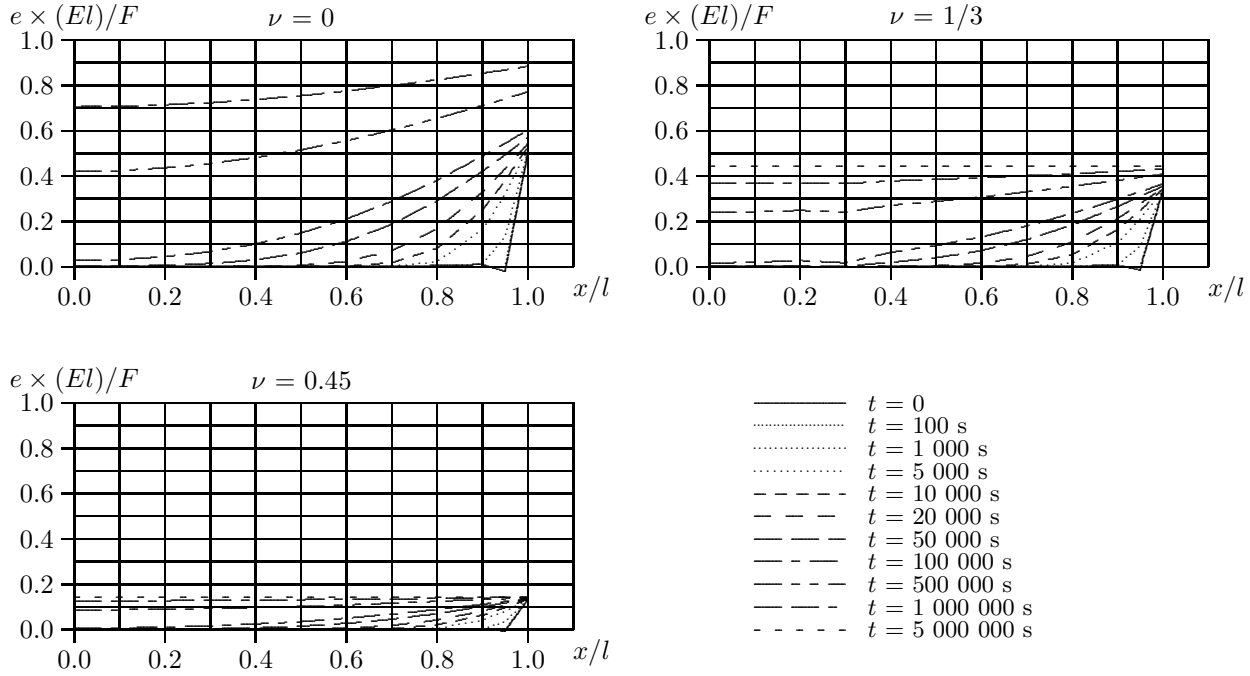

Figure F.9: Development volume strain for plane strain conditions and isotropic linear elasticity

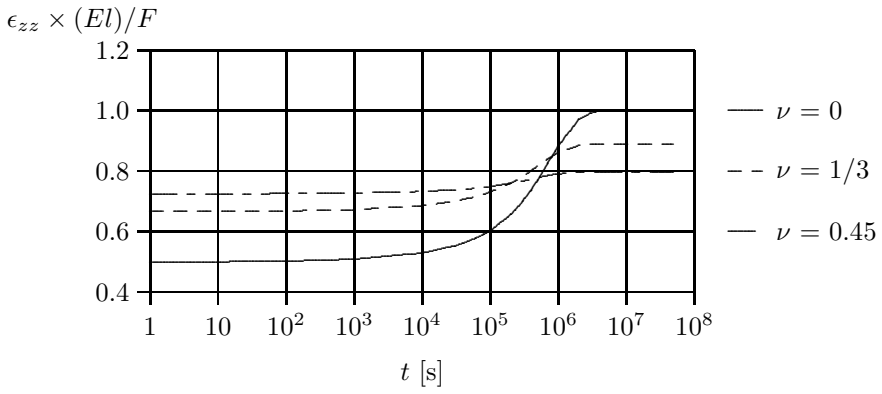

Figure F.10: Development of vertical strain for plane strain conditions and isotropic linear elasticity

Appendix G

Consolidation for cross–anisotropic axial–symmetric conditions

In this appendix the solution for isotropic linear elasticity presented in appendix E is extended for cross–anisotropy. Again the solution is derived in 4 steps:

step 1, the relevant expressions
Basic equations for axial symmetry:

$$\nabla^2 = \frac{\partial^2}{\partial r^2} + \frac{1}{r}\frac{\partial}{\partial r} + \frac{1}{r^2}\frac{\partial^2}{\partial \theta^2} + \frac{\partial^2}{\partial z^2}$$

$$\varepsilon_r = \frac{\partial u_r}{\partial r}, \quad \varepsilon_\theta = \frac{u_r}{r} + \frac{1}{r}\frac{\partial u_\theta}{\partial \theta}, \quad \varepsilon_{zz} = \frac{\partial u_{zz}}{\partial z}$$

$$\gamma_{\theta z} = \frac{\partial u_\theta}{\partial z} + \frac{\partial u_{zz}}{r\partial \theta}, \quad \gamma_{rz} = \frac{\partial u_r}{\partial z} + \frac{\partial u_{zz}}{\partial r}, \quad \gamma_{r\theta} = \frac{\partial u_r}{r\partial \theta} + \frac{\partial u_\theta}{\partial r} - \frac{u_\theta}{r}$$

Simplifications due to axial symmetry and the stiff plate on top:

axial symmetry: $\dfrac{\partial}{\partial \theta} = 0$

stiff plate on top: $\dfrac{\partial \varepsilon_{zz}}{\partial z} = \dfrac{\partial \varepsilon_{zz}}{\partial r} = 0$

no shear stresses and strains: $\gamma_{\theta z} = \ \gamma_{r\theta} = \gamma_{rz} = \tau_{\theta z} = \ \tau_{r\theta} = \tau_{rz} = 0$

So strain is expressed into:

$$\begin{aligned} \varepsilon_r &= \frac{\partial u_r}{\partial r} \\ \varepsilon_\theta &= \frac{u_r}{r} \\ \varepsilon_z &= \frac{\partial u_{zz}}{\partial z} \\ e &= \frac{\partial u_r}{\partial r} + \frac{u_r}{r} + \frac{\partial u_{zz}}{\partial z} = \frac{1}{r}\frac{\partial (r\, u_r)}{\partial r} + \frac{\partial u_{zz}}{\partial z} \end{aligned} \tag{G.1}$$

The stress–strain relationship is elaborated given in appendix B:

$$\begin{aligned} \sigma'_r &= Ae + 2G_{hh}\, \varepsilon_r + B\varepsilon_{zz} \\ \sigma'_\theta &= Ae + 2G_{hh}\, \varepsilon_\theta + B\varepsilon_{zz} \\ \sigma'_{zz} &= (A+B)\, e + D\varepsilon_{zz} \end{aligned} \tag{G.2}$$

Appendix H elaborates the equilibrium of forces for cross–anisotropic conditions in cartesian co-ordinates. For cylindrical co–ordinates the equilibrium condition is found in an equivalent way:

$$[A + 2G_{hh}] \nabla^2 e = \nabla^2 \sigma_w \tag{G.3}$$

The storage equation remains unaffected:

$$\frac{k}{\gamma_w} \nabla^2 \sigma_w = \frac{\partial e}{\partial t} \tag{G.4}$$

Combination of equation (G.3) and (G.4) gives:

$$\frac{k}{\gamma_w} [A + 2G_{hh}] \nabla^2 e = \frac{\partial e}{\partial t} \tag{G.5}$$

with $c = k [A + 2G_{hh}] / \gamma_w$:

$$\nabla^2 e = \frac{1}{c} \frac{\partial e}{\partial t} \tag{G.6}$$

step 2, the Laplace transformation
Solving equation (G.6) with Laplace transformation:

$$\nabla^2 \bar{e} = \frac{1}{c} [s\bar{e} - e_0], \quad e_0 = 0$$

$$\nabla^2 \bar{e} = \frac{s}{c} \bar{e}, \quad \rightarrow \quad \frac{\partial^2 \bar{e}}{\partial r^2} + \frac{1}{r} \frac{\partial \bar{e}}{\partial r} - \frac{s}{c} \bar{e} = 0$$

standard solution:

$$\bar{e} = C_1 J_0 (\lambda r) + C_2 Y_0 (\lambda r), \quad \lambda = \sqrt{\frac{-s}{c}} \tag{G.7}$$

Application of the Laplace transform to equation (G.3):

$$[A + 2G_{hh}] \nabla^2 \bar{e} = \nabla^2 \bar{\sigma}_w$$

$$\nabla^2 \bar{e} = \frac{\nabla^2 \bar{\sigma}_w}{A + 2G_{hh}}$$

$$\bar{e} = \frac{1}{A + 2G_{hh}} \bar{\sigma}_w + C_3, \quad \nabla^2 C_3 = 0 \tag{G.8}$$

$$\bar{e} = \frac{1}{r} \frac{\partial (r\bar{u}_r)}{\partial r} + \frac{\partial \bar{u}_{zz}}{\partial z}$$

$$\bar{\sigma}_w = [A + 2G_{hh}] [\bar{e} - C_3]$$

$$\bar{\sigma}_w = [A + 2G_{hh}] [C_1 J_0 (\lambda r) + C_2 Y_0 (\lambda r) - C_3] \tag{G.9}$$

$$\frac{1}{r} \frac{\partial (r\bar{u}_r)}{\partial r} = C_1 J_0 (\lambda r) + C_2 Y_0 (\lambda r) - \frac{\partial \bar{u}_{zz}}{\partial z} \tag{G.10}$$

Integration of equation (G.10) gives:

$$\frac{\bar{u}_r}{R} = C_1 \frac{J_1 (\lambda r)}{\lambda R} + C_2 \frac{Y_1 (\lambda r)}{\lambda R} - \frac{r}{2R} \frac{\partial \bar{u}_{zz}}{\partial z} + \frac{C_4}{rR} \tag{G.11}$$

Differentiation of equation (G.11) results in:

$$\frac{\partial \bar{u}_r}{\partial r} = C_1 \left[J_0 (\lambda r) - \frac{J_1 (\lambda r)}{\lambda r} \right] + C_2 \left[Y_0 (\lambda r) - \frac{Y_1 (\lambda r)}{\lambda r} \right] - \frac{1}{2} \frac{\partial \bar{u}_{zz}}{\partial z} - \frac{C_4}{r^2} \tag{G.12}$$

Using equation (G.2) stress and strain are expressed into:

$$\bar{e} = C_1 J_0 (\lambda r) + C_2 Y_0 (\lambda r) \tag{G.13}$$

$$\bar{\sigma}_w = [A + 2G_{hh}] [C_1 J_0 (\lambda r) + C_2 Y_0 (\lambda r) - C_3] \tag{G.14}$$

$$\bar{\sigma}'_r = A [C_1 J_0 (\lambda r) + C_2 Y_0 (\lambda r)] + 2G_{hh} \begin{bmatrix} C_1 \left[J_0 (\lambda r) - \dfrac{J_1 (\lambda r)}{\lambda r} \right] \\ +C_2 \left[Y_0 (\lambda r) - \dfrac{Y_1 (\lambda r)}{\lambda r} \right] - \dfrac{1}{2} \dfrac{\partial \bar{u}_{zz}}{\partial z} - \dfrac{C_4}{r^2} \end{bmatrix} + B \frac{\partial \bar{u}_{zz}}{\partial z} \tag{G.15}$$

$$\bar{\sigma}'_\theta = A [C_1 J_0 (\lambda r) + C_2 Y_0 (\lambda r)] + 2G_{hh} \left[C_1 \frac{J_1 (\lambda r)}{\lambda r} + C_2 \frac{Y_1 (\lambda r)}{\lambda r} \right] + 2G_{hh} \left[-\frac{1}{2} \frac{\partial \bar{u}_{zz}}{\partial z} + \frac{C_4}{r^2} \right] + B \frac{\partial \bar{u}_{zz}}{\partial z} \tag{G.16}$$

$$\bar{\sigma}'_z = (A + B) [C_1 J_0 (\lambda r) + C_2 Y_0 (\lambda r)] + D \frac{\partial \bar{u}_{zz}}{\partial z} \tag{G.17}$$

$$\bar{\sigma}_r = \bar{\sigma}'_r - \bar{\sigma}_w \tag{G.18}$$

$$\bar{\sigma}_\theta = \bar{\sigma}'_\theta - \bar{\sigma}_w \tag{G.19}$$

$$\bar{\sigma}_{zz} = \bar{\sigma}'_{zz} - \bar{\sigma}_w \tag{G.20}$$

step 3, solving for boundary conditions
In the equations (G.13) to (G.20) 5 unknown parameters remain; C_1, C_2, C_3, C_4 and $\partial \overline{u}_{zz}/\partial z$. Since $\bar{e}$ in equation (G.13) and $\bar{\sigma}'_r$ in equation (G.15) have a limited value when r reaches 0, it follows that $C_2 = C_4 = 0$. The remaining unknown parameters can be solved by the boundary conditions:

a) at $r = R \quad \sigma_w = g_1, \quad \rightarrow \quad \overline{\sigma}_w = \overline{g}_1$

b) at $r = R \quad \sigma_r = g_2, \quad \rightarrow \quad \overline{\sigma}_r = \overline{g}_2$

c) at $z = h \quad 1/A \int 2\pi r \sigma_{zz} \mathrm{d}r = g_3, \quad \rightarrow \quad 1/A \int 2\pi r \overline{\sigma}_{zz} \mathrm{d}r = \overline{g}_3$

The combination of boundary condition a and equation (G.14) gives:

$$C_3 = C_1 J_0 (\lambda R) - \frac{\overline{g}_1}{A + 2G_{hh}} \tag{G.21}$$

rewriting equation (G.18) gives:

$$\bar{\sigma}_r = AC_1 J_0 (\lambda r) + 2G_{hh} \left[C_1 J_0 (\lambda r) - C_1 \frac{J_1 (\lambda r)}{\lambda r} \right] + (B - G_{hh}) \frac{\partial \bar{u}_{zz}}{\partial z} - [A + 2G_{hh}] [C_1 J_0 (\lambda r) - C_1 J_0 (\lambda R)] - \overline{g}_1$$

$$\bar{\sigma}_r = -2G_{hh} C_1 \frac{J_1 (\lambda r)}{\lambda r} + [B - G_{hh}] \frac{\partial \bar{u}_{zz}}{\partial z} + [A + 2G_{hh}] C_1 J_0 (\lambda R) - \overline{g}_1$$

The application of boundary condition b to equation (G.18) gives:

$$\overline{g}_2 = -2G_{hh} C_1 \frac{J_1 (\lambda R)}{\lambda R} + [B - G_{hh}] \frac{\partial \bar{u}_{zz}}{\partial z} + [A + 2G_{hh}] C_1 J_0 (\lambda R) - \overline{g}_1$$

$$\frac{\partial \bar{u}_{zz}}{\partial z} = \frac{C_1}{B - G_{hh}} \left[2G_{hh} \frac{J_1 (\lambda R)}{\lambda R} - (A + 2G_{hh}) J_0 (\lambda R) \right] + \frac{\overline{g}_1 + \overline{g}_2}{B - G_{hh}} \tag{G.22}$$

Application of boundary condition c to equation (G.20) gives:

$$\bar{\sigma}_{zz} = C_1 (A + B) J_0 (\lambda r) + D \frac{\partial \overline{u}_{zz}}{\partial z} - (A + 2G_{hh}) \left[C_1 (J_0 (\lambda r) - J_0 (\lambda R)) + \frac{\overline{g}_1}{A + 2G_{hh}} \right]$$

$$\overline{\sigma}_{zz} = C_1 \left[(B - 2G_{hh}) J_0 (\lambda r) + \left[1 - \frac{D}{B - G_{hh}} \right] (A + 2G_{hh}) J_0 (\lambda R) \right] - \overline{g}_1 + \frac{D (\overline{g}_1 + \overline{g}_2)}{B - G_{hh}} + \frac{DC_1 2G_{hh}}{B - G_{hh}} \frac{J_1 (\lambda R)}{\lambda R} \tag{G.23}$$

with:

$$\overline{g}_3 = \int_0^R \frac{2\pi r}{\pi R^2} \bar{\sigma}_{zz} \mathrm{d}r$$

follows:

$$\overline{g}_3 = \int_0^R \frac{2r}{R^2} \left[\begin{array}{c} \left(B - 2G_{hh}\right) C_1 J_0\left(\lambda r\right) + \left(A + 2G_{hh}\right) C_1 J_0\left(\lambda R\right) \left[1 - \dfrac{D}{B - G_{hh}}\right] \\ -\overline{g}_1 + \dfrac{C_1 2 G_{hh} D}{B - G_{hh}} \dfrac{J_1\left(\lambda R\right)}{\lambda R} + \dfrac{D\left(\overline{g}_1 + \overline{g}_2\right)}{B - G_{hh}} \end{array} \right] \mathrm{d}r$$

$$\begin{aligned} \overline{g}_3 = \quad & 2\left(B - 2G_{hh}\right) C_1 \frac{J_1\left(\lambda R\right)}{\lambda R} + C_1\left(A + 2G_{hh}\right) J_0\left(\lambda R\right) \left[1 - \frac{D}{B - G_{hh}}\right] + \\ & \frac{2DG_{hh}}{B - G_{hh}} C_1 \frac{J_1\left(\lambda R\right)}{\lambda R} - \overline{g}_1 + \frac{D\left(\overline{g}_1 + \overline{g}_2\right)}{B - G_{hh}} \end{aligned}$$

$$C_1 = \frac{\overline{g}_3 + \overline{g}_1 - \dfrac{D\left(\overline{g}_1 + \overline{g}_2\right)}{B - G_{hh}}}{2\dfrac{J_1\left(\lambda R\right)}{\lambda R}\left[B - 2G_{hh} + \dfrac{DG_{hh}}{B - G_{hh}}\right] + \left(A + 2G_{hh}\right) J_0\left(\lambda R\right)\left[1 - \dfrac{D}{B - G_{hh}}\right]} \tag{G.24}$$

Equation (G.22) and (G.24) give:

$$\begin{aligned} \frac{\partial \bar{u}_{zz}}{\partial z} = & \frac{\left(\overline{g}_3 + \overline{g}_1 - \dfrac{D\left(\overline{g}_1 + \overline{g}_2\right)}{B - G_{hh}}\right)\left[\dfrac{2G}{B - G_{hh}} \dfrac{J_1\left(\lambda R\right)}{\lambda R} - \dfrac{A + 2G_{hh}}{B - G_{hh}} J_0\left(\lambda R\right)\right]}{2\dfrac{J_1\left(\lambda R\right)}{\lambda R}\left[\left(B - 2G_{hh}\right) + \dfrac{DG_{hh}}{B - G_{hh}}\right] + J_0\left(\lambda R\right)\left(A + 2G_{hh}\right)\left[1 - \dfrac{D}{B - G_{hh}}\right]} \\ & + \frac{\overline{g}_1 + \overline{g}_2}{B - G_{hh}} \end{aligned} \tag{G.25}$$

step 4, inverse transformation

The inverse transformation starts with finding an expression for the boundary conditions $\overline{g}_1$, $\overline{g}_2$ and $\overline{g}_3$. Standard triaxial testing with a radial pore pressure flow is modelled by $g_1 = g_2 = 0$, $g_3 = \sigma_b$. The boundary conditions in transformed conditions is then given by:

$$\begin{aligned} \overline{g}_1 &= 0 \\ \overline{g}_2 &= 0 \\ \overline{g}_3 &= \int_0^\infty \sigma_b \exp\left(-st\right) \mathrm{d}t = \frac{\sigma_b}{s} \end{aligned}$$

The expression for $\overline{\sigma}_w$ is then given by:

$$\frac{\overline{\sigma}_w}{\sigma_b} = \frac{J_0\left(\lambda r\right) - J_0\left(\lambda R\right)}{s\left[\dfrac{2J_1\left(\lambda R\right)}{\left[A + 2G_{hh}\right]\lambda R}\left[\left(B - 2G_{hh}\right) + \dfrac{DG_{hh}}{B - G_{hh}}\right] + J_0\left(\lambda R\right)\left(1 - \dfrac{D}{B - G_{hh}}\right)\right]} \tag{G.26}$$

Equivalent to appendix E the Heaviside expansion theorem is used for finding the inverse transform of equation (G.26). A removable root is found for $s = 0$, the other roots are found for values of defined by:

$$\frac{2J_1\left(\lambda R\right)}{\left[A + 2G_{hh}\right]\lambda R}\left[B - 2G_{hh} + \frac{G_{hh}D}{B - G_{hh}}\right] = J_0\left(\lambda R\right)\left[\frac{D}{B - G_{hh}} - 1\right]$$

$$\frac{J_1\left(\lambda R\right)}{J_0\left(\lambda R\right)} = C\lambda R, \quad C = \frac{1}{2}\left[\frac{A + 2G_{hh}}{B - 2G_{hh} + \dfrac{DG_{hh}}{B - G_{hh}}}\right]\left[\frac{D}{B - G_{hh}} - 1\right] \tag{G.27}$$

The values for s that fulfil condition (G.27) are indicated by s_j. The expression for σ_w is now given by:

$$\frac{\sigma_w}{\sigma_b} = \sum_{j=1}^{\infty} \frac{\left[J_0\left(\lambda_j r\right) - J_0\left(\lambda_j R\right)\right] e^{s_j t}}{s_j \dfrac{\partial}{\partial s}\left[\dfrac{2J_1\left(\lambda_j R\right)}{\left(A+2G_{hh}\right)\lambda_j R}\left[B - 2G_{hh} + \dfrac{G_{hh}D}{B-G_{hh}}\right] + J_0\left(\lambda_j R\right)\left(1 - \dfrac{D}{B-G_{hh}}\right)\right]}$$

Elaborating the differentiation of the denominator

$$\frac{\partial}{\partial s}\left(\frac{J_1\left(\lambda_j R\right)}{\lambda_j R}\right) = -\frac{2J_1\left(\lambda_j R\right)}{2\lambda_j R s_j} + \frac{1}{2s_j} J_0\left(\lambda_j R\right)$$

$$\frac{\partial}{\partial s}\left(J_0\left(\lambda_j R\right)\right) = -\frac{J_1\left(\lambda_j R\right)\lambda_j R}{2s_j}$$

$$\frac{\partial}{\partial s}\left[\frac{2J_1\left(\lambda_j R\right)}{\left(A+2G_{hh}\right)\lambda_j R}\left[B - 2G_{hh} + \frac{G_{hh}D}{B-G_{hh}}\right] + J_0\left(\lambda_j R\right)\left(1 - \frac{D}{B-G_{hh}}\right)\right] =$$

$$\frac{2}{A+2G_{hh}}\left[-\frac{J_1\left(\lambda_j R\right)}{\lambda_j R s_j} + \frac{1}{2s_j} J_0\left(\lambda_j R\right)\right]\left[\left(B - 2G_{hh}\right) + \frac{G_{hh}D}{B-G_{hh}}\right]$$

$$-\frac{J_1\left(\lambda_j R\right)}{2s_j}\left(\lambda_j R\right)\left(1 - \frac{D}{B-G_{hh}}\right) =$$

$$\frac{1}{s}\left[-\frac{2J_1\left(\lambda_j R\right)}{\left(A+2G_{hh}\right)\lambda_j R} + \frac{J_0\left(\lambda_j R\right)}{A+2G_{hh}}\right]\left[\left(B - 2G_{hh}\right) + \frac{G_{hh}D}{B-G_{hh}}\right] +$$

$$\frac{1}{s}\left[\frac{1}{2} J_1\left(\lambda_j R\right)\left(\frac{D}{B-G_{hh}} - 1\right)\lambda_j R\right]$$

Combination with equation (G.27) gives:

$$\frac{1}{s}\left[\frac{J_0\left(\lambda_j R\right)}{A+2G_{hh}}\left[B - 2G_{hh} + \frac{G_{hh}D}{B-G_{hh}}\right] + \left[\frac{\lambda_j R J_1\left(\lambda_j R\right)}{2} - J_0\left(\lambda_j R\right)\right]\left[\frac{D}{B-G_{hh}} - 1\right]\right]$$

Adding this result to equation (G.26) gives:

$$\frac{\sigma_w}{\sigma_b} = \sum_{j=1}^{\infty} \frac{\left[J_0\left(\lambda_j r\right) - J_0\left(\lambda_j R\right)\right] e^{s_j t}}{s\dfrac{1}{s}\left[\dfrac{J_0\left(\lambda_j R\right)}{A+2G_{hh}}\left[B - 2G_{hh} + \dfrac{DG_{hh}}{B-G_{hh}}\right] + \left[\dfrac{\lambda_j R}{2} J_1\left(\lambda_j R\right) - J_0\left(\lambda_j R\right)\right]\left[\dfrac{D}{B-G_{hh}} - 1\right]\right]} \tag{G.28}$$

rewriting gives:

$$\frac{\sigma_w}{\sigma_b} = \sum_{j=1}^{\infty} \frac{\left[\dfrac{J_0\left(\lambda_j r\right)}{J_0\left(\lambda_j R\right)} - 1\right] e^{s_j t}}{\left[\dfrac{B - 2G_{hh} + DG_{hh}/\left(B-G_{hh}\right)}{A+2G_{hh}}\right] + \left[\dfrac{\lambda_j R}{2}\dfrac{J_1\left(\lambda_j R\right)}{J_0\left(\lambda_j R\right)} - 1\right]\left[\dfrac{D}{B-G_{hh}} - 1\right]} \tag{G.29}$$

Function f(t)

Section 5.2 explains that the difference between the Biot equations and the Terzaghi–Rendulic solution for three dimensional consolidation is found in equation (G.3). Twice integrating equation (G.3) gives:

$$\left[A + 2G_{hh}\right] e = \sigma_w + f\left(x, y, z, t\right) \tag{G.30}$$

In the Terzaghi–Rendulic solution a direct relation between e and σ_w is assumed, leading to $f(x, y, z, t) = 0$. De Josselin de Jong [41] shows that in absence of rotations $f(x, y, z, t)$ reduces to $f(t)$ but not necessarily to 0. With the solutions found for e and σ_w an expression for $f(t)$ can be found. The Laplace transformation of equation (G.30) gives:

$$\left[A + 2G_{hh}\right] \overline{e} = \overline{\sigma}_w + \overline{f}(t) \tag{G.31}$$

With the equations (G.7) and (G.9) it is found that:

$$\overline{f}(t) = C_3 \left(A + 2G_{hh}\right) \tag{G.32}$$

With C_3 expressed by equation (G.21) it is found after rewriting that:

$$\overline{f}(t) = \frac{J_0\left(\lambda R\right)\left(\overline{g}_3 - \dfrac{D\left(\overline{g}_2 + \overline{g}_1\right)}{B - G_{hh}}\right) - \overline{g}_1\left[\dfrac{2J_1\left(\lambda R\right)}{\lambda R\left(A + 2G_{hh}\right)}\left(B - 2G_{hh} + \dfrac{DG_{hh}}{B - G_{hh}}\right) + \dfrac{DJ_0\left(\lambda R\right)}{B - G_{hh}}\right]}{\dfrac{2J_1\left(\lambda R\right)}{\lambda R\left(A + 2G_{hh}\right)}\left[B - 2G_{hh} + \dfrac{DG_{hh}}{B - G_{hh}}\right] + \dfrac{B - G_{hh} - D}{B - G_{hh}} J_0\left(\lambda R\right)} \tag{G.33}$$

The inverse transformation is found equivalent to the previous given inverse transforms of stress and strain. With condition (E.37) it is found for $g_1 = g_2 = 0$ and $g_3 = \sigma_b$ that:

$$f(t) = \frac{\left(A + 2G_{hh}\right)\left(B - G_{hh}\right)\sigma_b}{\left(B - G_{hh}\right)B + A\left(B - G_{hh} - D\right) - G_{hh}D} + \sum_{j=1}^{\infty} \frac{\sigma_b e^{s_j t}}{\left[\dfrac{B - 2G_{hh} + DG_{hh}/\left(B - G_{hh}\right)}{A + 2G_{hh}}\right] + \left[\dfrac{\lambda_j R}{2}\dfrac{J_1\left(\lambda_j R\right)}{J_0\left(\lambda_j R\right)} - 1\right]\left[\dfrac{D}{B - G_{hh}} - 1\right]} \tag{G.34}$$

Non–perfect drainage

Due to hydraulic resistance in the drains, porous stone and the pore water collection system boundary condition a might not hold in practice. To study the influence of non–perfect drainage system a time depending boundary condition can be used. Section 5.5 suggest the following boundary condition:

$$g_1 = -\frac{1}{3}\sigma_b e^{-\kappa t}$$

In which the parameters κ controls the drain pressure decay. The complete set of boundary conditions becomes:

$$\begin{aligned} g_1 &= -\left[\frac{1}{3} + \frac{K'}{J'}\right]\sigma_b e^{-\kappa t}, \quad \rightarrow \quad \overline{g}_1 = -\left[\frac{1}{3} + \frac{K'}{J'}\right]\frac{\sigma_b}{\kappa + s} \\ g_2 &= 0 \qquad \rightarrow \qquad \overline{g}_2 = 0 \\ g_3 &= \sigma_b \qquad \rightarrow \qquad \overline{g}_3 = \frac{\sigma_b}{s} \end{aligned}$$

Application of this set of boundary conditions to equation (G.13) gives:

$$\overline{\sigma}_w = \frac{\left[J_0\left(\lambda r\right) - J_0\left(\lambda R\right)\right]\sigma_b}{s\left[\dfrac{2J_1\left(\lambda R\right)}{\left(A + 2G_{hh}\right)\lambda R}\left(B - 2G_{hh} + \dfrac{DG_{hh}}{B - G_{hh}}\right) + \dfrac{B - G_{hh} - D}{B - G_{hh}} J_0\left(\lambda R\right)\right]} - \frac{\left[J_0\left(\lambda r\right) - J_0\left(\lambda R\right)\right]\left(\dfrac{1}{3} + \dfrac{K'}{J'}\right)\dfrac{B - G_{hh} - D}{B - G_{hh}}\sigma_b}{\left(\kappa + s\right)\left[\dfrac{2J_1\left(\lambda R\right)}{\left(A + 2G_{hh}\right)\lambda R}\left(B - 2G_{hh} + \dfrac{DG_{hh}}{B - G_{hh}}\right) + \dfrac{B - G_{hh} - D}{B - G_{hh}} J_0\left(\lambda R\right)\right]} - \left(\frac{1}{3} + \frac{K'}{J'}\right)\frac{\sigma_b}{\kappa + s} \tag{G.35}$$

The right hand side of equation (G.35) consists of three parts. In application of the inverse transformation each part can be transformed individually. The inverse transform of the first part has already been given by equation (G.29). The third part follows directly from boundary conditions or can be found in handbooks for standard solution:

$$\mathscr{L}^{-1}\left(\frac{1}{3} + \frac{K'}{J'}\right)\frac{\sigma_b}{\kappa + s} = \left(\frac{1}{3} + \frac{K'}{J'}\right)\sigma_b e^{-\kappa t}$$

For finding the inverse transform of the second part the Heaviside expansion theorem is used. The roots of the second term are given by:

$$s = -\kappa \quad \vee \quad \frac{2J_1(\lambda R)}{(A+2G_{hh})\lambda R}\left(B - 2G_{hh} + \frac{G_{hh}D}{B-G_{hh}}\right) + \frac{B-G_{hh}-D}{B-G_{hh}}J_0(\lambda R) = 0$$

The second group of roots equal the roots given by equation (G.27). The derivative of the denominator of the second term in equation (G.35) is given by:

$$\left[\frac{2J_1(\lambda R)}{(A+2G_{hh})\lambda R}\left(B - 2G_{hh} + \frac{G_{hh}D}{B-G_{hh}}\right) + \frac{B-G_{hh}-D}{B-G_{hh}}J_0(\lambda R)\right] +$$

$$\frac{\kappa+s}{s}\left[\frac{J_0(\lambda R)}{A+2G_{hh}}\left(B - 2G_{hh} + \frac{DG_{hh}}{B-G_{hh}}\right) + \left[\frac{\lambda R}{2}J_1(\lambda R) - J_0(\lambda R)\right]\left[\frac{D}{B-G_{hh}} - 1\right]\right]$$

Summation of the three parts gives the inverse transform of equation (G.35):

$$\frac{\sigma_w}{\sigma_b} = \sum_{j=1}^{\infty} \frac{\left[\frac{J_0(\lambda_j r)}{J_0(\lambda_j R)} - 1\right] e^{s_j t}}{\left[\frac{B - 2G_{hh} + DG_{hh}/(B-G_{hh})}{A+2G_{hh}}\right] + \left[\frac{\lambda_j R}{2}\frac{J_1(\lambda_j R)}{J_0(\lambda_j R)} - 1\right] + \left[\frac{D}{B-G_{hh}} - 1\right]} -$$

$$\sum_{j=1}^{\infty} \frac{\left[\frac{J_0(\lambda_j r)}{J_0(\lambda_j R)} - 1\right]\left(\frac{1}{3} + \frac{K'}{J'}\right)\frac{B-G_{hh}-D}{B-G_{hh}} e^{s_j t}}{\frac{\kappa+s_j}{s_j}\left[\frac{B - 2G_{hh} + DG_{hh}/(B-G_{hh})}{A+2G_{hh}}\right] + \left[\frac{\lambda_j R}{2}\frac{J_1(\lambda_j R)}{J_0(\lambda_j R)} - 1\right] + \left[\frac{D}{B-G_{hh}} - 1\right]} - \quad \text{(G.36)}$$

$$\frac{\left[J_0\left(\sqrt{\frac{\kappa}{c}}r\right)/J_0\left(\sqrt{\frac{\kappa}{c}}R\right) - 1\right]\left(\frac{1}{3} + \frac{K'}{J'}\right)\frac{B-G_{hh}-D}{B-G_{hh}} e^{-\kappa t}}{\left[\frac{2J_1\left(\sqrt{\frac{\kappa}{c}}R\right)\left(B - 2G_{hh} + \frac{DG_{hh}}{B-G_{hh}}\right)}{(A+2G_{hh})J_0\left(\sqrt{\frac{\kappa}{c}}R\right)\sqrt{\frac{\kappa}{c}}R} + \frac{B-G_{hh}-D}{B-G_{hh}}\right]} \quad - \left(\frac{1}{3} + \frac{K'}{J'}\right)e^{-\kappa t}$$

Isotropic loading

Using equations (G.9), (G.21) and (G.24) the pore pressure development for isotropic loading instead of axial loading is easily found. For the boundary conditions $g_1 = 0$ and $g_2 = g_3 = \sigma_b$ follows:

$$\frac{\overline{\sigma}_w}{\sigma_b} = \frac{\frac{B-G_{hh}-D}{B-G_{hh}}J_0(\lambda r) - J_0(\lambda R)}{s\left[\frac{2J_1(\lambda R)}{[A+2G_{hh}]\lambda R}\left[(B-2G_{hh}) + \frac{DG_{hh}}{B-G_{hh}}\right] + J_0(\lambda R)\left(1 - \frac{D}{B-G_{hh}}\right)\right]} \quad \text{(G.37)}$$

Equation (G.37) differs only from equation (G.26) by the constant $(B - G_{hh} - D)/(B - G_{hh})$. The inverse transform gives:

$$\frac{\sigma_w}{\sigma_b} = \sum_{j=1}^{\infty} \frac{\frac{B-G_{hh}-D}{B-G_{hh}}\left[\frac{J_0(\lambda_j r)}{J_0(\lambda_j R)} - 1\right] e^{s_j t}}{\left[\frac{B - 2G_{hh} + DG_{hh}/(B-G_{hh})}{A+2G_{hh}}\right] + \left[\frac{\lambda_j R}{2}\frac{J_1(\lambda_j R)}{J_0(\lambda_j R)} - 1\right] + \left[\frac{D}{B-G_{hh}} - 1\right]} \quad \text{(G.38)}$$

Note that the reciprocal value for the constant $(B - G_{hh} - D)/(B - G_{hh})$ can be rewritten, using the expressions given in the appendix B, into:

$$\frac{B-G_{hh}}{B-G_{hh}-D} = -\left(\frac{1}{3} + \frac{K'}{J'}\right)$$

Consolidation around a vertical drain

Based on the solution for consolidation of a triaxial sample the solution for consolidation around a vertical drain can be solved. This solution is found when solving equation (G.11) to (G.20) for a different set of boundary conditions. With ρ the radius of the drain and R the outer radius of the cylinder in which the drain is active, the following five boundary conditions describe the problem;

a) at $r = \rho \quad \sigma_w = 0, \quad \rightarrow \quad \overline{\sigma}_w = 0$

b) at $r = R \quad u_r = 0, \quad \rightarrow \quad \overline{u}_r = 0$

c) at $r = \rho \quad u_r = 0, \quad \rightarrow \quad \overline{u}_r = 0$

d) at $r = R \quad \partial\sigma_w/\partial r = 0, \quad \rightarrow \quad \partial\overline{\sigma}_w/\partial r = 0$

e) at $z = h \quad 1/A \int 2\pi r \sigma_{zz} \mathrm{d}r = \sigma_b, \quad \rightarrow \quad 1/A \int 2\pi r \overline{\sigma}_{zz} \mathrm{d}r = \overline{\sigma}_b$

The combination of boundary condition a and equation (G.14) gives:

$$C_3 = C_1 J_0(\lambda\rho) + C_2 Y_0(\lambda\rho) \tag{G.39}$$

The combination of boundary condition b and equation (G.11) gives:

$$\frac{1}{2}\frac{\partial \overline{u}_{zz}}{\partial z} = C_1 \frac{J_1(\lambda R)}{\lambda R} + C_2 \frac{Y_1(\lambda R)}{\lambda R} + \frac{C_4}{R^2} \tag{G.40}$$

The combination of boundary condition c and equation (G.11) gives:

$$C_4 = \rho R \left[\frac{\rho}{2R}\frac{\partial \overline{u}_{zz}}{\partial z} - C_1 \frac{J_1(\lambda\rho)}{\lambda R} - C_2 \frac{Y_1(\lambda\rho)}{\lambda R} \right] \tag{G.41}$$

Application of equation (G.40) gives:

$$C_4 = \frac{\rho R^2}{R^2 - \rho^2} \left[C_1 \left(\rho \frac{J_1(\lambda R)}{\lambda R} - R \frac{J_1(\lambda\rho)}{\lambda R} \right) + C_2 \left(\rho \frac{Y_1(\lambda R)}{\lambda R} - R \frac{Y_1(\lambda\rho)}{\lambda R} \right) \right] \tag{G.42}$$

The derivative of equation (G.14) gives, with C_3 independent of r:

$$\frac{\partial \overline{\sigma}_w}{\partial r} = -(A + 2G_{hh}) \left[C_1 \lambda J_1(\lambda r) + C_2 \lambda Y_1(\lambda r) \right]$$

with boundary condition d follows:

$$C_1 = -C_2 \frac{Y_1(\lambda R)}{J_1(\lambda R)} \tag{G.43}$$

Finally with boundary condition e and equation (G.17) and (G.20) :

$$\overline{\sigma}_b = \int_{\rho}^{R} \frac{2\pi r}{\pi (R^2 - \rho^2)} \overline{\sigma}_{zz} \mathrm{d}r$$

$$\overline{\sigma}_{zz} = (B - 2G_{hh}) \left[C_1 J_0(\lambda r) + C_2 Y_0(\lambda r) \right] + D \frac{\partial \overline{u}_{zz}}{\partial z} + (A + 2G_{hh}) C_3$$

$$\overline{\sigma}_b = (B - 2G_{hh}) \left[\begin{array}{l} C_1 \left(\dfrac{2R^2}{R^2 - \rho^2} \dfrac{J_1(\lambda R)}{\lambda R} - \dfrac{2\rho^2}{R^2 - \rho^2} \dfrac{J_1(\lambda\rho)}{\lambda\rho} \right) + \\ C_2 \left(\dfrac{2R^2}{R^2 - \rho^2} \dfrac{Y_1(\lambda R)}{\lambda R} - \dfrac{2\rho^2}{R^2 - \rho^2} \dfrac{Y_1(\lambda\rho)}{\lambda\rho} \right) \end{array} \right] + D \frac{\partial \overline{u}_{zz}}{\partial z} + (A + 2G_{hh}) C_3$$

Application of equation (G.39), (G.40), (G.42) and (G.43) gives:

$$C_2 = \frac{J_1(\lambda R)\, \overline{\sigma}_b}{\left[\begin{array}{l} \dfrac{\alpha}{\lambda R} \left(Y_1(\lambda\rho) J_1(\lambda R) - J_1(\lambda\rho) Y_1(\lambda R) \right) + \\ \qquad (A + 2G_{hh}) \left[Y_0(\lambda\rho) J_1(\lambda R) - Y_1(\lambda R) J_0(\lambda\rho) \right] \end{array} \right]} \tag{G.44}$$

and:

$$C_1 = \frac{-Y_1(\lambda R)\,\overline{\sigma}_b}{\left[\begin{array}{l}\dfrac{\alpha}{\lambda R}\left(Y_1(\lambda\rho)\,J_1(\lambda R) - J_1(\lambda\rho)\,Y_1(\lambda R)\right) + \\ \qquad (A+2G_{hh})\left[Y_0(\lambda\rho)\,J_1(\lambda R) - Y_1(\lambda R)\,J_0(\lambda\rho)\right]\end{array}\right]} \tag{G.45}$$

with:

$$\alpha = (2G_{hh} - B - D)\,\frac{2\rho R}{(R^2-\rho^2)} \tag{G.46}$$

With expressions available for C_1, C_2, C_3, C_4 and $\partial\overline{u}_{zz}/\partial z$ an expression for each stress and strain can be found. This is elaborated for ε_{zz}, u_r, ε_r, e, σ_w and σ'_r. From equations (G.40), (G.11), (G.12), (G.13), (G.14) and (G.15) is found in transformed conditions:

$$\overline{\varepsilon}_{zz} = \frac{\partial\overline{u}_{zz}}{\partial z} = \frac{2\rho R}{R^2-\rho^2}\left(\frac{Y_1(\lambda R)\,\dfrac{J_1(\lambda\rho)}{\lambda R} - J_1(\lambda R)\,\dfrac{Y_1(\lambda\rho)}{\lambda R}}{\left[\begin{array}{l}\dfrac{\alpha}{\lambda R}\left(Y_1(\lambda\rho)\,J_1(\lambda R) - J_1(\lambda\rho)\,Y_1(\lambda R)\right) + \\ \qquad (A+2G_{hh})\left[Y_0(\lambda\rho)\,J_1(\lambda R) - Y_1(\lambda R)\,J_0(\lambda\rho)\right]\end{array}\right]}\right) \times \overline{\sigma}_b \tag{G.47}$$

$$\frac{\overline{u}_r}{R} = \frac{\left[\begin{array}{l}-Y_1(\lambda R)\left[\dfrac{J_1(\lambda r)}{\lambda R} - \dfrac{\rho\left(R^2-r^2\right)}{r\left(R^2-\rho^2\right)}\dfrac{J_1(\lambda\rho)}{\lambda R}\right] + \\ \\ \quad J_1(\lambda R)\left[\dfrac{Y_1(\lambda r)}{\lambda R} - \dfrac{\rho\left(R^2-r^2\right)}{r\left(R^2-\rho^2\right)}\dfrac{Y_1(\lambda\rho)}{\lambda R}\right]\end{array}\right]}{\left[\begin{array}{l}\dfrac{\alpha}{\lambda R}\left(Y_1(\lambda\rho)\,J_1(\lambda R) - J_1(\lambda\rho)\,Y_1(\lambda R)\right) + \\ \qquad (A+2G_{hh})\left[Y_0(\lambda\rho)\,J_1(\lambda R) - Y_1(\lambda R)\,J_0(\lambda\rho)\right]\end{array}\right]} \times \overline{\sigma}_b \tag{G.48}$$

$$\overline{\varepsilon}_r = \frac{\left[\begin{array}{l}J_1(\lambda R)\left[Y_0(\lambda r) - \dfrac{Y_1(\lambda r)}{\lambda r} + R\dfrac{\rho\left(r^2+R^2\right)}{r^2\left(R^2-\rho^2\right)}\dfrac{Y_1(\lambda\rho)}{\lambda R}\right] - \\ \\ \quad Y_1(\lambda R)\left[J_0(\lambda r) - \dfrac{J_1(\lambda r)}{\lambda r} + R\dfrac{\rho\left(r^2+R^2\right)}{r^2\left(R^2-\rho^2\right)}\dfrac{J_1(\lambda\rho)}{\lambda R}\right]\end{array}\right]}{\left[\begin{array}{l}\dfrac{\alpha}{\lambda R}\left(Y_1(\lambda\rho)\,J_1(\lambda R) - J_1(\lambda\rho)\,Y_1(\lambda R)\right) + \\ \qquad (A+2G_{hh})\left[Y_0(\lambda\rho)\,J_1(\lambda R) - Y_1(\lambda R)\,J_0(\lambda\rho)\right]\end{array}\right]} \times \overline{\sigma}_b \tag{G.49}$$

$$\overline{e} = \frac{J_1(\lambda R)\,Y_0(\lambda r) - Y_1(\lambda R)\,J_0(\lambda r)}{\left[\begin{array}{l}\dfrac{\alpha}{\lambda R}\left(Y_1(\lambda\rho)\,J_1(\lambda R) - J_1(\lambda\rho)\,Y_1(\lambda R)\right) + \\ \qquad (A+2G_{hh})\left[Y_0(\lambda\rho)\,J_1(\lambda R) - Y_1(\lambda R)\,J_0(\lambda\rho)\right]\end{array}\right]} \times \overline{\sigma}_b \tag{G.50}$$

$$\overline{\sigma}_w = \frac{(A+2G_{hh})\left(-Y_1(\lambda R)\left(J_0(\lambda r) - J_0(\lambda\rho)\right) + J_1(\lambda R)\left(Y_0(\lambda r) - Y_0(\lambda\rho)\right)\right)\overline{\sigma}_b}{\left[\begin{array}{l}\dfrac{\alpha}{\lambda R}\left(Y_1(\lambda\rho)\,J_1(\lambda R) - J_1(\lambda\rho)\,Y_1(\lambda R)\right) + \\ \qquad (A+2G_{hh})\left[Y_0(\lambda\rho)\,J_1(\lambda R) - Y_1(\lambda R)\,J_0(\lambda\rho)\right]\end{array}\right]} \tag{G.51}$$

$$\overline{\sigma}'_r = \frac{\left[\begin{array}{l}-Y_1(\lambda R)\left[(A+2G_{hh})\,J_0(\lambda r) - 2G_{hh}\dfrac{J_1(\lambda r)}{\lambda r} - \xi(r)\,\dfrac{J_1(\lambda\rho)}{\lambda R}\right] + \\ \\ \quad J_1(\lambda R)\left[(A+2G_{hh})\,Y_0(\lambda r) - 2G_{hh}\dfrac{Y_1(\lambda r)}{\lambda r} - \xi(r)\,\dfrac{Y_1(\lambda\rho)}{\lambda R}\right]\end{array}\right]}{\left[\begin{array}{l}\dfrac{\alpha}{\lambda R}\left(Y_1(\lambda\rho)\,J_1(\lambda R) - J_1(\lambda\rho)\,Y_1(\lambda R)\right) + \\ \qquad (A+2G_{hh})\left[Y_0(\lambda\rho)\,J_1(\lambda R) - Y_1(\lambda R)\,J_0(\lambda\rho)\right]\end{array}\right]} \times \overline{\sigma}_b \tag{G.52}$$

with:

$$\xi(r) = \left(\frac{2\,(B-G_{hh})}{R^2} - \frac{2G_{hh}}{r^2}\right)\frac{\rho R^3}{R^2-\rho^2}$$

The inverse of equations (G.47) to (G.52) can be found using the Heaviside expansion theorem. The Heaviside expansion theorem starts with finding the roots of the denominator. The roots of the denominator are given by the values for s that fulfil:

$$s = 0 \quad \vee \quad \frac{Y_1(\lambda\rho)\,J_1(\lambda R) - J_1(\lambda\rho)\,Y_1(\lambda R)}{Y_0(\lambda\rho)\,J_1(\lambda R) - Y_1(\lambda R)\,J_0(\lambda\rho)} = -\frac{(A+2G_{hh})}{\alpha}\lambda R \tag{G.53}$$

Next the derivative of the denominator is needed. When d represents the denominator the following is found:

$$\frac{\partial d}{\partial s} = \left[\begin{array}{l}\frac{\alpha}{\lambda R}\left(Y_1(\lambda\rho)\,J_1(\lambda R) - J_1(\lambda\rho)\,Y_1(\lambda R)\right) + \\ (A+2G_{hh})\left[Y_0(\lambda\rho)\,J_1(\lambda R) - Y_1(\lambda R)\,J_0(\lambda\rho)\right]\end{array}\right] \times \frac{\partial}{\partial s}(s) + s \times \frac{\partial}{\partial s}\left[\begin{array}{l}\frac{\alpha}{\lambda R}\left(Y_1(\lambda\rho)\,J_1(\lambda R) - J_1(\lambda\rho)\,Y_1(\lambda R)\right) + \\ (A+2G_{hh})\left[Y_0(\lambda\rho)\,J_1(\lambda R) - Y_1(\lambda R)\,J_0(\lambda\rho)\right]\end{array}\right]$$

Application of condition (G.53) gives for s $\neq 0$:

$$\frac{\partial d}{\partial s} = \alpha\psi + (A+2G_{hh})\,\phi$$

with:

$$\psi = Y_1(\lambda\rho)\left[\frac{1}{2}J_0(\lambda R) - \frac{J_1(\lambda R)}{\lambda R}\right] + \frac{J_1(\lambda R)}{\lambda R}\left[\frac{\lambda\rho}{2}Y_0(\lambda\rho) - \frac{1}{2}Y_1(\lambda\rho)\right] - J_1(\lambda\rho)\left[\frac{1}{2}Y_0(\lambda R) - \frac{Y_1(\lambda R)}{\lambda R}\right] - \frac{Y_1(\lambda R)}{\lambda R}\left[\frac{\lambda\rho}{2}J_0(\lambda\rho) - \frac{1}{2}J_1(\lambda\rho)\right]$$

$$\phi = \frac{1}{2}\left[\lambda R J_0(\lambda R)\,Y_0(\lambda\rho) - \lambda R J_0(\lambda\rho)\,Y_0(\lambda R) - \lambda\rho Y_1(\lambda\rho)\,J_1(\lambda R)\right] + \frac{1}{2}\left[\lambda\rho Y_1(\lambda R)\,J_1(\lambda\rho) - J_1(\lambda R)\,Y_0(\lambda\rho) + J_0(\lambda\rho)\,Y_1(\lambda R)\right]$$

gives:

$$\frac{\varepsilon_{zz}}{\sigma_b} = \frac{1}{\sigma_b}\frac{\partial u_{zz}}{\partial z} = \frac{1}{A+B+D} + \frac{2\rho R}{R^2-\rho^2}\sum_{j=1}^{\infty}\frac{Y_1(\lambda_j R)\,\frac{J_1(\lambda_j\rho)}{\lambda_j R} - J_1(\lambda_j R)\,\frac{Y_1(\lambda_j\rho)}{\lambda_j R}}{\alpha\psi_j + (A+2G_{hh})\,\phi_j} \times e^{s_j t} \tag{G.54}$$

$$\frac{1}{\sigma_b}\frac{u_r}{R} = \sum_{j=1}^{\infty}\frac{\left[\begin{array}{c}J_1(\lambda_j R)\left[\frac{Y_1(\lambda_j r)}{\lambda_j R} - \frac{\rho\left(R^2-r^2\right)}{r\left(R^2-\rho^2\right)}\frac{Y_1(\lambda_j\rho)}{\lambda_j R}\right] - \\ Y_1(\lambda_j R)\left[\frac{J_1(\lambda_j r)}{\lambda_j R} - \frac{\rho\left(R^2-r^2\right)}{r\left(R^2-\rho^2\right)}\frac{J_1(\lambda_j\rho)}{\lambda_j R}\right]\end{array}\right]}{\alpha\psi_j + (A+2G_{hh})\,\phi_j} \times e^{s_j t} \tag{G.55}$$

$$\frac{\varepsilon_r}{\sigma_b} = \sum_{j=1}^{\infty}\frac{\left[\begin{array}{c}J_1(\lambda_j R)\left[Y_0(\lambda_j r) - \frac{Y_1(\lambda_j r)}{\lambda_j r}\right] - Y_1(\lambda_j R)\left[J_0(\lambda_j r) - \frac{J_1(\lambda_j r)}{\lambda_j r}\right] + \\ R\frac{\rho\left(r^2+R^2\right)}{r^2\left(R^2-\rho^2\right)}\left[\frac{J_1(\lambda_j R)\,Y_1(\lambda_j\rho)}{\lambda_j R} - \frac{Y_1(\lambda_j R)\,J_1(\lambda_j\rho)}{\lambda_j R}\right]\end{array}\right]}{\alpha\psi_j + (A+2G_{hh})\,\phi_j} \times e^{s_j t} \tag{G.56}$$

$$\frac{e}{\sigma_b} = \frac{1}{A+B+D} + \sum_{j=1}^{\infty}\frac{J_1(\lambda_j R)\,Y_0(\lambda_j r) - Y_1(\lambda_j R)\,J_0(\lambda_j r)}{\alpha\psi_j + (A+2G_{hh})\,\phi_j} \times e^{s_j t} \tag{G.57}$$

$$\frac{\sigma_w}{\sigma_b} = \sum_{j=1}^{\infty}\frac{(A+2G_{hh})\left[\begin{array}{c}J_1(\lambda_j R)\left(Y_0(\lambda_j r) - Y_0(\lambda_j\rho)\right) \\ -Y_1(\lambda_j R)\left(J_0(\lambda_j r) - J_0(\lambda_j\rho)\right)\end{array}\right]}{\alpha\psi_j + (A+2G_{hh})\,\phi_j} \times e^{s_j t} \tag{G.58}$$

$$\frac{\sigma_r}{\sigma_b} = \frac{E_h}{E_v}\frac{\nu_{vh}}{1-\nu_{hh}} \quad + \\ \sum_{j=1}^{\infty} \frac{\begin{bmatrix} J_1(\lambda_j R)\left[(A+2G_{hh})\,Y_0(\lambda_j r) - 2G_{hh}\dfrac{Y_1(\lambda_j r)}{\lambda_j r} - \xi(r)\,\dfrac{Y_1(\lambda_j \rho)}{\lambda_j R}\right] \\ -Y_1(\lambda_j R)\left[(A+2G_{hh})\,J_0(\lambda_j r) - 2G_{hh}\dfrac{J_1(\lambda_j r)}{\lambda_j r} - \xi(r)\,\dfrac{J_1(\lambda_j \rho)}{\lambda_j R}\right] \end{bmatrix}}{\alpha\psi_j + (A+2G_{hh})\,\phi_j} \times e^{s_j t} \tag{G.59}$$

with:

$$\xi(r) = \left(\frac{2(B-G_{hh})}{R^2} - \frac{2G_{hh}}{r^2}\right)\frac{\rho R^3}{R^2-\rho^2}$$

In accordance to equation (G.30) the following is found for function $f(t)$:

$$\overline{f}(t) = (A+2G_{hh})\,C_3 = (A+2G_{hh})\,[C_1 J_0(\lambda\rho) + C_2 Y_0(\lambda\rho)]$$

Application of equations (G.44) and (G.45) gives after inverse transformation:

$$f(t) = \frac{A+2G_{hh}}{A+B+D} + \sum_{j=1}^{\infty} \frac{(A+2G_{hh})\,[J_1(\lambda_j R)\,Y_0(\lambda_j \rho) - Y_1(\lambda_j R)\,J_0(\lambda_j \rho)]\,\sigma_b e^{s_j t}}{\alpha\psi_j + (A+2G_{hh})\,\phi_j} \tag{G.60}$$

It should be noted that for isotropic conditions $\alpha = 0$ and therefore $\overline{f}(t) = \overline{\sigma}_b$ leading to $f(t) = \sigma_b$. With equation (G.58) the average degree of consolidation U is given by:

$$U = \int_{\rho}^{R} \frac{2\pi r}{\pi(R^2-\rho^2)}\frac{\sigma_w}{\sigma_b}\mathrm{d}r \tag{G.61}$$

Elaborating equation (G.61) gives:

$$U = \frac{2(A+2G_{hh})}{R^2-\rho^2}\times \\ \sum_{j=1}^{\infty} \frac{\begin{bmatrix} J_1(\lambda_j R)\left[\dfrac{R}{\lambda_j}Y_1(\lambda_j R) - \dfrac{\rho}{\lambda_j}Y_1(\lambda_j \rho) - \dfrac{1}{2}\left(R^2-\rho^2\right)Y_0(\lambda_j \rho)\right] - \\ Y_1(\lambda_j R)\left[\dfrac{R}{\lambda_j}J_1(\lambda_j R) - \dfrac{\rho}{\lambda_j}J_1(\lambda_j \rho) - \dfrac{1}{2}\left(R^2-\rho^2\right)J_0(\lambda_j \rho)\right] \end{bmatrix}}{\alpha\psi_j + (A+2G_{hh})\,\phi_j} \times e^{s_j t} \tag{G.62}$$

Appendix H

Consolidation for anisotropic plane–strain conditions

This appendix extends the solution derived in appendix F to cross–anisotropic conditions. Again the solution derived in 4 steps

step 1, the relevant equations
To derive the solution for plane strain, cross–anisotropic conditions the stress–strain relationship elaborated in appendix B is used:

$$\begin{aligned}
\sigma'_{xx} &= Ae + 2G_{hh}\varepsilon_{xx} + B\varepsilon_{zz} \\
\sigma'_{yy} &= Ae + 2G_{hh}\varepsilon_{yy} + B\varepsilon_{zz} \\
\sigma'_{zz} &= (A+B)e + D\varepsilon_{zz} \\
\tau_{yz} &= G_{vh}\left[\frac{\partial u_{yy}}{\partial z} + \frac{\partial u_{zz}}{\partial y}\right] \\
\tau_{zx} &= G_{vh}\left[\frac{\partial u_{xx}}{\partial z} + \frac{\partial u_{zz}}{\partial x}\right] \\
\tau_{xy} &= G_{hh}\left[\frac{\partial u_{xx}}{\partial y} + \frac{\partial u_{yy}}{\partial x}\right]
\end{aligned} \tag{H.1}$$

Note the sign convention in which stress is chosen positive for tension while the pore pressure is chosen positive for pressure. The effective stress is then defined by:

$$\begin{aligned}
\sigma'_{xx} &= \sigma_{xx} + \sigma_w \\
\sigma'_{yy} &= \sigma_{yy} + \sigma_w \\
\sigma'_{zz} &= \sigma_{zz} + \sigma_w
\end{aligned} \tag{H.2}$$

Equilibrium yields:

$$\begin{aligned}
\frac{\partial \sigma'_{xx}}{\partial x} + \frac{\partial \tau_{xy}}{\partial y} + \frac{\partial \tau_{xz}}{\partial z} &= \frac{\partial \sigma_w}{\partial x} \\
\frac{\partial \tau_{yx}}{\partial x} + \frac{\partial \sigma'_{yy}}{\partial y} + \frac{\partial \tau_{yz}}{\partial z} &= \frac{\partial \sigma_w}{\partial y} \\
\frac{\partial \tau_{zx}}{\partial x} + \frac{\partial \tau_{zy}}{\partial y} + \frac{\partial \sigma'_{zz}}{\partial z} &= \frac{\partial \sigma_w}{\partial z}
\end{aligned} \tag{H.3}$$

Combination of (H.1) and (H.3) leads to:

$$\begin{aligned}
&A\frac{\partial e}{\partial x}+2G_{hh}\frac{\partial^2 u_{xx}}{\partial x^2}+B\frac{\partial^2 u_{zz}}{\partial x\partial z}+G_{hh}\frac{\partial^2 u_{xx}}{\partial y^2}+G_{hh}\frac{\partial^2 u_{yy}}{\partial y\partial x}+G_{vh}\frac{\partial^2 u_{xx}}{\partial z^2}+G_{vh}\frac{\partial^2 u_{zz}}{\partial z\partial x}=\frac{\partial \sigma_w}{\partial x}\\
&G_{hh}\frac{\partial^2 u_{xx}}{\partial x\partial y}+G_{hh}\frac{\partial^2 u_{yy}}{\partial x^2}+A\frac{\partial e}{\partial y}+2G_{hh}\frac{\partial^2 u_{yy}}{\partial y^2}+B\frac{\partial^2 u_{zz}}{\partial y\partial z}+G_{vh}\frac{\partial^2 u_{yy}}{\partial z^2}+G_{vh}\frac{\partial^2 u_{zz}}{\partial z\partial y}=\frac{\partial \sigma_w}{\partial y}\\
&G_{vh}\frac{\partial^2 u_{xx}}{\partial x\partial z}+G_{vh}\frac{\partial^2 u_{zz}}{\partial x^2}+G_{vh}\frac{\partial^2 u_{yy}}{\partial y\partial z}+G_{vh}\frac{\partial^2 u_{zz}}{\partial y^2}+(A+B)\frac{\partial e}{\partial z}+D\frac{\partial^2 u_{zz}}{\partial z^2}=\frac{\partial \sigma_w}{\partial z}
\end{aligned} \tag{H.4}$$

To simplify (H.4) the following assumptions are made:

- plane strain conditions result in: $\varepsilon_{yy}=0$
- stiff top on top $\partial\varepsilon_{zz}/\partial z=\partial\varepsilon_{zz}/\partial x=0$
- no shear stress $\tau_{zx}=\tau_{yx}=\tau_{zy}=0$

Application of these assumptions to equation (H.4) gives:

$$\begin{aligned}
A\frac{\partial e}{\partial x} &+ 2G_{hh}\frac{\partial^2 u_{xx}}{\partial x^2} &&= \frac{\partial \sigma_w}{\partial x}\\
A\frac{\partial e}{\partial y} & &&= \frac{\partial \sigma_w}{\partial y}\\
A\frac{\partial e}{\partial z} &+ B\frac{\partial e}{\partial z} &&= \frac{\partial \sigma_w}{\partial z}
\end{aligned} \tag{H.5}$$

Differentiation and summation changes equation (H.5) into:

$$A\nabla^2 e+2G_{hh}\frac{\partial^3 u_{xx}}{\partial x^3}+B\frac{\partial^2 e}{\partial z^2}=\nabla^2\sigma_w \tag{H.6}$$

Note that the volumetric strain can be rewritten into:

$$\begin{aligned}
&\nabla^2 e=\frac{\partial^2\varepsilon_{xx}}{\partial x^2}+\frac{\partial^2\varepsilon_{yy}}{\partial y^2}+\frac{\partial^2\varepsilon_{zz}}{\partial z^2},\quad \frac{\partial^2\varepsilon_{yy}}{\partial y^2}=\frac{\partial^2\varepsilon_{zz}}{\partial z^2}=0,\quad \nabla^2 e=\frac{\partial^2\varepsilon_{xx}}{\partial x^2}=\frac{\partial^3 u_{xx}}{\partial x^3}\\
&\frac{\partial^2 e}{\partial z^2}=\frac{\partial^2\varepsilon_{xx}}{\partial z^2}+\frac{\partial^2\varepsilon_{yy}}{\partial z^2}+\frac{\partial^2\varepsilon_{zz}}{\partial z^2},\quad \frac{\partial^2\varepsilon_{yy}}{\partial z^2}=\frac{\partial^2\varepsilon_{zz}}{\partial z^2}=0,\\
&\varepsilon_{xx}\text{ is constant at every } z\text{ - level},\quad \frac{\partial^2\varepsilon_{xx}}{\partial z^2}=0,\quad \frac{\partial^2 e}{\partial z^2}=0
\end{aligned}$$

Equation (H.6) can be rewritten into:

$$[A+2G_{hh}]\nabla^2 e=\nabla^2\sigma_w \tag{H.7}$$

The storage equation remains unaltered:

$$\frac{k}{\gamma_w}\nabla^2\sigma_w=\frac{\partial e}{\partial t} \tag{H.8}$$

Combination of equation (H.7) and (H.8) gives the consolidation equation:

$$\begin{aligned}
&\frac{k}{\gamma_w}[A+2G_{hh}]\nabla^2 e=\frac{\partial e}{\partial t}\\
&\text{or}\\
&\frac{\partial^2 e}{\partial x^2}=\frac{1}{c}\frac{\partial e}{\partial t},\quad \text{with}\quad c=\frac{k}{\gamma_w}[A+2G_{hh}]
\end{aligned} \tag{H.9}$$

step 2, the Laplace transformation
The solution of equation (H.9) can be found by using the Laplace transformation. Application of the Laplace transformation to the equation (H.9) gives:

$$\frac{\partial^2 \overline{e}}{\partial x^2} = \frac{1}{c}\left(s\overline{e} - e_0\right) \tag{H.10}$$

In which e_0 is the volumetric strain directly after loading, at $t = 0^+$. Since directly after loading the soil behaves undrained; $e_0 = 0$. Equation (H.10) reduces to:

$$\frac{\partial^2 \overline{e}}{\partial x^2} - \frac{s}{c}\overline{e} = 0 \tag{H.11}$$

Equation (H.11) is a linear ordinary second–order differential equation and can be solved by the standard solution : $\overline{e} = \exp(\lambda x)$:

$$\lambda^2 \exp(\lambda x) - \frac{s}{c}\exp(\lambda x) = 0;$$
$$\lambda = \pm\sqrt{\frac{s}{c}} \quad \text{and} \quad \overline{e} = C_1 \exp\left(\sqrt{\frac{s}{c}}x\right) + C_2 \exp\left(-\sqrt{\frac{s}{c}}x\right)$$

reformulation gives:

$$\overline{e} = C_1 \cosh\left(\sqrt{\frac{s}{c}}x\right) + C_2 \sinh\left(\sqrt{\frac{s}{c}}x\right) \tag{H.12}$$

with (H.12):

$$\overline{e} = \overline{\varepsilon}_{xx} + \overline{\varepsilon}_{zz}, \quad \overline{e} = \frac{\partial \overline{u}_{xx}}{\partial x} + \frac{\partial \overline{u}_{zz}}{\partial z}$$

is found in combination to equation (H.12):

$$\frac{\partial \overline{u}_{xx}}{\partial x} = C_1 \cosh\left(\sqrt{\frac{s}{c}}x\right) + C_2 \sinh\left(\sqrt{\frac{s}{c}}x\right) - \frac{\partial \overline{u}_{zz}}{\partial z} \tag{H.13}$$

The transform of equation (H.7):

$$\nabla^2 \overline{e} = \frac{\nabla^2 \overline{\sigma}_w}{[A + 2G_{hh}]}$$

leads to:

$$\overline{e} = \frac{\overline{\sigma}_w}{[A + 2G_{hh}]} + C_3, \quad \text{with } \nabla^2 C_3 = 0$$

$$\overline{\sigma}_w = [A + 2G_{hh}]\left[C_1 \cosh\left(\sqrt{\frac{s}{c}}x\right) + C_2 \sinh\left(\sqrt{\frac{s}{c}}x\right) - C_3\right] \tag{H.14}$$

The combination of (H.1), (H.12) and (H.13) gives the expressions for stress and strain in transformed conditions:

$$\overline{e} = C_1 \cosh\left(\sqrt{\frac{s}{c}}x\right) + C_2 \sinh\left(\sqrt{\frac{s}{c}}x\right) \tag{H.15}$$

$$\frac{\partial \overline{u}_{xx}}{\partial x} = C_1 \cosh\left(\sqrt{\frac{s}{c}}x\right) + C_2 \sinh\left(\sqrt{\frac{s}{c}}x\right) - \frac{\partial \overline{u}_{zz}}{\partial z} \tag{H.16}$$

$$\overline{\sigma}_w = [A + 2G_{hh}]\left[C_1 \cosh\left(\sqrt{\frac{s}{c}}x\right) + C_2 \sinh\left(\sqrt{\frac{s}{c}}x\right) - C_3\right] \tag{H.17}$$

$$\overline{\sigma}'_{xx} = A\overline{e} + 2G_{hh}\frac{\partial \overline{u}_{xx}}{\partial x} + B\frac{\partial \overline{u}_{zz}}{\partial z} \tag{H.18}$$

$$\overline{\sigma}'_{yy} = A\overline{e} + B\frac{\partial \overline{u}_{zz}}{\partial z} \tag{H.19}$$

$$\overline{\sigma}'_{zz} = A\overline{e} + B\overline{e} + D\frac{\partial \overline{u}_{zz}}{\partial z} \tag{H.20}$$

$$\begin{aligned}\sigma_{xx} &= \sigma_{xx} - \sigma_w \\ \sigma_{yy} &= \sigma_{yy} - \sigma_w \\ \sigma_{zz} &= \sigma_{zz} - \sigma_w\end{aligned} \tag{H.21}$$

step 3, solving for the boundary conditions
The equations (H.15) to (H.21) contain 4 unknown parameters: C_1, C_2, C_3 and $\partial\overline{u}_{zz}/\partial z$, which can be solved by the four boundary conditions:

a) at $x = 0$, $\quad \dfrac{\partial\sigma_w}{\partial x} = 0, \rightarrow \dfrac{\partial\overline{\sigma}_w}{\partial x} = 0$

b) at $x = l$, $\quad \sigma_w = 0 \rightarrow \overline{\sigma}_w = 0$

c) at $x = l$, $\quad \sigma_{xx} = 0 \rightarrow \overline{\sigma}_{xx} = 0$

d) at $z = h$, $\quad \int\limits_{-l}^{l} \dfrac{\sigma_{zz}}{2l}dx = \dfrac{2F}{2l} \rightarrow \int\limits_{-l}^{l} \dfrac{\overline{\sigma}_{zz}}{2l}dx = \dfrac{\overline{F}}{l}, \quad \overline{F} = \int\limits_{0}^{l} \overline{\sigma}_{zz}dx$

The combination of (H.17) and the boundary condition a gives:

$$\begin{aligned}\frac{\partial\overline{\sigma}_w}{\partial x} &= [A + 2G_{hh}]\left[C_1\sqrt{\frac{s}{c}}\sinh\left(\sqrt{\frac{s}{c}}x\right) + C_2\sqrt{\frac{s}{c}}\cosh\left(\sqrt{\frac{s}{c}}x\right)\right] \\ [A + 2G_{hh}]&\left[C_1\sqrt{\frac{s}{c}}\sinh(0) + C_2\sqrt{\frac{s}{c}}\cosh(0)\right] = 0\end{aligned}$$

$$C_2 = 0 \tag{H.22}$$

Combination of (H.17), (H.22) and boundary condition b leads to:

$$\overline{\sigma}_w = [A + 2G_{hh}]\left[C_1\cosh\left(\sqrt{\frac{s}{c}}l\right) - C_3\right] = 0$$

$$C_3 = C_1\cosh\left(\sqrt{\frac{s}{c}}l\right) \tag{H.23}$$

So equation (H.17) can be rewritten:

$$\overline{\sigma}_w = [A + 2G_{hh}]\,C_1\left[\cosh\left(\sqrt{\frac{s}{c}}x\right) - \cosh\left(\sqrt{\frac{s}{c}}l\right)\right] \tag{H.24}$$

The boundary condition c in combination with (H.2) (H.18), (H.15), (H.16), (H.22), (H.23) and (H.24) gives:

$$\begin{aligned}\overline{\sigma}_{xx} &= \overline{\sigma}'_{xx} - \overline{\sigma}_w \\ \overline{\sigma}_{xx} &= A\overline{e} + 2G_{hh}\frac{\partial\overline{u}_{xx}}{\partial x} + B\frac{\partial\overline{u}_{zz}}{\partial z} - \overline{\sigma}_w \\ \overline{\sigma}_{xx} &= AC_1\cosh\left(\sqrt{\frac{s}{c}}x\right) + 2G_{hh}\left[C_1\cosh\left(\sqrt{\frac{s}{c}}x\right) - \frac{\partial\overline{u}_{zz}}{\partial z}\right] + B\frac{\partial\overline{u}_{zz}}{\partial z} - \\ &\quad [A + 2G_{hh}]\left[C_1\left(\cosh\left(\sqrt{\frac{s}{c}}x\right) - \cosh\left(\sqrt{\frac{s}{c}}l\right)\right)\right]\end{aligned}$$

for $x = l$:

$$\overline{\sigma}_{xx} = AC_1\cosh\left(\sqrt{\frac{s}{c}}l\right) + 2G_{hh}\left[C_1\cosh\left(\sqrt{\frac{s}{c}}l\right) - \frac{\partial\overline{u}_{zz}}{\partial z}\right] + B\frac{\partial\overline{u}_{zz}}{\partial z} = 0$$

$$C_1 = -\frac{[B - 2G_{hh}]\dfrac{\partial\overline{u}_{zz}}{\partial z}}{[A + 2G_{hh}]\cosh\left(\sqrt{\dfrac{s}{c}}l\right)} \tag{H.25}$$

Combination of equations (H.2), (H.15), (H.16), (H.20), (H.22), (H.23), (H.24)and (H.25) result in:

$$\overline{\sigma}_{zz} = -\frac{[B-2G_{hh}]\,\dfrac{\partial \overline{u}_{zz}}{\partial z}}{[A+2G_{hh}]\cosh\left(\sqrt{\dfrac{s}{c}}l\right)}\,[A+B]\,\cosh\left(\sqrt{\frac{s}{c}}x\right) + D\frac{\partial \overline{u}_{zz}}{\partial z} + \frac{[B-2G_{hh}]\,\dfrac{\partial \overline{u}_{zz}}{\partial z}}{\cosh\left(\sqrt{\dfrac{s}{c}}l\right)}\,\left[\cosh\left(\sqrt{\frac{s}{c}}x\right) - \cosh\left(\sqrt{\frac{s}{c}}l\right)\right]$$

Boundary condition d with $\partial \overline{u}_{zz}/\partial z$ independent from x it follows :

$$\int_0^l \overline{\sigma}_{zz}dz = \left[-\frac{[B-2G_{hh}]\,[A+B]\,\dfrac{\partial \overline{u}_{zz}}{\partial z}}{[A+2G_{hh}]\cosh\left(\sqrt{\dfrac{s}{c}}l\right)}\frac{1}{\sqrt{\dfrac{s}{c}}}\sinh\left(\sqrt{\frac{s}{c}}x\right) + D\frac{\partial \overline{u}_{zz}}{\partial z}x + \frac{[B-2G_{hh}]\,\dfrac{\partial \overline{u}_{zz}}{\partial z}}{\cosh\left(\sqrt{\dfrac{s}{c}}l\right)}\times \left(\frac{1}{\sqrt{\dfrac{s}{c}}}\sinh\left(\sqrt{\frac{s}{c}}x\right) - x\cosh\left(\sqrt{\frac{s}{c}}l\right)\right)\right]_0^l = \overline{F}$$

$$\overline{F} = -\frac{[B-2G_{hh}]\,[A+B]\,\dfrac{\partial \overline{u}_{zz}}{\partial z}}{[A+2G_{hh}]\cosh\left(\sqrt{\dfrac{s}{c}}l\right)}\frac{1}{\sqrt{\dfrac{s}{c}}}\sinh\left(\sqrt{\frac{s}{c}}l\right) + D\frac{\partial \overline{u}_{zz}}{\partial z}l + [B-2G_{hh}]\,\frac{\partial \overline{u}_{zz}}{\partial z}\left(\frac{1}{\sqrt{\dfrac{s}{c}}}\frac{\sinh\left(\sqrt{\dfrac{s}{c}}l\right)}{\cosh\left(\sqrt{\dfrac{s}{c}}l\right)} - l\right)$$

rewriting:

$$\frac{\partial \overline{u}_{zz}}{\partial z} = \frac{\overline{F}}{\left[\dfrac{[B-2G_{hh}]}{\sqrt{\dfrac{s}{c}}}\tanh\left(\sqrt{\frac{s}{c}}l\right)\left[1-\dfrac{[A+B]}{[A+2G_{hh}]}\right] + [D-B+2G_{hh}]\,l\right]} \tag{H.26}$$

The solution for stress and strain in transformed conditions can now be found by a combination of equations (H.22), (H.23), (H.25), (H.26) to equations (H.15) to (H.20) and (H.2).

step 4, inverse transformation
The expression for pore pressure development in transformed conditions is found with (H.22), (H.23), (H.25) and (H.26)

$$\overline{\sigma}_w = \frac{-[B-2G_{hh}]\;\overline{F}\;\left[\dfrac{\cosh\left(\sqrt{\dfrac{s}{c}}x\right)}{\cosh\left(\sqrt{\dfrac{s}{c}}l\right)} - 1\right]}{\dfrac{B-2G_{hh}}{\sqrt{\dfrac{s}{c}}}\tanh\left(\sqrt{\frac{s}{c}}l\right)\left[1-\dfrac{A+B}{A+2G_{hh}}\right] + l\,[D-B+2G_{hh}]}$$

with the inverse of boundary condition d:

$$\overline{F} = \int_0^\infty F \exp(-st)\,\mathrm{d}t = \frac{F}{s}$$

$$\overline{\sigma}_w = \frac{-\left[B - 2G_{hh}\right]\ F\ \left[\dfrac{\cosh\left(\sqrt{\dfrac{s}{c}}x\right)}{\cosh\left(\sqrt{\dfrac{s}{c}}l\right)} - 1\right]}{s\left[\dfrac{B-2G_{hh}}{\sqrt{\dfrac{s}{c}}}\tanh\left(\sqrt{\dfrac{s}{c}}l\right)\left[1 - \dfrac{A+B}{A+2G_{hh}}\right] + l\left[D - B + 2G_{hh}\right]\right]} \tag{H.27}$$

The inverse transform of equation (H.27) can be found by the Heaviside expansion theorem. This theorem states that:

$$\text{if } \overline{\sigma}_w = \frac{t(s)}{n(s)}, \quad \text{then } \sigma_w = \sum_{j=1}^{\infty} \frac{t(a_j)}{\dfrac{d}{ds}n(a_j)} \exp(a_j t), \quad \text{with } a_j \text{ the roots of } n(s)$$

The roots of $n(s)$ are:

$$s = 0 \quad \vee \quad \frac{B-2G_{hh}}{\sqrt{\dfrac{s}{c}}}\tanh\left(\sqrt{\frac{s}{c}}l\right)\left[1 - \frac{A+B}{A+2G_{hh}}\right] + l\left[D - B + 2G_{hh}\right] = 0$$

For $s = 0$ the nominator of equation (H.27) vanishes. The solution $s = 0$ is a removable root and therefore not a part of the inverse transform. For the other roots it is found:

$$\tanh\left(\sqrt{\frac{s}{c}}l\right) = -\frac{l\left[D - B + 2G_{hh}\right]}{\left[1 - \dfrac{A+B}{A+2G_{hh}}\right]} \cdot \frac{\sqrt{\dfrac{s}{c}}}{\left[B - 2G_{hh}\right]}$$

$$\text{with } \alpha = -\frac{l\left[D - B + 2G_{hh}\right]}{\left[1 - \dfrac{A+B}{A+2G_{hh}}\right]\left[B - 2G_{hh}\right]}$$

The characteristic equation is found by:

$$\tanh\left(\sqrt{\frac{s}{c}}l\right) = \alpha\sqrt{\frac{s}{c}}l \tag{H.28}$$

Rewriting (H.28) for imaginary values for s gives:

$$\sinh\left(\sqrt{\frac{s}{c}}l\right) = \alpha\sqrt{\frac{s}{c}}l\cosh\left(\sqrt{\frac{s}{c}}l\right)$$

with the familiar expressions:

$$\cosh(y) = \cos(iy)$$
$$\sinh(y) = -i\sin(iy)$$
follows:
$$-i\sin\left(i\sqrt{\frac{s}{c}}l\right) = \alpha\sqrt{\frac{s}{c}}l\cos\left(i\sqrt{\frac{s}{c}}l\right)$$
$$-i\tan\left(i\sqrt{\frac{s}{c}}l\right) = \alpha\sqrt{\frac{s}{c}}l$$
$$\tan\left(i\sqrt{\frac{s}{c}}l\right) = \alpha\sqrt{\frac{s}{c}}l \cdot \frac{1}{-i} \cdot \frac{i}{i} = \alpha i\sqrt{\frac{s}{c}}l$$

The roots of equation (H.27) are those values for s, which fulfil:

$$\tan(\lambda) = \alpha\lambda, \quad \lambda = i\sqrt{\frac{s}{c}}l, \quad \alpha = -\frac{[D - B + 2G_{hh}]}{\left[1 - \frac{A+B}{A+2G_{hh}}\right][B - 2G_{hh}]} \tag{H.29}$$

The next step in finding the inverse transform of equation (H.27) is differentiating the denominator of (H.27). For differentiating the denominator first separable parts are differentiated:

$$\frac{d}{ds}\left(\frac{1}{\sqrt{\frac{s}{c}}}\right) = \frac{-1}{2c\left(\frac{s}{c}\right)^{\frac{3}{2}}}, \quad \frac{d}{ds}\left(\sqrt{\frac{s}{c}}l\right) = \frac{l}{2c\sqrt{\frac{s}{c}}}$$

$$\frac{d}{dx}(\tanh(x)) = \frac{1}{\cosh(x)}\frac{d}{dx}(\sinh(x)) + \sinh(x)\frac{d}{dx}\frac{1}{\cosh(x)} =$$

$$= 1 - \frac{\sinh^2(x)}{\cosh^2(x)} = \frac{1}{\cosh^2(x)}$$

$$\frac{d}{ds}\tanh\left(\sqrt{\frac{s}{c}}l\right) = \frac{l}{2c\sqrt{\frac{s}{c}}\cosh^2\left(\sqrt{\frac{s}{c}}l\right)}$$

$$\frac{d}{ds}\left(\frac{\tanh\left(\sqrt{\frac{s}{c}}l\right)}{\sqrt{\frac{s}{c}}}\right) = \tanh\left(\sqrt{\frac{s}{c}}l\right)\frac{d}{ds}\frac{1}{\sqrt{\frac{s}{c}}} + \frac{1}{\sqrt{\frac{s}{c}}}\frac{d}{ds}\tanh\left(\sqrt{\frac{s}{c}}l\right) =$$

$$\frac{\tanh\left(\sqrt{\frac{s}{c}}l\right)}{2c\left(\frac{s}{c}\right)^{\frac{3}{2}}} + \frac{l}{2s\cosh^2\left(\sqrt{\frac{s}{c}}l\right)}$$

Now the derivative of the denominator of (H.27) can be found:

$$\frac{\partial n}{\partial s} = \left[\frac{B - 2G_{hh}}{\sqrt{\frac{s}{c}}}\tanh\left(\sqrt{\frac{s}{c}}l\right)\left[1 - \frac{A+B}{A+2G_{hh}}\right] + l[D - B + 2G_{hh}]\right]\frac{\partial}{\partial s}(s) +$$

$$s\frac{\partial}{\partial s}\left[\frac{B - 2G_{hh}}{\sqrt{\frac{s}{c}}}\tanh\left(\sqrt{\frac{s}{c}}l\right)\left[1 - \frac{A+B}{A+2G_{hh}}\right] + l[D - B + 2G_{hh}]\right]$$

$$\frac{\partial n}{\partial s} = \left[\frac{B - 2G_{hh}}{\sqrt{\frac{s}{c}}}\tanh\left(\sqrt{\frac{s}{c}}l\right)\left[1 - \frac{A+B}{A+2G_{hh}}\right] + l[D - B + 2G_{hh}]\right] +$$

$$s(B - 2G_{hh})\left[\frac{l}{2s\cosh^2\left(\sqrt{\frac{s}{c}}l\right)} - \frac{\tanh\left(\sqrt{\frac{s}{c}}l\right)}{2c\left(\frac{s}{c}\right)^{\frac{3}{2}}}\right]\left[1 - \frac{A+B}{A+2G_{hh}}\right] \tag{H.30}$$

The roots defined by (H.29) reduce the first term of the right hand-side of equation (D.30) to 0.

Application of the found roots to the second part of (H.30) gives:

$$\lambda = i\sqrt{\frac{s}{c}}l \quad \rightarrow \quad \sqrt{\frac{s}{c}}l = -i\lambda$$
$$\frac{\partial n\left(a_j\right)}{\partial s} = \left[B - 2G_{hh}\right]\left[\frac{2G_{hh} - B}{A + 2G_{hh}}\right]\left[\frac{l}{2\cosh^2\left(-i\lambda\right)} - \frac{l\tanh\left(-i\lambda\right)}{-2\lambda i}\right]$$

with: $\sinh(-i\lambda) = i\sin\left(-\lambda\right) = -i\sin\left(\lambda\right)$
$\cosh\left(-i\lambda\right) = \cos\left(-\lambda\right) = \cos\left(\lambda\right)$
$\cosh^2\left(-i\lambda\right) = \cos^2\left(\lambda\right)$

$$\frac{\partial n\left(a_j\right)}{\partial s} = \left[B - 2G_{hh}\right]\left[\frac{2G_{hh} - B}{A + 2G_{hh}}\right]\left[\frac{l}{2\cos^2\left(\lambda\right)} + \frac{l\dfrac{-i\sin\left(\lambda\right)}{\cos\left(\lambda\right)}}{2\lambda i}\right] =$$
$$= \left[B - 2G_{hh}\right]\left[\frac{2G_{hh} - B}{A + 2G_{hh}}\right]\left[\frac{l}{2\cos^2\left(\lambda\right)} - \frac{l\tan\left(\lambda\right)}{2\lambda}\right]$$

Application of the roots given by (H.29) to the nominator of (H.27):

$$t\left(a_j\right) = -\left[B - 2G_{hh}\right]F\left(\frac{\cos\left(\lambda\dfrac{x}{l}\right)}{\cos\left(\lambda\right)} - 1\right)$$

with:

$$\lambda_j = i\sqrt{\frac{s_j}{c}}l, \quad \rightarrow \quad \frac{\lambda_j}{il}\cdot\frac{i}{i} = \sqrt{\frac{s_j}{c}}, \quad \rightarrow \quad s_j = -\frac{\lambda_j^2 c}{l^2}$$

The inverse transform of equation (H.27) is found:

$$\sigma_w = -\frac{F}{l}\sum_{j=1}^{\infty}\frac{\left[\dfrac{\cos\left(\lambda_j\dfrac{x}{l}\right)}{\cos\left(\lambda_j\right)} - 1\right]e^{\dfrac{-\lambda_j^2 ct}{l^2}}}{\left[\dfrac{2G_{hh} - B}{A + 2G_{hh}}\right]\left[\dfrac{1}{2\cos^2\left(\lambda_j\right)} - \dfrac{\tan\left(\lambda_j\right)}{\lambda_j}\right]} \tag{H.31}$$

with:

λ_j fulfils $\tan\left(\lambda_j\right) = \alpha\lambda_j, \quad \alpha = -\dfrac{\left[D - B + 2G_{hh}\right]}{\left[1 - \dfrac{A + B}{A + 2G_{hh}}\right]\left[B - 2G_{hh}\right]}$

Appendix I

3D Consolidation including compressible solids

Based on the derivation presented by appendix E the consolidation problem is solved including compressibility of the solid particles. Again the solution is derived in 4 steps.

step1, the relevant expressions
Chapter 2 introduces β_{sf}, the compressibility of solids due to an isotropic stress increment and β_{ss}, the compressibility of solids due to inter granular contact forces. Barends [7] presents the storage equation for compressible solids:

$$(1-n)\,\beta_{sf}\left(1-\frac{\beta_{sf}}{\beta}\right)\frac{\partial\sigma_w}{\partial t}+\left[1-(1-n)\,\frac{\beta_{ss}}{\beta}\right]\frac{\partial e}{\partial t}=\frac{k}{\gamma_{fg}}\nabla^2\sigma_w \tag{I.1}$$

Introduction of equation (2.15) reduces the conditions of equilibrium to:

$$\left[K+\frac{4}{3}G\right]\nabla^2 e=\alpha\nabla^2\sigma_w \tag{I.2}$$

with:

$$\alpha=1-\frac{\beta_{sf}}{\beta}$$

Twice integrating equation (I.2) gives:

$$\left[K+\frac{4}{3}G\right]e=\alpha\sigma_w+f(x,y,z,t) \tag{I.3}$$

De Josselin de Jong [41] shows that $f(x,y,z,t)$ reduces to $f(t)$ when deformations occur in absence of rotations. Since this condition is fulfilled for standard triaxial testing the following holds:

$$\left[K+\frac{4}{3}G\right]\frac{\partial e}{\partial t}=\alpha\frac{\partial\sigma_w}{\partial t}+\frac{\partial f}{\partial t} \tag{I.4}$$

Combination of the equations (I.1) and (I.4) while introducing:

$$\beta^*=(1-n)\,\beta_{sf}\left(1-\frac{\beta_{sf}}{\beta}\right)$$
$$\beta'=1-(1-n)\,\frac{\beta_{ss}}{\beta}$$

gives:

$$\frac{\partial\sigma_w}{\partial t}=\frac{K+\frac{4}{3}G}{\beta^*\left(K+\frac{4}{3}G\right)+\beta'\alpha}\frac{k}{\gamma_{fg}}\nabla^2\sigma_w-\frac{\beta'}{\beta^*\left(K+\frac{4}{3}G\right)+\beta'\alpha}\frac{\partial f(t)}{\partial t}$$

Introducing:

$$m_v = \frac{1}{K + \frac{4}{3}G}$$
$$c_1 = \frac{k}{(\beta^* + \beta'\alpha m_v)\,\gamma_{fg}}$$
$$c_2 = \frac{\beta'}{\frac{\beta^*}{m_v} + \beta'\alpha}$$

gives:

$$\frac{\partial \sigma_w}{\partial t} = c_1 \nabla^2 \sigma_w - c_2 \frac{\partial f(t)}{\partial t} \tag{I.5}$$

With:

$$c_3 = \frac{c_2}{c_1} = \frac{\beta' m_v \gamma_{fg}}{k}$$

this becomes:

$$\nabla^2 \sigma_w = \frac{1}{c_1}\frac{\partial \sigma_w}{\partial t} + c_3 \frac{\partial f(t)}{\partial t} \tag{I.6}$$

step 2, the Laplace transformation
Application of the Laplace transformation to equation I.6 gives:

$$\nabla^2 \overline{\sigma}_w = \frac{1}{c_1}\left[s\overline{\sigma}_w - \sigma_w(0)\right] + c_3\left(s\overline{f}(t) - f(0)\right) \tag{I.7}$$

In which $\sigma_w(0)$ and $f(0)$ refer to the initial values for σ_w and f. From section 4.3.1 follows:

$$\sigma_w(0) = -\frac{1}{3}B\sigma_b$$

The initial condition $f(0)$ is unknown and has to be solved by the boundary conditions. Rewriting equation (I.7) gives:

$$r^2\frac{\partial^2 \overline{\sigma}_w}{\partial r^2} + r\frac{\partial \overline{\sigma}_w}{\partial r} - r^2\frac{s}{c_1}\overline{\sigma}_w = \frac{r^2}{3c_1}B\sigma_b + c_3 r^2\left[s\overline{f}(t) - f(0)\right] \tag{I.8}$$

The solution for the non–homogeneous differential equation (I.8) consists of two parts, a complementary function, which is the solution for the related homogeneous function and a particular solution for the non–homogeneous part. The homogeneous part of equation (I.8) is given by:

$$r^2\frac{\partial^2 \overline{\sigma}_w^{(1)}}{\partial r^2} + r\frac{\partial \overline{\sigma}_w^{(1)}}{\partial r} - r^2\frac{s}{c_1}\overline{\sigma}_w^{(1)} = 0$$

which is solved using the standard solution:

$$\overline{\sigma}_w^{(1)} = D_1 J_0(\lambda r) + D_2 Y_0(\lambda r), \quad \lambda = \sqrt{\frac{-s}{c_1}} \tag{I.9}$$

In which D_1 and D_2 represents parameters to be solved by the boundary conditions and J_0 and Y_0 Bessel functions. The particular part of the solution for partial differential equation (I.8) is:

$$\overline{\sigma}_w^{(2)} = -\frac{1}{3s}B\sigma_b - \frac{c_3 c_1}{s}\left(s\overline{f}(t) - f(0)\right)$$

Summation of the expression for $\overline{\sigma}_w^{(1)}$ and $\overline{\sigma}_w^{(2)}$ gives:

$$\overline{\sigma}_w = D_1 J_0(\lambda r) + D_2 Y_0(\lambda r) - \frac{1}{3s}\sigma_b B - \frac{c_3 c_1}{s}\left(s\overline{f}(t) - f(0)\right) \tag{I.10}$$

The Laplace transform of equation (I.3) gives:

$$\left[K + \frac{4}{3}G\right]\overline{e} = \alpha\overline{\sigma}_w + \overline{f}(t)$$

Combination with equation equation (I.10) gives the Laplace transform of the volumetric strain:

$$\overline{e} = \frac{\alpha}{K + \frac{4}{3}G}\left[D_1 J_0(\lambda r) + D_2 Y_0(\lambda r) - \frac{1}{3s}B\sigma_b - \frac{c_1 c_3}{s}\left(s\overline{f}(t) - f(0)\right) + \frac{1}{\alpha}\overline{f}(t)\right] \tag{I.11}$$

For axial–symmetric conditions the following holds:

$$\overline{e} = \frac{1}{r}\frac{\partial(r\overline{u}_r)}{\partial r} + \frac{\partial\overline{u}_{zz}}{\partial z} \tag{I.12}$$

Combination of equations (I.11) and (I.12) yields:

$$\begin{aligned}\frac{\partial(r\overline{u}_r)}{\partial r} = {} & \frac{\alpha r}{K + \frac{4}{3}G}\left[D_1 J_0(\lambda r) + D_2 Y_0(\lambda r) - \frac{1}{3s}B\sigma_b - \frac{c_3 c_2}{s}\left(s\overline{f}(t) - f(0)\right) + \frac{1}{\alpha}\overline{f}(t)\right] \\ & - r\frac{\partial\overline{u}_{zz}}{\partial z}\end{aligned} \tag{I.13}$$

Integration and rewriting gives, using $\overline{u}_{zz}$ is independent of r:

$$\frac{\overline{u}_r}{R} = \frac{\alpha}{R\left(K + \frac{4}{3}G\right)}\left[\begin{array}{c}\frac{D_1}{\lambda}J_1(\lambda r) + \frac{D_2}{\lambda}Y_1(\lambda r) - \frac{r}{2}\frac{1}{3s}B\sigma_b \\ -\frac{r}{2}\frac{c_3 c_1}{s}\left(s\overline{f}(t) - f(0)\right) + \frac{r}{2\alpha}\overline{f}(t)\end{array}\right] - \frac{r}{2R}\frac{\partial\overline{u}_{zz}}{\partial z} + \frac{D_3}{rR} \tag{I.14}$$

Differentiating gives:

$$\frac{\partial\overline{u}_r}{\partial r} = \frac{\alpha}{K + \frac{4}{3}G}\left[\begin{array}{c}D_1\left(J_0(\lambda r) - \frac{1}{\lambda r}J_1(\lambda r)\right) + D_2\left(Y_0(\lambda r) - \frac{1}{\lambda r}Y_1(\lambda r)\right) + \\ -\frac{1}{2}\frac{1}{3s}B\sigma_b - \frac{1}{2}\frac{c_3 c_1}{s}\left(s\overline{f}(t) - f(0)\right) + \frac{1}{2\alpha}\overline{f}(t)\end{array}\right] - \frac{1}{2}\frac{\partial\overline{u}_{zz}}{\partial z} - \frac{D_3}{r^2} \tag{I.15}$$

The Laplace transform of the effective stresses is given by:

$$\begin{aligned}\overline{\sigma}'_r &= 2G\left[\frac{\partial\overline{u}_r}{\partial r} + \frac{\nu}{1-2\nu}\overline{e}\right] \\ \overline{\sigma}'_\theta &= 2G\left[\frac{\overline{u}_r}{r} + \frac{\nu}{1-2\nu}\overline{e}\right] \\ \overline{\sigma}'_{zz} &= 2G\left[\frac{\partial\overline{u}_{zz}}{\partial z} + \frac{\nu}{1-2\nu}\overline{e}\right]\end{aligned} \tag{I.16}$$

Application of equations (I.11), (I.14) and (I.15) gives:

$$\begin{aligned}\overline{\sigma}'_r = \quad & 2G\frac{\alpha}{K+\frac{4}{3}G}D_1\left[\frac{1-\nu}{1-2\nu}J_0(\lambda r)-\frac{1}{\lambda r}J_1(\lambda r)\right]+\\ & 2G\frac{\alpha}{K+\frac{4}{3}G}\left[D_2\left(\frac{1-\nu}{1-2\nu}Y_0(\lambda r)-\frac{1}{\lambda r}Y_1(\lambda r)\right)-\frac{1}{2(1-2\nu)}\frac{1}{3s}B\sigma_b\right]\\ & +2G\left[\frac{\alpha}{K+43G}\left(\frac{-1}{2(1-2\nu)}\frac{c_3c_1}{s}\left(s\overline{f}(t)-f(0)\right)+\frac{1}{2(1-2\nu)}\frac{1}{\alpha}\overline{f}(t)\right)-\frac{1}{2}\frac{\partial\overline{u}_{zz}}{\partial z}-\frac{D_3}{r^2}\right]\end{aligned}$$

$$\begin{aligned}\overline{\sigma}'_\theta = \quad & \frac{2\,G\,\alpha}{K+\frac{4}{3}G}\left[\begin{array}{c}D_1\left(\frac{1}{\lambda r}J_1(\lambda r)+\frac{\nu}{1-2\nu}J_0(\lambda r)\right)+D_2\left(\begin{array}{l}\frac{1}{\lambda r}Y_1(\lambda r)\\ +\frac{\nu}{1-2\nu}Y_0(\lambda r)\end{array}\right)-\left(\frac{2}{r}+\frac{\nu}{1-2\nu}\right)\frac{1}{3s}B\sigma_b-\\ \left(\frac{r}{2}+\frac{\nu}{1-2\nu}\right)\frac{c_3\;c_1}{s}\left(s\overline{f}(t)-f_0\right)+\left(\frac{2}{r}+\frac{\nu}{1-2\nu}\right)\frac{1}{\alpha}\overline{f}(t)\end{array}\right]\\ & -G\frac{\partial\overline{u}_{zz}}{\partial z}+2G\frac{D_3}{r^2}\end{aligned}$$

$$\overline{\sigma}'_{zz} = \quad 2G\left[\frac{\partial\overline{u}_{zz}}{\partial z}+\frac{\nu}{1-2\nu}\frac{\alpha}{K+\frac{4}{3}G}\left[\begin{array}{c}D_1J_0(\lambda r)+D_2Y_0(\lambda r)-\frac{1}{3s}B\sigma_b-\\ \frac{c_3c_1}{s}\left(s\overline{f}(t)-f(0)\right)+\frac{1}{\alpha}\overline{f}(t)\end{array}\right]\right]$$

The total stresses are given by:

$$\overline{\sigma}_r = \overline{\sigma}'_r - \overline{\sigma}_w \tag{I.17}$$

$$\overline{\sigma}_\theta = \overline{\sigma}'_\theta - \overline{\sigma}_w \tag{I.18}$$

$$\overline{\sigma}_{zz} = \overline{\sigma}'_{zz} - \overline{\sigma}_w \tag{I.19}$$

step 3, solving for boundary conditions
For $r \to 0$ $Y_0 = Y_1 = -\infty$ gives $D_2 = 0$, since stress and strain remain limited at $r = 0$. For the same reason $D_3 = 0$, since for $r = 0$, $D_3/r^2 \to \infty$. Three parameters have to be solved by the boundary conditions and initial conditions: D_1, $\partial\overline{u}_{zz}/\partial z$ and $\overline{f}(t)$
boundary conditions:

a $r = R \to \sigma_w = 0 \to \overline{\sigma}_w = 0$

b $r = R \to \sigma_r = 0 \to \overline{\sigma}_r = 0$

c $z = 0 \to 1/A \int 2\pi r\sigma_{zz}\,\mathrm{d}r = \sigma_b \to 1/A \int 2\pi r\overline{\sigma}_{zz}\,\mathrm{d}r = \overline{\sigma}_b$

Boundary condition a in combination to equation (I.10) gives:

$$D_1J_0(\lambda R) = \frac{1}{3s}B\sigma_b + \frac{c_3c_1}{s}\left(s\overline{f}(t)-f(0)\right) \tag{I.20}$$

Boundary condition b in combination to equation (I.17) and (I.20) gives:

$$\frac{1}{2}\frac{\partial\overline{u}_{zz}}{\partial z} = \frac{\alpha}{K+\frac{4}{3}G}\left[\left[\frac{B\sigma_b}{3s}+\frac{c_1c_3}{s}\left(s\overline{f}(t)-f(0)\right)\right]\left[\frac{1}{2}-\frac{1}{\lambda R}\frac{J_1(\lambda R)}{J_0(\lambda R)}\right]+\frac{1}{2\alpha(1-2\nu)}\overline{f}(t)\right] \tag{I.21}$$

Boundary condition c in combination to equation(I.19), (I.20) and (I.21) gives:

$$\overline{f}(t) = \frac{\overline{\sigma}_b - m\left[1-\frac{2}{\lambda R}\frac{J_1(\lambda R)}{J_0(\lambda R)}\right]\left[\frac{\sigma_bB}{3s}-\frac{c_3c_1}{s}f(0)\right]}{mc_3c_1\left[1-\frac{2}{\lambda R}\frac{J_1(\lambda R)}{J_0(\lambda R)}\right]+\frac{2G}{K+\frac{4}{3}G}\frac{1+\nu}{1-2\nu}} \tag{I.22}$$

With the expressions (I.20) to (I.22) the stresses and strains in transformed coordinates are found. For $\overline{\sigma}_w$ the following is found:

$$\overline{\sigma}_w = \frac{\left[\frac{J_0(\lambda r)}{J_0(\lambda R)} - 1\right]\left[\frac{l\sigma_b B}{3s} - l\frac{c_3 c_1}{s}f(0) + c_3 c_1 \overline{\sigma}_b\right]}{m\left[1 - \frac{2}{\lambda R}\frac{J_1(\lambda R)}{J_0(\lambda R)}\right]c_3 c_1 + l} \tag{I.23}$$

with:

$$l = \frac{2G}{K + 43G}\frac{1+\nu}{1-2\nu}$$

The volumetric strain $\overline{e}$ is then given by:

$$\overline{e} = \frac{\alpha\overline{\sigma}_b}{K+43G}\times$$

$$\frac{\left[l\left[\frac{J_0(\lambda r)}{J_0(\lambda R)} - 1\right] - \frac{m}{\alpha}\left(1 - \frac{2}{\lambda R}\frac{J_1(\lambda R)}{J_0(\lambda R)}\right)\right]\left(\frac{B}{3} - \frac{c_3 c_1 f(0)}{\sigma_b}\right) + c_3 c_1\left(\frac{J_0(\lambda r)}{J_0(\lambda R)} - 1\right) + \frac{1}{\alpha}}{mc_1 c_3\left(1 - \frac{2}{\lambda R}\frac{j_1(\lambda R)}{J_0(\lambda R)}\right) + l} \tag{I.24}$$

step 4, the inverse transform
The inverse transformation using the Heaviside theorem is explained in appendix E. Using this theorem gives for the pore pressure development:

$$\sigma_w = \sum_{j=1}^{\infty} \frac{\left[\frac{J_0(\lambda_j r)}{J_0(\lambda_j R)} - 1\right]\left[\frac{l\sigma_b B}{3} - lc_3 c_1 f(0) + c_3 c_1 \sigma_b\right] e^{s_j t}}{l - \frac{\left[(l + mc_1 c_3)\lambda_j R\right]^2}{4mc_3 c_1}} \tag{I.25}$$

and for the volumetric strain

$$e = \frac{\sigma_b}{l\left(K + \frac{4}{3}G\right)} + \frac{\alpha\sigma_b}{K + \frac{4}{3}G}\times$$
$$\sum_{i=1}^{\infty} \frac{\left[l\left(\left[\frac{J_0(\lambda_j r)}{J_0(\lambda_j R)} - 1\right] + \frac{1}{\alpha c_1 c_3}\right)\left(\frac{B}{3} - c_1 c_3\frac{f(0)}{\sigma_b}\right) + c_1 c_3\left(\frac{J_0(\lambda_j r)}{J_0(\lambda_j R)} - 1\right) + \frac{1}{\alpha}\right] e^{s_j t}}{l - \frac{\left[(l + mc_1 c_3)\lambda_j R\right]^2}{4mc_3 c_1}} \tag{I.26}$$

To finalise the solution an expression for $f(0)$ has to found.

$$\mathscr{L}^{-1}\frac{\overline{f}(t)}{\sigma_b} = \frac{f(t)}{\sigma_b} = \frac{1}{l} + \sum_{j=1}^{\infty} \frac{\left[1 + \frac{lB}{3c_1 c_3} - \frac{lf(0)}{\sigma_b}\right] e^{s_j t}}{l - \frac{\left[(l + mc_1 c_3)\lambda_j R\right]^2}{4mc_1 c_3}} \tag{I.27}$$

Application of t=0 to equation (I.27) gives an expression for $f(0)$. Note that $f(0)$ is also part of the summation. After rewriting is found:

$$\frac{f(0)}{\sigma_b} = \frac{\frac{1}{l} + \left(1 + \frac{lB}{3c_1 c_3}\right)A}{1 + lA}$$
$$A = \sum_{j=1}^{\infty} \frac{1}{l - \frac{\left[(l + mc_3 c_1)\lambda_j R\right]^2}{4mc_1 c_3}} \tag{I.28}$$

Bibliography

[1] Abousleiman Y., Cheng A.H.D., Cui L., Detournay E., Roegiers J.-C. (1996) Mandel's problem revisited, *Géotechnique* 46 No 2 pp 187–195

[2] Al–Tabbaa A. (1992) Finite element analyses of consolidation with radial peripheral drainage in: *Numerical Models in Geomechanics* Pande & Pietruszczak (eds.) pp. 441–451 4th int. symposium on numeical models in geomechanics, Swansea

[3] Al–Tabbaa A., Wood D.M. (1991) *Géotechnique* 41 no 4 pp. 571–585

[4] Atkinson J.H., Richardson D., Stallebrass S.E. (1990) Effect of recent stress history on the stiffness of overconsolidated soil, *Géotechnique* 40, No 4 pp 531–540

[5] Atkinson J.H. (2000) Non–linear soil stiffness in routine design, *Géotechnique* 50 No 5 pp 487–508

[6] Barends F.B.J. (1979) The compressibility of an air -water mixture in a porous medium, *LGM mededelingen* Part XX no 2-4 pp 49–66

[7] Barends F.B.J. (1992) Theory of Consolidation, *Lecture Notes TUD*

[8] Barends F.B.J. (1998) IDM for transient problems *private communication.*

[9] Barends F.B.J. (2002) The Squeeze Problem, in: *Learned and Applied, soil mechanics out of Delft* Barends & Steijger (eds.), Balkema, ISBN 90 5808 35 73

[10] Barron R.A. (1947) Consolidation of fine grained soils by drain wells, *ASCE transactions* pp 718-754

[11] Bellotti R., Jamiolkowski M., Lo Presti D. C. F., O'Neill D.A. (1996) Anisotropy of small strain stiffness in Ticino sand *Géotechnique* 46 No 1 pp 115–131

[12] Biot M.A. (1941) General theory of three dimensional consolidation, *Journal of applied physics* vol 12, pp 155–164

[13] Biot M.A. (1955) Theory of elasticity and consolidation for a porous anisotropic solid, *Journal of Applied Physics* vol. 26, pp 182–185

[14] Biot M.A., Willis D.G. (1957) The elastic coefficients of the theory of consolidation, *Journal of Applied Mechanics* vol 24 pp 594–601

[15] Bishop A.W., Hight D.W. (1977) The value of Poisson ratio's insaturated soils and rocks stressed under undrained conditions, *Géotechnique* 27 No 3 1977 pp 369–384

[16] Brodeau A. (1946) Corps Anisotropes Symtries Naturelles, *Publications Scientifiques et Techniques du ministre de l'air* N0 201, (in french)

[17] Carillo N.J. (1942) Simple Two and Three Dimensional Cases in Theory of Consolidation of Soils, *Journal of Mathematics and Physics* vol 21, pp 1–5

[18] Carroll M.M. (1979) An Effective Stress Law for Anisotropic Elastic Deformation, *Journal of Geophysical Research* Vol. 84 No B13 pp 7510-7512

[19] Cederbaum G., LePing L., Schulgasser K. (2000) *Poroelastic structures* Elsevier ISBN 0080436684

[20] Cheng A.H.D. (1997) Material Coefficients of Anisotropic Poroelasticity, *Int. J. Rock Min. Sci.* Vol 34 no 2 pp 199–205

[21] Chowdhury R.N. (1978) Effective Stress Parameters of Anisotropic Soil, *Journal of Geotechnical Engineering Division* GTI, pp 124–128

[22] Cryer C.W. (1963) A Comparison of the Three Dimensional Consolidation Theories of Biot and Terzaghi, *Quart. Journal of Mechanics and Applied Mathematics* Vol XVI pp 401–412

[23] Cui L., Cheng A.H.D., Kaliakin V.N., Abousleiman Y., Roegiers J.-C. (1996) Finite Element Analysis of Anisotropic Poro-elasticity: A generalized Mandel's problem and an inclined Borehole problem, *International Journal for Numerical and Analytical Methods in Geomechanics* vol 20 pp 381–401

[24] CUR (1996) *Building on Soft Soils, Design and construction of earth structures both on & into highly compressible subsoils of low bearing capacity* CUR report 162, Balkema Rotterdam, ISBN 90 5410 146 6

[25] Den Haan E.J., Uriel A.O., Rafnsson E.A. (1995) Theme report 7, special problem soils / soft rocks, in: *The interply between Geotechnical Engineering and Engineering Geology, volume 9 Theme reports*, proceedings of the 11^{th} European Conference on Soil Mechanics and Foundation Engineering, Danish Geotechnigal Society, Copenhagen

[26] Den Haan E.J., Kamao S. (2003) Obtaining isotache parameters from a C.R.S. K_0 oedometer, *Soils and Foundations* Vol 43 no 4 pp 203-214

[27] Den Haan E.J., Sellmeijer H.J.B. (2000) Calculation of Soft Ground Settlement with an Isotache Model, in: *Soft Ground Technology* Hanson & Termaat (eds.) ASCE special publication 112 pp 94-104

[28] Den Haan E.J. The B.H.P.A.M. Van M.A., De K_0–C.R.S. samendrukkingsproef (2001) *Geotechniek* no 5, pp 56–63

[29] Dyvik R., Madshus C. (1986) Lab Measurements of G_{max} Using Bender Elements, in:*Norwegian Geotechnical Institute, publication 161* NGI, Oslo

[30] Fjær E., Holt R.M., Horsrud P., Raaen A. M., Risnes R. (1992) *Petroleum related rock mechanics, Developments in Petroleum science* Elsevier ISBN 0-444-88913-2

[31] Fredlund D.G., Rahardjo H. (1993) *Soil Mechanics For Unsaturated Soils* John Wiley, ISBN 0-471-85008-X

[32] Gibson R.E, Knight K., Taylor P.W. (1964) A critical experiment to examine theories of three dimensional consolidation, *European Conference on Soil Mechanics* Wiesbaden pp 1–17

[33] Gibson R.E., Gobert A., Schiffmann R.L.(1990) On Cryer's problem with large displacements and variable permeability, *Géotechnique* 40 No4 pp 627-631

[34] Graham J., Houlsby G. T. (1983) Anisotropic elasticity of a natural clay, *Géotechnique* 33 no 2 pp 165-180

[35] Hearmon R.F.S (1961) *An introduction to applied anisotropic elasticity* Oxford University Press

[36] Hird C.C., Pierpoint N.D. (1994) A non-linear elastic model for overconsolidated clay based on strain energy, in: *Numerical methods in Geotechnical Engineering* Smith (ed.) Balkema Rotterdam, ISBN 9054105100

[37] Hird C.C., Pierpoint N.D. (1998) Stiffness determination and deformation analysis for a trial excavation in Oxford Clay in: *pre-failure deformation behaviour of geometarials* Jardine et al. (eds.) Thomas Telford, London, ISBN 0727726420

[38] Jiang G-L, Tatsuoka F., Flora A., Kokesi J. (1997) Inherent and strass-state-induced anisotropy in very small strain stiffness of a sandy gravel, *Géotechnique* 47 No 3, pp 509-521

[39] Jardine R.J. (1992) Some observations on the kinematic nature of soil stiffness *Soils and Foundations* Vol 32 no 2, pp 111-124

[40] De Josselin De Jong G. (1960) De Spanningsverdeling in een homogeen anisotroop elastisch halfmedium, *LGM mededelingen* Deel V, no 2 pp 33–51 (in Dutch)

[41] De Josselin De Jong G. (1963) Consolidatie in drie dimensies, *LGM mededelingen* deel VII no 3 pp 57–73 (in Dutch)

[42] De Josselin De Jong G. (1963) Consolidatie in drie dimensies, II operatorrekening *LGM mededelingen* deel VIII no 2 pp 25–38 (in Dutch)

[43] De Josselin De Jong G. (1964) Consolidatie in drie dimensies, III bolvormige symmetrie *LGM mededelingen* deel VIII no 3 pp 53–65 (in Dutch)

[44] De Josselin De Jong G., Verruijt A. (1965) Primary and Secondary Consolidation of a Spherical Clay Sample *Proc. 6^{th} Int. Conf. Soil M. & F. Engineering sect* 2/25 pp 254 Montreal

[45] Jovičič V., Coop M.R., Simić M. (1996) Objective criteria for determining G_{max} from bender element tests, *Géotechnique* 46 no 2, pp 357-362

[46] Keverling Buisman A.S., Huizinga T.K. (1948) Compution of a Quay Wall in: *Proceedings of the 2^{nd} int. conf. on soil mech. and foundation eng.* Rotterdam

[47] Karádi G., Nagy I.V. (1961) Investigations into the validity of the linear seepage law, IAHR 9^{th} convention, Belgrade

[48] Kondner R.L., Zelasko J.S. (1963) A hyperbolic stress–strain formulation for sands in: *proceedings of the 2nd panamerican conf. on soil mech. and foundation eng.* Sao Paulo

[49] Kuwano R., Connolly T.M., Jardine R.J. (2000) Anisotropic stiffness measurements in a stress-path triaxial cell *Geotechnical testing Journal* 23 no 2 pp 141-157

[50] Kuwano R., Jardine R.J. (2002) On the applicability of cross anisotropic elasticity to granular materials at very small strains, *Géotechique* 52 no 10, pp 727-749

[51] Lancelotta, R.(1995) *Geotechnical Engineering* Balkema Rotterdam, ISBN 9054101792

[52] De Leeuw H.E. (1964) Consolidatie in drie dimensies, VII cilindervormige symmetrie *LGM mededelingen* no 2 pp 17–48 (in Dutch)

[53] De Leeuw H.E. (1965) The theory of three-dimensional consolidation applied to cylindrical bodies *Proc.* 6^{th} *Int. Conf. Soil M. & F. Engineering sect* 2/23 pp 287 Montreal

[54] Lings M.L., Pennington D.S. Nash D.F.T.(2000) Anisotropic stiffness parameters and their measurement in an stiff natural clay *Géotechnique* 50, no 2 pp 109-125

[55] Lings M.L.(2001) Drained and Undrained elastic stiffness parameters *Géotechnique* 51, No 6 pp 555-565

[56] Love A.E.H.(1927) *A treatise on the mathematical theory of elasticity* 4th edn. Cambridge University Press

[57] Mandel J. (1953) Consolidation des Sols (étude mathématique) *Géotechnique* 3 pp 287–299 (*in french*)

[58] Nederlands Normalisatie-instituut (1995) *Geotechniek bepaling van de volumieke massa van vaste (grond)delen. Pyknometer, NEN5111* Delft (*in Dutch*)

[59] Nederlands Normalisatie-instituut (1991) *Geotechniek, TGB 1990, Basiseisen en belastingen, NEN6740* (*in Dutch*)

[60] Nur A., Byerlee J.D. (1971) An Exact Effective Stress Law for Elastic Deformation of Rock with Fluids *Journal of Geophysical Research* vol. 76 No 26 pp 6414-6419

[61] Pickering D.J. (1970) Anisotropic parameters for soil *Géotechnique* 20 No 3, pp 271-276

[62] Parry R.H.G., Wroth C.P. (1981) Shear stress–strain properties of soft clay, in: *soft clay engineering developments in geotechnical engineering* E.W. Brand & R.P. Brenner (eds.) Elsevier Amsterdam ISBN 0–444–4178–2

[63] Raymond G. P. (1970) Discussion: Stresses and displacements in a cross anisotropic soil, by L. Barden *Géotechnique* 20 no 4 pp 456 - 458

[64] Rendulic L. (1935) Der hydrodynamische Spannungsausgleich in zentral entwässerten Tonzylindern *Wasserwirtschaft u. Technik* vol. 2 pp 250-253, 269-273

[65] Skempton A.W. (1954) The pore-pressure coefficients A and B, *Géotechnique* nr 4 pp 143-147

[66] Skempton A.W., Petley D.J. (1970) Ignition loss and other properties of peats and clays from Avonmouth, King's Lynn and Cranberry Moss, *Géotechnique* 20 no 4 pp 343-356

[67] Stokoe K.H.II., Lee J.N.–K., Lee S.H.H. (1991) Characterization of soil in calibration chambers with seismic waves *Calibration Chamber Testing* Huang A.B. (ed.) Elsevier Science Publishing pp 363-376.

[68] Schofield A.N., Wroth C.P. (1968) *Critical state soil mechanics* McGraw-Hill London

[69] Technische Adviescommissie voor de Waterkeringen (1996) *Technisch rapport Geotechnische classificatie van veen* Delft (in Dutch)

[70] Terzaghi K. (1925) *Erdbaumechanik auf Bodenphysikalischer Grundlage* Deuticke Verlag Vienna

[71] Terzaghi K. (1943) *Theorectical Soil Mechanics* Wiley New York

[72] Timoshenko S.P., Goodier J.N. (1970) *Theory of Elasticity, third edition, international student edition* LCCCN 69-13617 McGraw-Hill Kogakusha ltd

[73] Thompson M., Willis J.R. (1991) A Reformation of the Equations of Anisotropic Poroelasticity *Transactions of ASME* vol. 58 pp 612-616

[74] Verruijt A. (1965) Consolidatie in drie dimensies, V bolsymmetrische consolidatie in een oneindig massief, *LGM mededelingen* deel IX no 3 pp 49–72 (in Dutch)

[75] Verruijt A. (1965) Consolidatie in drie dimensies VI bolsymmetrische consolidatie en laboratoriumproeven, *LGM mededelingen* deel X no (1) pp 1–22 (in Dutch)

[76] Verruijt A. (1969) Elastic storage of aquifers in: *Flow through porous media* de Wiest (ed.) R.J.M. Academic Press

[77] Verruijt A. (1982) The Theory of Consolidation *Proc. NATO/ASI, Mechanics of Fluids in Porous Media* Newark Delaware, USA

[78] Viggiani G., Atkinson J.H. (1995) Interpretation of bender element tests, *Géotechnique* 45 no. 1 pp 149-154

[79] Watt J.P., Davies G.F, O'Connel R.J. (1976) The Elastic Properties of Composite Materials *Reviews of Geophysics and Space Physics* 14 pp 541-563

[80] Wood D.M.(1998) *Soil Behaviour and Critical State Soil Mechanics* Cambridge University Press, digital reprint ISBN 0-521-33782-8

[81] Wesley L.D.(1975) *Influence of stress path and anisotropy on the behaviour of soft alluvial clay* PhD Thesis University of London

[82] Yimsiri S., Soga K. (2003) Small-strain stiffness anisotropy: relationship between continuum model and micromechanics model, in: *Deformation Characteristics of Geomaterials*, Di Benedetto et al (eds.) Swets & Zeitlinger, Lisse ISBN 90 5809 604 1

[83] Zdravkovic L., Jardine R.J. (1997) Some anisotropicstiffness characteristics of a silt under general stress conditions, *Géotechnique* 47 no 3, pp 407-437

[84] Zwanenburg C., Van M.A., Brassinga H.E. (2002) Validation of consolidation behaviour of soft soil using sand piles or sand walls, in: *proceedings of the international conference on physical modelling in geotechnics* Phillips R., Guo P., Popescu R. (eds.) St. John's pp 949-953

Samenvatting

De invloed van anisotropie op het consolidatiegedrag van veen

Het gedrag van veen kan worden beschreven in termen als sterk samendrukbaar, heterogeen en anisotroop. Omdat monsters meestal verticaal worden gestoken en alleen met zeer grote inspanning horizontaal of onder een willekeurige hoek worden gestoken is informatie over het gedrag van veen in andere dan verticale richting schaars. In de huidige praktijk wordt dan ook weinig aandacht besteed aan het anisotrope gedrag van veen. In principe kan elke grondeigenschap zoals doorlatendheid, stijfheid of sterkte een anisotroop karakter hebben. Dit proefschrift beperkt zich tot anisotropie in stijfheid en onderzoekt de mogelijkheid om met min of meer conventionele laboratoriumtechnieken de mate van anisotropie van een veenmonster te bepalen.

Het anisotrope gedrag van veen kan worden verklaard door de aanwezigheid van vezels in het materiaal. Afhankelijk van de mate van verwering en organische oorsprong van het veen zullen de vezels bijdragen aan de stijfheid. Als de vezels zijn georiënteerd in één vlak kan verwacht worden dat de stijfheid loodrecht op dit vlak anders is dan de stijfheid die in dit vlak werkt. Anisotropie als gevolg van de aanwezigheid van vezels staat bekend onder de naam structuur anisotropie. Omdat veen een zeer samendrukbaar materiaal is mag worden verwacht dat asymmetrisch belasten eveneens leidt tot een verschil in stijfheid in verschillende richtingen. Dit type van anisotropie staat bekend als geïnduceerde anisotropie.

Het consolidatiegedrag van grond wordt voor een groot deel bepaald door de stijfheid van het materiaal. Verschillen in stijfheid zullen dan ook leiden tot een verschillend consolidatiegedrag. Onder speciale omstandigheden zal het consolidatiegedrag afwijken van de welbekende monotone afname van de wateroverspanning. Deze speciale omstandigheden worden bijvoorbeeld voor een conventionele triaxiaalproef gevonden wanneer een monster wordt geplaatst tussen twee stijve platen terwijl het monster aan de buitenrand draineert. De buitenste rand van het monster zal dan bijna instantaan consolideren. Gelijk met het afstromen van het water uit de buitenrand zal de buitenrand een volumerek ondergaan. In het midden van het monster is de consolidatie nog niet op gang gekomen. Er is hier nog geen water afgestroomd noch treedt er volumerek op. Samen met de stijve plaat zal de volumerek van de buitenrand leiden tot een herverdeling van spanning waarbij een deel van de belasting van de buitenrand wordt overgedragen naar het midden van het monster. Als gevolg hiervan zal de waterspanning in het midden van het monster eerst toenemen. Pas wanneer de consolidatie in het hart van het monster start zal ook hier de waterspanning afnemen. Deze initiële toename van de wateroverspanning als gevolg een herverdeling van spanning staat bekend onder de naam Mandel–Cryer effect. De maximale waarde die de piek kan bereiken is sterk afhankelijk van de stijfheidsparameters van het beschouwde monster. De vraag kan nu gesteld worden of het meten van deze piek kan worden gebruikt voor parameterbepaling.

De analytische oplossing van het consolidatieprobleem van een cilindervormig grondmonster laat zien dat anisotropie het consolidatiegedrag op drie wijzen beïnvloed. Als eerste wordt genoemd het Mandel–Cryer effect. De maximale waarde die de piek bereikt wordt voor een belangrijk deel bepaald door de stijfheid van het beproefde materiaal. Voor een materiaal met een relatief grote radiale stijfheid en een relatief geringe axiale stijfheid voorspelt de analytische oplossing een groot Mandel–Cryer effect. Terwijl voor de omgekeerde omstandigheden, een relatief geringe radiale

stijfheid en relatief hoge axiale stijfheid, slechts een verwaarloosbare Mandel–Cryer piek wordt verwacht. De tweede wijze waarop anisotropie het consolidatiegedrag beïnvloedt is de initiële wateroverspanning direct na belasten. Initieel, direct na belasten, zal het monster ongedraineerd reageren. Voor een volledig verzadigd monster betekent dit dat het monster vervormt onder een constant volume. Voor isotroop materiaalgedrag volgt dan dat de toename van de waterspanning gelijk is aan de toename van de isotrope totaal spanning. Voor anisotroop materiaalgedrag draagt de deviator spanning ook bij aan de volumerek. Dit leidt tot een andere initiële wateroverspanning. Het derde aspect is de hydrodynamische periode. Dit is niet nader uitgewerkt.

De wiskundige analyse is gebaseerd op lineair elastisch materiaal gedrag. Grondgedrag, met name het gedrag van slappe weinig draagkrachtige grondsoorten, is sterk door plasticiteit beïnvloed. Zelfs voor kleine rekken treden er blijvende vervormingen op. Echter voor overgeconsolideerde monsters kan de stijfheid worden beschreven met equivalente elastische moduli die een geringe mate van plasticiteit verdisconteren. In de vergelijking van de wiskundige analyse met de meetdata zijn dergelijke moduli in toegepast.

Teneinde de wiskundige analyse te verifiëren is een aantal triaxiaalproeven uitgevoerd op veenmonsters. De waterspanningen in het hart van het monster zijn gemeten door gebruik te maken van een miniatuur drukopnemer die verbonden is met een naald. Door de naald door het vlies in het monster te steken bereikt het uiteinde van de naald precies het hart van het monster.

Metingen van waterspanning aan conventionele triaxiaal monsters vertonen nauwelijks het Mandel–Cryer effect. Dit kan worden verklaard door de weerstand in de drains, die het uitgeperste water afvoeren, in combinatie met de sterk variabele doorlatendheid van veen. Omdat de invloed van drainweerstand voor kleine monsters relatief groter is dan voor grote monsters, is een grootschalige proef uitgevoerd. Metingen van de drukken in de drains tonen aan dat de drainweerstand in de grootschalige proef verwaarloosbaar is. De grootschalige proef is in twee fasen uitgevoerd. De eerste fase bestaat uit metingen na een geringe isotrope voorbelasting. In de tweede fase zijn metingen uitgevoerd na een axiale voorbelasting. In de eerste fase laten de gemeten waterspanningen slechts een klein Mandel–Cryer effect zien. De metingen uit deze fase kunnen niet worden gefit op de analytische oplossing. De metingen uit de tweede fase laten een duidelijk Mandel–Cryer effect zien. De metingen sluiten goed aan bij de wiskundige analyses. Een nadere beschouwing van de doorlatendheid van het beproefde veen laat zien dat tijdens de eerste fase de doorlatendheid aanzienlijk varieerde. Terwijl tijdens de tweede fase de verandering in doorlatendheid verwaarloosbaar is.

De metingen van zowel de conventionele als de grote monsters laten duidelijk de invloed van anisotropie op de initiële wateroverspanning zien. Deze invloed wordt teruggevonden in het effectieve spanningpad, ESP, tijdens ongedraineerd belasten. Voor isotroop overgeconsolideerd materiaalgedrag zal het ongedraineerde ESP verticaal verlopen, voor anisotrope overgeconsolideerde condities zal het ESP onder een hoek verlopen. Hoe groter deze hoek, hoe groter de mate van anisotropie. Uit de metingen blijkt dat de mate van anisotropie sterk afhangt van de belastingsgeschiedenis van het monster. Voor isotroop voorbelaste condities laten de beproefde monsters slechts een verwaarloosbare mate van anisotropie zien. De axiaal voorbelaste monsters laten een duidelijk afwijkende hoek in het ESP zien hetgeen duidt op een toename van anisotropie. De toename is voor horizontaal gestoken monsters vergelijkbaar met die voor verticaal gestoken monsters. Ondanks de axiale voorbelasting tonen metingen aan dat met name de stijfheid in radiale richting is toegenomen. De resultaten kunnen worden verklaard door het voorspannen van de vezels. De monsters zijn, zowel in horizontale als in verticale richting, gestoken onder een vlak maaiveld. Niet alleen de triaxiaalproeven, maar ook oedometer,- en simple shear proeven laten weinig verschil zien in resultaten tussen de horizontaal en verticaal gestoken monsters voor niet voorbelaste of isotroop voorbelaste condities. Voor deze condities hebben de vezels niet of nauwelijks een oriëntatie. Als gevolg van de axiale voorbelasting worden de vezels in een bepaalde richting gestrekt en raken in elkaar verstrikt. Dit leidt tot een toename van de radiale stijfheid. Omdat de metingen vergelijkbare resultaten opleveren voor zowel de horizontaal als voor de verticaal gestoken monsters kan worden geconcludeerd dat de aanwezigheid van de vezels op zich nog niet tot anisotropie leidt. De

anisotropie van het beproefde materiaal heeft een sterk geïnduceerde component.

Er kan worden geconcludeerd dat voor conventionele triaxiaalproeven metingen van het Mandel–Cryer effect niet kunnen worden gebruikt voor het bepalen van de mate van anisotropie van veen. Zelfs met een proefopstelling waarin drainweerstand geen rol speelt zal de veranderende doorlatendheid het Mandel–Cryer effect maskeren. Echter de helling van de ongedraineerde ESP voor overgeconsolideerde monsters kan goed worden gebruikt voor het vaststellen van de mate van anisotropie van het beproefde materiaal.

De toepassing van het meten van de ongedraineerde ESP voor de bepaling van de mate van anisotropie wordt geïllustreerd door een serie proeven op overgeconsolideerde veenmonsters die zijn gestoken onder en naast de dijk van het eiland Marken. De monsters die onder de dijk zijn gestoken zijn duidelijk meer axiaal voorbelast, als gevolg van het gewicht van de waterkering, dan de monsters die ter plaatse van de teen van de dijk gestoken zijn. De ongedraineerde ESP van de monsters afkomstig van onder de dijk hebben een duidelijk grotere helling dan die van de monsters afkomstig uit de teen van de dijk. Dit geeft een hogere mate van anisotropie aan voor de monsters die van onder de dijk afkomstig zijn.

Een geheel ander voorbeeld van radiale consolidatie wordt gevonden rondom een verticale drain. Analytische oplossingen voor het consolidatieprobleem rondom een verticale drain laten zien dat het Mandel–Cryer effect voor isotroop materiaalgedrag niet optreedt. Echter voor anisotroop materiaal voorspelt de analytische oplossing niet alleen een gering Mandel–Cryer effect, maar tevens een versnelling of een vertraging van het consolidatie proces dat sterker is dan uit het verschil in consolidatie coëfficiënt verwacht mag worden.

C. Zwanenburg, *The influence of anisotropy on the consolidation behaviour of peat* proefschrift, Technische Universiteit Delft. Delft University Press, 2005

About the Author

Cor Zwanenburg was born on 26^{th} of July 1971 in Rotterdam. In 1989 he attended Delft University of Technology where he started a civil engineering study. During his study he specialised in hydraulic engineering. He cooperated in a long–term study on river bifurcations that was conducted on the Bangladesh University of Engineering Technology, BUET in Dhaka Bangladesh. After returning to Delft he graduated in 1995.

Since 1996 he works as a consultant at GeoDelft. His activities at GeoDelft mainly involve consultancy for soft soil problems, regarding embankments for (rail)road constructions and dikes. He joined several research groups initiated by CUR and CROW concerning settlement and stability. From 2000 to 2001 he was involved in the design of full scale field test on a river dike along the river De Lek in The Netherlands. The test was successfully conducted in 2001.

Since April 2001 he was in detachment at Delft University of Technology for four days a week. There he started a study on consolidation of soft soils under supervision of Prof. dr. F.B.J. Barends. The results of the study are presented in this thesis.